AN ABSTRACT OF THE DISSERTATION OF

Colby D. Mangini for the degree of Doctor of Philosophy in Radiation Health Physics
presented on November 26, 2012.
Title: Beta-Particle Backscatter Factors and Energy-Absorption Scaling Factors for Use with Dose-Point Kernels

Abstract approved:_____
David M. Hamby

'Hot particle' skin dosimetry calculations are commonly performed using homogeneous dose-point kernels (DPK) in conjunction with scaling and backscatter models to account for non-homogeneous geometries. A new scaling model for determining the actual DPK for beta-particles transmitted by a high-Z source material has been developed. The model is based on a determination of the amount of mono-energetic electron absorption that occurs in a given source thickness through the use of EGSnrc (Electron Gamma Shower) Monte Carlo simulations. Integration over a particular beta spectrum provides the beta-particle DPK following self-absorption as a function of source thickness and radial depth in water, thereby accounting for spectral hardening that may occur in higher-Z materials. Beta spectra of varying spectral shapes and endpoint energies were used to test our model for select source materials with $7.42 < Z \leq 94$. A new volumetric backscatter model has also been developed. This model corrects for beta-particle backscattering that occurs both in the source medium and in the atmosphere surrounding the source. Hot particle backscatter factors are constructed iteratively through selective integration of point-source backscatter factors over a given source geometry. Selection criteria are based on individual source-point positions within the source and determine which, if any, backscatter factors are used. The new scaling model and backscatter model were implemented into the DPK-based code VARSKIN 4 for extensive dose testing and verification. Verification results were compared to equivalent Monte Carlo simulations. The results demonstrate that significant improvements can be made to DPK-based models when dealing with high-Z volumetric sources in non-homogeneous geometries.

Beta-Particle Backscatter Factors and Energy-Absorption Scaling Factors for Use With Dose-Point Kernels

by

Colby D. Mangini

A DISSERTATION

submitted to

Oregon State University

in partial fulfillment of
the requirements for the
degree of

Doctor of Philosophy

Presented November 26, 2012
Commencement June 2013

Doctor of Philosophy dissertation of Colby D. Mangini presented on November 26, 2012.

APPROVED:

Major Professor, representing Radiation Health Physics

Head of the Department of Nuclear Engineering and Radiation Health Physics

Dean of the Graduate School

I understand that my dissertation will become part of the permanent collection of Oregon State University libraries. My signature below authorizes release of my dissertation to any reader upon request.

Colby D. Mangini, Author

ACKNOWLEDGEMENTS

This research was made possible by a Nuclear Regulatory Commission (NRC) grant. Without it, I would likely not have realized the need for this work. I am very grateful to the NRC for giving me the opportunity to address their research needs.

I am also very grateful for having an exceptional doctoral committee and want to thank Dr. Higley, Dr. Reese, Dr. Krane, Dr. Minc, and of course, my advisor, Dr. David Hamby. Dr. Hamby has been more than I could have ever asked for in an advisor. His years of experience have been an invaluable asset throughout this entire experience. Rather than instructing me on what to do when a crossroad was reached, Dr. Hamby provided guidance and asked thought provoking questions that allowed me to reach the correct path on my own. In fact, Dr. Hamby always provided a working atmosphere that made me feel as though I was a colleague and not a subordinate. And for not, I am ever grateful.

I would also like to thank Jarvis Caffrey for his help with EGSnrc. Without Jarvis going to Italy and learning EGSnrc from the gentleman that wrote the code, this work would be forever lost in MCNP simulations.

Lastly, I would like to thank my family. My parents put three children through the same liberal arts college over a seven year period. Without their love, support, and sacrifices, I would not be where I am today. I met my wife, Kyla, during that time in college and we married shortly after graduation. Returning to graduate school after we had already started our careers and life together was a difficult decision to make. I owe a great debt of thanks to wife for providing unconditional support and encouragement as I strived to achieve such a lofty goal. I am done with school now, I promise.

TABLE OF CONTENTS

TABLE OF CONTENTS (Continued)

Page

TABLE OF CONTENTS (Continued)

Page

TABLE OF CONTENTS (Continued)

Page

LIST OF FIGURES

LIST OF FIGURES (Continued)

Figure Page

LIST OF FIGURES (Continued)

Figure Page

LIST OF FIGURES (Continued)

Figure Page

LIST OF FIGURES (Continued)

Figure Page

LIST OF FIGURES (Continued)

Figure Page

LIST OF FIGURES (Continued)

Figure Page

LIST OF FIGURES (Continued)

Figure Page

LIST OF TABLES

Table Page

LIST OF APPENDICES

LIST OF APPENDIX FIGURES

Figure Page

LIST OF APPENDIX TABLES

Beta-Particle Backscatter Factors and Energy-Absorption Scaling Factors for Use with Dose-Point Kernels

1 Introduction

1.1 Motivation

The motivation for this research was to develop 'hot particle' dose-point kernels (DPK) that can be used to account for internal source absorption, source backscattering, and atmospheric backscattering when computing beta-particle skin doses. We have accomplished this by developing two separate models: a scaling model to predict non-homogeneous DPK's in the presence of a high-Z source material, and a volumetric backscatter model to predict the dose perturbations from both source and atmospheric backscattering. The models are applicable to all beta-emitting radionuclides; spherical, cylindrical and slab source geometries; and source materials with $7.42 < Z \leq 94$.

The term 'hot particle' refers to a small, highly radioactive particle containing fuel fragments or activation products. Hot particles are typically found at nuclear reactor facilities and nuclear materials facilities. Their physical size makes them nearly invisible with a nominal diameter ranging from several μm to ~1 mm. This allows them to cling to one's skin or clothing without notice, resulting in high, localized skin doses from the emitted beta-particles and low-energy gamma rays.

In the U.S., the Nuclear Regulatory Commission (NRC) is charged with monitoring its licensees for compliance with the regulatory dose limits for the skin, as defined in Title 10, Part 20, of the *Code of Federal Regulations* (CFR). The skin depths and dose limits chosen by the NRC are influenced in part by the recommendations of the International Commission on Radiation Protection (ICRP), specifically ICRP Publications 60 (1991) and 103 (2007). Compliance with 10CFR20 requires that dose levels to the skin be assessed at a depth of 7 mg cm^{-2} (0.007 cm) over 10 cm^2 area. A skin depth of 7 mg cm^{-2} corresponds to the nominal

depth of the basal-cell layer of the epidermis which is identified in ICRP Publication 59 (1992) as being highly susceptible to ionizing radiation damage.

Dose verification and compliance with 10CFR20 requires accurate determination of worker skin doses through some form of measurement or computational technique. The two most common computational methods used for determining skin doses are Monte Carlo particle transport and DPK-based codes. Monte Carlo transport codes such as Monte Carlo n-Particle version 5 (MCNP5) (Brown, 2003) and Electron-Gamma-Shower (EGSnrc) (Kawarakow and Bieloajew 1998; Kawarakow 2000; Kawarakow and Rogers 2000) are viewed as the standard for dose calculations due to their superior accuracy and ability to simulate nearly any source/target geometry encountered in practice. However, they require that the user have a prerequisite level of coding expertise and can have long computation times.

DPK-based codes, such as VARSKIN (Traub 1987; Durham 1992, 2006; Hamby 2011) rely on the numerical integration of a point kernel over the source volume and the dose region of interest. While this is computationally much faster than Monte Carlo simulation, accuracy is often sacrificed. In one way or another, all DPK's relate the dose at a given point to a radiation source at some other point in the same medium. The medium for which the DPK is defined is typically water, as this allows for direct comparison with tissue. If the source material is not water, various scaling techniques can be used to equate the beta-particle track in the source to an "equivalent" water distance. The DPK at the equivalent water distance is then used in the calculation of dose. These scaling methods have been shown to be highly inaccurate for calculating dose for high-*Z* sources, with discrepancies increasing with Z, source size and skin depth.

Current scaling methods are insufficient for beta-particle self-absorption and beta spectra hardening that occurs in the high-*Z* source material (Cross 2001; Reynaert 2001; Cho 2004; Sherbini 2008), and subsequently overestimate dose at shallow depths while underestimating dose at greater depths. The overestimation at shallow depths is partially offset by the increase in dose that can result from internal source backscattering of beta-particles toward the skin. While this scattering contribution has been studied extensively for medical physics applications, it is limited to point-source assumptions and has not yet been expanded to

volumetric sources. In addition to internal source scatter, DPK's must consider the amount of electron scattering that will occur in the medium surrounding the source (i.e., atmospheric scattering). Significant work has been done by Cross (1991b, 1992c) to address this issue for point-sources, however, the volumetric model developed by Durham (2006) for VARSKIN is very limited in its accuracy and applicability.

1.2 Objectives

The first objective of this research is to develop a beta energy-absorption scaling model for high-Z source materials. Its intended use is for the creation of non-homogeneous DPK's applied in hot particle skin dosimetry calculations.

The second objective of this research is to develop a volumetric backscatter model for typical hot particle geometries. The model will estimate dose perturbations due to both source and atmospheric backscattering. The backscatter model, as well as the scaling model, will be applicable to all beta-emitting radionuclides; spherical, cylindrical, and slab source geometries; and source materials with $7.42 < Z \leq 94$

2 Literature Review

2.1 Anatomy of the Skin and Radiation Effects

ICRP Publication 59 (1992) groups the many complex layers of human skin into two main structures: the epidermis encompasses the outermost layers, whereas the dermis consists of the deeper layers (Fig. 2.1). The epidermis is stratified with the first 15-20 layers, or 25% of the total epidermal thickness, containing dead cells. This section of the epdidermis is called the stratum corneum. Directly beneath the stratum corneum are 4-5 layers of cells making up the stratum granulosum. Cells in the stratum granulosum become progressively flattened due to the loss of their cytoplasmic organelles and eventually the nucleus degenerates.

The term 'basal layer' is given to the single layer of cells which make up the stratum germinativum. The basal layer, in addition to the preceding stratum spinosum layers, provides the structural and proliferative functions for the epidermis. As a result, ICRP Publication 59 (1992) reports these two layers to be the most viable and radiosensitive of the epidermis.

The dermis is structurally divided into two distinct layers: the superficial papillary dermis and the deeper, thicker reticular dermis. The primary functions of the papillary dermis are thermoregulation and supporting the stratum germinativum, whereas the reticular dermis is the primary structural and mechanical component of the skin. The thickness of the dermis varies with body location. ICRP Publication 59 (1992) reports a range of 1.0-3.0 mm, about 10 times the epidermal thickness.

The deterministic effects resulting from irradiation of the skin have been extensively reviewed by Hopewell (1990). Of those effects, ICRP Publication 59 (1992) and Hopewell (1991) have outlined the following acute deterministic effects to be of greatest concern when dealing with beta and low-energy x-ray radiation.

- Moist desquamation (4-6 week onset time): loss of the cells in the basal layer of the epidermis after high-dose acute exposure to the skin by moderate to high-energy β radiation or low-energy x-rays.

- Acute ulceration (<14 day onset time): an early loss of the epidermis and deeper dermal tissue caused by interphase death of the fibroblasts and vascular endothelial cells after irradiation from hot particles.

- Acute epithelial necrosis (<10 day onset time): interphase death of post mitotic cells in the upper viable layers of the epidermis after exposure to low-energy beta-particles of energies ≤ 0.2 MeV maximum energy.

Stochastic effects resulting from skin exposure in both penetrating and non-penetrating radiations are expected to arise in the basal layer of the epidermis at a nominal depth of 7 mg cm^{-2}. However, the risk of stochastic effects is of much less concern when dealing with hot particle radiation. The National Council of Radiation Protection and Measurement (NCRP) Report No. 106 (1989) and Charles (1991) have reported that the number of cells at risk following hot particle radiation is so small that the risk of cancer induction is negligible. As a result, ICRP Publication 59 (1992) presents acute ulceration as the end-point to be prevented for hot particle exposures.

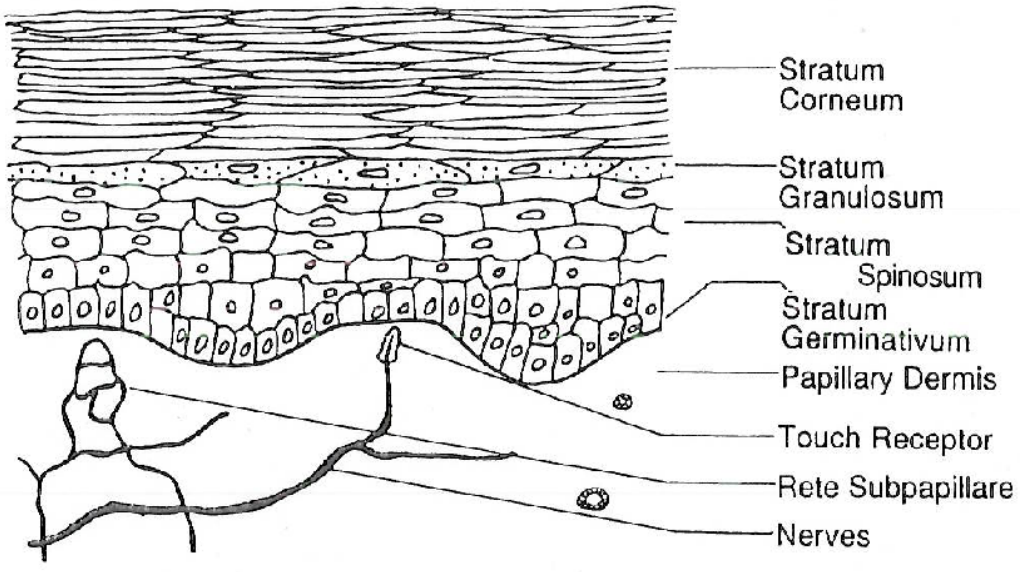

Fig. 2.1. Diagram of the different layers of the epidermis in human skin (ICRP Publication 59 1992).

2.2 Recommendations and Regulations

Charles (1990) found 10-15 mg cm^{-2} to be the optimal monitoring depth for preventing acute ulcerations from hot particle exposure. He used biological data from pigs on the deterministic effects following hot-particle beta exposure of various beta energies and source sizes. His work concluded that the average dose delivered within a few hours over an area of 1 cm^2 should be limited to 1 Sv for small sources with dimensions less than about 1 mm. Charles' findings are in agreement with those initially reported by Hopewell (1986). However, in NCRP Report No. 130 (1999), it is recommended that for hot particles on the skin, the limiting dose be 5 Sv averaged over the most exposed 1 cm^2 of skin at a depth of 7 mg cm^{-2}.

ICRP Publication 60 (1991) has chosen an overall monitoring skin depth of 7 mg cm^{-2} as this is the nominal depth in which stochastic effects are expected to be seen in the basal layer of the epidermis. Uniform exposures which are limited by stochastic effects are averaged over the whole area of the body. For localized exposures resulting in acute deterministic effects however, such as those expected by hot particles, the ICRP recommendation is for the dose to be average over a 1 cm^2 area, regardless of the area exposed. The ICRP recommended annual skin dose limit for both uniform and localized exposure is 0.5 Sv.

While NRCP Report No.130 (1999) initially recommended hot particle skin exposures should be limited to 5 Sv at a depth of 7 mg cm^{-2} and averaged over an exposure area of 1 cm^2, this recommendation was modified in NCRP Statement No. 9 (2001). In order to account for instances when hot particles were off the skin, the NCRP changed its recommendation to 0.5 Sv averaged over the most highly exposed 10 cm^2 of skin. The reasoning was that the degree of movement of a particle on clothing or hair and the separation between the particle and skin are difficult to account and quantify. Therefore, averaging the dose over an area of 10 cm^2 was found to provide a simple way to account for such conditions and provide a harmonious limit.

Prior to NCRP Statement No. 9 (2001), 10CFR20 adopted an annual skin dose limit of 0.5 Sv. The dose was to be measured at a skin depth of 7 mg $cm^{-2}$and averaged over the contiguous 1 cm^2 area receiving the highest exposure. However, the Issue Summary 2002-10

(2002) put forth by the NRC notified its licensees of changes in the regulatory dose limit for the skin in 10CFR20. As with the NCRP change, the averaging area in 10CFR20 was increased from 1 cm^2 to 10 cm^2. Issue Summary 2002-10 (2002) cites NRC funded research that has shown exceeding the skin dose limit of 0.5 Sv as a result of hot particle exposure does not pose a health hazard and will not result in the same risk as exceeding other organ or whole body dose limits. As a result of the change, exposures to areas less than 10 cm^2 will in effect, be subject to higher regulatory dose limits permitted under the old rule. Publication 103 (2007) by the ICRP maintains the same recommendation for skin dose monitoring as first established in ICRP Publication 60 (1991).

2.3 Hot Particles

The term 'hot particle' refers to a small, highly radioactive particle containing fuel fragments or activation products. Hot particles are typically found at nuclear reactor facilities and nuclear materials facilities. Their physical size makes them hardly visible, with a nominal diameter ranging from several μm to ~1 mm. This allows them to cling to one's skin or clothing without notice, resulting in high, localized skin doses from the emitted beta-particles and low-energy gamma rays. NCRP Report No. 130 (1999) lists the following common hot particle radionuclides: ^{51}Cr, ^{54}Mn, ^{59}Fe, ^{60}Co, ^{89}Sr, ^{90}Sr, ^{90}Y, ^{95}Nb, ^{95}Zr, ^{103}Ru, ^{141}Ce, ^{144}Ce, and ^{144}Pr. Of those listed, ^{60}Co is the most common. Cobalt-based alloys are commonly used in valves and pumps, as they are very resistant to wear. However, when those components undergo small amounts of wear, the stable ^{59}Co particles that break loose undergo neutron activation in the reactor core, thereby creating ^{60}Co. Other activation products include ^{51}Cr, ^{54}Mn and ^{59}Fe. These are typically found in activated rust particles. The remaining nuclides in the list are fission products that could have escaped the fuel element.

The first recorded use of the term 'hot particle' was over 40 years ago in reference to the increased risk posed by extremely non-uniform dose patterns in the lungs as the result of minute beta sources from radioactive fallout. At that time, it was believed by some that the non-uniform dose delivered by hot particles resulted in an increased carcinogenic risk. This idea was coined the 'hot particle hypothesis'. However, Albert (1967) showed that electron

and beta radiation that produces a sieve pattern of exposure reduces the tumourigenic effect and delays tumor appearance. Charles (1988) demonstrated the same results using various source arrays and concluded that uniform beta-particle exposures are the most carcinogenic.

Over the years, there have been numerous reports from nuclear facilities of hot particle exposures. In the United States, Reece (1991) discusses a June 1986 incident where an employee at the McGuire nuclear station received a hot particle dose of 0.107 Sv. In October 1986, an employee received a skin dose of 5.12 Sv on the hand and in November of the same year, an employee at the Summer plant received a dose of 4.20 Sv on the hand. In 1998, two hot particles were found at the Vandellos II nuclear power plant in Tarragon, Spain. The particles were recovered from the floor and no exposures were reported. Bakali, et al. (2001) presented dose calculations and measurements for these particles with the highest measured skin dose rate being 0.162 Sv h^{-1}.

Charles and Harrison (2007) provide an extensive review and history of hot particle sources. They use a case study to exemplify the current state of hot particle dosimetry, radiobiology, and epidemiology. Their case study is based on discrete fragments of irradiated fuel found in 1995 on the foreshore at the Doureay nuclear site in Scotland. The principal radionuclides contained in the fuel fragments were ^{137}Cs and $^{90}Sr/^{90}Y$. Charles and Harrison presented an analysis of possible doses and risks for the following biological pathways: skin exposure, eye exposure, ear exposure, ingestion, and inhalation. They concluded that one of the more active particles found on the shores (10^5 Bq ^{137} Cs) would only result in a skin dose rate of about 0.30 Sv h^{-1}. Exposure times of more than 15 hours would be needed for acute ulcerations to appear.

2.4 Dose-Point Kernels for Hot Particle Dosimetry

2.4.1 Empirical Point Kernels

The spatial distribution of energy absorption from beta-particle sources is the basic physical information required for beta-particle dosimetry. These distributions form the basis of absorbed dose from an isotropic point-source in an infinite homogeneous medium. Water is

typically the medium that is chosen to represent tissue, as it is a very close approximation. The work of Loevinger (1954, 1956) was pioneering in the determination of the first 'point-source energy distribution function'.

Through the use of various sets of experimental data in air and polystyrene, Loevinger (1956) developed a relatively simple mathematical function that was able to account for 90-95 percent of the beta energy absorption, with reasonable accuracy. His two-parameter formula yielded the point-source energy distribution function, I (with units of absorbed energy per gram of tissue per disintegration), at a distance r from a point-source of beta-particles where $r = \mu x$. The first parameter, μ, is the beta absorption coefficient of a given material in units of $cm^2\ g^{-1}$. Loevinger introduced a normalization factor, k, ensuring that the average beta-particle energy was returned when the distribution was integrated over all space. His formula can be written as

$$r^2 I = k\left\{\left[c - re^{1-(r/c)}\right]_1 + \left[re^{1-r}\right]_2\right\}, \tag{2.1}$$

where

$$[\ ]_1 \equiv 0, r \geq c. \tag{2.2}$$

The second parameter in his formula, c, gives the value of the first square bracket when $r = 0$ and the value of r at which the first bracket is equal to zero. Loevinger (1956) provided the following values soft tissues values for c,

$$c = \begin{cases} 1 & 0.17 < E_0 < 0.5 \text{ MeV} \\ 1.5 & 0.5 < E_0 < 1.5 \text{ MeV}. \\ 2 & 1.5 < E_0 < 3 \text{ MeV} \end{cases} \tag{2.3}$$

where E_0 is the maximum energy of the beta spectrum and soft tissue is the absorption material.

2.4.2 Moments-Method Point Kernels

Spencer (1955) used the moments method to numerically solve the electron transport equation in the steady state. His calculations were based on the following assumptions: (1) the electrons are in a homogeneous medium, extending in all directions around the source to a distance greater than the electron range; (2) range straggling due to large single-energy losses occurring in both the radiative and inelastic collisions are neglected; and (3) the electrons lose their energy continuously until their kinetic energy is completely exhausted. The last assumption yields the following expression for the residual range, r_0,

$$r_0 = \int_0^{E_0} \frac{dE}{dE/dr}, \tag{2.4}$$

where E is the kinetic energy of an electron as it slows down, E_0 is the initial electron energy, and dE/dr is the average rate of energy loss, i.e., stopping power. Residual range was later called the 'continuous slowing down approximation' (CSDA) range.

Once the 'residual range moments' for electron flux, $I_0(r/r_0)$, were determined, Spencer (1955) calculated the energy dissipation distribution, $I(r)$, where r is the radial distance from an isotropic point-source at the center of a spherical volume. These two terms can be related using

$$I(r) = \frac{1}{r_0}\int_0^{r_0} dr\left(\frac{dE}{dr}\right) I_0(r / r_0). \tag{2.5}$$

Equation (2.5) assumes that each electron contributing to the flux, $I_0(r/r_0)$, at r/r_0 dissipates energy at the average rate dE/dr per unit path length traversed. Spencer (1959) re-wrote the energy dissipation distribution such that it was a scaled, dimensionless function, $J(\mu)$,

$$J(\mu, E_0) = \frac{I(r)}{(dE/dr)_{E_0}}, \tag{2.6}$$

where μ is the scaled distance of r/r_0, $(dE/dr)_{Eo}$ is the stopping power at E_0, and $I(r)dr$ is the average energy per electron dissipated in the spherical shell between r and $r+dr$.

Spencer (1959) tabulated $J(\mu,E_0)$ for mono-energetic electron energies ranging from 0.025 to 10 MeV for scaled distance of μ at increments of 0.025μ up to 0.975μ. He provided results for carbon (Z=6), aluminum (Z=13), copper (Z=29), tin (Z=50), and lead (Z=82), in addition to air and polystyrene. He also included formula and methods for interpolation in both energy and Z. In addition to point-source distributions, Spencer tabulated distributions for plane perpendicular sources.

The integration of $J(\mu,E_0)$ over a known beta spectrum provides the energy dissipation distribution required for beta-particle dosimetry. This was originally performed by Cross (1967) for 15 beta-emitting radionuclides. He showed that for a beta point-source of a normalized energy spectrum, the dose rate at a distance r can be determined by

$$J'(r) = \frac{B}{4\pi r^2} \int_0^{E_{\max}} N(E)\left(\frac{dE}{dr}\right) J(\mu, E)dE, \qquad (2.7)$$

where E_{max} is the endpoint energy of the beta spectrum, $N(E)dE$ is the fraction of beta-particles emitted per MeV per disintegration that have energies between E and $E+dE$, dE/dr is the stopping power of an electron of initial energy E, and B is a constant to convert dose per electron to rad/mCi-h. When compared to measured beta point-source dose distributions for beta endpoint energies from 0.16 to 3.58 MeV, Cross found good agreement (<4%) up to the distance in which 95% of the beta energy was absorbed. Discrepancies beyond this distance were attributed to the lack of energy-loss straggling inherent in Spencer's data. Cross (1982) further extended his list to 95 radionuclides years later where he provided tables of $r^2J'(r)$ for both isotropic point-sources and isotropic plane sources.

Similar to Cross, Berger (1971) used Spencer's data to tabulate a 'scaled absorbed-dose distribution', F, for a number of radionuclides and monenergtic electrons in water. His tabulated kernels spanned 75 common beta-emitting radionuclide and monenergetic electron energies ranging from 0.025 to 4 MeV. Berger re-wrote Spencer's dimensionless energy dissipation distribution as

$$J(\mu, E_0) = 4\pi r^2 \frac{E_0}{(dE/dr)_{E_0}} \Phi(r, E_0), \qquad (2.8)$$

where $\Phi(r,E_0)$ is the 'specific absorbed fraction' and represents the fraction of energy deposited per gram at a distance r from a point-source. The quantity $4\pi\rho r^2\Phi(r,E_0)dr$ is the fraction of emitted energy that is absorbed in a spherical shell of radius r, thickness dr, density ρ, and is normalized such that

$$4\pi\rho\int_0^\infty r^2\Phi(r,E_0)dr = 1. \tag{2.9}$$

As with Spencer and Cross, Berger (1971) used a scaled distance when tabulating his data. Rather than using the CSDA range, he used the radial distance at which 90% of the emitted electron energy was deposited, X_{90}. His dimensionless scaled distance was written as $\xi = r/X_{90}$. For mono-energetic electrons, Berger defined the relationship between the scaled absorbed-dose distribution and the specific absorbed fraction as

$$F(\xi,E_0) = 4\pi\rho r^2\Phi(r,E_0)\frac{dr}{d\xi} = 4\pi\rho r^2 X_{90}\Phi(r,E_0). \tag{2.10}$$

When a distribution of electron energies is considered, the specific absorbed fraction is given by

$$\Phi_\beta = \frac{1}{E_{av}}\int_0^{E_{\max}} E\ N(E)\Phi(x,E)dE, \tag{2.11}$$

where

$$E_{av} = \int_0^{E_{\max}} E\ N(E)dE. \tag{2.12}$$

The scaled absorbed dose distribution is then

$$F_\beta(\xi) = 4\pi\rho r^2\Phi_\beta(r)\frac{dr}{d\xi} = 4\pi\rho r^2 X_{90}\Phi_\beta(r), \tag{2.13}$$

where X_{90} is determined from the beta-particle energy distribution.

Berger estimated his tabulated $F(\xi,E_0)$ values to have an accuracy of 4% or better at distance $r \leq 0.9X_{90}$ from the source. For $r > 0.9X_{90}$, the results are expected to be less accurate and to underestimate the absorbed dose. Similar results were expected for $F_\beta(\xi)$ with an accuracy of 4% or better at a distance $r \leq X_{90}$ from the source. Berger attributed any differences between his absorbed-dose distributions and those of Cross (1967) to the method of computation and slight differences in the input data for electron mean energy and beta-particle range.

Berger's (1971) scaled tabulation of $F(\xi,E_0)$ and $F_\beta(\xi)$ allowed for convenient absorbed dose calculations once one calculated the 90-percentile distance for the electron/beta-particle in question. Having done so, one could look up the appropriate scaled absorbed-dose distribution, use Eq. (2.10) or Eq. (2.13) to solve for $\Phi(r,E_0)$ or $\Phi_\beta(r)$, respectively, and then calculate tissue absorbed dose rate using

$$R(r,E_0) = A\ n\ k\ E_0\ \Phi(r,E_0), \tag{2.14}$$

for monenergetic electrons, and

$$R_\beta(r) = A\ n_\beta\ k\ E_{av}\ \Phi_\beta(r), \tag{2.15}$$

for beta-emitter. In both equations, A is the source activity in disintegrations per second, n is the number of electrons or betas emitted per disintegration, and k is a constant equal to 1.6E-08 g-rad/MeV.

Through manipulation of Cross' (1982) beta dose distributions, Chabot (1988) developed an alternative point kernel approach for absorbed dose calculations. His dose-point kernel, similar in form to those used in photon dosimetry, is given by

$$R_\beta(r) = \frac{C\ A\ B(r)\ S_m e^{(-\nu r)}}{4\pi r^2}, \tag{2.16}$$

where $B(r)$ is a dose buildup factor, S_m is the effective value of the collision mass stopping power (Mev mg^{-1} cm^2), ν is the attenuation coefficient (cm^{-1}) for unit density water, and C is a unit conversion constant. As with the point kernels proposed by Cross (1967, 1982) and

Berger (1971), Chabot's kernel based on Spencer's theory (1955, 1959) allowed for an easy evaluation of both point-point beta dose rates and average dose rates over a specified area or volume.

2.4.3 Monte Carlo Point Kernels

Monte Carlo particle transport allows for the transport problem of particles in matter to be solved with a very high degree of accuracy, provided that one has existing knowledge of the elementary collision processes. Methods for Monte Carlo calculations for electron were originally published in great detail by Berger (1963). In his ground breaking work, Berger proposed the use of 'condensed histories' when simulating the transport of electrons. In general particle transport, particles are 'born' according to a predetermined source distribution. Once born, the particle travels a given distance to a point of collision and loses energy as determined by a probability distribution based on the total interaction cross section. The particle then scatters at an angle to the next point of collision according to the corresponding differential scatter cross section. This process is known as the random walk and is repeated until the particle is absorbed or leaves the defined geometry. Each birth to 'death' process is called a 'history'.

The main issue with the simulation of electron transport in matter is the number of 'histories' required for tracking the particle as it slows down. Given the Coulombic nature of electrons, typical fast electrons and resulting secondary electrons will undergo hundreds of thousands of interactions before they can be absorbed. When combined with the number of histories required for acceptable statistical uncertainty, the nature of electron interactions creates an insurmountable computing challenge. The condensed history method proposed by Berger (1963) condenses a large number of transport and collision processes into a single electron 'step'. The net effect of many interactions in each step is sampled from pertinent multiple scattering theories.

Berger's original work also defined two basic classes of condensed history algorithms: Class 1 schemes and Class 2 schemes. The two schemes differ mainly in how they handle secondary electron and bremsstrahlung transport. In Class 1 algorithms, individual elastic collisions are grouped together to form a single multiple scattering step. This technique

groups all the cross sections (energy straggling, multiple scattering, knock-on electrons) and utilizes a predetermined set of path lengths. Sampling is performed at the end of the step so that energy is conserved. The condensed random walk is based on the continuous slowing down approximation and is regarded in terms of path lengths and decreasing energy associated with the total stopping power, $-dE/ds$. The corresponding energy and path lengths are related by

$$\Delta E_n = E_n - E_{n+1} = \int_{s_n}^{s_{n+1}} \frac{dE}{ds} ds, \tag{2.17}$$

where E_n and E_{n+1} represent each energy grid and s_n and s_{n+1} represent path lengths. E_{n+1} is selected from a distribution that takes into account the Landau (1944) and Blunck-Leisegeng (1950) theories for energy-loss straggling.

An advantage of a Class 1 algorithm is that it permits the use of Goudsmit–Saunderson's (1940) multiple-scattering theory, valid for arbitrary scattering angles. However, the primary disadvantage of a Class 1 algorithm is that there is no correlation between primary and secondary particles. While range and total energy loss are calculated for each major step, angular deviation and secondary particle production are sampled within a major step by dividing it into smaller substeps. Local energy deposition is determined by an average energy loss rate determined at the beginning of each substep based upon restricted stopping power. Secondary particles such as bremsstrahlung and knock-on electrons (high-energy electrons ionized from atomic orbitals) are sampled from a probability distribution at the end of each substep, but no correlation is made between angular deviation and secondary particle energy. Consequently, there is no conservation of energy and momentum during the interactions.

Class 2 algorithms on the other hand, model interactions discretely such that primary and secondary particles are always correlated. This is accomplished by defining a threshold for energy loss where events above this threshold are simulated explicitly. Berger (1963) referred to such collisions as 'catastrophic'. Bremsstrahlung processes above an energy threshold E_γ and inelastic collisions having knock-on electrons above E_δ are considered to be 'catastrophic' collisions and are modeled explicitly. Secondary particle energy and scatter angle are then sampled as a correlation so that energy changes are entirely conserved within each step.

Substeps are also used in Class II algorithms to sample for angular deviation and to determine the restricted energy loss rate. Accordingly, events below the threshold value are accounted for in the CSDA model (Class 1 methodology). While this directly monitors energy loss between events, it also requires that cross sections are determined during the transport, which makes it difficult to implement the Goudsmit–Saunderson multiple-scattering theory. Class 2 algorithms will typically implement the Moliere (1948) multiple scattering theory, which limits net-multiple scattering angle (Berger 1963; Kawrakow 2000).

The development of Monte Carlo electron transport codes over the years has brought with it the tabulation of increasingly accurate electron and beta dose-point kernels. Energy deposition measurements in spherical shells of water centered on an isotropic point-source provide the physical information needed to reproduce the moment-based kernels originally published by Cross (1967, 1982) and Berger (1971). Coincidently, Berger (1973) was one of the first to obtain Monte Carlo based point kernels for mono-energetic electrons in an infinite water medium. He used the electron/photon transport code, ETRAN, which he developed while working with Seltzer (1968, 1988). Berger provided point kernels for mono-energetic electrons in an infinite water medium with energies up to 10 MeV and demonstrated that the main advantage of Monte Carlo-based energy deposition kernels over moment-based kernels is the ability to account for energy-loss straggling.

Kocher and Eckerman (1987) used Berger's new point kernels when calculating electron/beta-particle dose-rate conversion factors for about 500 radionuclides. Their dose-rate factors in tissue were normalized to an activity concentration of 1 Bq cm^{-2} and tabulated at various skin depths, including the biologically significant depth of 7 mg cm^{-2}. Berger's (1973) results were also implemented by Prestwich (1989) in developing beta DPK's for radionuclides common in the field of radioimmunotherapy. The inclusion of energy-loss straggling was found to significantly increase dose estimates at distances greater than approximately 75% of the CSDA range.

Seltzer (1988, 1991) provided adjustments to the ETRAN algorithm for improved energy-loss straggling and re-tabulated Berger's Monte Carlo DPK's while extending the energies up to 20 MeV. The ETRAN code became the basis for the general-purpose electron/photon transport codes developed by Bielajew et al. (1992), Integrated TIGER Series (ITS). Using

the updated ETRAN/ITS codes, Cross (1991a) produced dose rate distributions for electrons and beta-particles incident normally on water in an infinite homogeneous medium. His data were tabulated as a function of skin depth, *z*, covering electron energies of 0.01 to 10 MeV and over 96 beta-emitting radionuclides. Doses were averaged over 1 cm^2 and 100 cm^2 areas. Cross found his broad beam dose distributions to agree to within a few percent with those calculated by a significantly different Monte Carlo code, EGS4 (to be discussed later). He also demonstrated good agreement to within a few percent when compared to Spencer's (1959) original moment-based kernels. As expected, larger discrepancies were seen towards the tail of the CSDA range.

Cross (1992a) would later produce an extensive list of beta and electron dose distributions in an Atomic Energy of Canada report for isotropic plane and point-sources on both a water-water and an air-water interface. The significance of the air-water interface studies will be discussed in detail in Section 2.5.2. Electron dose distributions for isotropic plane sources were reported as the dimensionless quantity,

$$j(z / r_0, E) = J(z, E)\ \rho\ r_0 / E, \tag{2.18}$$

where $J(z,E)$ is the dose per electron cm^2 below the center of the plane source. Analogous to Berger's (1971) dimensionless presentation of data, the similar shapes of the scaled dose distributions varies little with energy, thereby allowing for accurate interpolation between limited amounts of data. Cross reported beta dose rate distributions for plane sources as the dose rate per disintegration cm^{-2} Bq^{-1} at a depth *z* below the center of the source, given by

$$J'(z) = B \int_0^{E_{\max}} N(E)\, j(z / r_0, E) \frac{E}{\rho r_0} dE. \tag{2.19}$$

He calculated these distributions based on the assumption that the dose at a depth z averaged over 1 cm^2 (or 100 cm^2) from a 1 Bq isotropic point-source is equal to the dose at a depth *z* on axis of a 1 cm^2 (or 100 cm^2) area isotropic plane source uniformly contaminated by 1 Bq cm^{-2}. Cross (1992a, 1992b) also tabulated point-source dose distributions for 147 radionuclides in infinite water media using the ACCEPT Monte Carlo code (part of the ITS family of codes). He found his data to be within 2% of Seltzer's (1991) ETRAN data, except at very short

distances where differences were up to several percent**.** Cross (1992b) demonstrated similar agreement between both EGS4 and experimental results.

Over the last 10 years or so, two Monte Carlo transport codes have emerged as the standards for electron transport; Monte Carlo N-Particle (MCNP) and Electron Gamma Shower (EGS). MCNP is a Class 1 algorithm with electron transport physics based on the ETRAN/ITS platform (Briessmeister 1997; Brown 2003). The MCNP family of codes is maintained by a large group at Los Alamos National Laboratory and was originally created for neutron-photon transport in reactor calculations. The great flexibility of MCNP however, causes simulation times to be much larger for electron transport than other more particle-specific codes, such as EGS. Nevertheless, MCNP4, MCNPX, and MCNP5 have been used extensively for electron and beta dose distribution calculations.

Rogers (2006) provides an excellent and thorough history of the Electron Gamma Shower family of codes. He credits its inception to the work of Ralph Nelson whose contribution to EGS code systems continued up until the release of EGS4 (Nelson 1985). The most recent version, EGSnrc, is a result of the work by Kawrakow, Rogers, and Bieloajew (Kawarakow and Bieloajew 1998; Kawarakow 2000; Kawarakow and Rogers 2000). While both EGS4 and EGSnrc are Class 2 codes, there were substantial changes made to EGS4 when transitioning to EGSnrc. Kawrakow (1998, 2000) incorporated a new any-angle multiple elastic scattering theory based on Rutherford single elastic scattering cross sections, an exact boundary crossing algorithm, and an improved electron step algorithm, thereby eliminating any step-size dependency. Since electron multiple-scattering theory assumes an infinite homogeneous medium, energy steps for which the electron crosses a boundary will violate this assumption, thereby inhibiting the accuracy of the Monte Carlo code. Therefore, Kawrakow determined that the best possible solution is to eliminate multiple scattering at interfaces entirely and transition to single-scatter direct transport at any region within a specified length from a boundary (default is three elastic mean-free paths). These improvements allow EGSnrc to simulate the energy deposition in the thin walls of an ionization chamber (called the Fano test) to an accuracy level 0.1% (independent of energy step size) when compared to experimental results (Kawarakow and Rogers 2000).

Other transport codes that are often used for electron transport simulations include PENELOPE, GEANT4, and GATE (Rogers 2006). PENELOPE is a coupled electron-photon transport code based on a Class 2 algorithm. GEANT4 is also a Class 2 algorithm transport code and has applications in high energy physics, space and radiation, and medical applications. GEANT4 is the basis for GATE, a simulation toolkit designed for nuclear medicine applications (Rogers 2006).

There have been numerous studies published comparing the dose-point kernels of the mentioned Monte Carlo transport codes. It should be noted however, the intent of these studies was not necessarily to re-tabulate DPK's, but rather use DPK's to test the accuracy of a given Monte Carlo code for purposes of electron-photon transport. Deterministic computer codes that utilize tabulated DPK's rely on the extensive data produced by Berger (1971, 1973), Cross (1992a, 1992b, 1992c), and Seltzer (1991). These codes will be discussed in Section 2.6 and include VARSKIN (Traub 1987; Durham 1992, 2006; Hamby 2011), K-SKIN (Park, 2009), and NISTKIN (NRCP Report No.130 1999). Nonetheless, a selection of these studies is discussed below with an emphasis on code comparison and parameter dependencies.

Simpkin (1990) calculated DPK's for both mono-energtic electrons and select beta emitters using EGS4. He compared his results to Berger (1973), the latest version of ETRAN, and to kernels based on Spencer's (1959) original data. Analogous to all other Monte Carlo kernels, EGS4 provided results that were a major improvement on Spencer's as he completely ignored secondary electron production and transport. Through comparison of EGS4 with Berger's (1973) kernels, he further validated error corrections made by Selzter (1991) in how ETRAN sampled the Landau distribution for energy-loss straggling.

Wang (2001) performed a comparison between EGS4, EGSnrc, and MCNP4 in which he examined the electron/beta depth dose curves for a parallel beam and the radial dose distributions for isotropic point-sources. He found EGS4/EGSnrc doses to be between 10% and 30% less than MCNP doses at greater depths and between 5% and 10% more than MCNP at shallow depths. Wang attributed this to the different multiple scattering theories that the two family of codes employ. These results were confirmed by Caffrey (2012) using EGSnrc and MCNPX (Section 2.7).

Chibani (2002) calculated dose distributions in various homogeneous media and compared results between EGSnrc, MCNP, and measurements. Of note in Chibani's results was the influence on the energy indexing algorithm for MCNP. While EGSnrc had very small differences when compared to measurements, MCNP results varied significantly in the choice of electron energy indexing algorithm. Overall, MCNP results that used the Integrated TIGER Series algorithm (ITS) were in much better agreement with EGSnrc and measured results, as opposed to those that used the MCNP (default) algorithm. MCNP results which utilized the default indexing algorithm had a tendency to shift energy deposition to greater depths.

Schaart (2002) and Reynaert (2002) later demonstrated that running MCNP with the ITS algorithm improves the results of MCNP when scoring energy depositions in small volumes, as one would do when calculating energy deposition distributions. The MCNP-default indexing algorithm assigns transport parameters based on the energy group that the electron currently lies within, whereas the ITS algorithm assigns the parameters from the energy group whose upper boundary is closest to the electron energy. Reynaert concluded that the default mode of MCNP could lead to serious errors when calculating dose distributions around beta sources. Schaart came to a similar conclusion stating that the default indexing mode in MCNP is not consistent with the definition of the energy groups and their boundaries, thereby leading to significant errors. The MCNP-default algorithm results in higher dose collection than ITS-style, because MCNP-default style causes electrons to correspond to scattering power data at higher energies. In addition, Schaart (2002) and Reynaert (2002) demonstrated that MCNP has both a step and substep dependency, unlike EGSnrc which was shown to be step-size independent (Kawrakow 1998, 2000). As with the default indexing algorithm, choosing too fine of a step size causes the energy deposition distribution to shift towards greater depths. Therefore, care should be taken when high resolution is required. The work of Schaart and Reynaert helps to explain the discrepancies reported by both Simpkin (1990) and Chibani (2002).

Mainegra (2005) provided verification of EGSnrc by calculating dose kernels for mono-energetic electrons ranging from 0.05 to 3 MeV and for ^{32}P and ^{90}Y. For mono-energetic electrons, Mainegra found excellent agreement with the EGS4 results of Simpkin (1990) and differences of a few percent when compared to Berger (1973) and Cross (1992). The largest differences occur toward the end of the electron paths. Mainegra attributed discrepancies

among different Monte Carlo codes to the different methods of sampling energy losses and angular deflections. Kernels for ^{32}P and ^{90}Y compared very well to those calculated by both Simpkin (1990) and Prestwitch (1987).

More recently, Uusijarvi (2009) compared PENELOPE to GEANT4, MCNPX, and ETRAN by comparing electron DPK's at energies of 0.01, 0.1, 0.5 and 1.0 MeV. He found excellent agreement when comparing the codes at distances less than 90% of the CSDA range. When using MCNP, Uusijarvi used the ITS energy indexing algorithm as recommended by Schaart (2002) and Reynaert (2002) and limited the number of substeps to three. Sidlova (2010) found better agreement between EGSnrc and MCNPX when implementing the ITS algorithm, as well. Maigne (2011) compared electron dose calculations using GATE/GEANT4, EGSnrc, and MCNP for energies between 0.015 and 20 MeV. He noted good agreement between the three codes at energies greater than 0.05 MeV with the largest discrepancy being ~6% (MCNP vs GATE). Similar to Uusijarvi (2009) and Sidlova (2010), Maigne bypassed the default MCNP energy indexing algorithm and used the ITS algorithm.

2.5 Corrections to Dose-Point Kernels

2.5.1 Scaling Methods for Non-Homogeneous Geometries

The derivation of electron and beta-particle dose distributions in various media from those calculated in water relies on the observation that distributions in different low-Z media have very nearly the same shape. Cross (1967, 1968, 1982, 1992a) demonstrated through both measurements and calculations that they differ only by a distance 'scaling factor' and a closely related renormalization factor. Approximately similar shapes are expected for low-Z elements because the variations of both rate of energy loss and scattering probability with Z are nearly independent of their variations with energy. For media with $Z \leq 18$, Cross found that the value of the quantity $F(r) = r^2J(r)$ at a distance r (cm) in a medium is related to the value F_w at r_s in water by

$$F(r) = \eta_w F_w(r_s), \tag{2.20}$$

where η_w is the 'scaling factor', or attenuation per g cm^{-2} of the medium relative to water, r_s is the scaled distance of $\eta_w(\rho/\rho_w)r$,and ρ is the medium density in units of g cm^{-3}. The dose, $J(r)$, is given by

$$J(r) = \eta_w{}^3(\rho/\rho_w)^2 J_w(r_s). \tag{2.21}$$

That is to say, the absorbed dose in air at a distance r is proportional to the dose in water at a scaled distance of $0.9(\rho_{air}/\rho_w)r$, where 0.9 is the scaling factor for air relative to water. The normalization factor, $\eta_w{}^3(\rho/\rho_w)^2$, is derived from the requirement that the total energy deposited, $4\pi\int_0^\infty F(r)dr$, be the same for all media.

Cross (1967, 1968, 1982, 1992a) showed that the scaling factor for a given medium is proportional to the product of the mass stopping power in the medium relative to that in water, S/S_w, and a function of the effective Z of the medium,

$$Z_{eff} = \frac{\sum w_i Z_i{}^2 / A_i}{\sum w_i Z_i / A_i}, \tag{2.22}$$

where w_i is the fraction by weight of the element of atomic number Z_i and mass number A_i and the summation is over all elements of the medium. He then obtained the function of Z_{eff} by plotting it against the ratio of η_w to S/S_w. The resulting curve fit allows for the derivation of scaling factors using

$$\eta_w = (0.777 + 0.03756Z_{eff} - 0.00066Z_{eff}{}^2)\,S/S_w, \tag{2.23}$$

with an estimated standard error of ±1.5%. Since relative stopping powers vary somewhat with energy, Cross arbitrarily chose the quotient of the ranges of 500 keV electrons (r_{water}/r_{medium}) to be the average mass stopping power of the medium relative to water. In media for which ranges were not available, approximate values of S/S_w were calculated from the empirical expression,

$$\frac{S}{S_w} = 2.106 \sum \frac{w_i Z_i}{A_i} \left[1 - \frac{\ln Z_i}{11.5} \right]. \tag{2.24}$$

Since Eq's. (2.23) and (2.24) are accurate only for $Z_{eff} \leq 18$, adjustments were presented by Cross (1967, 1968, 1982, 1992a) in order to obtain scaling factors for media with $Z_{eff} > 18$. Cross found that extrapolation of low-Z scaling factors to those obtained from experimental data for $Z_{eff} > 13$ provided a consistent fit, except at very large values of Z_{eff}. However, both the scaling factor and the ratio of the average mass stopping powers were relative to aluminum (Z=13), as opposed to water (or air, as with his 1967 work). The resulting curve fit is given by

$$\eta_{Al} = 0.818(1 + 0.0284 Z_{eff}) S / S_{Al}, \tag{2.25}$$

and is assumed valid (not explicitly written in literature) for Z less than and greater than 18. Therefore, it is possible to estimate a more accurate η_w for $Z_{eff} > 18$ using

$$\eta_{m/water} = \frac{\eta_{m/Al}}{\eta_{water/Al}}. \tag{2.26}$$

Once again, for media (m) in which ranges at 500 keV were not available, approximate values of S/S_{Al} were calculated from the empirical expression,

$$\frac{S}{S_{Al}} = 2.59 \sum \frac{w_i Z_i}{A_i} \left[1 - \frac{\ln Z_i}{13} \right]. \tag{2.27}$$

Despite this correction, Cross (1967, 1968, 1982, 1992a, 2001) warned that scaling factors for $Z_{eff} > 18$ are considerably less accurate and should be used with great caution for media with $Z_{eff} > 40$.

This semi-empirical model developed by Cross has two main applications. The first one, as mentioned above, is to determine electron and beta-particle dose distributions in homogeneous media from those calculated in water. Berger (1971) adopted the use of Cross's scaling method when comparing his scaled absorbed distributions in different media. He showed that if $F^{(1)}(\xi, E_0)$ and $F^{(2)}(\xi, E_0)$ were the scaled distributions around the same mono-

energetic point-source in two different media for which the scaling law holds, Eq. (2.21) yields

$$F^{(1)}(\xi, E_0) = F^{(2)}(\xi, E_0). \tag{2.28}$$

Similarly, for beta-particle sources,

$$F_\beta^{(1)}(\xi) = F_\beta^{(2)}(\xi). \tag{2.29}$$

The functional dependence of the scaled absorbed dose distribution on ξ is therefore independent of the medium density under conditions in which the scaling law applies. The medium property dependency is accounted for through the adoption of X_{90} normalization.

The second, and perhaps more useful application, is determining the equivalent effect on energy deposition that various materials have in non-homogeneous, multi-layer geometries. Deterministic computer codes such as VARSKIN (Traub 1987; Durham 1992, 2006; Hamby 2011), K-SKIN (Park 2009), and NISTKIN (NRCP Report No.130 1999) utilize a simplified version of Cross' scaling law. Scaling in non-homogeneous geometries is performed by setting η_w equal to one, thus simple density scaling is used. This procedure is performed for all materials (no limitation on *Z*) and can be used to find the scaled distance, r_s, in multi-layer geometries where

$$r_s = r_w + r_1(\rho_1/\rho_w) + r_2(\rho_2/\rho_w) + \ldots r_n(\rho_n/\rho_w). \tag{2.30}$$

Dose is then calculated at the physical distance $r = r_w + r_1 + r_2 + \ldots r_n$ from the source using the DPK value defined at r_s. The advantage of this simplification is that the users of DPK codes are only required to know the density of the various materials involved. Computationally, the increased burden of accounting for η_w would be negligible.

In his work involving near-field beta dose distributions from ^{32}P impregnated arterial stents, Janicki (1999) demonstrated that a value for η_w of unity can lead to significant errors. As a result, he provided a slight modification to Cross' scaling law for multi-layer geometries, given by

$$J(r) = \eta_w(r)\left(\frac{\langle \eta_w \rho \rangle_m}{\rho_w}\right)^2 J_w\left(\frac{\langle \eta_w \rho \rangle_m}{\rho_w} r\right), \tag{2.31}$$

where $\langle \eta_w \rho \rangle_m$ is the line average of the *local* scaling factor $\eta_w(r)$ times the *local* density $\rho(r)$ along the beta path. The materials used by Janicki were relatively low in density and included the following; water, polymethyl methacrylate (ρ=1.19 g cm^{-3} and η_w=0.949), polytetraflourothylene (ρ=2.20 g cm^{-3} and η_w=0.871), and polyethylene terephthalate (ρ=1.24-1.43 g cm^{-3} and η_w=0.919). Comparisons with experimental results showed that Eq. (2.31) and density scaling (η_w=1) yields similar deviations of 10% for distances close to the ^{32}P stent surface. However, at larger distances, Janicki's (1999) model underestimates dose by ~10% while density scaling underestimates dose by as much as 25-30%. The results of this study are limited to the high energy beta of ^{32}P (E_{max} = 1.708 MeV) and low density/Z_{eff} media.

Marcu (1998a) recommended the addition of a backscattering attenuation factor, n_B, to Cross's scaling law when dealing with planar interfaces of dissimilar media. The interface or multi-layer configuration differs from the homogeneous case due to the contribution of backscattering to the dose, as given by

$$J(r) = \eta_w J_w\left(r_s\right) n_B. \tag{2.32}$$

Marcu determined the backscattering attenuation factor for ^{32}P beta sources in media with $8<Z<50$ using

$$1 - n_B = \frac{J_i - J_h}{J_h}, \tag{2.33}$$

where J_h is the dose in water in a homogeneous geometry and J_i is the dose in water with medium "*i*" as the backscattering material. From this definition of n_B it is easy to see that the scaled dose from Eq. (2.32) will be reduced if more backscattering takes place in medium "*i*" than in water. It was assumed by Marcu (1998a) that the energy lost by backscattering will affect the energy deposited in medium "*i*" uniformly. A strong linear fit was obtained for n_B versus log(Z+1). The method was checked on three randomly chosen elements; zirconium (Z=40), germanium (Z=32), and iron (Z=26). When compared to ITS Monte Carlo

simulations, Marcu found discrepancies of less than 5% up to the distance in which 95% of the beta energy is deposited in medium "*i*". The model presented by Marcu is limited to ^{32}P planar interfaces and lacks depth dependence for the energy lost due to backscattering. More importantly however, the model cannot be used for volumetric sources of uniform activity distribution, such as in the case for hot particles. Marcu's model would only be applicable to beta-particles emitted from the top of the source.

In an investigation of the scaling factor for water to bone, Marcu (1998b) provided another improvement to Cross' scaling model through the use of a 'modulation function', according to

$$J_B(x) = \eta_w{}^3(\rho/\rho_w)^2 J_w\left(\eta_w x\right) M(x), \tag{2.34}$$

where the modulation function is given as

$$M(x) = \frac{J_{B'}(x)}{J_S(x)}. \tag{2.35}$$

The actual dose in bone is given as $J_{B'}(x)$ and the dose in water scaled to bone is given as $J_S(x)$, as determined by Cross' scaling method. The quantity x is the dimensionless depth with respect to the electron CSDA range in bone. Marcu used ITS Monte Carlo simulations to determine the point-source DPK's for mono-energetic electrons in both water and bone. He examined electron energies of 0.1, 0.5, 1.0, 1.5, and 2.0 MeV, energies which cover the majority of beta-particle spectra. Modulation functions for each energy were determined with a six-degree polynomial fit and provided a scaling correction of up to 8% for depths between 0 and 85% of the electron range in bone. While the results of this study can be integrated over common beta-particle spectra for improved DPK scaling in non-homogeneous media, its applicability is limited to bone (ρ=1.85 g cm^{-3}, Z_{eff} =8.743).

Despite the modifications made by Cross (1967, 1968, 1982, 1992a) for higher-*Z* media, there have been numerous studies showing significant discrepancies with Monte Carlo simulations. In calculating beta dose distributions for ophthalmic applicators, Cross (2001) reported differences between scaled DPK's and Monte Carlo calculations of 14-18% for planar ^{106}Ru-^{106}Rh applicators and up to 30% for concave applicators. The ophthalmic

applicators used in this study were secured to a 0.9 mm silver (Z = 47) backing and encapsulated with 0.1 mm of silver. In an attempt to explain these differences, Cross compared the dose in water from two ^{106}Ru-^{106}Rh planar sources, one with a 0.1 mm silver encapsulation and one with an encapsulation being 0.1 mm of "water" with a density of 13.4 g cm^{-3}, i.e., 1.34 mm of water. According to the scaling law, these two 'thicknesses' should attenuate beta-particles from a point-source in infinite homogeneous media of silver and water by the same amount. Therefore, the two ^{106}Ru-^{106}Rh beta distributions should be the same. Using Monte Carlo simulations for the two geometries, Cross (2001) found that the distributions differ by an amount that increases with distance where the betas transmitted by the silver are more penetrating. His results showed that the betas transmitted by the silver window had a significantly harder spectrum than those transmitted by an "equivalent" water window.

An alternative to Cross's scaling method was presented by Reynaert (2001) for DPK applications. Similar to the work done by Janicki (1999), Reynaert was investigating DPK's for impregnated arterial stents. In doing so, Reynaert used EGS4 to calculate DPK's surrounding ^{32}P, ^{198}Au, and ^{188}Re beta point-sources. He then performed the same calculations with the sources surrounded by increasing thicknesses of stainless steel. The diameter of the 'absorption sphere' was varied from 1 μm to 1 mm, a thickness that completely absorbed the betas. Reynaert then calculated a self-absorption factor, which he defined as the ratio between the dose in a homogeneous medium to the dose at the same physical distance in the presence of a steel sphere. The factor was given as a function of the distance to the point-source and the distance traveled through the stainless steel. For a given thickness of steel, the self-absorption factor increases with distance and theoretically reaches infinity because of the smaller beta range in steel. The dose at a distance r in water from betas transmitted by steel of thickness t can be calculated using

$$J(r+t) = \frac{J_w(r+t)}{SAF(t)}, \tag{2.36}$$

where SAF is the self-absorption factor and J_w is the dose in a homogeneous water medium.

When compared to a full Monte Carlo calculation for complex ^{32}P and ^{198}Au stent geometries, the DPK model proposed by Reynaert gave nearly identical results. Radiochromatic film measurements were used to test ^{188}Re-stent dose calculations. The DPK results were within 5% of film measurements for depths where doses are high enough to be statistically reliable. Using Cross' scaling model and a steel-to-water scaling factor of 0.932, Reynaert calculated $J(r+t)$ and SAF values for direct comparison purposes. He showed that the scaling model greatly overestimated the effect of the steel sphere, especially at larger distances and for larger steel radii. Reynaert showed that a scaling factor of about 0.75 would be needed to provide acceptable agreement. It should be noted that the scaling factor of 0.932 is in slight disagreement with the 1.011 value calculated by Fox (2000). However, the value determined by Fox would only increase the discrepancies observed by Reynaert.

In a comparison study performed by Cho (2004), dose calculations around electron-emitting metallic spherical sources were analyzed using both MCNP4 and scaled DPK's. Doses were determined up to the X_{90} distance for electron energies ranging from 0.5 to 3.0 MeV. The media tested were aluminum (Z=13), titanium (Z=22), silver (Z=47), and platinum (Z=78). Cho used two different scaling methods when using the DPK's. He used the density scaling method (η_w=1) that is implemented in most DPK computer codes and he used a linear range ratio method developed by Charlton (1970). This method is based on the assumption that the path length L (cm) in medium Z_1 is equivalent, in terms of energy loss, to a path length of $n_l L$ in a medium of atomic number Z_2. Here, n_l is defined as the "linear range ratio" and is equal to the ratio of the range in medium Z_1 to the range in medium Z_2;

$$n_l = \frac{r_0(Z_1)}{r_0(Z_2)}. \tag{2.37}$$

Regardless of the scaling method used however, Cho found that the discrepancy between MCNP and scaled DPK calculations increased with Z and depth in water. The observed maximum discrepancies for silver and platinum were 80% and 100%, respectively. Discrepancies for aluminum and titanium were typically less than 50% up to the X_{90} distance for the density scaling method and less than 20% for the linear range ratio method. Cho also noted that the scaling models tend to deviate from MCNP more at higher energies, as well as

higher-Z. He partly attributed this phenomenon to the fact that bremsstrahlung produced in the volume sources is not properly accounted for in the scaled DPK models.

2.5.2 Backscatter Correction

2.5.2.1 Air Scattering

Inherent in the development of beta DPK's is the assumption of an infinite homogeneous medium. While scaling methods are used to account for the non-homogeneous media which transmit the beta-particles, an additional adjustment is required to correct for the lack of atmospheric scattering in the non-existent water medium. For example, when a DPK is applied to a point-source on an air-water interface, the isotropic nature of DPK's assumes that betas emitted away from the source point have the ability to backscatter in an infinite homogeneous water medium and possibly contribute to the energy deposition at the dose point of interest. This scenario is of particular importance for hot particle skin dosimetry.

The work of Chung (1991) and Crawford (1991) clearly demonstrate this phenomenon. Through the use of Monte Carlo simulations, Chung showed that DPK's for ^{60}Co (E_{av}= 0.0965 MeV) will overestimate skin dose calculations averaged over 1 cm^2 dose areas at a depth of 7 mg cm^{-2} by 14% to 37%. He attributed this difference to the lack of air backscattering present in Monte Carlo simulations. Crawford found similar results for ^{36}Cl (E_{av}= 0.2735 MeV) at the same dose area and depth. DPK calculations were 38% to 46% higher than Monte Carlo results when a point-source was placed at an air-water interface. However, when a water-water interface was used, the results were close together. Crawford also examined the effect of the low-energy beta emitter, ^{14}C (E_{av}=0.0494 MeV). He showed that the deviation between DPK and Monte Carlo was only ~10% for ^{14}C point-sources with an air-water interface.

Based on the results of Crawford (1991) and Chung (1991), it was concluded that a backscatter factor was required for accurate beta-particle DPK skin dose calculations. Cross (1991b, 1992c) developed such a factor and defined it as the ratio of the dose near a contaminated plane surrounded by water to that at the same distance below an equally contaminated air-water boundary. Using dose distributions from isotropic point-sources for

both water-water and air-water boundaries, Cross (1992c) published a simple fit expression for the backscatter factor at the skin depth of 7 mg cm^{-2}, given by

$$B(70\mu m)_{water} = 1.302 + 0.1563(\ln E) - 0.00576(\ln E)^2 - 0.00273(\ln E)^3, \qquad (2.38)$$

where E is the maximum beta energy in MeV. The equation applies to energies between 0.15 and 3.5 MeV. Cross chose a dose averaging area of 100 cm^2. As discussed previously, the backscatter factor can also be used on axis for uniformly contaminated 100 cm^2 area plane sources. Cross (1992c) demonstrated that if skin depths are expressed in terms of the maximum range of the beta-particles, the backscatter factor is nearly independent of energy and decreases rapidly with depth. However, given the biological significance of 7 mg cm^{-2}, he published Eq. (2.38) as opposed to a depth dependent backscatter factor.

Cross (1991b, 1992c) also examined the dose relationship due to backscattering in air and dose area. He found that in the presence of an air-water boundary, the dose at 7 mg cm^{-2} averaged over an area of 100 cm^2 exceeds the dose for a 1 cm^2 area from and isotropic point-source at the air-water interface directly above the two dose areas. The difference depended on the maximum beta energy. Cross showed that for maximum energies below 2 MeV the dose to the 100 cm^2 area can exceed that of the 1 cm^2 area by as much as 11%. This difference is attributed to the effect of air backscattering, which will increase with dose averaging area. At energies above 2 MeV, scattering in air is insignificant. However, the beta range in water is expected to exceed the radius of the 1 cm^2 area, thereby increasing the dose to larger areas. The importance of these findings is that backscatter factors determined using a dose area of 100 cm^2 will overestimate the effect of backscattering in air, and therefore under underestimate the correction needed for smaller dose areas.

Despite these limitations, the backscatter factor presented by Cross has been implemented by the DPK codes, VARSKIN (Traub 1987; Durham 1992, 2006; Hamby 2011) and K-SKIN (Park, 2009). Both codes apply the correction factor to all dose averaging areas and at all skin depths for both isotropic point- and plane-sources. The model provided by Cross was modified slightly to allow for extension to skin depths other than 7 mg cm^{-2} and to account for source covers and/or air gaps between the source and skin surface. The maximum beta energies were translated into corresponding X_{90} distances. These distances were then scaled

using the 7 mg cm^{-2} skin depth. It was then assumed that the curve fit in Eq. (2.38) will shift to the right for deeper skin depths and shift to the left for shallower skin depths. In order to account for source covers and air gaps, the "skin depth" was taken as the total density scaled distance, similar to Eq. (2.30). As discussed above, it is likely for errors to be introduced if Cross's correction factor is used for smaller dose averaging areas.

An alternative backscatter model was introduced by Chibani (1995). Unlike Cross, Chibani (1995) tabulated his backscatter factor as a function of radial distance and angular direction. Chibani used the GEPTS Monte Carlo code (Gamma, Electron, and Positron Transport System) to model a semi-infinite water medium with an air/water scattering medium. He calculated the specific absorbed fraction in water for spherical volumes with thickness ΔR around R and with a solid angle width $\Delta(\cos\theta)$, where θ is the angle between the position vector R and the axis normal to the scattering surface. Chibani performed these calculations for electron energies ranging from 0.05 MeV to 4 MeV in both water-water and air-water boundary media. His data were presented in tabular form as a function of E, R, and θ and were found to vary insignificantly for energies less than 1 MeV. Chibani found that the effects of backscatter were most significant for large θ values at R depths approaching the CSDA range of the electron. When θ was less than ~60 degrees, the effects of backscatter were negligible at depths approaching the CSDA range and at depths close to zero. By determining the backscatter factor with respect to radial distance and angular direction, Chibani was able to account for all dose averaging areas. However, he provided no testing results of his data through beta spectra and dose area integration.

Most recently, Aydarous (2008) examined the effects of backscattering on skin dosimetry for hot particles. He calculated backscatter factors in a way similar to Cross. Using MCNP4, Aydarous determined the dose at a skin depth of 7 mg cm^{-2} for spherical sources in both medium-tissue and tissue-tissue interface geometries. The media used were air, aluminum, iron, silver, and gold. Sources were centrally embedded at the interfaces and had a density of 1 g cm^{-3} (water) and radii ranging between 0.0001 cm and 0.1 cm. The dose averaging area was varied from 0.00001 cm^2 to 1 cm^2. Of interest however is the combination of the air medium, 0.0001 cm source radius, and 1 cm^2 dose averaging area. This particular configuration approximates the backscatter factor for point-sources and allows for comparison with Cross' data.

It can be shown that for a range of beta energies, Cross's data underestimates the correction factor. The discrepancy is larger at lower energies, such as ^{60}Co (E_{max} = 0.32 MeV), where Cross predicts 1.12 and Aydarous predicts 1.23 as the backscatter factor. However, the two are in closer agreement for high energy betas like ^{90}Y (E_{max} = 2.281 MeV) where Cross predicts 1.36 and Aydarous predicts 1.44. The discrepancy at the lower energy is likely due to the difference in dose averaging areas. As Cross (1991b, 1992c) previously demonstrated, 100 cm^2 dose areas will overestimate the effect of scattering in air for air-water media at maximum beta energies less than 2.0 MeV. This effect was further supported by Aydarous as he demonstrated a significant decrease in the backscatter factor for ^{60}Co in air when the dose area was reduced below 0.01 cm^2.

When the assumption is made that the source in question is volumetric and should not be approximated as a point-source, the issue of scattering becomes a greater challenge. In this case, scattering must be considered both inside and outside of the source. Aydarous (2008) was able to demonstrate the effect that volumetric source size has on the backscatter factor in air. The backscatter factor for ^{60}Co decreased from 1.23 to 1.06 when the source radius was increased from 0.0001 cm to 0.1 cm. Likewise, the correction factor for ^{90}Y decreased from 1.44 to 1.07. As a result of the geometric configuration used by Aydarous, some of this decrease is attributed to attenuation of betas emitted from the upper half of the spherical source. When air is used as the scattering material, there will be much less attenuation of betas emitted from the upper hemisphere of the source.

In the development of VARSKIN Mod 2, Durham (1992) chose not to include a backscatter factor for volumetric sources. He stated that for sources with finite thickness, the majority of the dose will come from the portion of the source that is nearest the skin. Since most hot particles are of a density greater than water, the DPK will probably underestimate the dose due to the amount of backscatter from the portion of the source above. He concluded that this underestimation in dose is compensated for, within the accuracy of the calculations, by the overestimate of backscatter from portions of the source that are farthest from the skin.

Durham (2006) later found that a backscatter correction is needed for volumetric sources that have dimensions smaller than the range of the beta-particle. In his study, Durham used MCNP4 to model uniformly distributed cylindrical sources with thicknesses equal to the

diameter. The source was completely embedded into a semi-infinite water volume with the top surface of the source being flush to the top surface of the water volume. On top of the water volume was either an identical semi-infinite water volume (water-water interface) or a semi-infinite air volume (air-water interface). Doses were measured at a depth of 7 mg cm^{-2} below the bottom surface of the source. Dimensions of the dose averaging area were not provided. Durham modeled the source configuration in this fashion so that backscattering in air versus water was the only variable that could affect the dose calculations. If the sides of the source were not covered in the air-water interface model, the betas emitted from the sides of the source would have a larger contribution to the dose than in the water-water interface model. Monte Carlo simulations were performed using a source material of iron (ρ=7.86 g cm^{-3}) with the thickness of the source being varied from 1 μm to the range of the beta. Nuclides were chosen to cover a wide range of spectra endpoint energies. Durham found the backscatter factor for volume sources to be

$$B(70\mu m)_{water} = 1.1018 - 0.060\ln(\Delta t_{source} / X_{99}), \qquad (2.39)$$

where Δt_{source} is the source thickness (or diameter for spheres) and X_{99} is the distance in which 99% of the beta-particles energy is deposited in water. The source thickness includes the density scaled thicknesses of the source, source cover, and any possible air gaps between the source and the skin. Durham concluded that for very small sources ($\Delta t_{source} < 0.05X_{99}$), Eq. (2.39) reduced to the point-source backscatter factor of Cross (1991a, 1992b). In addition, Durham found that for sources with a thickness greater than the X_{99} distance, no backscatter factor was required since the source is considered "infinitely thick" and the Berger (1971) DPK is assumed accurate.

The model purposed by Durham however, does not address the change in the backscatter factor with respect to skin depth. At deeper skin depths, the effect of dose contributions from backscatter is expected to be greatly diminished as demonstrated by Chibani (1995). The model only accounts for scattering in the non-existent water on top of the source and not the sides, thereby underestimating the backscatter factor. The results of this assumption could be more severe for spherical sources. Lastly, Durham's backscatter factor does not address the possibility of increased backscatter towards the dose region that can occur in higher-*Z* sources.

2.5.2.2 Source Scattering

Dose perturbations around the interface of water and higher-*Z* media have been studied extensively in the field of medical physics (Cho 1999; Buffa 2004; Lee 2004). Applications such as the ^{32}P impregnated arterial stents studied by Janicki (1999) and the ^{106}Ru-^{106}Rh ophthalmic applicators studied by Cross (2001) involve the use of metallic applicators. These applicators serve as backscattering materials and have been shown to increase dose as a function of tissue depth.

Cho (1999) used EGS4 to examine the dose backscatter factor for energies ranging from 0.1 to 3 MeV and scattering materials with *Z* of 13 to 78. He assumed a point-source was sandwiched between a scattering slab and a water slab where the slab thicknesses were greater than the range of the electron. Dose depth profiles in the water were then compared to those found in an infinite homogeneous water medium. The dose averaging area was 0.78 cm^2. The ratio of these two yield the dose backscatter factor defined by Cross (1991a, 1992b). Cho found the maximum backscatter factor to range from 10% to 60% depending on electron energy and scattering material. Curve fit parameters were given for each energy-*Z* combination to determine the backscatter factor as a function of distance from the interface, *x*:

$$B(x) = m_0 + \sum_{i=1}^{3} m_i (\log_{10} x)^i, \tag{2.40}$$

where m_0 and m_i are the fit parameters. Limitations were placed on the minimum value of *x* due to the use of logarithms in the fit equation.

Buffa (2004) preformed a similar study using EGSnrc in which he determined the backscatter factors over the same energy and *Z*. Unlike Cho (1999) however, Buffa chose a power *h* polynomial to fit his data in order to obtain better behavior with respect to the series of logarithms that diverge near the interface (as $x \rightarrow 0$) where the backscatter effect is greatest. His fit equation is given by

$$B(x) = \sum_{i=0}^{h} m_i x^i. \tag{2.41}$$

Buffa compared his backscatter factors to those of Cho (1999) and found good agreement over all energy-*Z*-depth combinations for which Cho reported results. Deviations were attributed to the different dose averaging areas used between the two. Buffa chose his areas based on the CSDA range of the electron. As a result, dose areas for energies greater than 0.5 MeV exceeded the 0.78 cm^2 areas used by Cho, thereby producing slightly larger backscatter factors. Using *Z* of 79 and and electron energy of 0.1 MeV as an example, Buffa demonstrated an increase in the maximum backscatter factor from ~1.50 to ~1.95 when the lateral dimensions of the dose area are increased from 0.01 cm to 1.0 cm. Deviations are also attributed to the choice of Monte Carlo transport code. Buffa (2004) noted that EGS4, which was used by Cho (1999), tends to underestimate the electron backscatter near the interface, whereas EGSnrc correctly predicts this effect. This is due to the addition of an exact-boundary crossing algorithm to EGSnrc (Kawrakow 1998, 2000).

Similar to the work of Chibani (1995), Buffa (2004) examined the radial dependence on the backscatter factor. Buffa divided the 1D dose areas described above into 3D voxels with dimensions of 1/60 of the electron CSDA range in water. The radial distance in the *yz*-plane was taken as the root of the y^2 and z^2 sum. Buffa showed the backscatter factor was symmetrical in the *y*-*z* directions, but a shift in the maximum factor away from the $x = 0$ axis was observed as *Z* decreased. He attributed this to the increase in the average scattering angle as *Z* is increased. The magnitude of this effect decreased with an increase in energy from 0.1 to 1 MeV. As with the 1D backscatter factor, the maximum value in the 3D model increased with an increase in *Z*. Buffa was able to provide curve fits for each energy-*Z*-depth combination using the polynomial function,

$$B(x = x_0) = \sum_{i=0}^{h} m_i\Big|_{x=x_0} \cdot x^i, \tag{2.42}$$

where x_0 is the normal distance from the interface and *r* is the radial distance. No previously published 3D results were available for comparison.

Buffa (2004) also examined the effect of scattering thickness on backscatter factors. He varied the thickness of the backscattering material in order to determine the minimum thickness required for a complete backscatter contribution to dose. He found that the

backscatter factor increased with an increase in scattering material thickness. The minimum thickness was found to be about a third of the electron CSDA range in the scattering material; it decreased slightly with increasing Z and increased slightly with increasing electron energy.

While the models presented by Cho (1999) and Buffa (2004) are based on mono-energetic electrons, backscatter factors for beta-particles can be determined by integration over a given beta spectrum. Conversely, they may be determined directly by using a beta source rather than mono-energetic electron sources. Lee (2004) used MCNP4 to determine beta backscatter factors directly for ^{32}P, ^{90}Sr/^{90}Y, ^{45}Ca, ^{142}Pr, and ^{185}W for scattering materials with Z up to 78. Calculations were performed using the same geometrical setup as Cho (1999), and a fit using the same equation form as Eq. (2.40) was found. Overall, results were comparable to those of Cho and Buffa. Lee validated his results by comparing ^{32}P backscatter factors with Z of 13 to both experimental results and EGS4 simulations. He found that they corresponded reasonably well.

In all of the studies discussed above, point-source geometries were used when determining dose perturbations in the presence of water-high-Z interfaces. The dependence on source geometry was not studied. It was concluded that backscatter factors obtained using point-sources can be generally applied to the DPK method for more complex source geometries through iteration. This extension to volume sources will likely lead to an overestimate in the backscatter factor as the thickness of scattering material will vary throughout the source, as demonstrated by Buffa (2004). In addition, betas emitted near the side of the source will experience less backscatter due to the varied scattering geometry (i.e., presence of air). The geometrical variations become even more complicated when spherical sources are assumed.

2.6 Dose-Point Kernel Codes

Dose-point kernel (DPK) codes are used as an alternative to the slower, more complicated, yet more accurate Monte Carlo codes in calculating dose. They provide fairly accurate estimates of beta and gamma absorbed dose from hot particles. Examples of DPK codes include VARSKIN 4 (Traub 1987; Durham 1992, 2006; Hamby 2011), K-SKIN (Park 2009), and NISTKIN (NRCP Report No.130 1999). As mentioned throughout the discussions above,

these types of codes rely on a pre-determined DPK, a scaling method, and a backscatter correction model. Doses are calculated through numerical integration methods where the DPK is integrated over the entire source volume and dose averaging area. For example, dose is estimated in VARSKIN using the following kernel,

$$\dot{D}_{\beta}(r)\left[\frac{Gy}{\sec}\right]=\frac{1.6x10^{-10}\left[\frac{J\ \mathrm{g}}{MeV\ \mathrm{kg}}\right]\cdot A\left[\frac{dis}{\sec}\right]\cdot Y\left[\frac{\beta}{dis}\right]\cdot\overline{E_{\beta}}\left[\frac{MeV}{\beta}\right]\cdot F_{\beta}(\xi)}{4\pi r^{2}\cdot\rho\left[\frac{\mathrm{g}}{cm^{3}}\right]\cdot X_{90}\left[cm\right]}, \qquad (2.43)$$

where $F_{\beta}(\xi)$ is the Berger (1971) scaled absorbed dose distribution. The parameter ξ represents the density scaled distance (includes distances in the source, source cover, clothing, and air) from the source point to the dose point, written as a ratio with respect to the X_{90} distance. The distance r is the physical distance between the source point and the dose point.

The code KSKIN is nearly identical to VARSKIN 4 in functionality. It can be used for volumetric, disc, and point-sources and uses the same backscattering and scaling models. The main difference however is the choice of DPK. While VARSKIN 4 uses the moment-based Berger (1971) DPK, KSKIN uses the Monte Carlo based Seltzer (1991) DPK. Park (2009) has demonstrated that the use of Monte Carlo based DPK's results in improved accuracy when compared to MCNPX simulations, particularly near the end of the beta range. This is expected given the neglect of energy-loss straggling in the moment-based DPK's. The NISTKIN code was developed by the National Institute of Standards and Technology for the sole purpose of the NCRP Report No. 130 (1999). As with KSKIN, Seltzer DPK's are the basis for NISTKIN dosimetry. Density scaling was used for non-homogeneous media, however no backscatter model was incorporated, as the code was only designed for hot particle calculations (volumetric in nature).

The accuracy of DPK codes depends on the nature of the kernels, the scaling method, and backscatter correction model used. With the advancement in Monte Carlo transport codes and Monte Carlo based DPK's over the years, an improvement to DPK code accuracy is mainly limited to scaling methods and backscatter correction models. In a recent beta-dose verification of VARSKIN 3 (Durham 2006), Sherbini (2008) demonstrated that, overall, VARSKIN 3 shows good agreement with MCNP5 simulations over a range of source

geometries, beta energies, and skin depths. Point-source and disk-source calculations were within a few percent at depths between 7 mg cm^{-2} and 100 mg cm^{-2} (dose areas of 1 cm^2). However, some unexpected deviations were observed for cylinder, sphere, and slab geometries. Agreement with MCNP5 was within 20% for volumetric sources made of water and in most cases within 10%. The exceptions were iron slab and iron sphere doses at 7 mg cm^{-2} from ^{60}Co, for which the results differed by as much as 45% and 35%, respectively (only iron and water was tested). These differences increased further with skin depth and differed by a factor of 2 near the end of the beta range. The results observed by Sherbini are similar in nature to those seen by Marcu (1998b), Janicki (1999), Reynaert (2001), and Cross (2001). In all cases, the discrepancies between the chosen scaling method and Monte Carlo results were attributed to either self-absorption of the beta or unaccounted spectral hardening.

Updating the Berger (1971) DPK to a Monte Carlo based DPK will improve the VARSKIN 3 results presented by Sherbini (2008) simply by accounting for energy-loss straggling. Additional improvements to VASKIN 3 and DPK codes in general can be made by incorporating an updated point-source and disk-source backscatter model that is dose-area and skin-depth dependent. The backscatter model developed by Cross (1991b, 1992c) is only defined for 100 cm^2 dose areas and skin depths of 7 mg cm^{-2}. However, the large discrepancies seen for high-*Z* source geometries is likely due to the density scaling method and limitations of the volumetric backscatter model used in VARSKIN 3. An accurate scaling model should be able to account for mono-energetic electron self-absorption at all energies and in all source materials. By doing so, the model would correctly account for beta spectral hardening that can occur in higher-*Z* sources, thereby improving dose estimates with depth. Dose perturbations from internal source scattering presumably increased the discrepancies found by Sherbini, as DPK's are unable to account for such scattering in volumetric sources. Additionally, the correction for atmospheric scattering was limited in derivation and does not account for variations in source geometry, *Z*, and skin depth. A complete scattering model should address scattering effects, both internal and external to the source, and account for these three variables.

2.7 Monte Carlo Skin Dosimetry

Hot particle dosimetry presents a special case in which dose must be calculated to very thin regions of tissue near the surface of the skin. This presents a difficult challenge for nearly all Monte Carlo codes due to the systematic errors introduced by boundary crossing. These errors typically have little effect on dose volumes of significant size (relative to the particles range), but the impact within such small volumes may be severely exaggerated. The condensed history techniques required to transport electrons by Monte Carlo methods are based upon the application of multiple-scatter theories developed to explain electron transport on larger scales in infinite homogeneous media. Electron behavior is therefore typically well-modeled within any given volume, but the underlying assumptions inherently break down as the particle crosses a boundary.

Boundary crossing has in fact been a serious shortcoming for Monte Carlo electron transport since its inception. The typical approach has been to simply terminate the electron's major step as it crosses a boundary. This prevents electrons near the entrance region of a given medium from behaving as if they are still within the previous medium. As Schaart (2002) explains, this simple termination introduces a systematic error as the average energy loss rate for that step was sampled with the assumption that the electron would in fact traverse the entire step length.

Kawrakow and Rogers (2000) reevaluated these boundary crossing methods during the development of EGSnrc, as they sought to improve its accuracy beyond that of earlier EGS versions. A new transport method was developed that removed the problem of multiple-scatter boundary crossing errors by eliminating condensed history techniques near boundaries entirely. The code instead monitors the distance from a particle to a wall and switches the electron transport method into single-scatter calculations until the electron crosses or exits the boundary region.

Extensive work has been completed by Caffrey (2012) examining the dose volume thickness dependence of the Monte Carlo transport codes EGSnrc and MCNPX. In his work, dose volumes were segmented within the water at various depths beginning at 7 mg cm^{-2} and extending to 1000 mg cm^{-2}. The radius of each dose volume was set at 0.564 cm, equating to

a 1 cm^2 planar area. Dose volume thickness was treated as an independent variable and set to 10, 20, 30, 40, and 50 μm thicknesses to determine the effects of dose volume thickness upon calculation consistency. Each dose volume was centered upon the depth of interest, ie: the (10 μm x 1 cm^2) volume at 7 mg cm^{-2} resided between 6.5 mg cm^{-2} and 7.5 mg cm^{-2}. A mono-energetic electron point-source was placed directly above the skin (water) surface to avoid losing particles generated within the boundary. Mono-energetic source problems using 1 MeV and 250 keV electrons were evaluated separately.

Caffrey's results demonstrated that MCNPX strongly overestimated doses in shallow tissue depths for both 1 MeV and 250 keV electrons when compared to EGSnrc (Fig. 2.2, Fig. 2.3). Shallow dose at 7 mg cm^{-2} was overestimated by approximately 22% from 1 MeV electrons and by approximately 7% for 250 keV electrons. A transition toward underestimation occurs in deeper tissue volumes. This is seen as a strongly negative percentage deviation, though the overall dose consequence there is less than that for shallow dose. The extent of these discrepancies was found to be strongly dependent upon the thickness of the dose volumes in question. Increased layer thickness results in stronger agreement between MCNPX and EGSnrc, presumably due to the reduced fractional contribution of systematic errors near the volume boundary. The accuracy improvements gained with each added thickness appears to decrease, however, suggesting that continued additions to thickness will not necessarily result in agreement between MCNPX and EGSnrc.

In agreement with existing literature (Kawrakow 1998, 2000), no dependence upon volume size was noted in this investigation for EGSnrc. Also in agreement with existing literature (Wang 2001; Schaart 2002; Reynaert 2002) MCNPX demonstrated little consistency between calculations of varying dose region thickness. The systematic errors introduced by boundary crossing in the MCNP algorithm become very prominent as total cell size was reduced. These effects are present at lower energies and further exaggerated at high energies. Changing the number of substeps within each major step by modifying the ESTEP parameter will likely improve agreement to some extent, but this will result in much longer computation times to achieve equivalent statistical uncertainties (Schaart 2002).

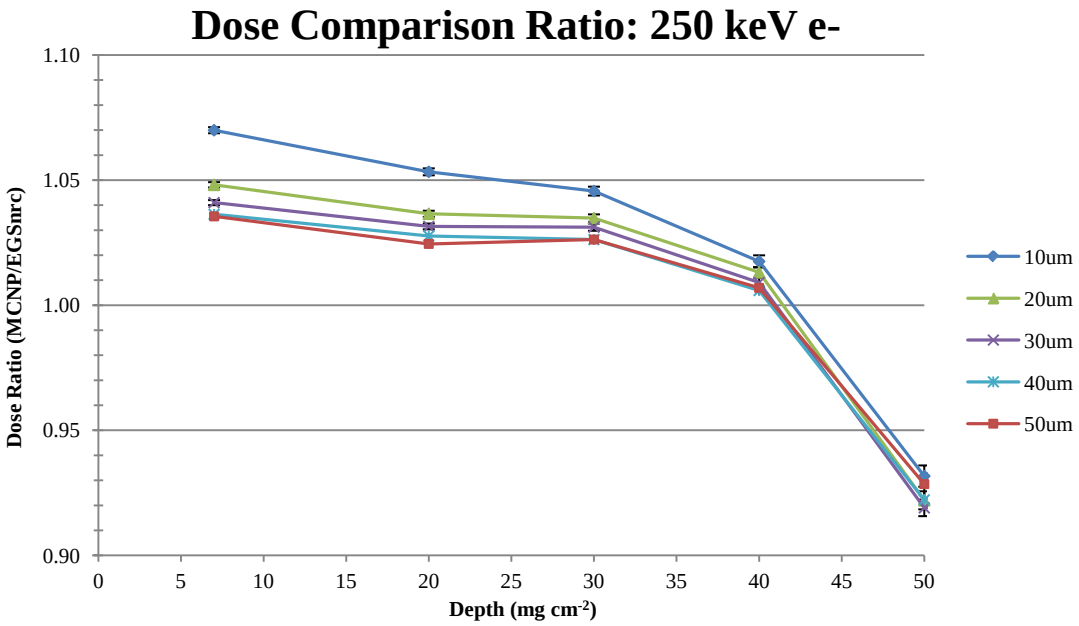

Fig. 2.2. Dose deviation from a mono-energetic point-source of 250 keV electrons at the air-water interface to thin layers at 7, 20, 30, 40, and 50 mg cm^{-2} (with permission of Jarvis Caffrey).

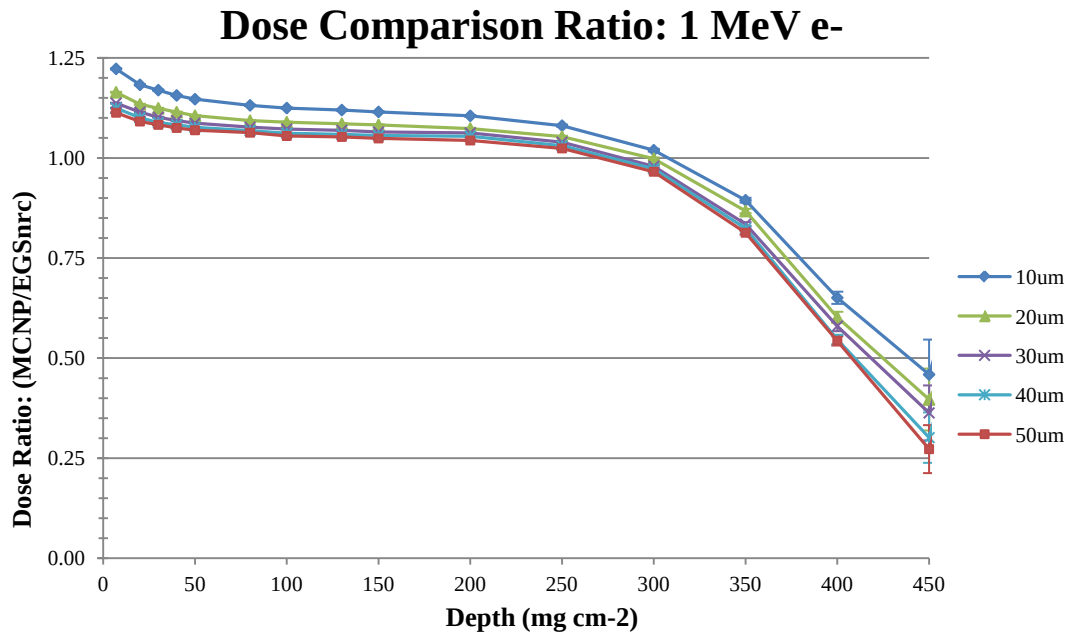

Fig. 2.3. Dose deviation from a mono-energetic point-source of 1 MeV electrons at the air-water interface to thin layers located between 7 and 450 mg cm^{-2} (with permission of Jarvis Caffrey).

3 Background

3.1 Heavy Charged Particle Interactions with Matter

The primary energy loss mechanism for all charged particles is based on the interactions between the electric field of the charged particle passing through matter and the electric fields of nearby atomic orbital electrons. The basic principles involved are most easily seen when examining heavy collisions of charged particles (protons, alphas, fission fragments). A more detailed study of electron interactions in matter follows.

Consider (Fig. 3.1) a particle of mass M (which is large compared to the mass of an electron, m_0) and charge Z moving with a velocity V in the positive x direction at a normal distance of b. An electron, positioned at the origin of an x-y coordinate system and at a distance r from mass M, will experience a force towards M equal to

$$F = \frac{kZe^2}{r^2}, \tag{3.1}$$

where the value of k is 8.98975 x 10^9 N m^2 C^{-2}. When M reaches the y-axis, the component F_x will reverse direction, resulting in no net motion in the x direction (Johns & Cunningham 1983). However, the component F_y will be in the same direction and result in a net impulse in the positive y direction. This impulse is written as

$$\Delta p = \int_0^\infty F_y dt = \int_0^\infty \frac{kZe^2}{r^2}\frac{b}{r}dt = kZe^2\int_0^\infty \frac{b}{(b^2+V^2t^2)^{3/2}}dt = \frac{2kZe^2}{Vb}. \tag{3.2}$$

If M is large compared to m_0, the degree of deflection with respect to its original path of travel will be very small. Despite this, energy will be transferred to the electron, as given by

$$\Delta E_b = \frac{\Delta p^2}{2m_0} = \frac{2k^2Z^2e^4}{m_0V^2b^2} = \frac{k^2Z^2e^4}{m_0b^2}\frac{M}{E}, \tag{3.3}$$

where $E = ½ MV^2$ and is the kinetic energy of mass M. Equation (3.3) shows that the energy transferred to the electron is inversely proportional to the kinetic energy of the heavy charged particle. This is a direct result of the high velocity of the charged particles at this energy and the short duration spent in the vicinity of the electron. It can also be seen from Eq. (3.3) that the energy transferred is inversely proportion to b^2. The distance b is often called the *impact parameter* and represents the distance by which the charge particle misses making a direct hit on the electron (Johns & Cunningham 1983).

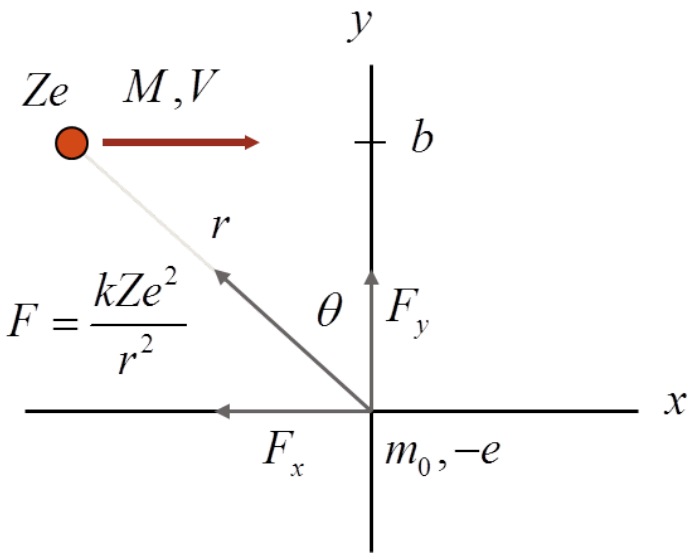

Fig. 3.1. Representation of the loss in energy of a heavy charged particle with an electron located at the origin.

In traversing a distance dx in a material with uniform electron density, n, a charged particle will encounter $2\pi nb(db)dx$ electrons at an impact parameter between b and $b + db$. The energy lost by the charged particle per unit distance traveled is $2\pi nb(db)\Delta E_b$. The total linear rate of energy loss is found by integration over all possible energy losses, or equivalently, all possible impact parameters (Turner 2007). Using Eq.(3.3) it can be shown that

$$-\frac{dE}{dx} = 2\pi n \int_{\Delta E_{b\min}}^{\Delta E_{b\max}} \Delta E_b b db = \frac{4\pi n k^2 Z^2 e^4}{m_0 V^2} \int_{b_{\min}}^{b_{\max}} \frac{db}{b} = \frac{4\pi n k^2 Z^2 e^4}{m_0 V^2} \ln \frac{b_{\max}}{b_{\min}}. \quad (3.4)$$

The quantity *dE/dx* is called the *stopping power* and describes the amount of energy lost per unit length along the track of the particle. The energy limits of integration are replaced with the minimum and maximum impact parameters. The lower limit of *b* is governed by the requirement that particles remain separated by a distance b_{min}, at least as large as their de Broglie wavelength (Turner 2007). At the upper limit for *b*, the energy transferred to an orbital electron will be insufficient to overcome its binding (or excitation) energy and the atom will not be ionized (or excited). The electron will simply be pulled from its equilibrium position and then return (Johns & Cunningham 1983).

The semi-classical expression in Eq. (3.4) requires additional numerical analysis with quantum theory. For this, the mean excitation energy, *I*, is introduced. The mean excitation energy is a quantum-mechanically derived quantity that is directly correlated to b_{max}; the larger its value, the smaller is b_{max}. In addition, when sufficient energy is transferred to an electron, relativistic effects must be considered. Therefore, using relativistic quantum mechanics, Bethe derived the following expression for the stopping power of a heavy charged particle in a uniform medium (Knoll 2000),

$$-\frac{dE}{dx} = \frac{4\pi k^2 e^4 z^2}{m_0 v^2} NZ \left[\ln\left(\frac{2m_0 v^2}{I} \right) - \ln\left(1-\beta^2\right) - \beta^2 \right], \quad (3.5)$$

where

- *z* is the atomic number of radiation particle;
- *v* is the velocity of radiation particle (β = v/c);
- *e* is the charge of the electron;
- m_0 is the rest mass of the electron;
- *k* is 8.98975 x 10^9 N m^2 C^{-2}
- *N* is the atom density of absorber material (*nZ*);
- *Z* is the atomic number of absorber material; and
- *I* is the effective ionization potential of absorber.

For nonrelativistic particles (v<<c) however, only the first term in the brackets is significant. As can been seen from Eq.(3.5), as the particle loses energy and slows down, the rate of energy loss increases roughly as $1/E$ ($1/v^2$). The rate of energy loss will then increase very rapidly near the end of the particle track until the charge is reduced though electron pickup (electron chemically bonding to the charged particle), at which point the rate drops suddenly to zero. This large $-dE/dx$ near the end of the track was first observed by Bragg (1904) and is called the *Bragg peak*.

The stopping power in Eq. (3.5) is typically called the "linear" stopping power and has units of energy per unit distance. Since the derivation of Eq.(3.5) is based on Coulomb interactions, it is also called the *collisional stopping power*, or the *ionization stopping power* (Shultis & Faw 2008). The mass stopping power, *S*, of a material is obtained by dividing the linear stopping power by density and typically has units of MeV mg^{-1} cm^2;

$$S = \frac{1}{\rho}\left(-\frac{dE}{dx}\right). \tag{3.6}$$

Mass stopping powers are very useful quantities since they do not differ greatly for materials with similar atomic composition. In addition, mass stopping powers for gasses are independent of pressure.

3.2 Electron (Beta-Particle) Interactions

3.2.1 Beta-Particles

Beta-particles are the same physically as electrons. While electrons are often considered to be mono-energetic, beta-particles will have a distribution of possible energies with a maximum, or endpoint energy. Their energy distributing is a direct result of their origin; beta decay of a radionuclide. Beta decay occurs when a nucleus is energetically unstable due to its proportion of neutrons and protons. In the event where the nucleus is neutron rich, a neutron, in effect, will transform into a proton and an electron, or beta-particle (Shultis & Faw 1996). The inherent energy distribution of beta-particles stems from the fact that the beta is

accompanied in the nuclear transformation by an antineutrino, an essentially massless particle with no charge. The energy released in the decay process (*Q* value) is shared by the beta-particle and the antineutrino. Beta decay takes the form of

$$ {}^{A}_{Z}X \rightarrow {}^{A}_{Z+1}Y + {}^{0}_{-1}\beta + \overline{\nu}, \tag{3.7} $$

where $\overline{\nu}$ is the antineutrino. The *Q* value associated with Eq. (3.7) can be calculated from the atomic masses of nuclides *X* and *Y* using

$$ Q_{\beta-} = \left[M\left({}^{A}_{Z}X\right) - M\left({}^{A}_{Z+1}Y\right) \right] c^2. \tag{3.8} $$

The use of the c^2 term is a direct result of Einstein's theory of relativity, $E=m\,c^2$. The endpoint of the beta energy distribution represents the event where the antineutrino receives no kinetic energy. The average beta energy can be approximated as one-third of the endpoint energy, or when the energy distribution is known, it can be calculated more precisely using

$$ E_{av} = \int_{0}^{E_{\max}} E\ N(E)dE, \tag{3.9} $$

where E_{max} is the endpoint energy of the beta spectrum, $N(E)dE$ is the fraction of beta-particles emitted per MeV per transformation that have energies between *E* and $E+dE$ (Shultis & Faw 1996). The discussion below will apply to both electrons and beta-particles.

3.2.2 Stopping Power

Like heavy charged particles, electrons will slow down in matter through Coulombic interactions that result in either ionization or excitation of atoms. However, the collisional stopping power for electrons will differ from that of heavy charged particles in two important respects. Due to the small mass of the electron, collisions with orbital electrons (same mass) can result in rather large energy losses with significant changes in directions. The maximum energy that can be transferred to a *secondary* electron is one-half of the incident electron energy. This restriction comes from the fact that the electron which emerges from a collision with the most energy is assumed to be the original electron. The second caveat, also related to

the electron mass, is that interactions with the electric field of the nucleus become more important for electrons and can result in energy loss through radiative emissions (Johns & Cunningham 1983). Therefore, the total stopping power for electrons is determined by considering both collisional and radiative losses, as given by

$$\left(-\frac{dE}{dx}\right)_{total} = \left(-\frac{dE}{dx}\right)_{col} + \left(-\frac{dE}{dx}\right)_{rad}. \tag{3.10}$$

An expression similar to Eq. (3.5) has also been derived by Bethe for the collisional stopping power of electrons in a uniform medium (Turner 2007);

$$\left(-\frac{dE}{dx}\right)_{\text{col}} = \frac{4\pi n k^2 e^4}{mc^2\beta^2}\left[\ln\frac{2mc^2\tau\sqrt{\tau+2}}{\sqrt{2}I} - \frac{1-\beta^2}{2}\left[1+\frac{\tau^2}{8}-(2\tau+1)\ln 2\right]\right], \tag{3.11}$$

where

$$\tau = \frac{E}{m_0 c^2}.$$

Equation (3.11) does not take into account the multiple changes in direction that can occur when an electron slows down. If used to plot $-dE/dx$ versus x, it will falsely exhibit a sharp Bragg peak for electrons. However, the tortuous path length of an electron in matter will result in a smearing-out effect and the Bragg peak will not be identical to that of a heavy charged particle (Johns & Cunningham 1983).

The radiative losses of an electron traversing matter can be explained using the Larmor relationship (Podgoršak 2006). The Larmor relationship from classical electromagnetism states that charged particles emit radiation as they are accelerated or decelerated according to the equation,

$$P = \frac{q^2 a^2}{6\pi\varepsilon_0 c^3}, \tag{3.12}$$

where P is the power radiated by the charged particle, q is the charge, a is the acceleration, ε_0 is the permittivity of free space, and c is the speed of light. The electromagnetic radiation emitted as a charged particle slows down is called bremsstrahlung. The deflections of a charged particle in its Coulomb interactions with the absorbing material provide the acceleration required for bremsstrahlung production. The acceleration is proportional to the product of the charge on the incident particle and the nucleus, and is inversely proportional to the mass of the incident particle. Therefore, bremsstrahlung is most important for light particles, such as electrons, in high atomic number materials. The radiative stopping power for electrons is a result of bremsstrahlung and is given by

$$\left(-\frac{dE}{dx}\right)_{\text{rad}} = \frac{4nk^2Z(Z+1)e^4\tau}{137mc^2}\left[\ln 2\tau - \frac{1}{3}\right], \tag{3.13}$$

where τ is equal to the kinetic energy of the electron divided by its rest energy (Knoll 2000). The factors of τ (E) and Z in the numerator of Eq. (3.13) demonstrate that bremsstrahlung production is more important for high-energy electrons and in high atomic number absorbing media. The ratio of the two energy loss mechanisms is approximated by

$$\frac{\left(dE/dx\right)_{rad}}{\left(dE/dx\right)_{col}} \sim \frac{ZE}{700}. \tag{3.14}$$

An estimate of the radiation yield can give an indication of the electron energy that is potentially carried away from the local point of interaction (Turner 2007). An electron with kinetic energy E (MeV) in an absorber of atomic number Z will have a radiation yield approximated by

$$Y \cong \frac{6x10^{-4}\,EZ}{1-6x10^{-4}\,EZ}. \tag{3.15}$$

As an example, electrons in aluminum (Z=13) will have a radiation yield of ~1.6% at an electron energy of 2 MeV, whereas lead (Z=82) will result in a radiation yield of ~9.0% at the same energy.

3.2.3 Restricted Stopping Power

Electrons lose energy primarily through a large number collisions, as demonstrated by the radiation yield above. For the most part, the energy is deposited near the track of the incident particle through ionization and excitation. In this situation, the energy *lost* by the electron is the energy *absorbed* at the target. However, some electrons, called "delta rays" or "knock-on electrons", receive enough energy to create their own tracks of ionization and excitation, thus carrying energy away from the initial electron track. The restricted stopping power is used to associate local energy loss in a target more closely with the energy that is actually absorbed locally (Turner 2007). The restricted stopping power is defined as the linear rate of energy loss due only to collisions in which the energy transferred does not exceed a specified Δ. The term *linear energy transfer* (LET) is synonymous with restricted stopping power and is defined as

$$LET_{\Delta} = \left(-\frac{dE}{dx} \right)_{\Delta}, \tag{3.16}$$

with the symbol LET_{∞} denoting the usual (unrestricted) stopping power.

3.2.4 Energy Straggling and Electron Range

The microscopic interactions undergone by electrons (or any charged particle) vary somewhat randomly, resulting in a statistical distribution of energy loss and number of collisions along its path. As a result, there will be a spread of energy distribution after a mono-energetic electron passes through a given layer of absorber. The width of the energy distribution is the measure of energy straggling and will vary with distance along the particle track. Energy straggling will initially increase along the electron track and then begin to lessen as its mean energy has been greatly reduced (Knoll 2000).

Energy straggling, in addition to large angular deflections, will have a significant impact on the range of an electron. The reciprocal of the stopping power yields the average distance traveled per energy loss. If it were true that an electron traveled along a straight path and lost energy continuously, then integration of this value for an electron of initial kinetic energy E_0 would give the range, R (Shultis & Faw 1996);

$$R = \int_0^{E_0} \frac{dE}{-\left(dE/dx\right)_{tot}}. \tag{3.17}$$

The statistical fluctuations and energy straggling along the path of an electron make it difficult to identify an unambiguous "range". However, the range measured in Eq. (3.17) can be used to identify an effective path length based on the continuous slowing-down approximation (CSDA). Inherent in this approximation is the assumption that the electron slows down continuously with no energy-loss fluctuations, no secondary electron or delta-ray production, and with a mean energy loss per unit path length given by the total linear stopping power evaluated at the electron's current energy (Shultis & Faw 1996). It should be noted that for heavy charged particles, the amount of range straggling around the CSDA range is narrowly distributed due to their near straight paths. However, this is not the case for electrons due to their tortuous path in matter. As a rule of thumb, the average deepest penetration for electrons is roughly one-half the CSDA range (Turner 2007).

As with linear stopping power, ranges are typically written in terms of density. Detailed analysis of experimental data has shown that the ability to absorb energy from electrons depends mainly on the number of absorbing electrons present in the absorber. The electron density varies with physical density to a much larger degree than it does with atomic number. Therefore, it is more practical and convenient to write linear distances as density thicknesses (density x thickness) with units of mass per unit area. This allows for beta-particle ranges to be calculated using universal empirical equations (Cember 1996):

$$R_\beta = 412E^{1.265-0.0954\ln E} \quad \text{for } 0.01 \le E \le 2.5 \text{ MeV}, \tag{3.18}$$

and

$$R_\beta = 530E - 106 \quad \text{for } E > 2.5 \text{ MeV}, \tag{3.19}$$

where R is expressed in the density thickness units (mg cm^{-2}) and E is the maximum beta-particle energy (in MeV).

3.2.5 Backscatter

As stated previously, electrons often undergo large-angle deflections along their paths due to their small mass. This leads to the phenomenon of backscattering, in which an electron entering an absorber may undergo sufficient deflection such that it re-emerges from the surface through which it entered. These backscattered electrons do not deposit all of their energy in the absorber, and therefore the backscattering process can have a significant impact on absorbed dose. Electrons with high incident energy and absorbers with low atomic number have the lowest probability for backscattering. Therefore, backscattering typically occurs when low-energy electrons enters a region of high atomic number or high mass density (Knoll 2000). Electrons backscatter by nuclear elastic scattering, which is the glancing of an electron off an atomic nucleus. Nuclear elastic scattering takes place when the relative size of the atomic nucleus is large and the relative electron charge density of the atom (Z/A) is low. Lower values of Z/A generally occur for large atomic mass numbers (A).

3.3 Electron (Beta-Particle) Dose Calculations

3.3.1 Absorbed Dose

The *absorbed dose* is defined as the amount of energy deposited per unit mass of any material. The original unit for absorbed dose was the *rad* (radiation absorbed dose), which is equivalent to the absorption of 100 ergs of energy in 1 g of absorbing material (Martin 2006). The SI unit is the *gray* (Gy) and is defined as the absorption of 1 J of energy per kilogram of absorbing material. The two units are related through the relationship

$$\begin{aligned} 1\ \text{Gy} &= 1\ \text{J/kg} \\ &= 100\ \text{rad}. \end{aligned}$$

The *equivalent dose* (measured in SI units of Sieverts, Sv) is the product of absorbed dose and a radiation weighting factor, w_r, or historically the quality factor, Q. This factor takes into account the biological effectiveness in humans of different radiation types due to differences in energy transfer rates (e.g. LET) (Martin 2006). Radiation particles with higher LET's will

cause more biological damage per unit distance travelled and will thus have a higher radiation weighting factor. Since this factor for electrons is unity, for a given absorbed dose, the equivalent dose is the same.

Effective dose (also measured in Sv) is the product of tissue specific, equivalent dose and a series of tissue weighting factors for each organ type, summed. The tissue weighting factor, w_t, generally accounts for the fetal cancer risk to various organs following radiation exposure of those organs. Effective dose is typically a measure of stochastic effects (e.g. cancer) and is not a focus in this work. Doses in this work will be measured as absorbed dose, and since the radiation weighting factor for betas is unity, absorbed dose will equal equivalent dose.

3.3.2 Dose-Point Kernels

Spatial distributions of absorbed dose are expressed in terms of point kernels and associated scaled dimensionless dose distributions. The expected absorbed dose at a distance r from an isotropic point-source of mono-energetic electrons of energy E is denoted $J(r, E)$. It is convenient to express the point kernel J in terms of a dimensionless dose distribution $F(r/r_0, E)$ where r_0 is the CSDA range of the electron. The kernel can be written as

$$J(r,E) = \frac{E}{4\pi r^2 \rho r_0} F(r / r_0, E), \tag{3.20}$$

where ρ is the density of the absorbing medium with units of mass per unit volume. It can be inferred from Eq. (3.20) that the fraction of E deposited between radii r and dr is $(dr/r_0)\cdot F(r/r_0, E)$ (Shultis & Faw 1996). In the case of beta-particles, Eq. (3.20) can be written as

$$J_\beta(r) = \frac{1}{4\pi r^2} \int_0^{E_{\max}} \frac{E\ N(E)}{r_0(E)} F(r / r_0, E)\ dE. \tag{3.21}$$

Dose-point kernels are discussed in great detail in Section 2.4 and will therefore not be examined in any more detail at this time.

3.3.3 Numerical Integration of Dose-Point Kernels

DPK codes such as VARSKIN 4 (Traub 1987; Durham 1992, 2006; Hamby 2011) and K-SKIN (Park 2009) rely on an accurate and fast numerical integration method to calculate dose from a volumetric source to a given dose area. A typical integration process divides the source into very small subvolumes (source points). The dose averaging area is divided into points at which the dose rate is to be calculated (dose points). The dose points (60 are used for this discussion) are positioned along the radius of a dose-averaging disk at a specified dose depth (Fig. 3.2). Since the source geometry (cylindrical is used for this discussion) is symmetric about the dose-averaging area, dose points represent concentric isodose circles that describe the radial dose profile at a given depth in skin.

For each of the 60 dose points, a numerical integration is performed over the area of the cylindrical source at a given height in the source represented by 8 elevations (z), 8 radii (r'), and 8 angular locations (θ). The dose rate at a dose point on an isodose circle of radius d' is evaluated using

$$\dot{D}(d') = S_v \int_0^{2\pi} \int_0^R \int_0^Z r' \; B(z, r', \theta) \; dz \; dr' \; d\theta, \tag{3.22}$$

where $B(z,r',\theta)$ is the dose per disintegration (rad nt^{-1}) from a source point with source-coordinates (cylindrical) of z, r', and θ, R and Z are the source radius and height, and S_v is the volumetric source strength (nt cm^{-3}). This procedure is repeated for each dose point beginning at the center of the irradiation area and extending to its edge. The dose rate averaged over an area at depth in the tissue is then calculated using

$$\bar{D} = \frac{2\pi \int_0^R \dot{D}(d') \; d' \, dd'}{\pi R^2}. \tag{3.23}$$

where R is the radius of the dose averaging area.

The integration starts by choosing one of the eight elevation points (▲) in the source (Fig. 3.2). At one of these elevations, one of eight concentric circles (radial source-points ●) is chosen. One of these circles is then subdivided into eight source-points at 45-degree angles

from each other (angular source-points ★). Finally, the dose rate is calculated at each dose point from each of these eight source-points at a given elevation and radius. The contribution to the dose from the first four points is compared to the contribution of the last four points in a given circle. If the relative difference between the two contributions is less than 0.01 percent, then convergence of the integral for the circle is considered to be achieved, and the procedure is repeated at the next radial position. If the relative difference between the two contributions is greater than the relative error, each of the two contributions is further subdivided into eight additional source-points, and the above procedure is repeated for each of the two sets of eight points. This process, known as the Newton-Cotes eight-panel quadrature routine, provides a fast and accurate method of numerically integrating complex functions such as dose-point kernels (Durham 1992, 2006; Hamby 2011).

.

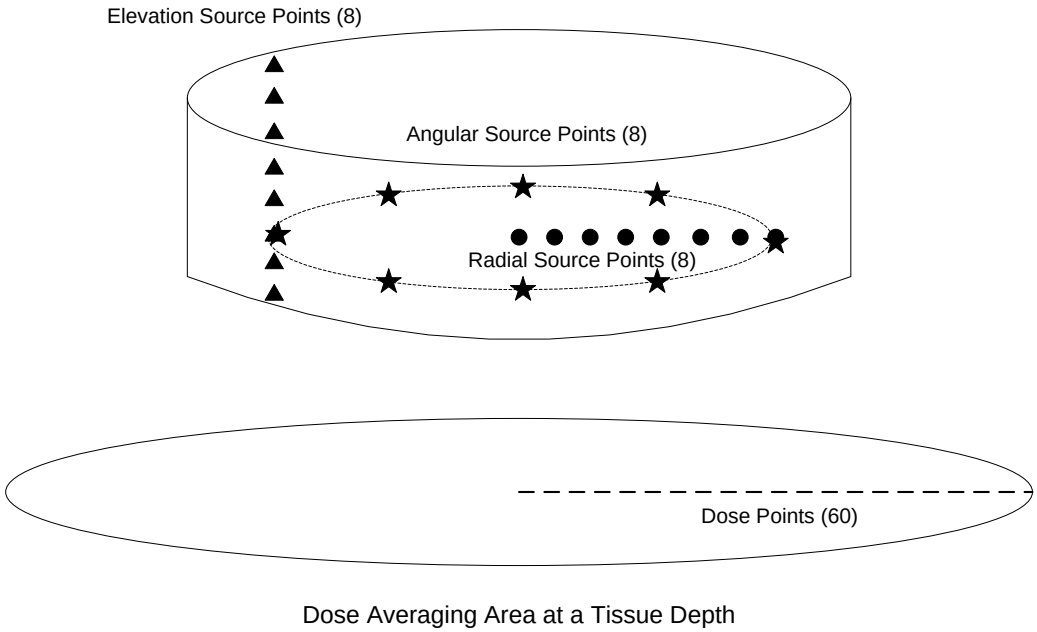

Fig. 3.2. Schematic representation of the eight-panel quadrature routine used to calculate dose for a symmetric source (redrawn from Durham 2006).

4 Methods

4.1 Introduction

In this section, a detailed methodology for completing the objectives outlined in Section 1.2 is provided: (1) development of a new scaling model for high-Z hot particle sources; (2) and an accompanying comprehensive backscatter model. Both models are applicable to source materials with $7.42 < Z \leq 94$ and all beta-emitting radionuclides. Meeting these objectives requires considerable amounts of data collection and analysis. Methods for handling these tasks are also addressed.

4.2 Homogeneous Dose-Point Kernels

The Monte Carlo transport code, EGSnrc, was used to determine the radial energy distributions (or DPK's) and X_{90} values for $7.42 < Z \leq 94$ (Fig. 4.1, Table 4.1) at electron energies of 0.01 MeV$\leq E \leq$ 8 MeV (30 total values). An isotropic mono-energetic point-source was positioned at the center of concentric spherical shells of the respective media (Fig. 4.2). For all simulations, the shell thickness was 5% of the CSDA electron range, as taken from ESTAR of the National Institute of Standards and Technology (NIST). The last shell was at a radius 150% of the CSDA range to ensure complete absorption of the electron energy (excluding radiative-losses). The maximum energy of 8 MeV covers all beta-particle endpoint energies published in ICRP Publication 107 (2008). The minimum energy of 0.01 MeV is based on the 0.001 MeV lower limit of electron cross-section data available in EGSnrc. In addition, the ESTAR CSDA range of a 0.01 MeV electron is only 0.252 mg cm^{-2}.

As discussed in Section 2.4.3, MCNP can be used to accurately determine energy deposition kernels when the ITS energy indexing algorithm is used and when special care is taken for high-resolution measurements. EGSnrc on the other hand, was not only shown to be step-size independent, but it is significantly faster at transporting electrons than MCNP. For example, MCNP requires 103 minutes of CPU time to measure energy deposition kernels for

1 MeV electrons in water (10^6 particle histories), whereas EGSnrc requires ~9 minutes for the same simulation. This difference becomes even larger as electron energy and material *Z* increases. For these reasons, EGSnrc is used as the Monte Carlo code of choice for all simulations pertaining to the scaling and scattering models.

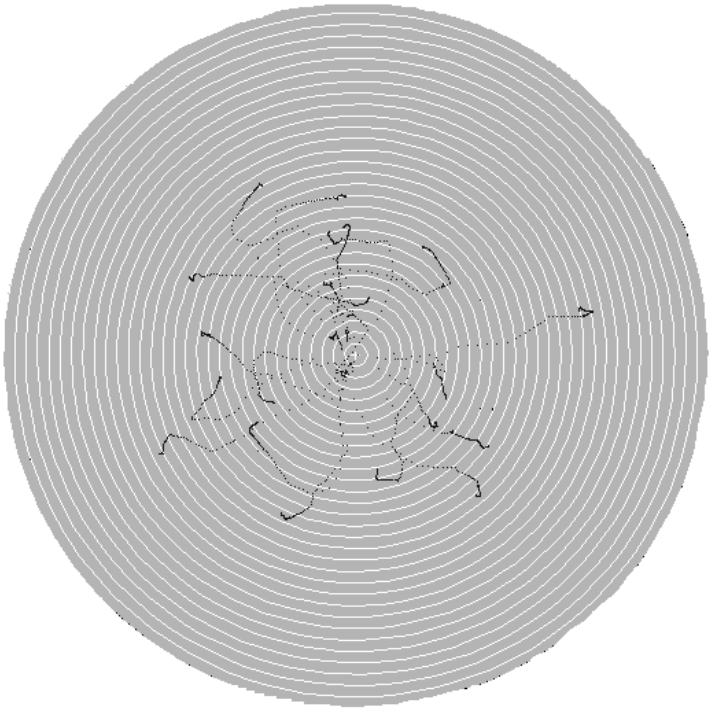

Fig. 4.1. Schematic of EGSnrc geometry for determining point-source radial DPK's. Eachshell thickness is 5% of the CSDA electron range. Total spherical radius is 150% of CSDA electron range. Simulated electron tracks are represented by the dark dotted lines.

Table 4.1. List of source materials used to develop the scaling model. Material selection covered a wide range of densities and atomic numbers.

Element	***Z***	**Density (g cm^{-3})**
Aluminum	13	2.70
Titanium	22	4.54
Iron	26	7.87
Gallium	31	5.91
Rubidium	37	1.63
Zirconium	40	6.51
Ruthenium	44	12.37
Silver	47	10.50
Tin	50	7.31
Barium	56	3.59
Neodymium	60	7.01
Gadolinium	64	7.90
Ytterbium	70	6.90
Tantalum	73	16.65
Platinum	78	21.45
Lead	82	11.35
Actinium	89	10.07
Plutonium	94	19.84

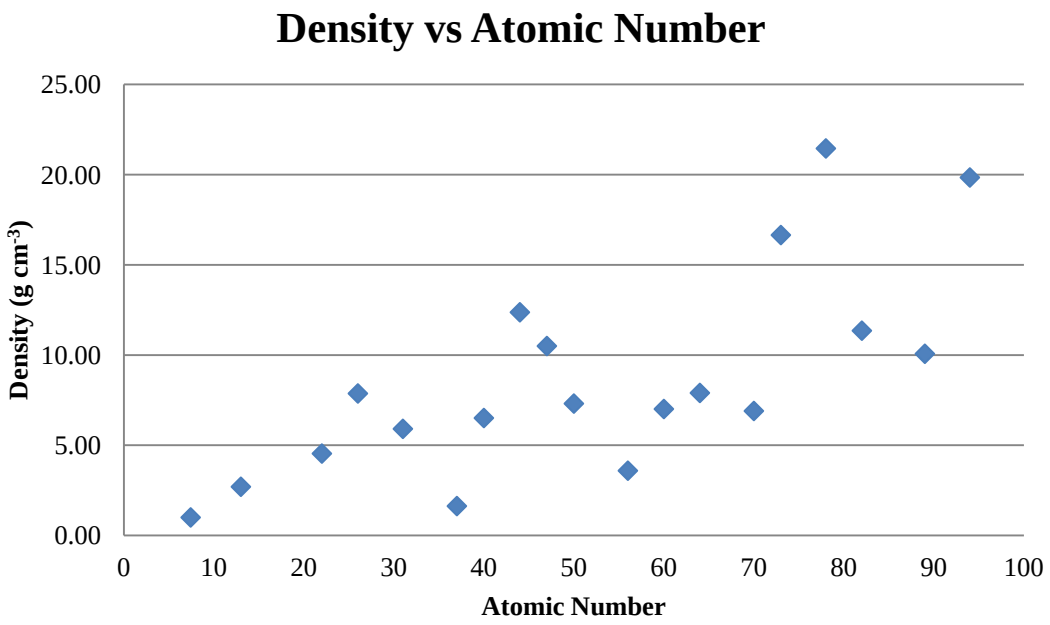

Fig. 4.2. Graph demonstrating the wide range of densities and atomic numbers used in development of the scaling model. All materials were solid in nature (except water).

EGSnrc simulations were performed using the EDKnrc user code. The NRC (National Research Council, Canada) user code EDKnrc can be used to calculate Energy Deposition Kernels (EDK) for photons or electrons (mono-energetic or polyenergtic) forced to interact at the center of a spherical geometry (Rogers 2011). The code can output energy deposition kernels in user defined spherical shells. The number of particle histories was set to one million and transport parameters were set to default settings except as noted below:

- PEGS data sets with AE=AP=1 keV;
- Set ECUT=PCUT=1 keV;
- Turn on Rayleigh scattering;
- Set bremsstrahlung cross sections to NIST.

PEGSs data sets are the material cross section data used by EGSnrc. The parameters of AE and AP determine the lowest energy for which the cross section values are defined.

Generally, when AE and AP are lowered (minimum of 1 keV), the accuracy of the calculation increases; however the computation time (CPU) increases as well (Kawrakow and Rogers 2000). Electrons with energies below AE will not be transported and their energy will be assumed to deposit locally. The same is true for photons (AP). The parameters ECUT and PCUT are related to AE and AP in that when an electron/photon energy falls below ECUT/PCUT, its energy is assumed to deposit locally. It is not possible to set ECUT and PCUT below AE and AP, respectively. These two parameters represent the Δ value in restricted stopping powers.

Turning on the Rayleigh scattering parameter allows for the simulation of coherent scattering. Raleigh scattering for bremsstrahlung photons may become important below ~1 MeV for high-Z materials and below 100-200 keV in low-Z materials. The updated NIST database for nuclear bremsstrahlung is strongly recommended for electron energies below 1-2 MeV with negligible improvements over default Bethe-Heitles cross sections above ~ 50 MeV. Sampling from the NIST database is faster at low energies but slower at high energies (Kawrakow and Rogers 2000).

The EDKnrc input files were written using Tool Command Language (TCL) scripts; allowing for the seamless creation and archiving of thousands of input files. The execution of the input files was performed on a Windows system (Intel Core 2 Quad 2.67 GHz, 64-bit Operating System). Automation of this task was accomplished with a Batch script. The script executed all material-energy simulations and archived the desired output files accordingly. Processing of the output was done with a Bash Shell script and FORTRAN code. A Cygwin terminal was used to execute the Bash Shell script. Bash Shell scripting was chosen for this function over Batch as it has more functionality and user options. The Bash Shell script parsed a target output file and sent the DPK data (shell radius, energy deposition data, and statistical uncertainty) to the FORTRAN code.

The FORTRAN code read in the DPK data and zeroed out total (radiative and primary loss mechanisms) energy depositions for which the primary statistical uncertainty was greater than 5.0%. The 32 DPK values were then expanded to 1500 evenly spaced linear values using a cubic spline function and the data was tabulated with respect to the midpoint radius of each spherical shell. The X_{90} value for each material-energy combination was found using

$$4\pi\rho \int_0^{X_{90}} r^2 \Phi(r, E_0) dr = 0.90, \quad (4.1)$$

where $\Phi(r,E_0)$ is the fraction of energy deposited per gram at a distance r from a point-source. The quantity $4\pi\rho r^2\Phi(r, E_0)dr$ is the fraction of emitted energy that is absorbed in a spherical shell of radius r, thickness dr, and density ρ.

4.3 Non-Homogeneous Dose-Point Kernels

Non-homogeneous point-source DPK's were determined for $7.42 < Z \leq 94$ at 0.01 MeV $\leq E \leq$8 MeV using EGSnrc Monte Carlo simulations. The user code, particle histories, and transport parameters were the same as those listed in Section 4.2. The intent of non-homogeneous DPK's is to determine how energy is deposited in water spherical shells after a mono-energetic electron has been emitted from the center of a sphere composed of some media other than water. The center absorbing sphere represents the source material and was varied for 18 elements (Table 4.1) with $7.42 < Z \leq 94$ with electron energies ranging from 0.01 MeV $\leq E \leq$8 MeV with 30 total energies. The radius of the center sphere was varied from 5% to 110% (complete electron absorption expected at 115%) of the X_{90} value in increments of 5%. The X_{90} value, calculated in Section 4.2, was chosen for the absorption-sphere radii over the CSDA range as it ensures an equal number of data points for each material-energy combination. However, the radii of the surrounding water spherical shells were increased in 5.0% increments of the CSDA range in order to facilitate direct DPK comparisons with homogeneous data.

As with homogeneous DPK's, a TCL script was used to create and archive the input files and a Batch script automated the execution of these files.

4.4 Scaling Parameters

4.4.1 Overview

The determination of the scaling parameters was accomplished through the use of a Bash Shell script and a FORTRAN code. The script parsed the EGSnrc output files for both the homogeneous (water) and non-homogeneous energy deposition kernels, in addition to dimensions such as shell radii and source material radii. These values were sent to a FORTRAN code that determined the depth-scaling and energy-scaling parameters, as described below. The script also tabulated the FORTRAN results along with the corresponding source material *Z*, source material ρ, source material radii, and energy for plotting.

4.4.2 Depth-Scaling Parameter

The DPK scaling model consists of two parameters: a depth-scaling parameter (*DSP*) and an energy-scaling parameter (*ESP*). As with the homogeneous DPK data detailed in Section 4.2, data processing was performed with a Bash Shell script and FORTRAN code. The script parsed the homogeneous (in this section, homogeneous implies a water medium) and non-homogeneous DPK data and sent it the FORTRAN code for processing and scaling parameter determination.

The depth-scaling parameter is dependent on the maximum range of the electron in both the homogeneous and the non-homogeneous media. After total energy deposition values with primary statistical uncertainties greater than 5.0% were zeroed out, the DPK data sets were expanded to 1500 values using a cubic spline function. Restricting the statistical uncertainty to 5.0% preserved the accuracy of the Monte Carlo simulation data, whereas the spline expansion to 1500 data points increased the precision level of desired data analysis.

Data analysis within the FOTRAN code began with determining the range of the electron in both the homogeneous and non-homogeneous geometries. Given the difficulty of determining an absolute electron range due to energy straggling and a torturous path, the radius at which 99.0% energy deposition occurred was chosen as a range estimate. The range in the homogeneous case was found by summing the DPK in each successive spherical shell

until the 0.99 fraction was obtained. This was accomplished using Eq. (4.1) by replacing X_{90} with X_{99} and 0.90 with 0.99. In the non-homogeneous case, the DPK data begins with the first spherical shell following the absorption sphere. However, energy lost in the sphere is added to the energy deposition total when determining the shell radius at which 99.0% energy deposition occurs;

$$4\pi\rho R^2\Phi(R,E_0)+4\pi\rho\int_0^{X_{99}} r^2\Phi(r,E_0)dr=0.99, \tag{4.2}$$

where $\Phi(R,E_0)$ is the fraction of energy deposited per gram in a sphere of radius R centered on an isotropic point-source. The quantity $4\pi\rho R^2\Phi(R,E_0)$ is the fraction of emitted energy that is absorbed in a sphere of radius R and density ρ.

The difference in ranges between the homogeneous and non-homogeneous data is therefore attributed to the absorption sphere in the non-homogeneous case. For a given absorption radius, the resulting difference in ranges is called the depth-scaling parameter,

$$DSP(R,E_0,\rho,Z)=X_{99\_H}-X_{99\_NH}, \tag{4.3}$$

where X_{99_H} is the homogeneous electron range, X_{99_NH} is the non-homogeneous electron range, ρ and Z are the absorption material density and atomic number, respectively. The FOTRAN code concluded by writing the depth-scaling parameter, absorption-sphere radius, and electron energy to an output file for plotting and further data analysis.

As an example, consider a source material of iron (Z = 26, ρ=7.874 g cm^{-3}) and an electron energy of 1 MeV. The radius of the iron sphere is chosen to be $0.5X_{90}$ (0.0222 cm) to allow for sufficient electron self-absorption. Due to the presence of the 0.0222 cm of iron, the electron range in the non-homogeneous shells is 0.120 cm less than the homogeneous range (Fig. 4.3). Therefore, for a 1 MeV electron traversing 0.0222 cm of iron, the depth-scaling parameter will be 0.120 cm. Shifting the homogeneous DPK data to the left by this amount will equate the ranges and provide the necessary depth adjustment (Fig. 4.4).

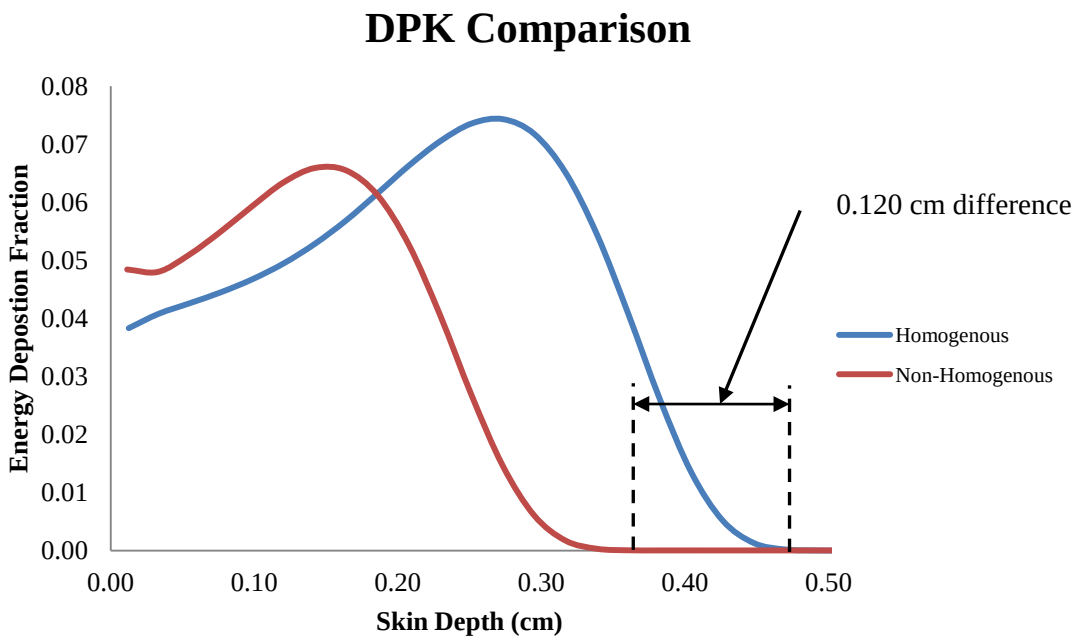

Fig. 4.3. Comparison of 1 MeV electron DPK's for the homogeneous water case and the case when the electron traverses iron source material of thickness 0.0222 cm.

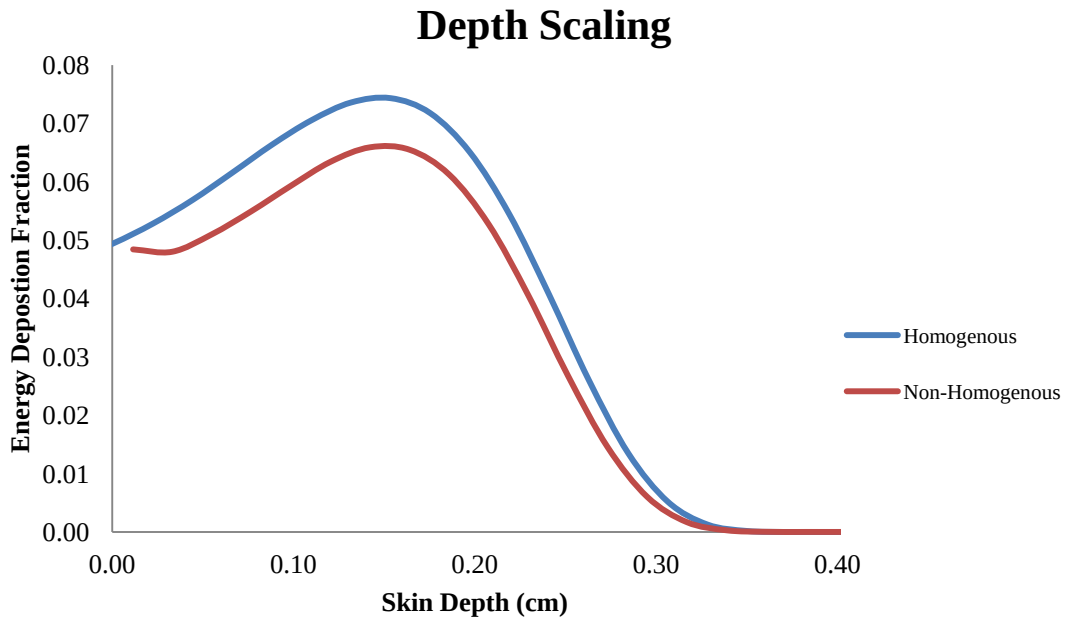

Fig. 4.4. Example of depth scaling on the homogeneous DPK curve. The depth-scaling parameter was determined to be 0.120 cm.

4.4.3 Energy-Scaling Parameter

The energy-scaling parameter is a direct result of energy conservation at distances within the electron's maximum range, or X_{99} (neglecting radiative loses beyond this distance). Once the homogeneous curve is shifted according to the depth-scaling parameter (Fig. 4.4), the total energy deposition is found for each case. In the homogeneous case, this is performed in the FORTRAN code by summing the homogeneous DPK's for radii between the depth-scaling parameter and the X_{99} distance,

$$4\pi\rho \int_{DSP}^{X_{99}} r^2 \Phi(r, E_0) dr = E_{total}. \tag{4.4}$$

Similarly, the total energy deposition in the non-homogeneous case is found by summing DPK's from 0 to X_{99}. The law of energy conservation requires the two be equal. Therefore, the energy-scaling parameter is found by taking the ratio of the non-homogeneous total to the homogeneous total,

$$ESP(R, E_0, \rho, Z) = \frac{4\pi\rho \int_{0}^{X_{99}} r^2 \Phi_{NH}(r, E_0) dr}{4\pi\rho \int_{DSP}^{X_{99}} r^2 \Phi_{H}(r, E_0) dr}. \tag{4.5}$$

Applying the resulting ratio to the homogeneous DPK equates the total energy depositions in the two geometries. For the example described in Section 4.4.2, an energy-scaling parameter of 0.887 is computed. Thus, energy conservation is achieved by multiplying the homogeneous curve by the energy-scaling parameter of 0.887 (Fig. 4.5).

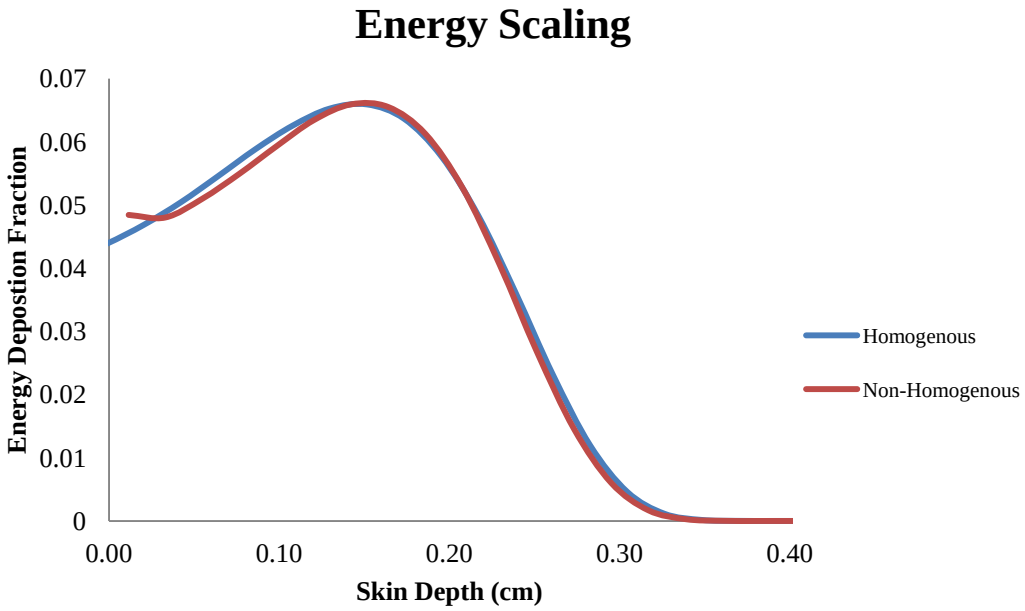

Fig. 4.5. Example of energy scaling on the homogeneous DPK curve presented in Fig. 4.4. The energy-scaling parameter was determined to be 0.887.

Once the *ESP*'s and *DSP*'s were determined, the Bash Shell script tabulated the results along with the corresponding source material *Z*, source material ρ, source material radii, and energy. Further analysis was performed and the results were plotted using a 3D surface plotting and curve fitting software package, TableCurve 3D. These findings are detailed in Section 5.3.

4.5 Beta-Particle Dose-Point Kernels

The end goal of the scaling model is the determination of non-homogeneous DPK's for beta-emitting radionuclides. By determining the depth and energy-scaling parameters for all energies between 0.01 and 8 MeV, it is possible to determine the non-homogeneous beta DPK for any known beta energy spectrum. This is accomplished by integrating over the beta energy spectrum for each source *Z*/thickness using

$$\Phi_{\beta}(R,Z,\rho)=\frac{1}{E_{av}}\int_{0}^{E_{\max}} ESP(R,E,Z,\rho)E\ N(E)\Phi(r,E)dE, \qquad (4.6)$$

where r is the *DSP*-adjusted spherical shell radius, E_{max} is the endpoint energy of the beta spectrum, $N(E)dE$ is the fraction of beta-particles emitted per MeV per disintegration that have energies between E and $E+dE$, and

$$E_{av}=\int_{0}^{E_{\max}} E\ N(E)dE. \qquad (4.7)$$

For example, if the nuclide and source material in question are ^{60}Co and iron, the scaling parameters are used to create an n x m array of DPK's for ^{60}Co with source radii ranging from 0 to $a{\cdot}X_{90}$ of iron and the water radii ranging from 0 to $b{\cdot}X_{90}$ of water. The parameter a will be based on complete beta-energy absorption in the source material and b will be based on complete beta-energy absorption in water when the source thickness is zero.

Non-homogeneous beta-particle DPK's were determined by incorporating *ESP* and *DSP* fit equations into the VARSKIN's FORTRAN code, SADCALC.f. SADCALC.f utilizes ICRP Publication 107 (2008) beta-particle spectra to calculate homogeneous water DPK's for each beta-particle present in a given dose calculation. Altering the code to produce the n x m array of non-homogeneous DPK's was successfully accomplished. Linear interpolation was used to accommodate all source media with $7.42 \leq Z \leq 94$.

Non-homogeneous DPK's were calculated for a wide range of beta energies (Table 4.2) and source materials (Table 4.3). The absorption-sphere radius was varied from 0.1 to 1.8 X/X_{90}. Stainless steel and uranium oxide were chosen as they represent common hot particle materials. Tungsten alloy was chosen to demonstrate the model's ability to handle high-density media. Beta-particle spectra are provided in Appendix G.

Table 4.2. List of nuclides used in scaling and scattering models.

Nuclide	**E_{av} (MeV)**	**X_{90} (cm)**
^{60}Co	0.0958	0.033
^{90}Sr	0.196	0.083
^{210}Bi	0.307	0.212
^{135}I	0.375	0.239
^{89}Sr	0.583	0.321
^{32}P	0.695	0.363
^{56}Mn	0.832	0.634
^{90}Y	0.934	0.533
^{144}Pr	1.217	0.696

Table 4.3. Source materials used for non-homogeneous beta-particle DPK testing.

Alloy	**Z_{eff}**	**Density (g cm^{-3})**
Stainless Steel (SS_302)	25.81	8.06
Tungsten Alloy (Mallory2000)	72.79	18.00
Uranium Oxide	87.88	10.96

4.6 Backscatter Model

4.6.1 Planar Dose Profiles

Point-source planar dose profiles were determined for the scattering media of water, air, and source materials with $7.42 < Z \leq 94$ (Table 4.1) at electron energies of 0.01 MeV $\leq E \leq$ 8 MeV using EGSnrc Monte Carlo simulations. The planar dose volumes were 1 mg cm^{-2} thick, with a maximum normal depth of 1000 mg cm^{-2}. The dose averaging areas were 1 cm^2 and 10 cm^2, consistent with the monitoring areas recommended by ICRP Publication 103 (2007) and NCRP Statement No. 9 (2001), respectively. The scattering medium was assumed infinite (>> electron range) in both thickness and lateral extent.

The EGSnrc simulations were performed using the DOSRZnrc user code with default transport parameters, except for ECUT, PCUT, AE, and AP. These parameters were the same as those listed in Section 4.2. DOSRZnrc simulates the passage of electrons in a finite, right cylindrical geometry. The user can define a specified number of planes and right cylinders to

produce the desired dose volumes. The geometry for these simulations was constructed using the 1000 planes and 2 cylinders described above. An outer cylinder of radius 5.64 cm (100 cm^2 area) was added to the dose collection area to properly account for scattering at the edge of the 10 cm^2 dose region (Fig. 4.6). Each dose volume was centered upon the depth of interest; e.g., the (10 μm x 1 cm^2) volume at 7 mg cm^{-2} resided between 6.5 mg cm^{-2} and 7.5 mg cm^{-2}. A mono-energetic electron point-source was placed directly above the water-scattering medium interface to avoid losing particles generated within the boundary. One million particle histories were used for each simulation. As with the scaling model, a TCL script and a Batch script were used to write and execute all EGSnrc input files.

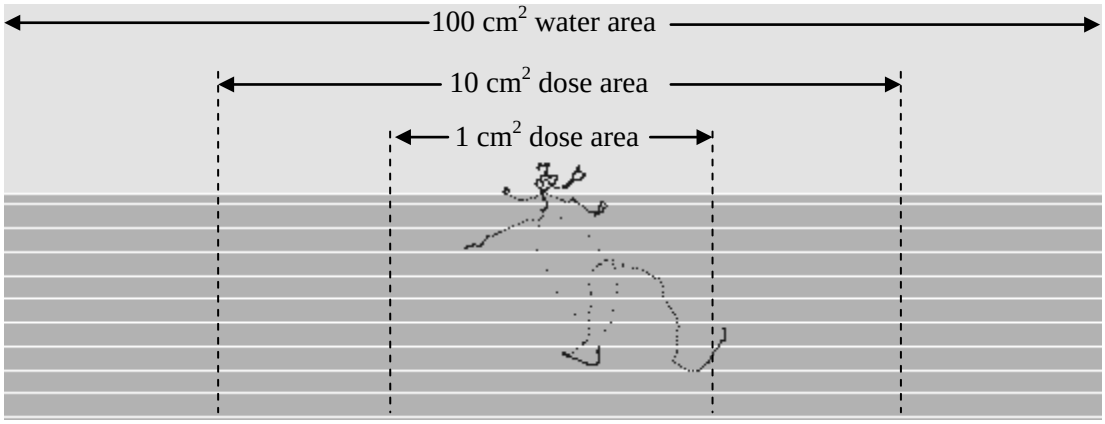

Fig. 4.6. Generic DOSRZnrc geometry for point-source planar dose profiles. The point-source is placed at the center of the light gray-dark gray interface with doses distributions being scored in the dark gray cylindrical water volumes. The light gray volume represents the scattering medium. Electron tracks are represented by the dark dotted lines.

A simple FORTRAN code and accompanying Bash Shell script were used to parse the EGSnrc output files and perform required data analysis. Planar-dose profiles for the 1 cm^2 dose area were zeroed out if the statistical uncertainty was greater than 5.0%. The dose for the 10 cm^2 area was determined by summing the dose in the 1 cm^2 dose area and the dose on the cylindrical shell of radii 0.564 cm (1 cm^2 area) and 1.784 cm (10 cm^2 area). Statistical uncertainty for the 10 cm^2 data was found by propagating the error using

$$\%Error_{10cm^2} = \frac{\sqrt{(E_{1cm^2} \bullet \%Error_{1cm^2})^2 + (E_{10cm^2-1cm^2} \bullet \%Error_{10cm^2-1cm^2})^2}}{E_{1cm^2} + E_{10cm^2-1cm^2}}, \quad (4.8)$$

where E_{1cm^2} is the energy deposited in the 1 cm^2 dose area, $E_{10cm^2\text{-}1cm^2}$ is the energy deposited in the shell of radii 0.564 cm and 1.784 cm, and $\%Error_{1cm^2}$ and $\%Error_{10cm^2\text{-}1cm^2}$ are their respective statistical uncertainties. Similar to the 1 cm^2 case, Planar-dose profiles were zeroed out if the propagated statistical uncertainty was greater than 5.0%.

4.6.2 Beta-Particle Backscatter Factors

In general, a backscatter factor is found by taking the ratio of the planar dose when the scattering material is present (non-homogeneous case) to that when water is present (homogeneous case). Air scattering corrections are often inversely reported such that they are greater than or equal to one (Cross 1991b, 1992c). Regardless, these backscatter factors will be dependent on electron energy, backscattering medium *Z*, normal depth, and dose averaging area. When applied to a beta-emitting nuclide, the backscatter factor for a given dose averaging area will take the form of

$$B_\beta(Z,z) = \frac{\int_0^{E_{\max}} D_{A,S}(Z,z,E)N(E)dE}{\int_0^{E_{\max}} D_W(z,E)N(E)dE}, \quad (4.9)$$

where z is the normal depth, D_W is the dose in the water-water geometry, $D_{A,S}$ is either the dose in the air-water geometry or the dose in the source-water geometry, and $N(E)dE$ is the fraction of beta particles emitted per MeV per disintegration that have energies between E and $E+dE$. TableCurve 3D surface plotting and curve fitting software was used to determine mono-energetic electron planar dose profile curve fits for use in Eq. (4.9).

Once planar dose profile curve fits were determined, they were implemented into SADCALC.f. The ICRP 107 beta spectra were then used to calculate the beta-particle backscatter factor of Eq. (4.9). Linear interpolation was used for all $7.42 < Z \leq 94$.

4.6.3 Scatter Medium Thickness

Additional scattering simulations were performed using the DOSRZnrc user code in order to determine/estimate the effect that a finite thickness (less than the range of the electron/beta) of scattering material will have. Unlike Section 4.6.1, the scattering medium was finite in thickness and varied as a ratio of scattering medium density thickness (X) to the beta X_{90} distance in the medium (estimated by equating the X_{90} distance in water to a density thickness). The minimum ratio was 0.0001 and the maximum was 1.5. The lateral dimensions of the scattering medium remained infinite however. Planar-dose profiles in each case were determined for 18 high-Z materials (Table 4.1) using nine beta-emitters covering a range of average energies (Table 4.2). The planar dose volumes were 1 mg cm^{-2} thick, with a maximum normal depth of 1000 mg cm^{-2} and an area of 1 cm^2. All transport parameters were the same as Section 4.6.1.

The scattering effectiveness of the finite scattering medium is used to estimate the 'finite' backscatter factor as a percentage of that in an infinite scattering medium geometry. It is given by

$$SE(X/X_{90},\mathrm{Z},\mathrm{z}) = \frac{D_{SW_{finite}}(X/X_{90},\mathrm{Z},\mathrm{z}) - D_{WW}(X/X_{90},\mathrm{Z},\mathrm{z})}{D_{SW_{infinite}}(X/X_{90},\mathrm{Z},\mathrm{z}) - D_{WW}(X/X_{90},\mathrm{Z},\mathrm{z})}, \qquad (4.10)$$

where D_{SW} is the depth dependent dose at a normal depth z in the presence of a source-water interface and D_{WW} is the depth dependent dose in the presence of a water-water interface. When the thickness of the scattering medium approaches that of an infinite medium, the scattering effectiveness approaches 100%. As before, a TCL script and a Batch script were used to write and execute all EGSnrc input files. A Bash Shell script and a FORTRAN code were used for data parsing and the calculation of the scattering effectiveness for each scenario.

4.6.4 Volumetric Backscatter Factor

The transition from point-source backscatter factors to volumetric backscatter factors has yet to be studied in the literature. While Durham (2006) noted that his volumetric backscatter factor reduced to Cross' (1991b, 1992c) point-source factor when the cylindrical source

thickness was less than ~0.05 X_{99} of the beta-particle, no attempt has been made in the literature to use point-source factors in the creation of volumetric backscatter factors (or to use them selectively in a numerical integration of dose). In this section, we present a method that will provide an estimate of volumetric backscatter factors using the point-source factors described in Section 4.6.2. It is important to remember that it is not possible to determine the absolute volumetric backscatter factor using the same procedures as point-sources. This is due to the largely different attenuation properties of air and water and their impact on the respective dose calculations. Therefore, a number of assumptions and estimations must be made.

The method is based on a selective integration process over the entire source volume. Rather than applying an overall correction factor to final dose calculations, scattering corrections are applied at each step of the numerical integration of dose. If desired, the 'volumetric' correction factor could then be determined by taking the ratio of overall dose with the applied point-source scattering corrections to the overall dose without. Selection criteria are used to determine the proper type and amount of scattering correction for which to account. Scattering corrections are broken down into three components: source-water interface corrections (for the top and bottom of the source), air-water interface corrections (for both the top and the sides of the source), and air-source interface corrections (for the sides of the source).

4.6.4.1 Source Scatter for Top and Bottom of Source

During the numerical integration process (described in Section 3.3.3) for an 'infinitely large' source (dimensions > range of beta-particle), only source points positioned directly at the source-water interface (i.e., source-skin interface) will require the full application of the source-water scattering data (Fig. 4.7). Source points positioned above this interface (Fig. 4.8) require a more advance treatment. In this case, there is expected to be an increase in the energy absorption (i.e., dose) from downward scattering taking place in the upper portion of the source, as well as a decrease in dose from upward scattering in the lower portion of the source. If the contribution from downward scattering is greater than the contribution from upward scattering, the dose will be increased for that source-point kernel. Likewise, when the upward contribution is greater, the dose will be decreased. It can be seen from this argument

that when the source point is at the top of the source, the application of both air-water (discussed in Section 4.6.4.3) and source-water correction results in an effective air-source correction.

Scattering contributions from both upward and downward scattering are determined using Eq. (4.10). The scattering material thicknesses for the top and bottom of the source are given by the normal distances from the source-point to the upper- and lower-most points of the source, respectively. The source backscatter correction factor (BSCF) is then determined by multiplying net scattering effectiveness by the beta-particle source-water scattering correction for point-sources;

$$Source\ BSCF_{top/bottom} = SW(SE_{top} - SE_{bottom}), \tag{4.11}$$

where SW is the beta-particle source-water scattering correction for point-sources, SE_{top} is the scattering effectiveness for the top portion of the source, and SE_{bottom} is the scattering effectiveness for the bottom portion of the source. The 'skin depth' at which the scattering factor is determined takes into account the normal density thickness of both the source and tissue through which the beta-particle must traverse.

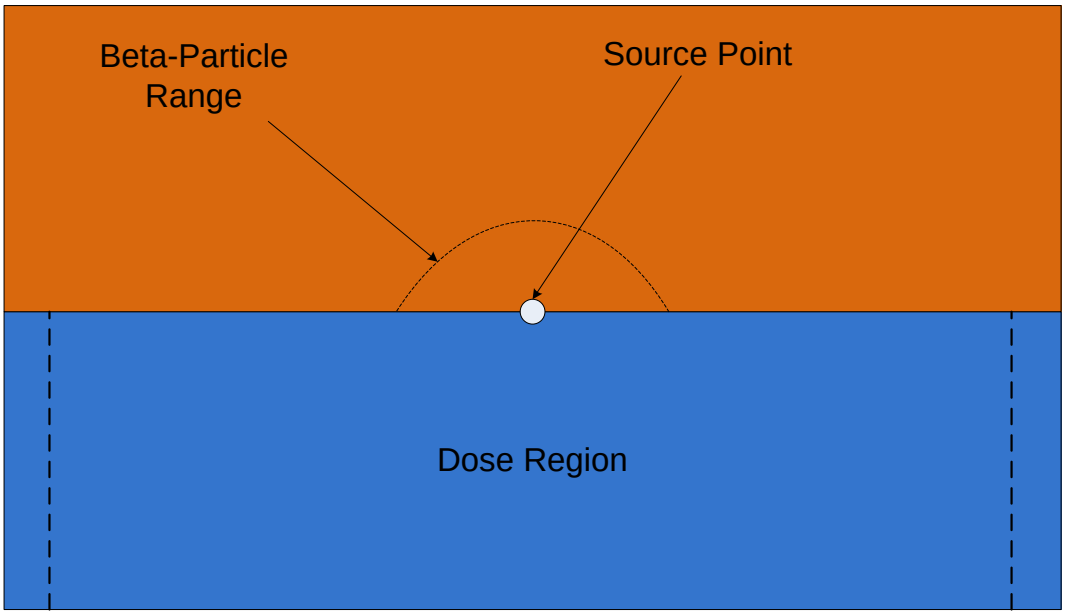

Fig. 4.7. Schematic demonstrating conditions in which full source-water scattering corrections are applied. The dimensions of the source (orange) are greater than the range of the beta-particle.

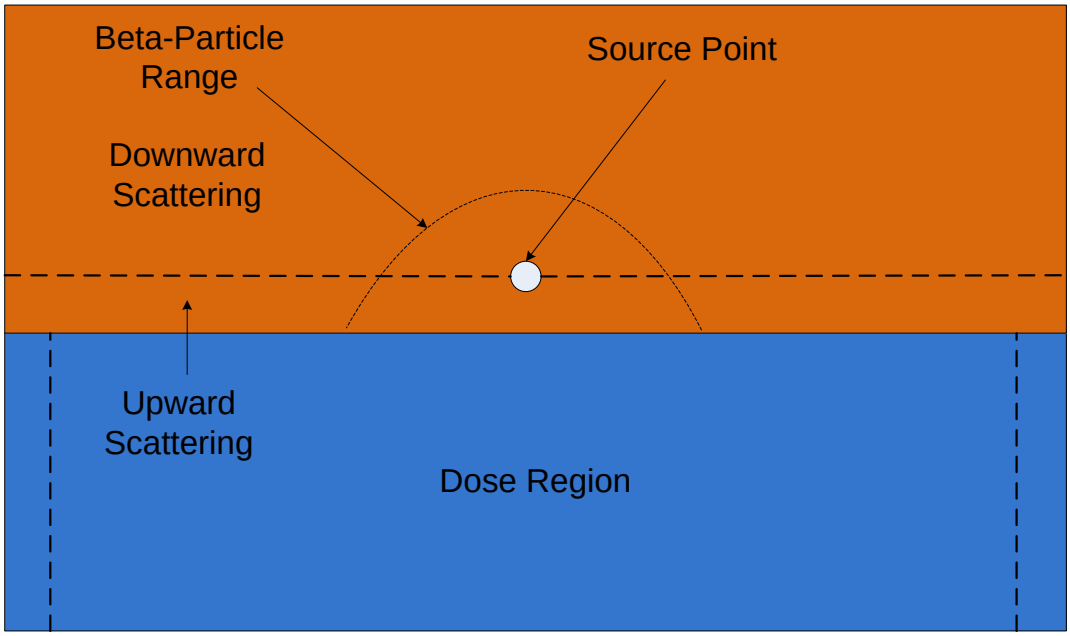

Fig. 4.8. Schematic demonstrating conditions in which partial source-water scattering corrections are applied. The lower portion of the source causes upward scattering away from the dose region and the upper portion of the source causes downward scattering towards the dose region.

4.6.4.2 Source Scatter for Sides of Source

The point-source factors described in Section 4.6 assume that the source medium is infinite in both height and lateral extent. And as such, application to source points near or on the side of the source jeopardizes the accuracy of the results. However, approximations can be made in order to estimate source-scatter corrections for the sides of the source.

When the dimensions of the source are larger than the range of the beta, source points toward the center and the top-center of the source have minimal impact on dose. Therefore, source-points on both sides and the bottom of the source become more important. Using the results (Fig. 5.63) of the scattering effectiveness study described in Section 4.6.3, it is estimated that scattering contributions from the sides of the source will reach a maximum when the scattering media thickness is 1.0 X/X_{90} and greater. Linear interpolation is used for X/X_{90} values less than 1.0.

Unlike source scattering for the top and bottom of the source, during the numerical integration process, the direction of the beta-particle needs to be considered when correcting for side scatter. Side scattering should only be accounted for when the beta-particle's path is directed away from the source and travels through air prior to reaching the dose region. The assumption is that a beta-particle emitted in the 180 degree opposite direction would be permitted to backscatter off of the source's side and still contribute to dose.

The amount of source material directly above the source point (considered the 'lateral' dimension in this case) will also have an impact on the scattering effectiveness. If the source point is located on the very top corner of the source, the probability of a backscattering event toward the dose region is greatly decreased. On the other hand, if the source point is at the very bottom corner of the source, the probability of backscattering event toward the dose region is much greater. It is estimated that the normal distance to the upper most point of the source must be greater than 0.5 X/X_{90} (or ½ of the 'height' requirement) in order to have 100% scattering effectiveness from the top portion of the source. Therefore, the net scattering correction is given by

$$Source\ BSCF_{side} = SA\frac{X_{top}}{0.5}(X_{op\_side} - X_{side}), \tag{4.12}$$

where *SA* is the beta-particle source-air scattering correction for point-sources (ratio of source-water to air-water correction factor), X_{side} is the normal distance to the side of the source that the beta travels through, X_{op_side} is the normal distance to the opposite side of the source, and X_{top} is the normal distance to the top of the source. All distances are in terms of X/X_{90}. If X_{top} is greater than 0.5, full scattering correction is applied by setting X_{top} equal to 0.5. Similarly, if X_{side} or X_{op_side} are greater than 1.0, they are set equal to 1.0.

As the energy of the beta-particle decreases and the scattered path angle relative to the air-water interface increases, the probability of the scattered beta depositing energy in the dose area greatly decreases (Fig. 4.10). Conversely, high-energy betas are expected to have a contribution extending to the very edge of the dose area when scattered beta-particles enter the dose region at high incident angles. It is assumed that the scattering correction from the top and bottom of the source does not accurately account for such contributions due to its inherent geometry. Without knowing the angle at which a particular beta backscatters and likely enters the dose region at each stage of the integration process, it is very difficult to correctly apply this additional correction factor. Therefore, the angle of incident (Fig. 4.9) is used to estimate the frequency at which large angle scattering events occur. The side-scattering correction is only applied when the incident angle is greater than 70 degrees (further explained in Section 5.6.4) and when the density corrected path length (includes source and air) to the edge of the dose region, or the maximum scattered beta path length, is less than the beta-particle X_{90} distance. The latter limitation prevents the side-scatter correction from being applied to low-energy beta-particles, where this form of scatter is believed unlikely (as explained above).

As with scattering from the top/bottom of the source, the ‘skin depth’ at which the scattering factor is determined takes into account the normal density thickness of both the source and tissue through which the beta-particle must traverse.

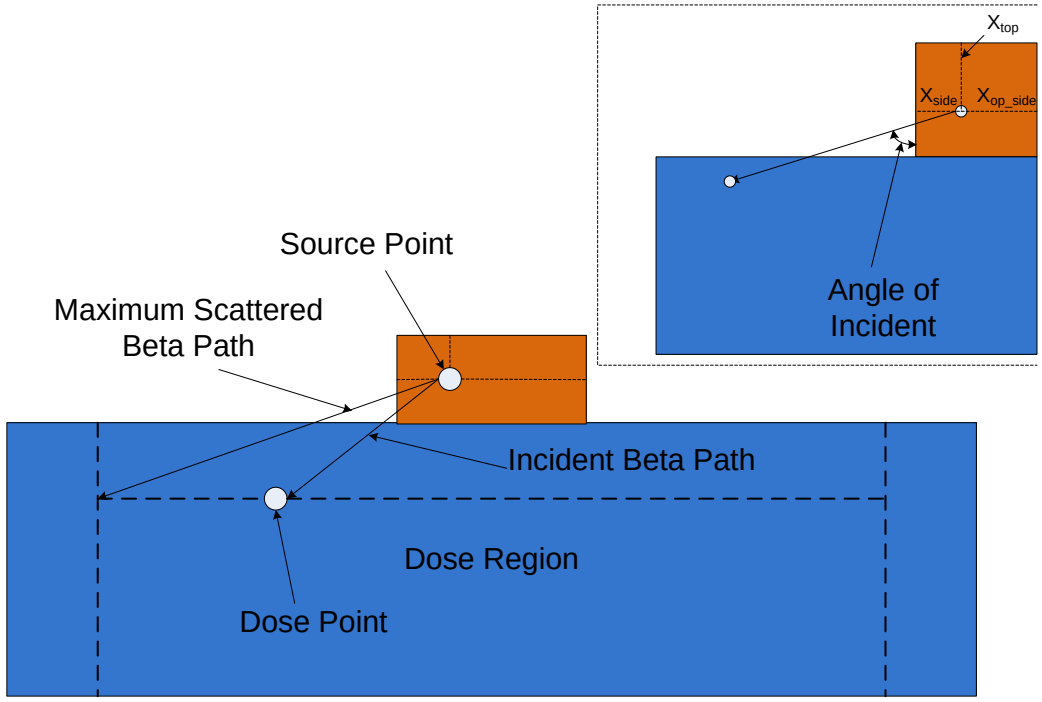

Fig. 4.9. Schematic illustrating parameters used to determine the amount of side-scatter correction applied to high-energy beta-particles emitted from large sources.

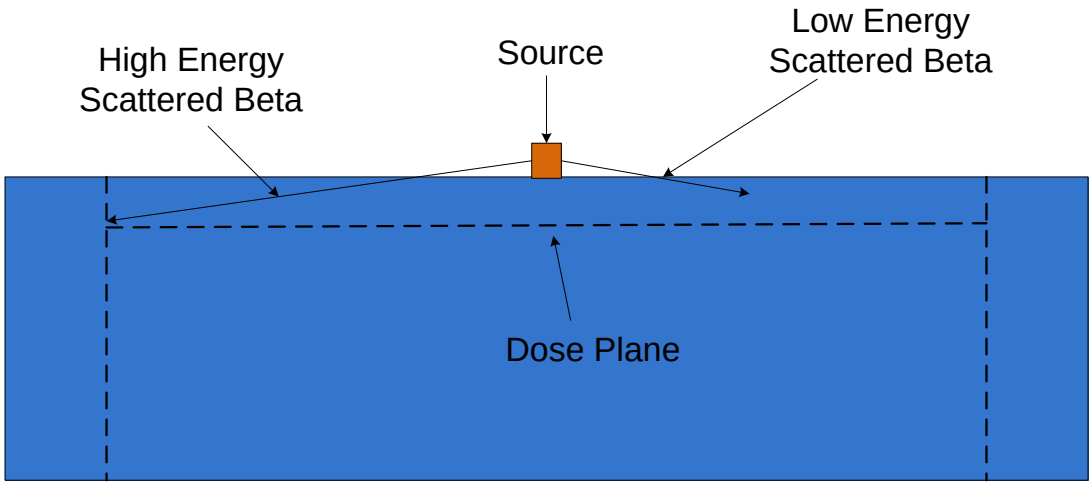

Fig. 4.10. Schematic illustrating beta energy limitations of side-scatter corrections. Both scattering paths assume the same incident angle.

4.6.4.3 Air Scatter for Top and Sides of Source

The application of air-water interface scattering correction factors is more difficult than with a source-water interface. In order to estimate the scattering effectiveness when source material is present between the air-water interface, simple linear interpolation is used. The two extreme cases are when there is no source material between the air and water boundaries (Fig. 4.11) and when the path length out of the top or sides of the source is equal to or greater than the range of the beta. The scattering effectiveness would be 100% and 0%, respectively. The assumption is that if a backscattered beta-particle can escape the source, there is a chance that a dose-contributing scatter event may still occur if water were surrounding the source. This is seen as a conservative estimate as a beta-particle that travels 1.8 X/X_{90} (range estimate, Durham 2006) out of the top of a source will theoretically not be able to backscatter and contribute to dose at any depth.

The overall air BSCF is found using a weighted average. The BSCF's are calculated for all surfaces for which the beta-particle can escape and reach air. Scattering contributions from the top of the source receive a 50% weight and the remaining 50% is evenly divided among the sides of the source. For cylinders and spheres, the shortest distance to the outer surface and the 180 degree opposite distance represent the two side distances (Fig. 4.12). For slabs, four sides are used: the normal distances to the *x*-coordinate sides and the normal distances to the *y*-coordinate sides. The scattering reductions (for cylinders and spheres) are therefore given by

$$Air\ BSCF_{top} = AW\ 0.5\frac{1.8 - X_{top}}{1.8}, \tag{4.13}$$

$$Air\ BSCF_{side} = AW\ 0.25\frac{1.8 - X_{side}}{1.8}, \tag{4.14}$$

and

$$Air\ BSCF_{op\_side} = AW\ 0.25\frac{1.8 - X_{op\_side}}{1.8}, \tag{4.15}$$

where AW is beta-particle air-water scattering correction for point-sources, X_{top}, X_{side}, and X_{op_side} are the distances to the top and sides of the source in terms of X/X_{90}.

Unlike the source scattering corrections, no depth adjustments need to be made for materials traversed by the beta-particle prior to entering the dose region. This is due to the fact that corrections are being made for scattering events occurring outside the source. The distance to the air-water interface is considered negligible in terms of beta attenuation (assumed to be completely air). The overall air scattering correction is found by summing the three components above.

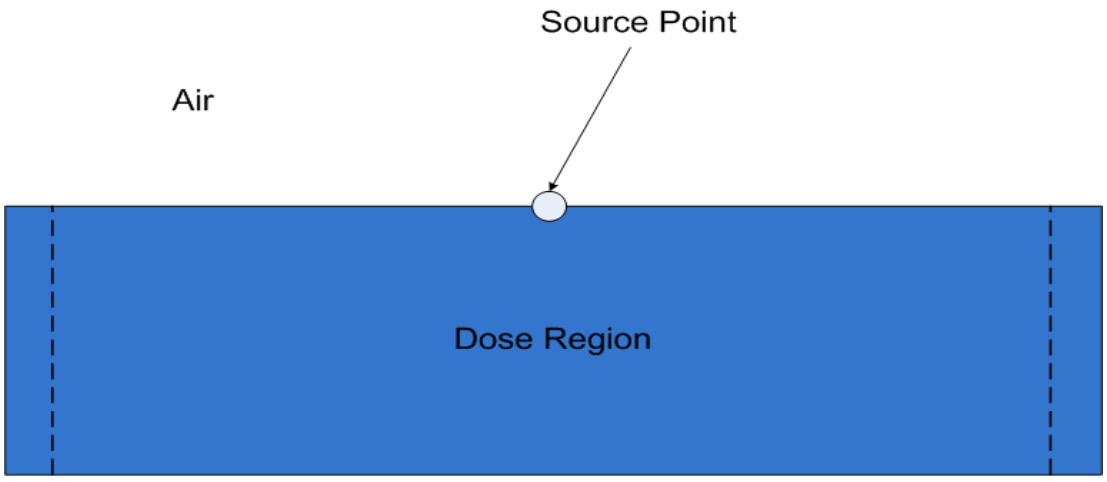

Fig. 4.11. Schematic demonstrating conditions in which a full air-water scattering corrections are applied.

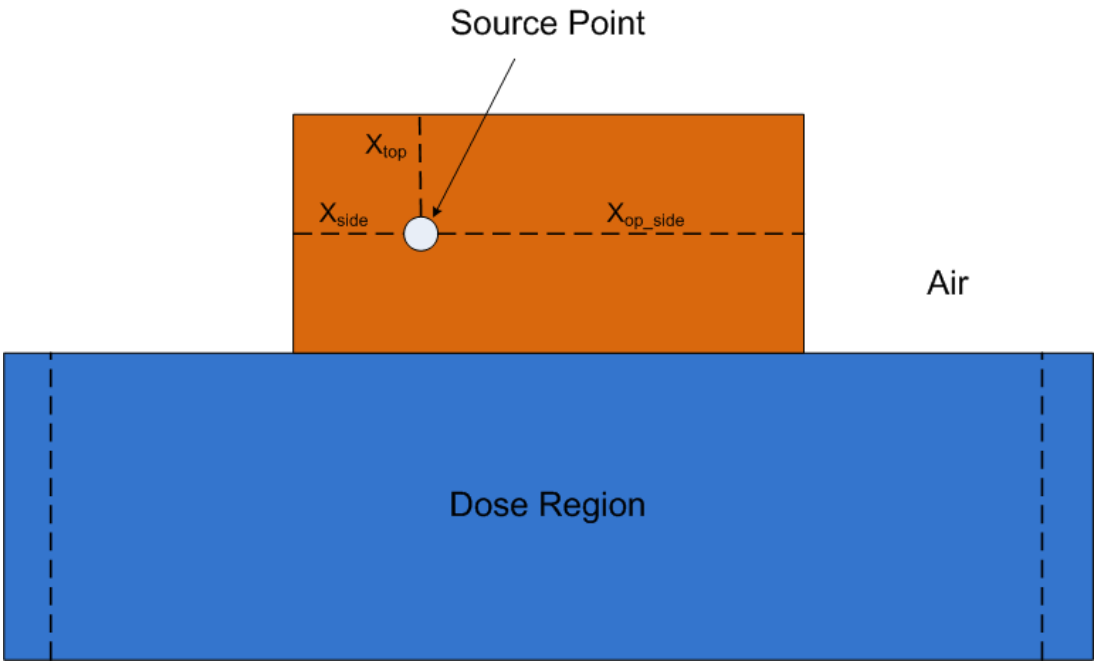

Fig. 4.12. Schematic demonstrating conditions in which air-water scattering corrections are applied. When the distance to the top and sides of the source are less than 1.8*X_{90}, a partial air-scattering correction is applied.

4.7 Model Verification with Hot Particle Dosimetry

The intended purpose of both the scaling and scattering models is to improve the accuracy of hot particle skin-dose calculations using deterministic computer codes such as VARSKIN 4 (Traub 1987; Durham 1992, 2006; Hamby 2011). As mentioned in Section 2.6, VARSKIN 4 utilizes simple density scaling (η_w = 1.0), Cross' (1991b, 1992c) point-source correction factor for air scatter, Durham's (2006) volume-source correction for air scatter, and completely ignores source scattering. These models were replaced with the scaling and scattering models presented herein order to complete an extensive hot particle skin dosimetry verification.

Dose-point kernel-based skin doses calculated using VARSKIN 4 (w/ new models) were compared to EGSnrc Monte Carlo simulations. EGSnrc was used as the Monte Carlo code of choice for reasons explained in Section 2.7. The 'cavity' user code was used to create

volumetric sources. The C++ user code 'cavity' is an advanced EGSnrc application that was originally designed to calculate the dose to the cavity of an ionization chamber. However, 'cavity' is not restricted to cylindrically symmetric geometries. Practically any chamber can be modeled with this user code by using the extensive capabilities of the general purpose geometry package (Kawarakow 2000; Kawarakow and Rogers 2000).

Using the 'cavity' user code, spherical, cylindrical, disc, and slab sources were constructed from stainless steel, uranium oxide, and tungsten alloy (Table 4.4). There were 5 different source dimensions (Table 4.5) used with the smallest being 0.0005 cm and the largest being 0.05 cm. Each source was then modeled with 9 different beta emitters (Table 4.6), ranging from ^{60}Co (E_{av} = 96 keV) to ^{144}Pr (E_{av} = 1.22 MeV). Skin doses were calculated at 10 depths ranging from 4 mg cm^{-2} to 100 mg cm^{-2}. Skin depths were chosen to cover all biologically significant depths discussed in Section 2.1. Dose averaging areas of both 1 and 10 cm^2 were used. In total, 1,080 simulations were run to test the validity of both the scaling model and scattering model when incorporated into a dose-point kernel code. The source materials, geometries, and sizes cover a wide range of possible hot particle source geometries. Additionally, the nuclides chosen span both the high and low end of possible beta-particle energies seen in hot particles.

Table 4.4. Source materials used for results verification.

Alloy	**Z_{eff}**	**Density (g cm^{-3})**	**Atomic Weight (g mol^{-1})**
Stainless Steel (SS_302)	25.81	8.06	55.54
Tungsten Alloy (Mallory2000)	72.79	18.00	177.65
Uranium Oxide	87.88	10.96	211.72

Table 4.5. Source dimensions used for results verification. All units are in centimeters.

Sphere (R)	**Cylinder (RxH)**	**Slab (LxWxH)**	**Disc (RxH)**	**Source Name**
0.0005	0.0005 x 0.001	0.001 x 0.001 x 0.0005	0.0005 x 0.00025	1
0.001	0.001 x 0.002	0.002 x 0.002 x0.001	0.001 x 0.0005	2
0.005	0.005 x 0.01	0.01 x 0.01 x 0.005	0.005 x 0.0025	3
0.01	0.01 x 0.02	0.02 x 0.02 x 0.01	0.01 x 0.005	4
0.05	0.05 x 0.1	0.1 x 0.1 x 0.05	0.05 x 0.025	5

Table 4.6. List of nuclides used for results verification. The number of particles histories for EGSnrc 'cavity' simulations are listed.

Nuclide	E_{ave} (MeV)	X_{90} (cm)	# Histories
^{60}Co	0.0958	0.033	5.0E06
^{90}Sr	0.196	0.083	5.0E06
^{210}Bi	0.307	0.212	1.0E06
^{135}I	0.375	0.239	1.0E06
^{89}Sr	0.583	0.321	1.0E06
^{32}P	0.695	0.363	1.0E06
^{56}Mn	0.832	0.634	2.0E05
^{90}Y	0.934	0.533	2.0E05
^{144}Pr	1.217	0.696	2.0E05

All transport parameters were held at their default settings (ECUT, PCUT, AE, and AP were the same as those listed in Section 4.2). The number of particle histories (Table 4.6) was held constant for each nuclide, independent of the source geometry and material. Only dose calculations with a relative error less than 5.0% were kept for analysis. As before, a TCL script and a Batch script were used to write and execute all EGSnrc input files. A Bash Shell script was used for data parsing. Similar procedures were performed for executing VARSKIN 4. Since VARSKIN only calculates dose at a single depth, 10,800 computations were required. A TCL script was used to create the necessary input files for VARSKIN and a Bash Shell script was used to execute the code and parse the output.

It should be noted that moment-based DPK's of VARSKIN 4 were updated with the EGSnrc DPK's calculated in Section 4.2 for the purposes of this research. Doing so allowed for a more accurate comparison with hot particle skin doses calculated from Monte Carlo methods.

5 Results and Discussion

5.1 Homogeneous Dose-Point Kernels

When the simulations outlined in Section 4.2 were carried out, the results were used primarily for developing the scaling model. Given the extensive work already performed in the literature and the replicative work performed here, homogeneous DPK's require little if any discussion. Results are presented here however for completeness.

As demonstrated by Berger (1971), scaling of the spherical radii with respect to X_{90} is convenient for presentation and tabulation purposes, as it allows homogeneous DPK's of monoenergtic electrons of varying energy to be plotted (or tabulated) over the same domain (Fig. 5.1). This observation can also be seen for homogeneous DPK's of the same electron energy, in different media (Fig. 5.2). Plotting energy deposition kernels with respect to shell radius, x, demonstrates the E and Z dependence of the Bethe equation (Eq. (3.11)) discussed in Section 3.2.2 (Fig. 5.3, Fig. 5.4). If the shell thickness (or the number of shells over the range of the electron) is not equal for all DPK's on a single graph, it is useful to divide the DPK value by the shell thickness such that the integration of energy deposited is equal. The medium Z is given in the legend of each plot in parenthesis.

Homogeneous DPK data were also used in the calculation of X_{90} values for all homogeneous material/energy combinations (partial listing, Table 5.1). These values were then used to determine the radii of the non-homogeneous DPK absorption spheres.

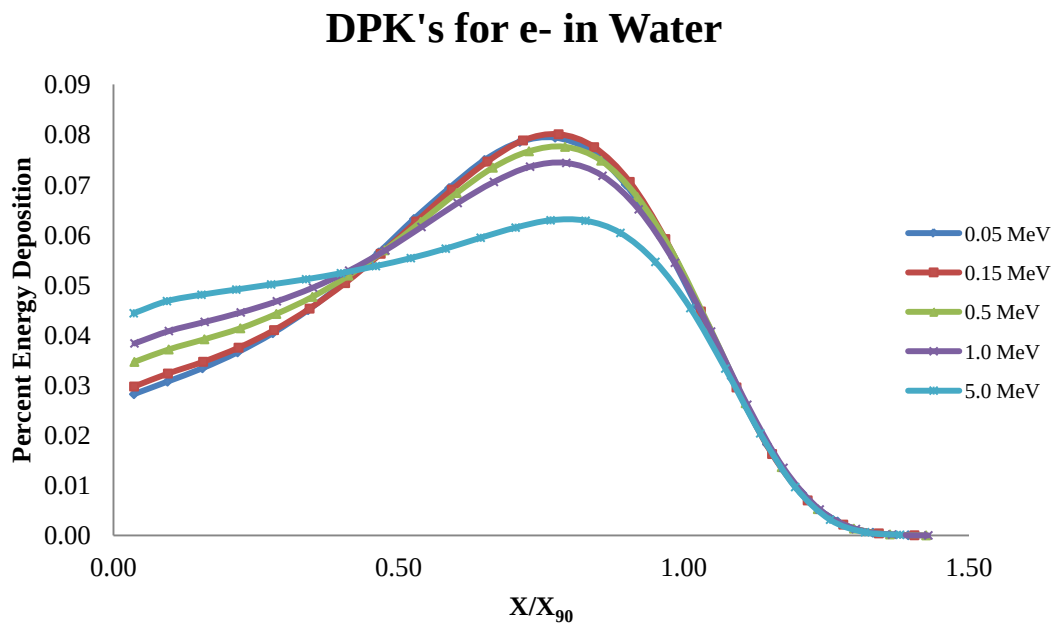

Fig. 5.1. Dose-point kernels for monenergetic electrons in water.

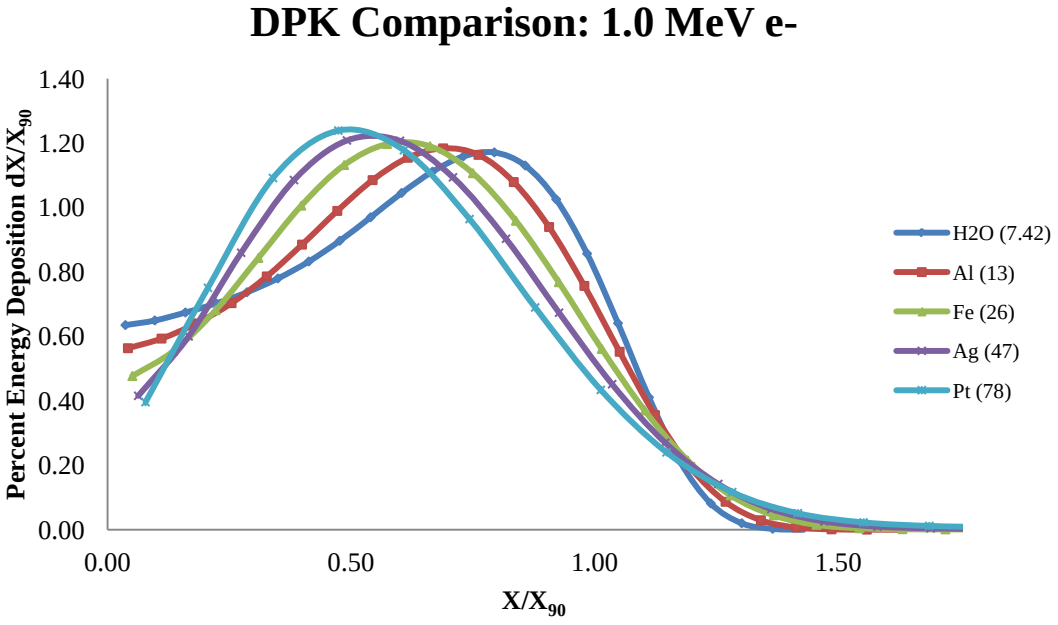

Fig. 5.2. DPK comparison for 1.0 MeV electrons in various media.

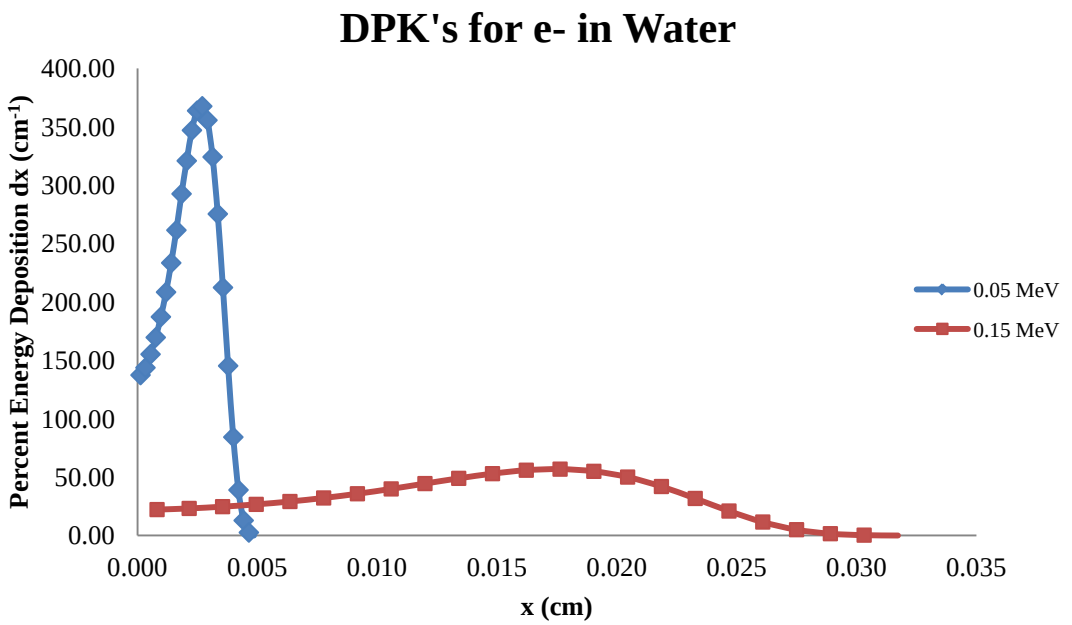

Fig. 5.3. DPK curves demonstrating energy dependence of *dE/dx*.

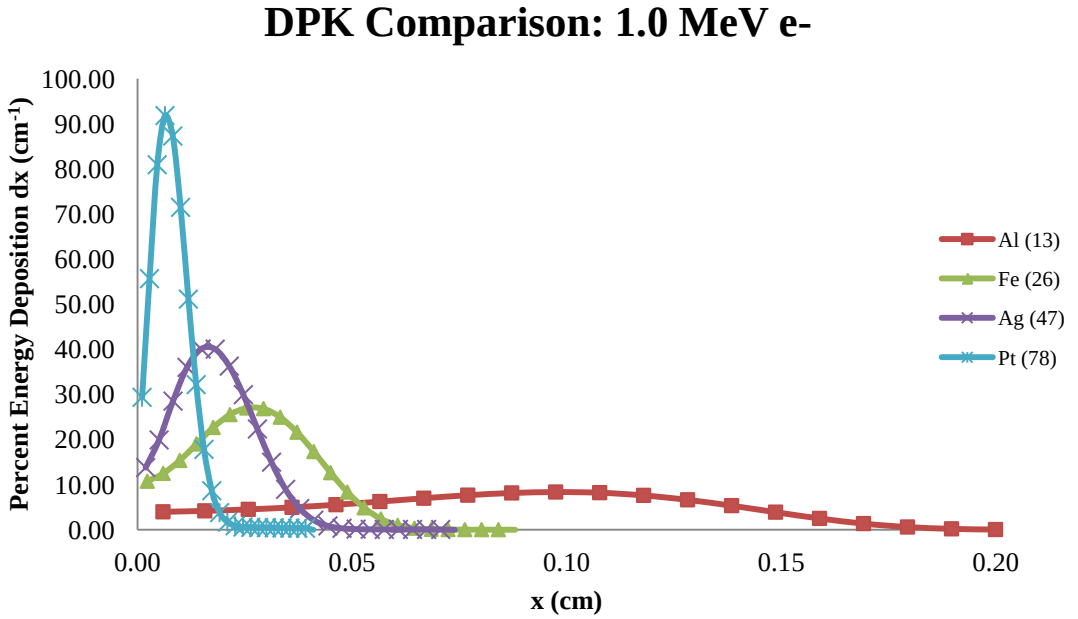

Fig. 5.4. DPK curves demonstrating *Z* dependence of *dE/dx*.

Table 5.1. Calculated X_{90} values for mono-energetic electrons in various media.

	X_{90} (cm)				
Energy (MeV)	**H2O**	**Al (13)**	**Fe (26)**	**Ag (47)**	**Pt (78)**
1.00E-02	2.01E-04	8.90E-05	3.07E-05	2.49E-05	1.42E-05
2.00E-02	6.91E-04	2.97E-04	9.85E-05	7.58E-05	4.08E-05
3.00E-02	1.42E-03	6.04E-04	1.97E-04	1.47E-04	7.70E-05
4.00E-02	2.36E-03	9.96E-04	3.21E-04	2.36E-04	1.21E-04
5.00E-02	3.49E-03	1.47E-03	4.70E-04	3.42E-04	1.73E-04
6.00E-02	4.79E-03	2.01E-03	6.40E-04	4.62E-04	2.30E-04
7.00E-02	6.26E-03	2.62E-03	8.32E-04	5.95E-04	2.94E-04
8.00E-02	7.88E-03	3.28E-03	1.04E-03	7.42E-04	3.63E-04
1.00E-01	1.15E-02	4.79E-03	1.51E-03	1.07E-03	5.16E-04
1.50E-01	2.26E-02	9.34E-03	2.93E-03	2.05E-03	9.65E-04
2.00E-01	3.59E-02	1.48E-02	4.63E-03	3.21E-03	1.49E-03
2.50E-01	5.08E-02	2.09E-02	6.54E-03	4.51E-03	2.07E-03
3.00E-01	6.70E-02	2.76E-02	8.61E-03	5.92E-03	2.70E-03
3.50E-01	8.43E-02	3.46E-02	1.08E-02	7.40E-03	3.36E-03
4.00E-01	1.02E-01	4.20E-02	1.31E-02	8.95E-03	4.06E-03
4.50E-01	1.21E-01	4.96E-02	1.55E-02	1.06E-02	4.78E-03
5.00E-01	1.40E-01	5.74E-02	1.79E-02	1.22E-02	5.50E-03
5.50E-01	1.59E-01	6.54E-02	2.04E-02	1.39E-02	6.25E-03
6.00E-01	1.79E-01	7.36E-02	2.29E-02	1.56E-02	7.02E-03
7.00E-01	2.19E-01	9.01E-02	2.81E-02	1.91E-02	8.57E-03
8.00E-01	2.60E-01	1.07E-01	3.35E-02	2.27E-02	1.02E-02
9.00E-01	3.02E-01	1.24E-01	3.89E-02	2.64E-02	1.18E-02
1.00E+00	3.44E-01	1.41E-01	4.43E-02	3.01E-02	1.35E-02
2.00E+00	7.76E-01	3.18E-01	1.01E-01	6.88E-02	3.08E-02
3.00E+00	1.21E+00	4.96E-01	1.59E-01	1.09E-01	4.90E-02
4.00E+00	1.65E+00	6.74E-01	2.18E-01	1.49E-01	6.76E-02
5.00E+00	2.08E+00	8.50E-01	2.76E-01	1.91E-01	8.63E-02
6.00E+00	2.51E+00	1.03E+00	3.34E-01	2.31E-01	1.06E-01
7.00E+00	2.94E+00	1.20E+00	3.93E-01	2.72E-01	1.26E-01
8.00E+00	3.36E+00	1.38E+00	4.50E-01	3.13E-01	1.45E-01

5.2 Non-Homogeneous Dose-Point Kernels

Below is a sample of non-homogeneous DPK's as determined from the procedures in Section 4.3 (Fig. 5.5 - Fig. 5.8). The radii of each absorption sphere is given in the plot legend as a ratio to the absorption material X_{90} As expected, the DPK curves shift to the left (decreased electron range) as the radius of the absorption sphere increases. The presence of an energy deposition peak disappears when the radius gets sufficiently large. At this point, the electron has minimal energy to transfer to the water medium and will have already slowed down to a point of producing a *Bragg*-like peak.

The dependence on Z is observed by plotting the non-homogeneous DPK's of a single electron energy and absorption-sphere radius (Fig. 5.9). The variation within the curves is interesting given the fact that an equal amount of energy (~.66 MeV) was deposited in the 0.5 X/X_{90} radius absorption spheres. Therefore, the DPK data in the proceeding spherical water shells is for the same electron energy in each case (as indicated by the approximately equal area under each curve). It is clear from the curves that electrons traversing a lower-Z medium will enter the water shells with a higher dE/dx. This will cause the electron to lose energy more quickly in the water shells and have a subsequently shorter range.

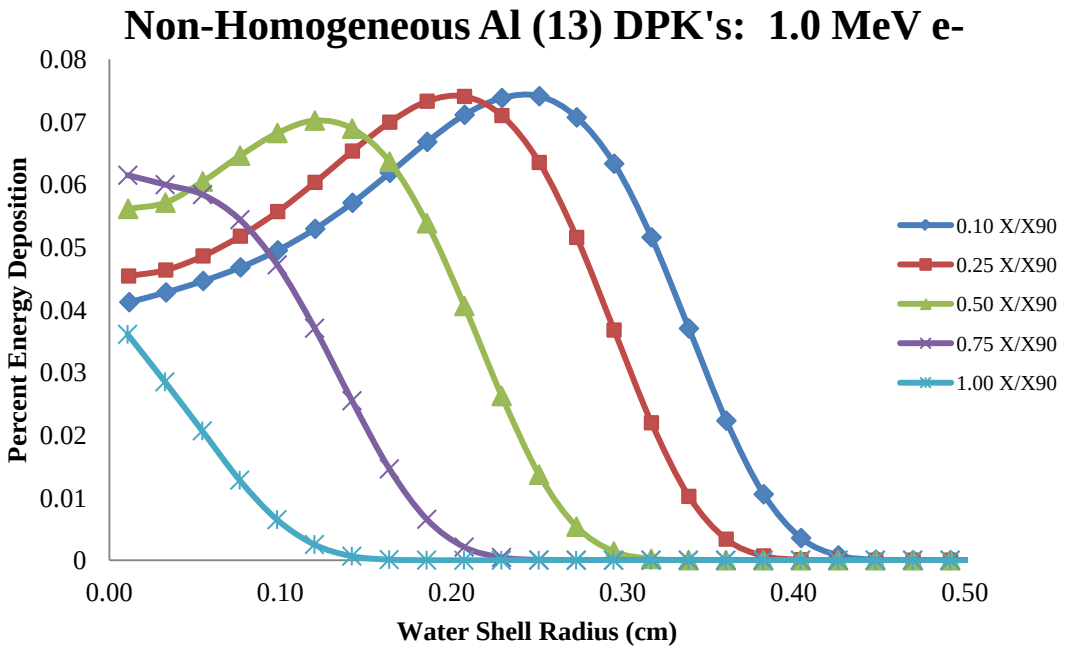

Fig. 5.5. Non-homogeneous DPK's surrounding an aluminum absorption sphere. The radius of the absorption sphere is given as a fraction of the X_{90} value.

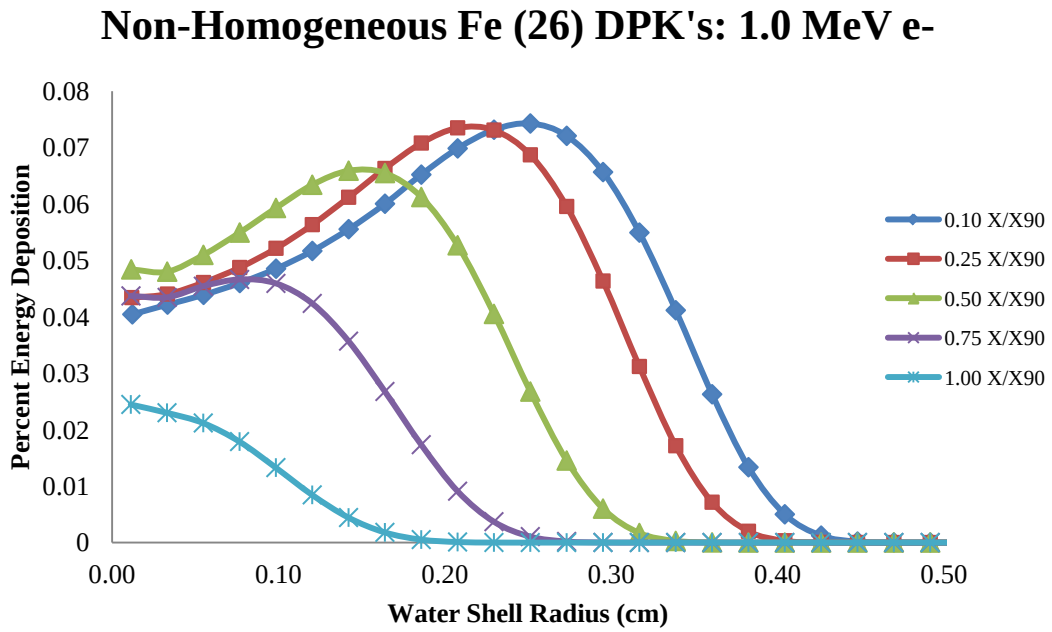

Fig. 5.6. Non-homogeneous DPK's surrounding an iron absorption sphere. The radius of the absorption sphere is given as a fraction of the X_{90} value.

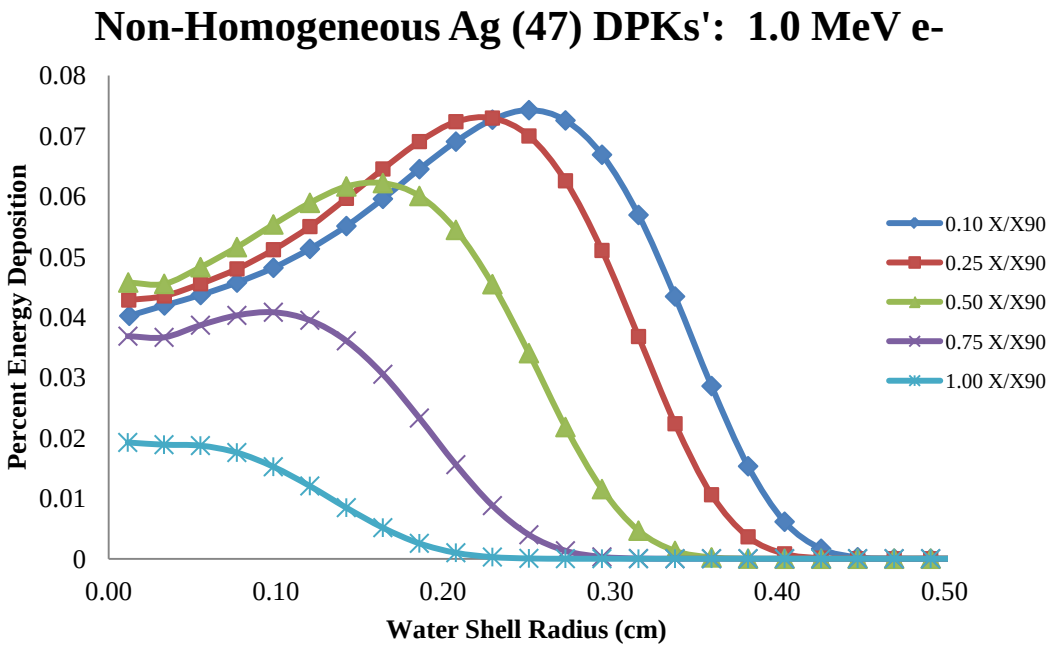

Fig. 5.7. Non-homogeneous DPK's surrounding a silver absorption sphere. The radius of the absorption sphere is given as a fraction of the X_{90} value.

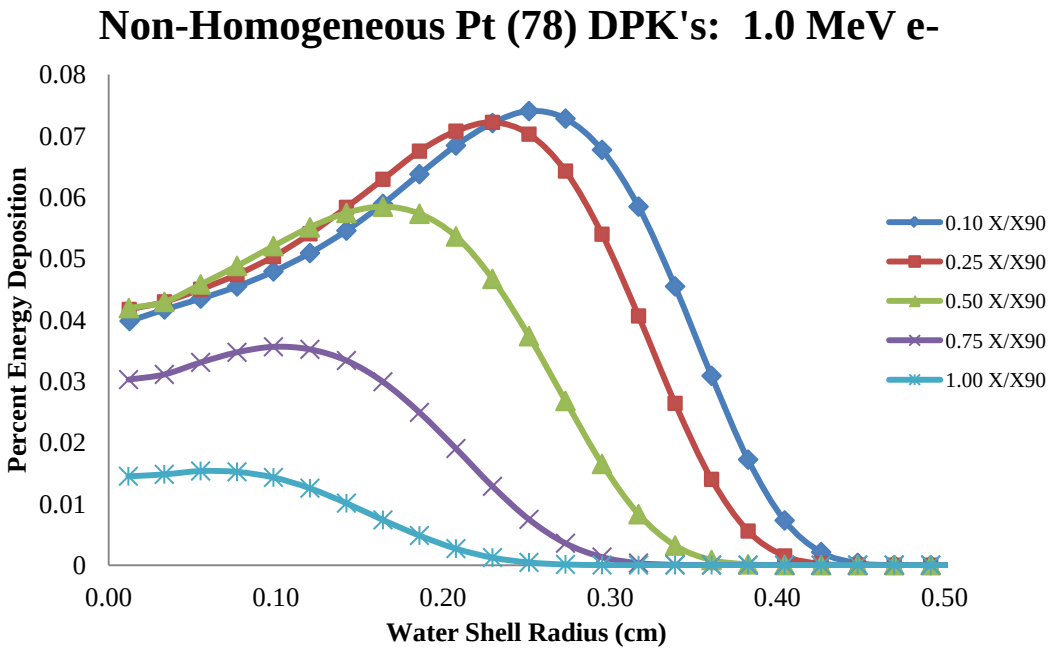

Fig. 5.8. Non-homogeneous DPK's surrounding a platinum absorption sphere. The radius of the absorption sphere is given as a fraction of the X_{90} value.

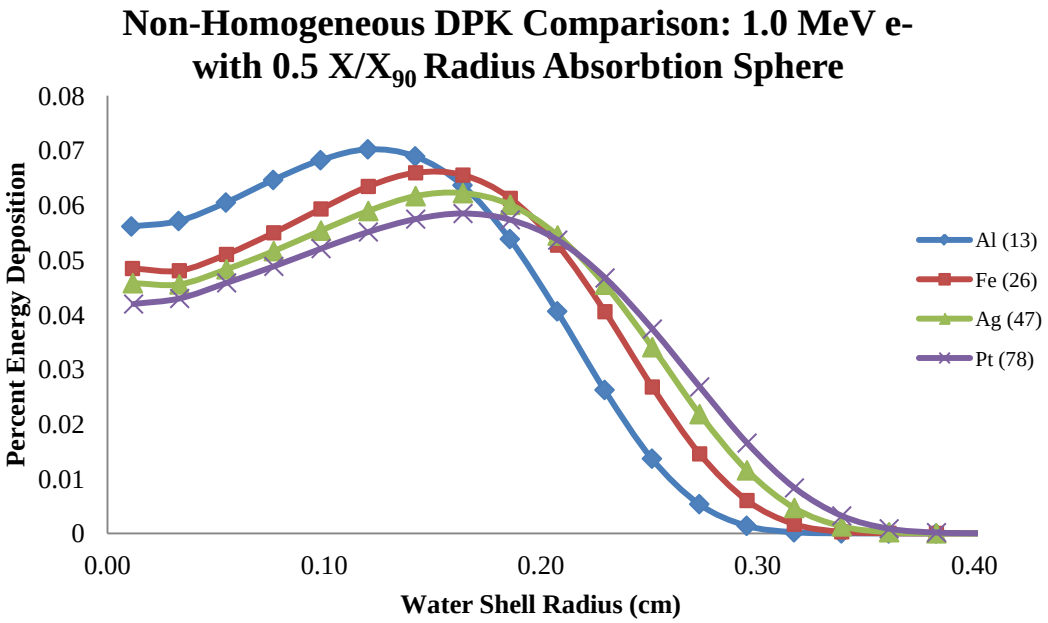

Fig. 5.9. Comparison of non-homogeneous DPK's for 1.0 MeV electrons with a 0.5 X/X_{90} absorption-sphere radius.

5.3 Scaling Model

5.3.1 Curve Fit Data

The mono-energetic electron depth and energy-scaling parameters were determined using the FORTRAN code described in Section 4.4. Sample results of the FORTRAN code output are presented in graphical form (Fig. 5.10 - Fig. 5.13) for select materials and electron energies. The curves labeled as 'actual' represent the non-homogeneous DPK's determined in Section 5.2. The curves labeled as 'scaled' represent the homogeneous water DPK following application of the FORTRAN-determined *ESP*'s and *DSP*'s. The results demonstrate the ability to accurately scale homogeneous water DPK's to non-homogeneous DPK's for a range of electron energies, material *Z*, and absorption-sphere radii using the *ESP*'s and *DSP*'s generated in this work. Greatest discrepancies are found for large radii, however the contribution to dose in these circumstances is less significant than for smaller radii, where accuracy is higher.

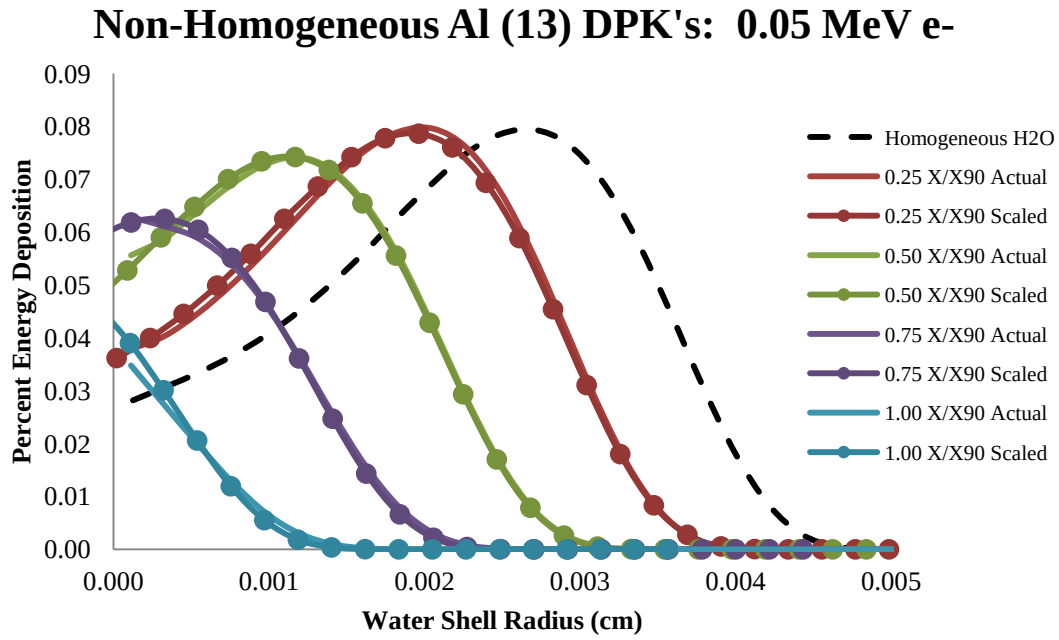

Fig. 5.10. Mono-energetic electron scaling data (aluminum) used in determining scaling model curve fits.

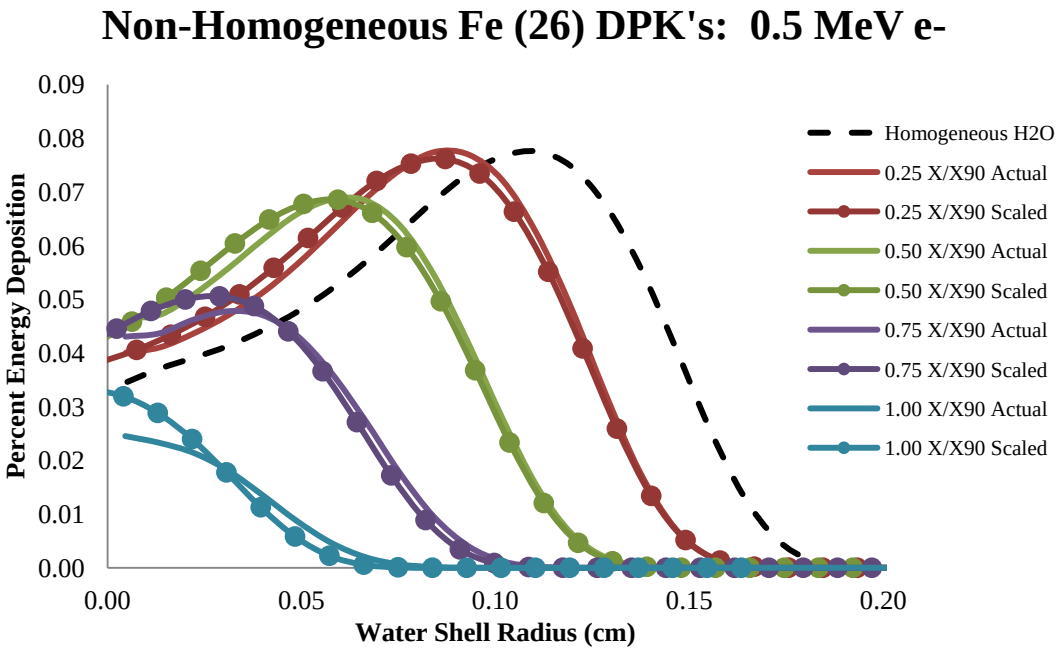

Fig. 5.11. Mono-energetic electron scaling data (iron) used in determining scaling model curve fits.

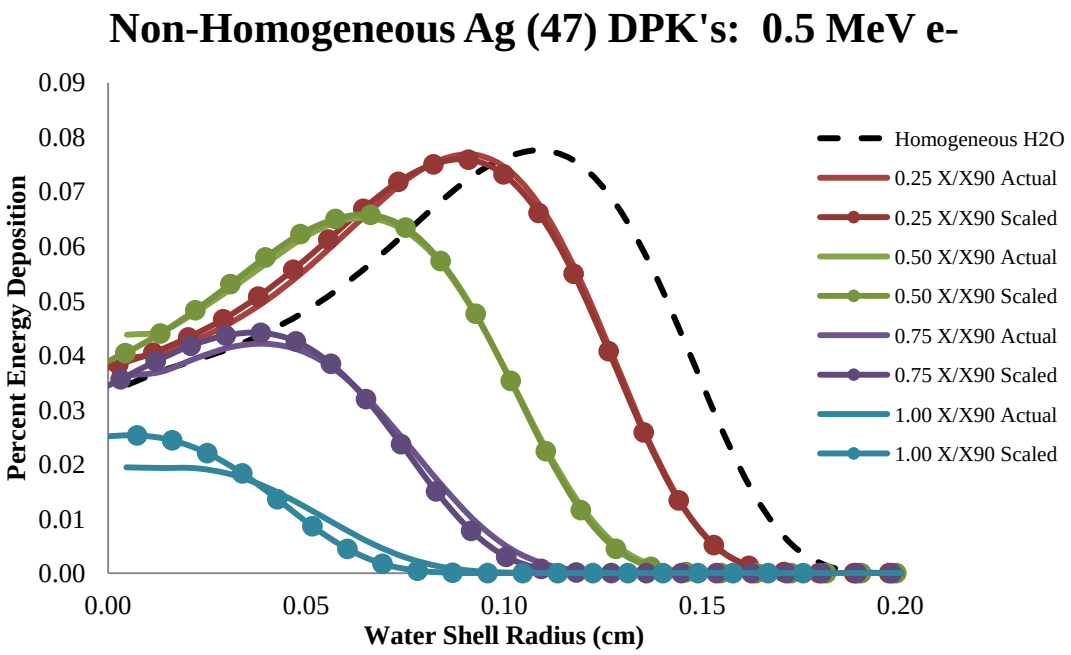

Fig. 5.12. Mono-energetic electron scaling data (silver) used in determining scaling model curve fits.

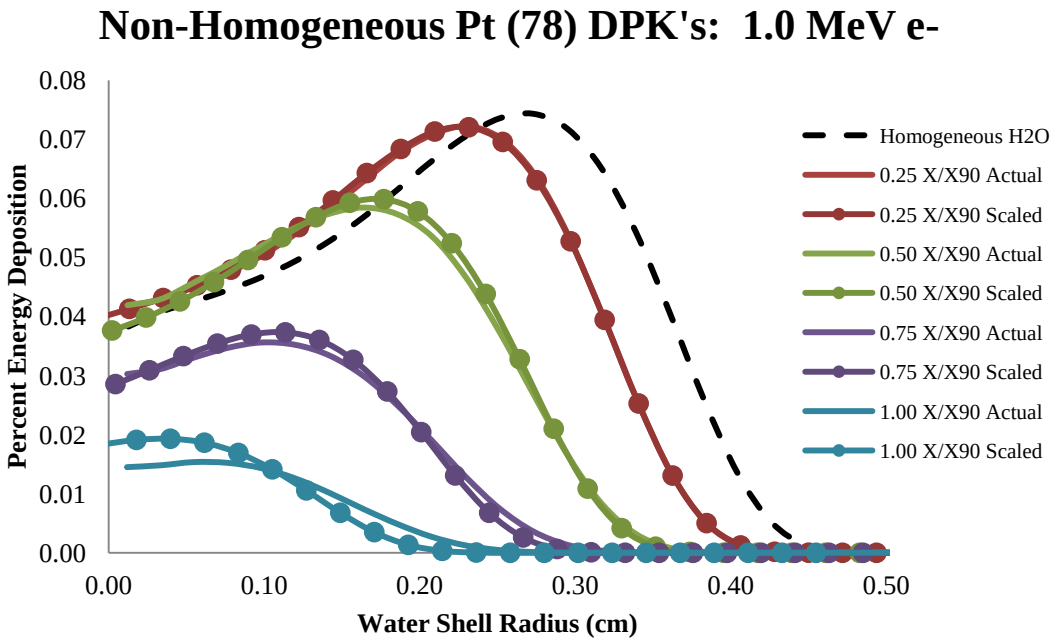

Fig. 5.13. Mono-energetic electron scaling data (platinum) used in determining scaling model curve fits.

5.3.2 Depth-Scaling Parameters

The FORTRAN results for all energy/medium/radius combinations (Table 4.1, Table 5.1) were imported into the TableCurve 3D software package for surface fitting. Separate fits were found for each material *Z*. Due to the large range of energy values, the natural logarithm of energy was used. Similarly, the absorption-sphere radii were expressed as the natural logarithm of density thickness. The natural logarithm of the depth-scaling parameter was chosen as the plotted dependent variable.

When plotted together, the variability with respect to *Z* is difficult to discern as they all follow the same curvature with little separation (Fig. 5.14, Fig. 5.15). However, examination of a single energy allows for a better comparison (Fig. 5.16). The variation in *DSP*'s at small radii is greatest with essentially no variability at large radii. Each curve is linear with a slope near unity. This is expected since density thickness is often used to estimate "water equivalent" path length for electrons in non-aqueous media (Cho 2004). The small *Z* dependence, coupled with 18 curve fits, allows for accurate interpolation for any $7.42 < Z \leq 94$

All curve fits for the *DSP*'s took the form of

$$LN(DSP\ (cm)) = \frac{(a + bx + cx^2 + dx^3 + ey)}{(1 + fx + gx^2 + hx^3 + iy)}, \tag{5.1}$$

where *x* is $LN(E\ (MeV))$ and y is $LN(X_x * \rho_x\ (g\ cm^{-2}))$. The terms X_x and ρ_x refer to the radius and density of the absorption sphere. The form of Eq. (5.1) was chosen because it was the equation that had the largest R^2 value ($\geq$0.9999) and was able to fit all 18 plots. The fit parameters (Table F 1) for each function demonstrated a slight *Z* dependence.

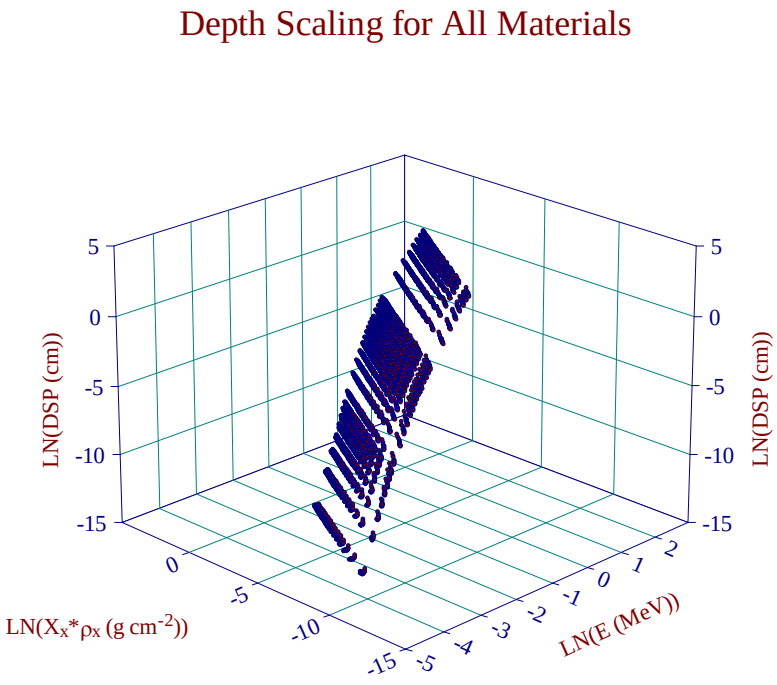

Fig. 5.14. TableCurve 3D plot of depth-scaling data for all source materials used in scaling model.

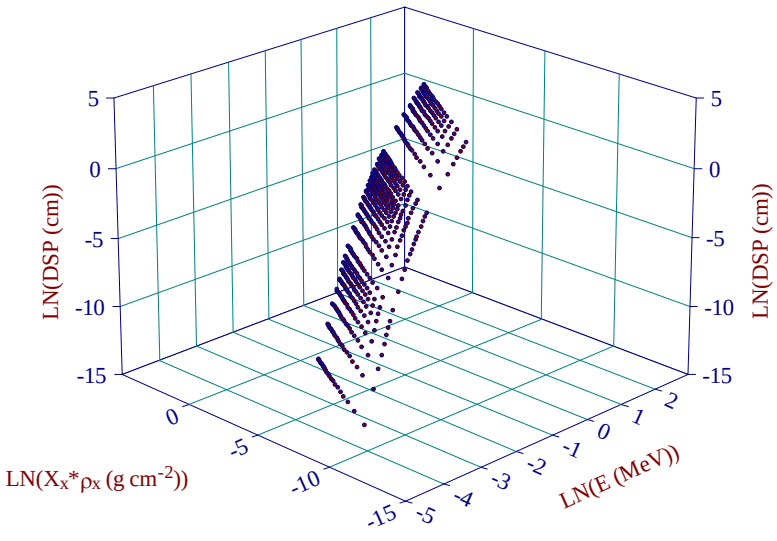

Fig. 5.15. TableCurve 3D plot of depth-scaling data for iron source material.

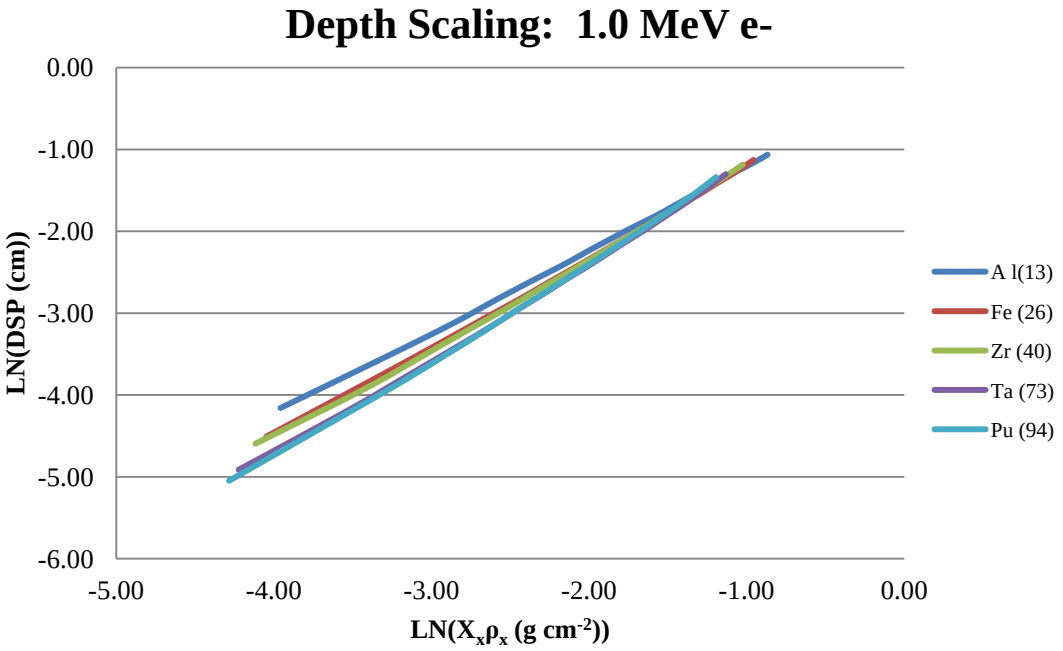

Fig. 5.16. Comparison of DSP's for a range of source materials with 1.0 MeV electrons.

5.3.3 Energy Scaling Parameters

As with the case of depth scaling, the natural logarithm of energy was used to decrease variability over the range of energies examined. The variability associated with the absorption-sphere radius was minimized by expressing it as a ratio of density thickness to the X_{90} distance in water, $X_x * \rho_x \; / \; X_{90w}$. The natural logarithm of the depth-scaling parameter multiplied by the initial electron energy, $LN(ESP*E_0)$, was chosen as the dependent variable. While the quantity of $ESP*E_0$ has no physical meaning, using it as the dependent variable produced tighter fitting surface plots than simply using *ESP*. Since E_0 is a known quantity, solving for *ESP* is simple.

The variability of the *ESP* curves (Fig. 5.17, Fig. 5.18) with respect to *Z* is more pronounced than the *DSP* curves. Examination of a single electron energy and select media allows for a better analysis (Fig. 5.19). The variation of *ESP*'s becomes quite large as the absorption-sphere radius increases. As *Z* approaches that of water (Z_{eff} of 7.42), the *ESP* approaches 1.0, as expected. As *Z* increases, the amount of energy reduction following depth

scaling increases. Once again, this is expected given the lower profile of high-*Z* non-homogeneous DPK curves (Fig. 5.9) for the same absorption-sphere radius (with respect to X/X_{90}). Despite this increased variability, interpolation within surface plots is not seen as an issue.

All curve fits for the *ESP*'s took the form

$$LN(E * ESP\ (MeV)) = \frac{(a + bx + cx^2 + dx^3 + ey + fy^2)}{(1 + gx + hx^2 + iy + jy^2)} \qquad (5.2)$$

where x is $LN(E\ (MeV))$ and y is $X_x * \rho_x\ /\ X_{90w}$. The terms X_x and ρ_x refer to the radius and density of the absorption sphere. The above equation was chosen because it was the equation that had the largest R^2 value ($\geq$0.999) and was able to fit all 18 plots. As with the *DSP*'s, fit parameters (Table F 2) demonstrated a slight *Z* dependence.

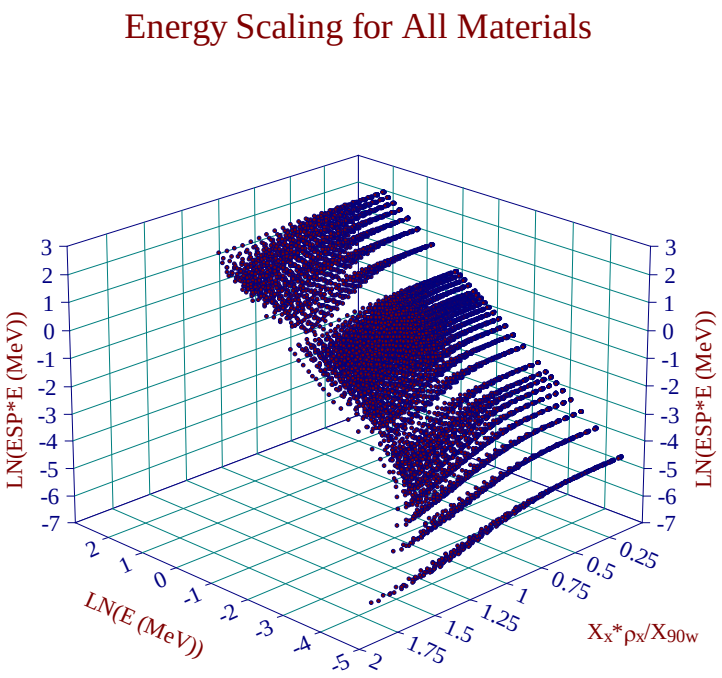

Fig. 5.17. TableCurve 3D plot of energy-scaling data for all source materials used in scaling model.

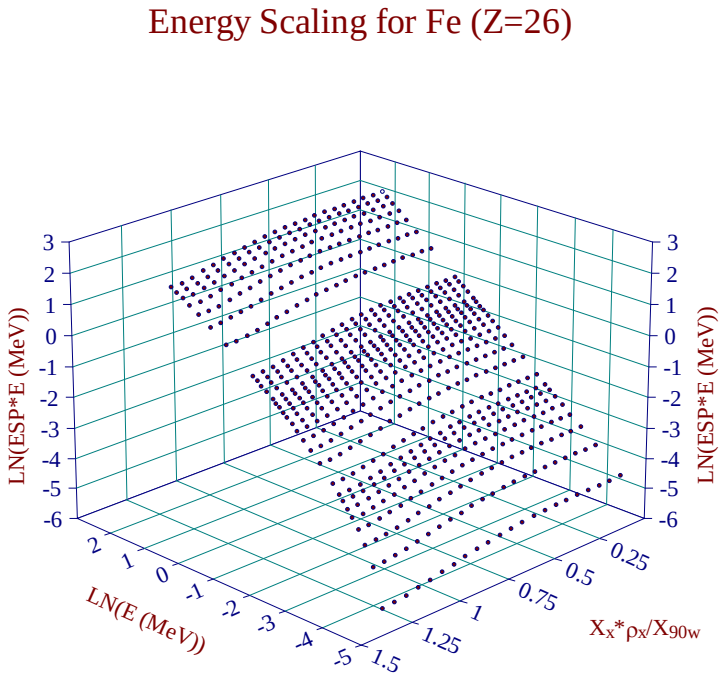

Fig. 5.18. TableCurve 3D plot of energy-scaling data for iron source material.

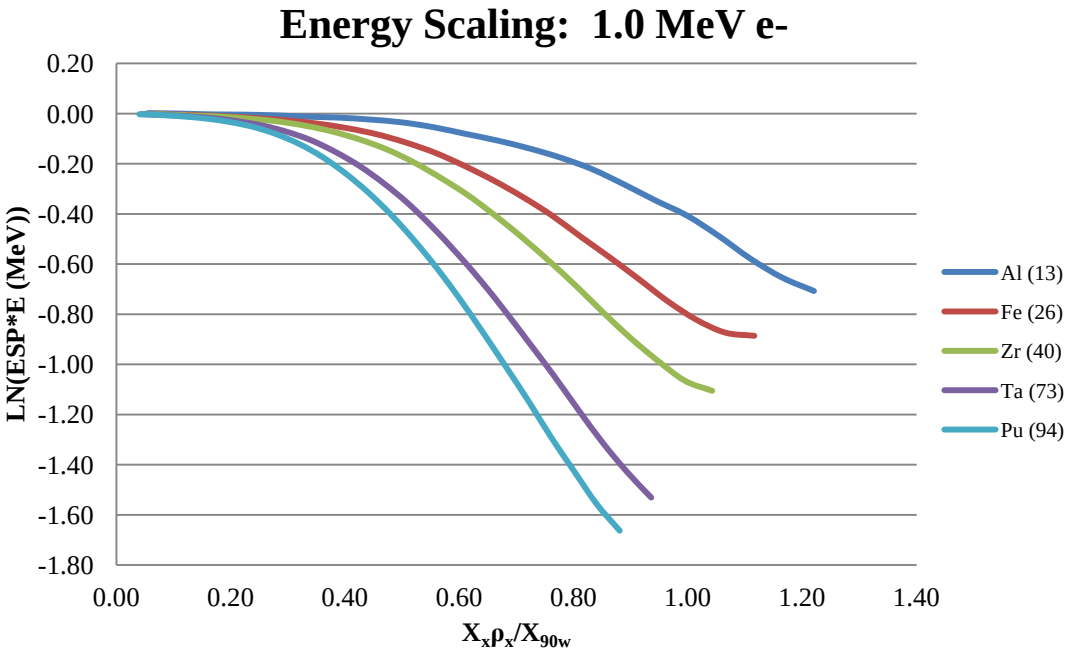

Fig. 5.19. Comparison of ESP's for a range of source materials with 1.0 MeV electrons.

5.4 Beta-Particle Non-Homogeneous Dose-Point Kernels

As described in Section 4.5, non-homogeneous DPK's for beta-emitters can be found by integrating both energy and depth-scaling parameters over the beta energy spectrum according to Eq. (4.6). Non-homogeneous DPK's were found for all beta-particles listed in Table 4.2 and all source materials listed in Table 4.3. The absorption-sphere radius was varied from 0.1 to 1.8 X/X_{90}. Results were consistent across all beta energies and all sources (Z). Therefore, a representative sample of results is provided here to demonstrate improvements over the literature.

Non-homogeneous stainless steel (ρ=8.06 g cm^{-3}, Z_{eff} =25.81) DPK's for ^{90}Sr beta-particles (E_{ave}=0.196 MeV) yield excellent results over all absorption-sphere radii (Fig. 5.20 - Fig. 5.23). The curves labeled as 'EGSnrc' represent non-homogeneous DPK's determined directly from EGSnrc simulations (EDKnrc user code) with an ICRP 107 ^{90}Sr source particle. The curves labeled as 'Mangini' represent the non-homogeneous DPK's generated in SADCALC.f using the *ESP* and *DSP* fit equations (determined in this work) and the curves labeled as 'Cross' are for SADCALC.f DPK's generated with a Cross (1967, 1968, 1982, 1992a) scaling factor of (η_w) 1.016. Relative errors for EGSnrc data are all less than 5.0% with most values having errors less than 1.0%.

The Cross scaling factor was calculated using the method outlined in Section 2.5.1 for Z_{eff} > 18 and is in close agreement with the 1.011 value calculated by Fox (2000). Equation (2.25) was used to first calculate η_{Al} for water (1.26) and stainless steel (1.28). The ratio of the two (according to Eq. (2.26)) yields the final η_w value of 1.016. The ratio of the mass stopping power for water was found using Eq. (2.24), with Eq. (2.27) being used for stainless steel. Unlike the tungsten alloy and uranium oxide results presented below, density scaling was not used for literature comparison given the closeness of η_w to unity.

For stainless steel (relatively low-Z), the largest discrepancies in Cross' model (and subsequent improvement with the new model) were found in spherical shells directly following the absorption sphere. Cross' model overestimates the DPK value at these depths. Conversely, his model underestimates the DPK value at larger depths; a pattern predicted by spectral hardening. While the discrepancies with the new model were greatest at larger

absorption spheres (Fig. 5.23), it is important to remember that energy deposition in water following these spheres is insignificant compared to smaller spheres (Fig. 5.20). In this particular case, the largest deviation occurred for the 1.40 X/X_{90} sphere in the 0.025 X/X_{90} water shell and was found to be ~ 15%.

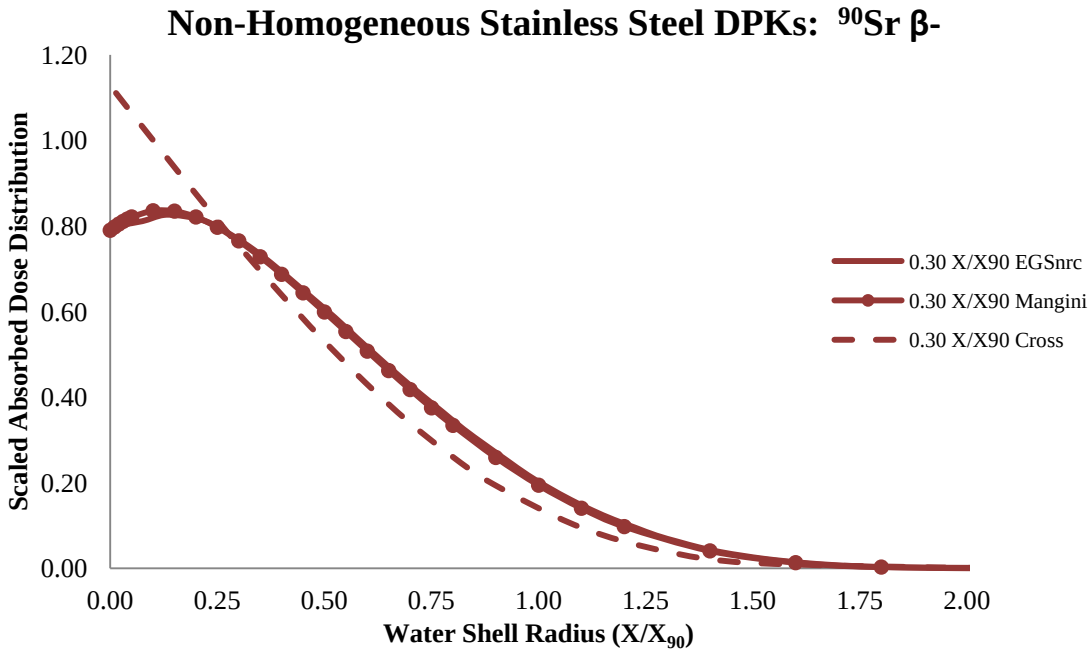

Fig. 5.20. Comparison of non-homogeneous DPK results for ^{90}Sr beta-particles positioned at the center of a stainless steel absorption sphere with a 0.30 X/X_{90} radius.

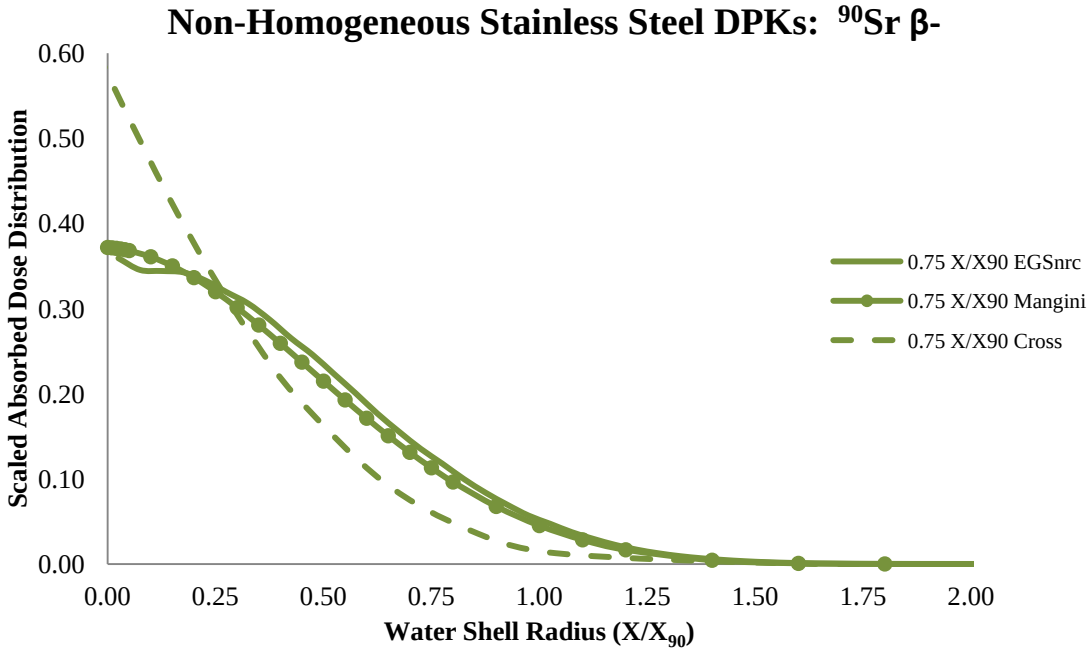

Fig. 5.21. Comparison of non-homogeneous DPK results for ^{90}Sr beta-particles positioned at the center of a stainless steel absorption sphere with a 0.75 X/X_{90} radius.

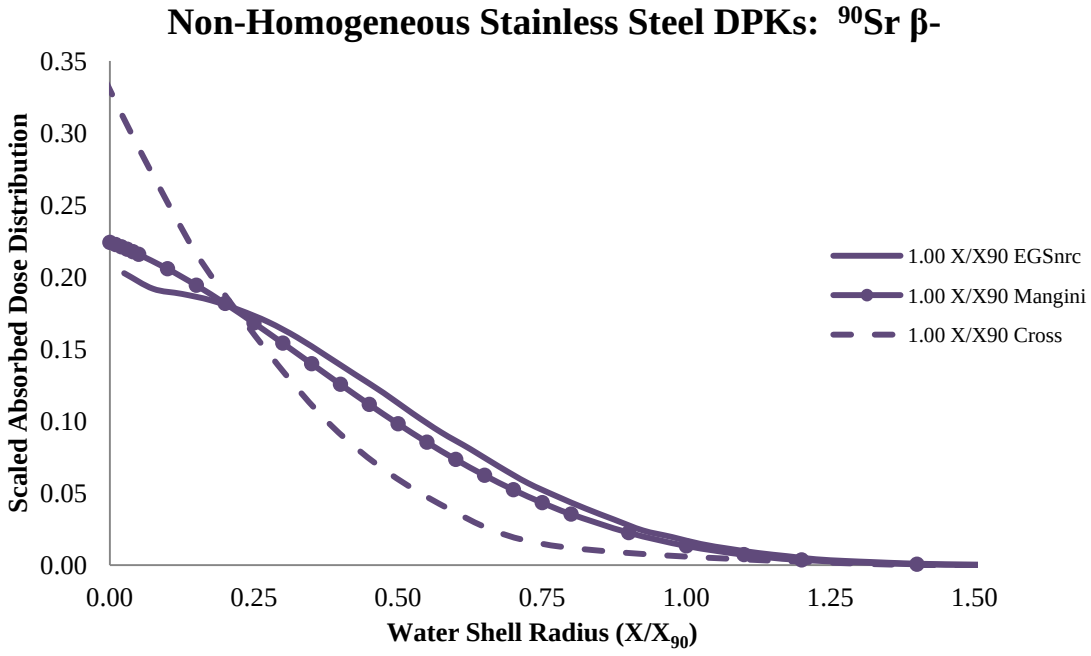

Fig. 5.22. Comparison of non-homogeneous DPK results for ^{90}Sr beta-particles positioned at the center of a stainless steel absorption sphere with a 1.00 X/X_{90} radius.

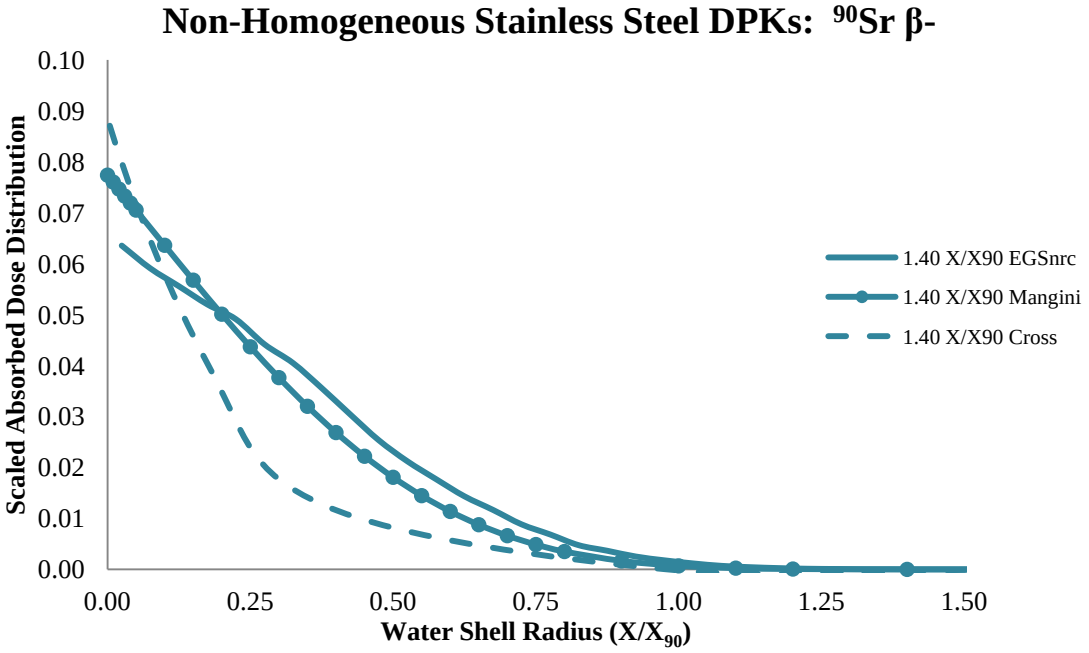

Fig. 5.23. Comparison of non-homogeneous DPK results for ^{90}Sr beta-particles positioned at the center of a stainless steel absorption sphere with a 1.40 X/X_{90} radius.

Cross cautions against the use of his scaling model for Z greater than 40 as significant errors are expected to occur (Cross 1967, 1968, 1982, 1992a). Nonetheless, for comparisons sake, Cross scaling factors for tungsten alloy (ρ=18.00 g cm^{-3}, Z_{eff} =72.79) and uranium oxide (ρ=10.96 g cm^{-3}, Z_{eff} =87.88) have been calculated using the same method as stainless steel. Those values were found to be 1.42 (η_{Al} = 1.78) and 1.60 (η_{Al} = 2.02), respectively. While Cross' model has been shown by Janicki (1999) to be an improvement over simple density scaling (η_w = 1.0), his work involved low-Z media when the scaling factor was typically less than 1.0. Therefore, density scaling is also examined for tungsten alloy and uranium oxide to compare these two models and to demonstrate their subsequent, and expected, failure for high-Z media. This was not warranted for stainless steel since its scaling factor is already near unity. Curves labeled as 'Density' use η_w of 1.0 and curves labeled as 'Cross' use the material-specific η_w.

The scaling model presented here provides excellent agreement with EGSnrc as Z is increased (Fig. 5.24 - Fig. 5.31) for both ^{32}P beta-particles (E_{ave}=0.695 MeV) and ^{144}Pr beta-

particles (E_{ave}=1.217 MeV). Results are nearly identical to those presented for ^{90}Sr beta-particles in stainless steel with largest deviations occurring at the largest absorption-sphere radii (Fig. 5.27, Fig. 5.31)

The success of the new model presented here is further exemplified by the failure of both the density scaling model and Cross' model for these high-*Z* media. For smaller absorption-sphere radii, density scaling provides a better estimate of the non-homogeneous DPK (Fig. 5.24, Fig. 5.28). On the other hand, when the radius is increased, the density scaled DPK becomes increasingly inaccurate, particularly in shallow water shells (Fig. 5.26, Fig. 5.30). The overall inaccuracy of both models is likely due to their simplicity and their inability to account for spectral hardening.

As with the stainless steel non-homogeneous DPK's, the results presented here support the observations made in the literature (Cross 2001; Reynaert 2001; Cho 2004; Sherbini 2008) that beta-particles transmitted by high-*Z* media have a significantly harder spectrum than those transmitted by an 'equivalent' water window and are subsequently more penetrating. Neither Cross' model nor the simple density scaling model is able to account for this phenomenon, especially when *Z* is greater than 40. This is clearly seen by the overestimation of DPK values at shallow depths and the underestimation of DPK values at greater depths. The model presented here provides nearly identical non-homogeneous DPK's at all depths, regardless of *Z* and absorption-sphere radii.

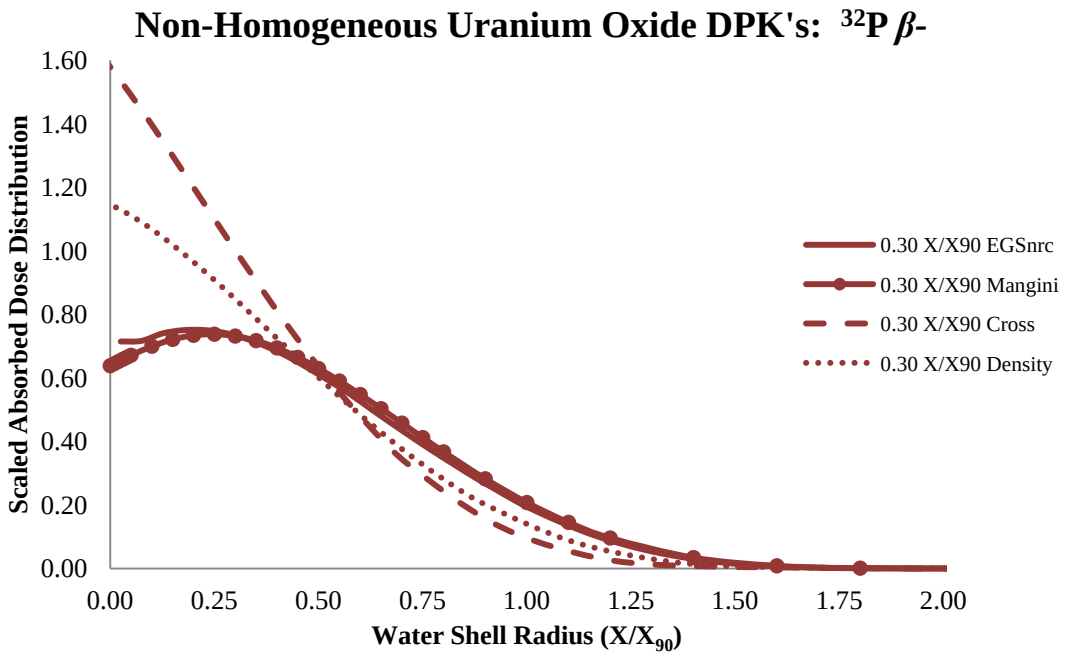

Fig. 5.24. Comparison of non-homogeneous DPK results for ^{32}P beta-particles positioned at the center of a uranium oxide absorption sphere with a 0.30 X/X_{90} radius.

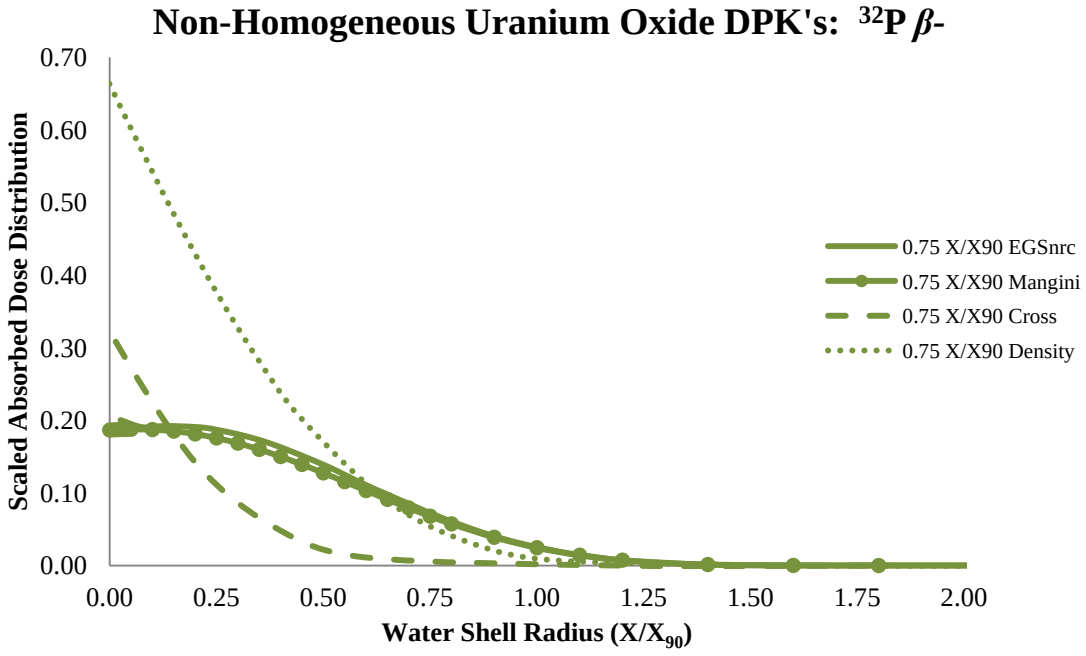

Fig. 5.25. Comparison of non-homogeneous DPK results for ^{32}P beta-particles positioned at the center of a uranium oxide absorption sphere with a 0.75 X/X_{90} radius.

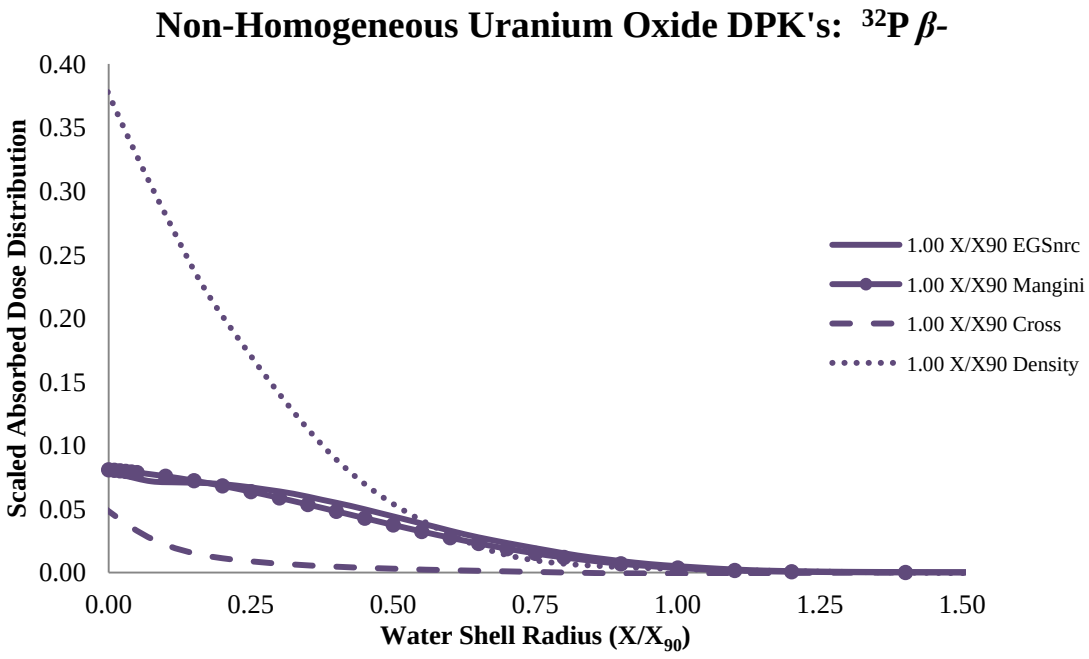

Fig. 5.26. Comparison of non-homogeneous DPK results for ^{32}P beta-particles positioned at the center of a uranium oxide absorption sphere with a 1.00 X/X_{90} radius.

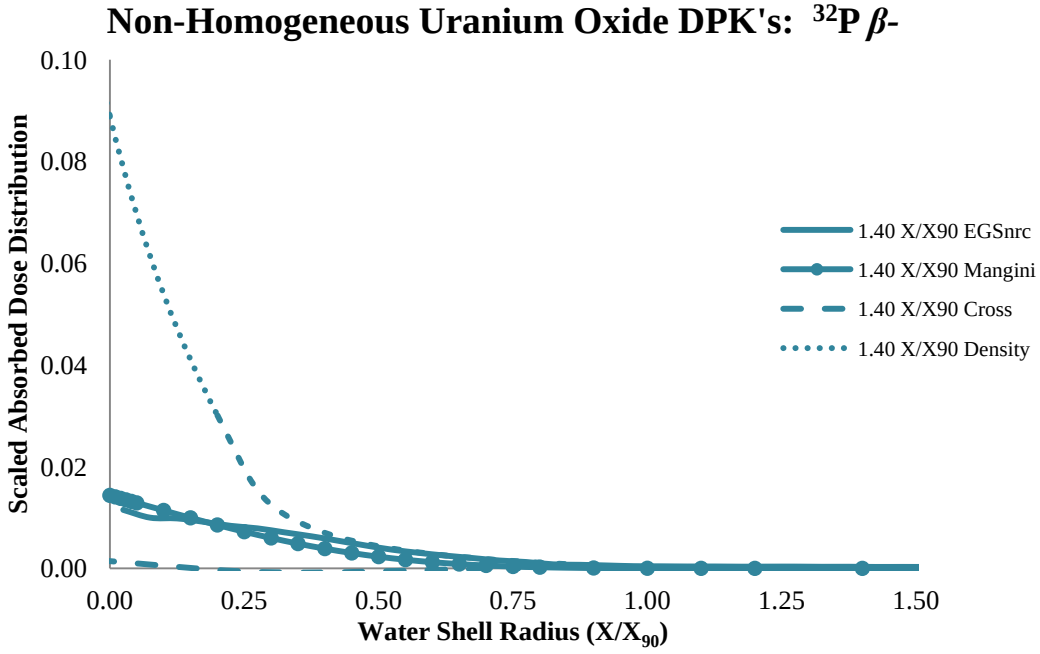

Fig. 5.27. Comparison of non-homogeneous DPK results for ^{32}P beta-particles positioned at the center of a uranium oxide absorption sphere with a 1.40 X/X_{90} radius.

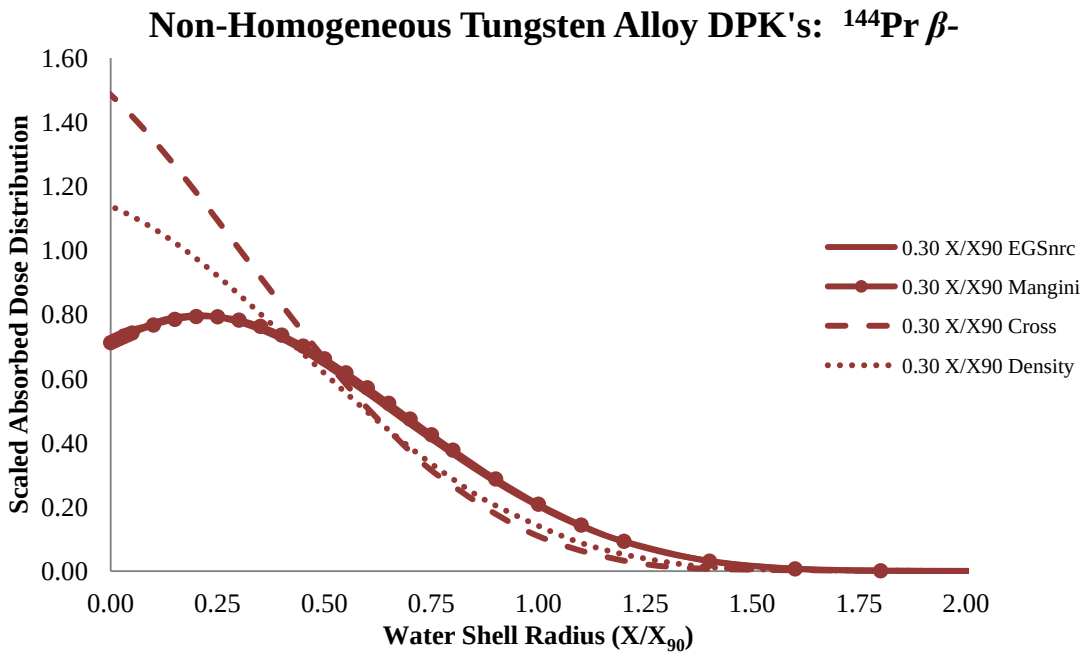

Fig. 5.28. Comparison of non-homogeneous DPK results for ^{144}Pr beta-particles positioned at the center of a tungsten alloy absorption sphere with a 0.30 X/X_{90} radius.

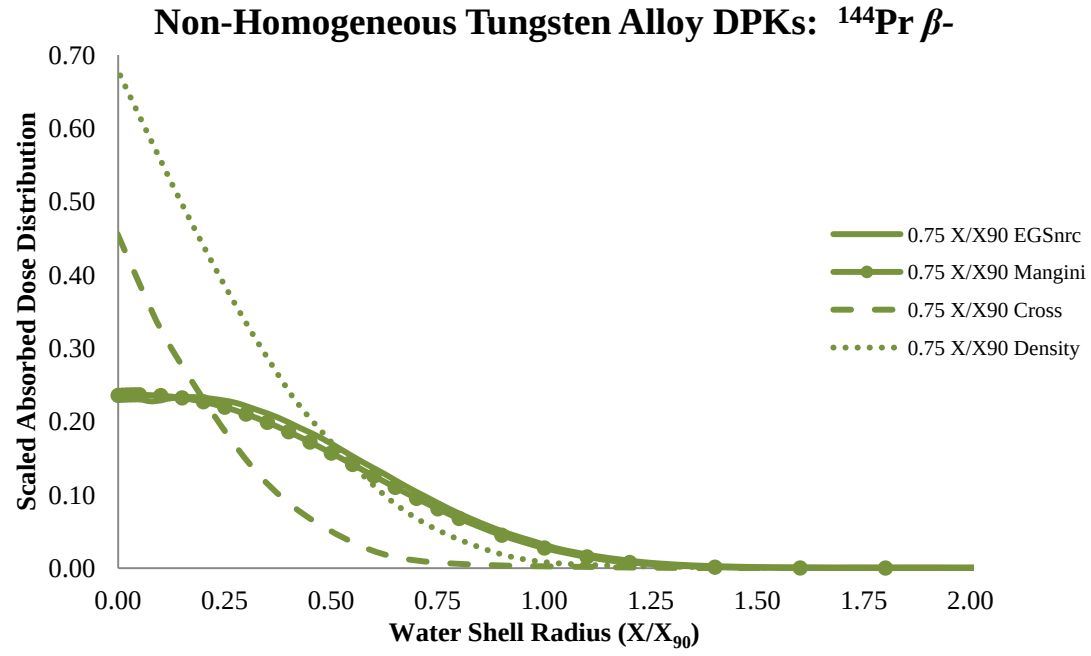

Fig. 5.29. Comparison of non-homogeneous DPK results for ^{144}Pr beta-particles positioned at the center of a tungsten alloy absorption sphere with a 0.75 X/X_{90} radius.

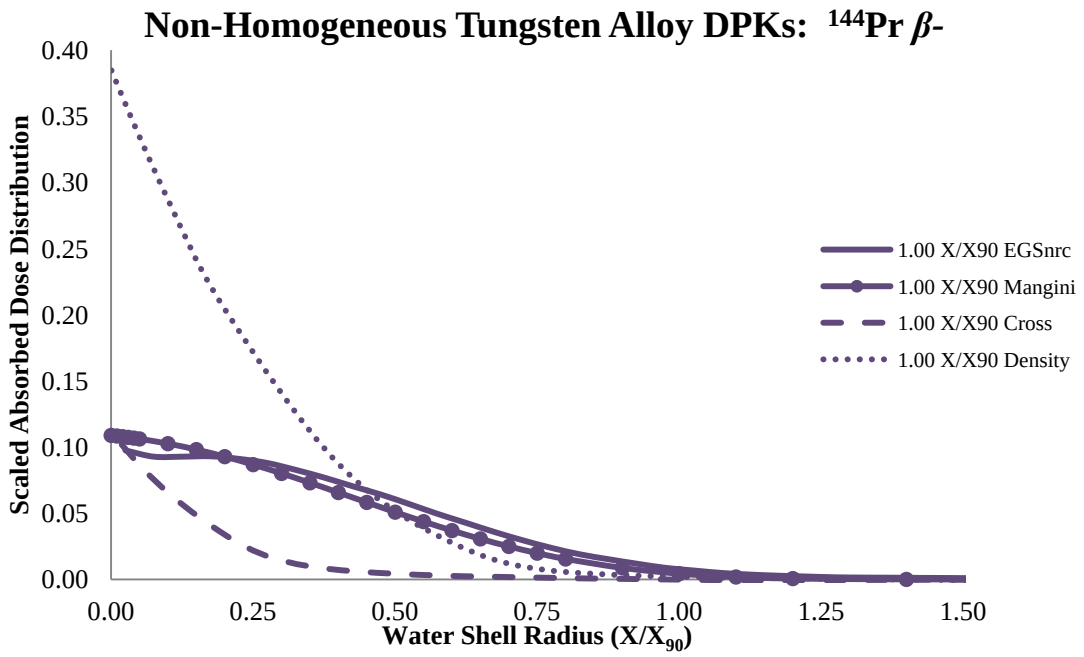

Fig. 5.30. Comparison of non-homogeneous DPK results for ^{144}Pr beta-particles positioned at the center of a tungsten alloy absorption sphere with a 1.00 X/X_{90} radius.

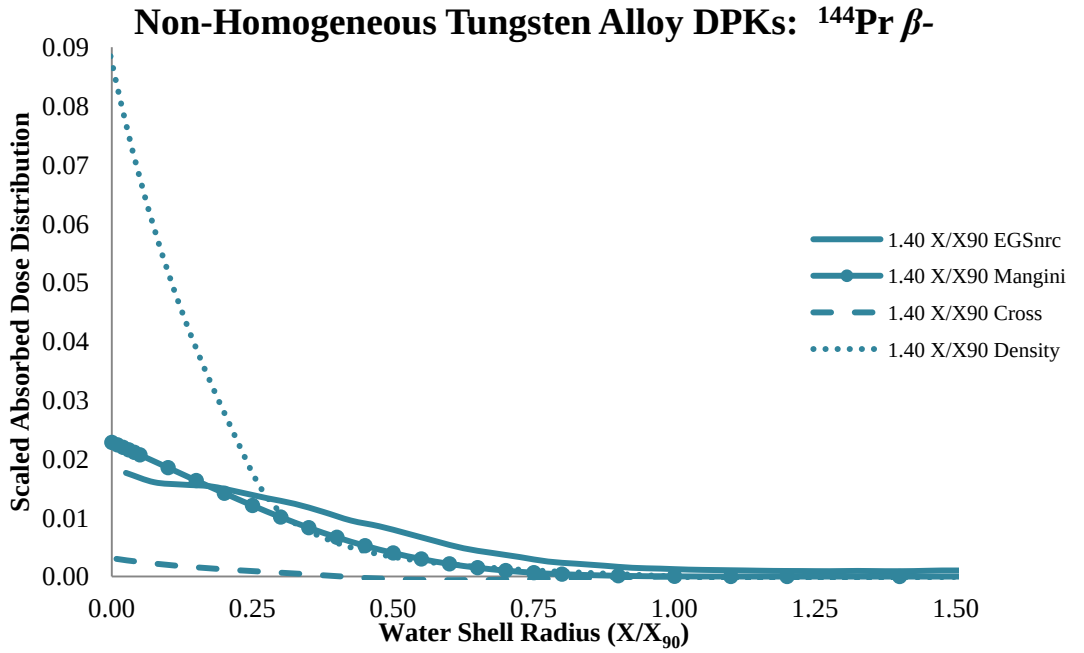

Fig. 5.31. Comparison of non-homogeneous DPK results for ^{144}Pr beta-particles positioned at the center of a tungsten alloy absorption sphere with a 1.40 X/X_{90} radius.

Given the observations made both in the literature and in the findings presented here, it is important to show the effect that Z has on Cross' model and density scaling as Z is increased from a relatively low value (13) to a relatively high value (87.88). Using ^{144}Pr beta-particles and an absorption-sphere radius of 0.30 X/X_{90} as an example, it is easy to show the progression of the two scaling models as Z is increased. When the absorption sphere is made of aluminum (Z = 13, η_w = 0.91), both models provide a very accurate estimate of the EGSnrc non-homogeneous DPK's (Fig. 5.32). While the effects of spectrum hardening begin to show when Z is increased to 25.81 (stainless steel), the models still provide a reasonable DPK estimation (Fig. 5.33) given their simplicity. As Z is increased to 47 (silver, η_w = 1.21, η_{Al} = 1.26), 72.79 (tungsten alloy), and 87.88 (uranium oxide), the hardening effect becomes more and more pronounced (Fig. 5.34 - Fig. 5.36) and the models begin to fail. The same results can be demonstrated using a 1.00 X/X_{90} absorption-sphere radius.

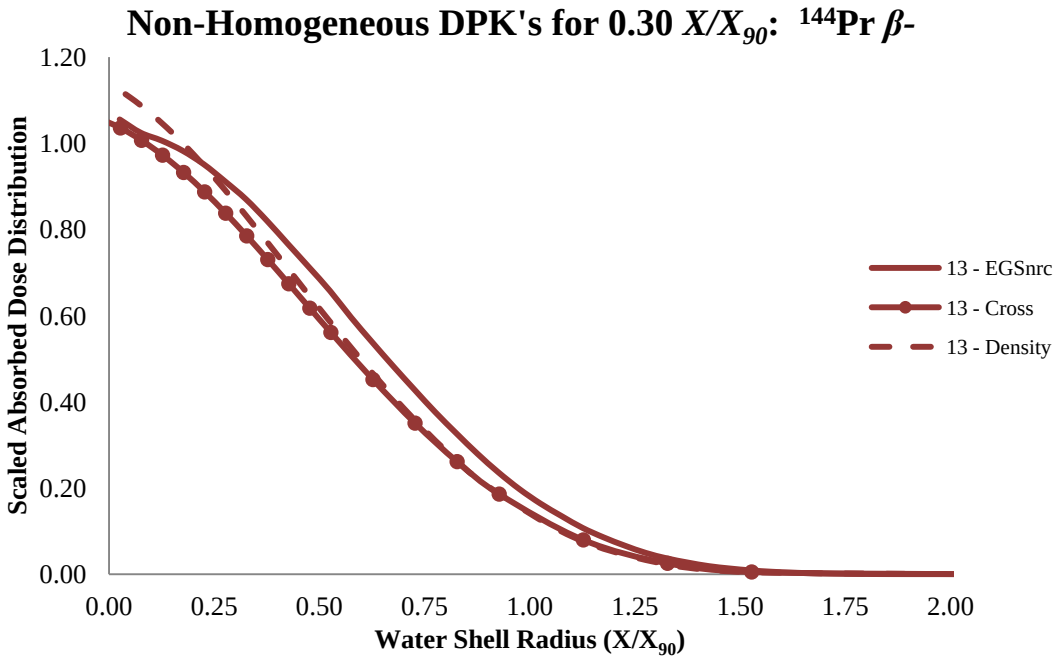

Fig. 5.32. Comparison of non-homogeneous DPK's for Z of 13 and absorption-sphere radius of 0.30 X/X_{90}.

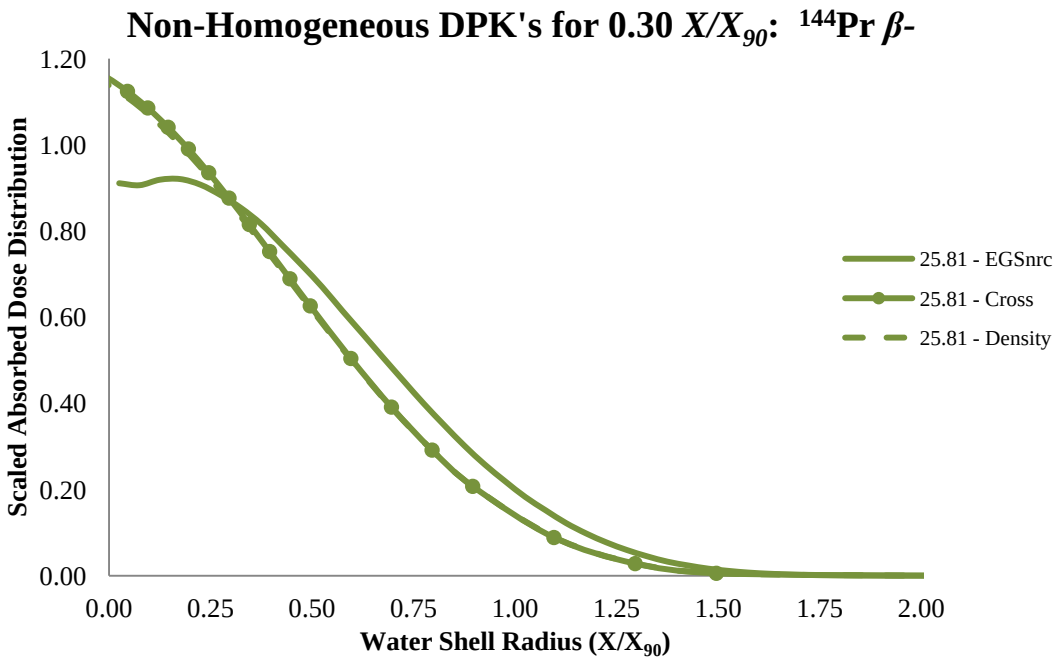

Fig. 5.33. Comparison of non-homogeneous DPK's for Z of 25.81 and absorption-sphere radius of 0.30 X/X_{90}.

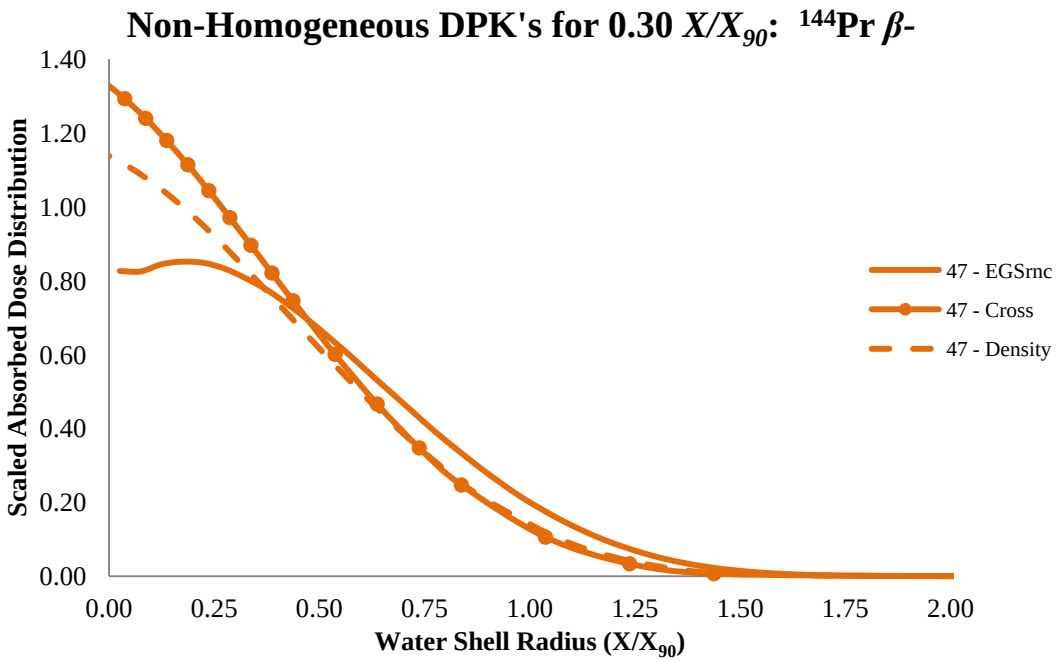

Fig. 5.34. Comparison of non-homogeneous DPK's for Z of 47 and absorption-sphere radius of 0.30 X/X_{90}.

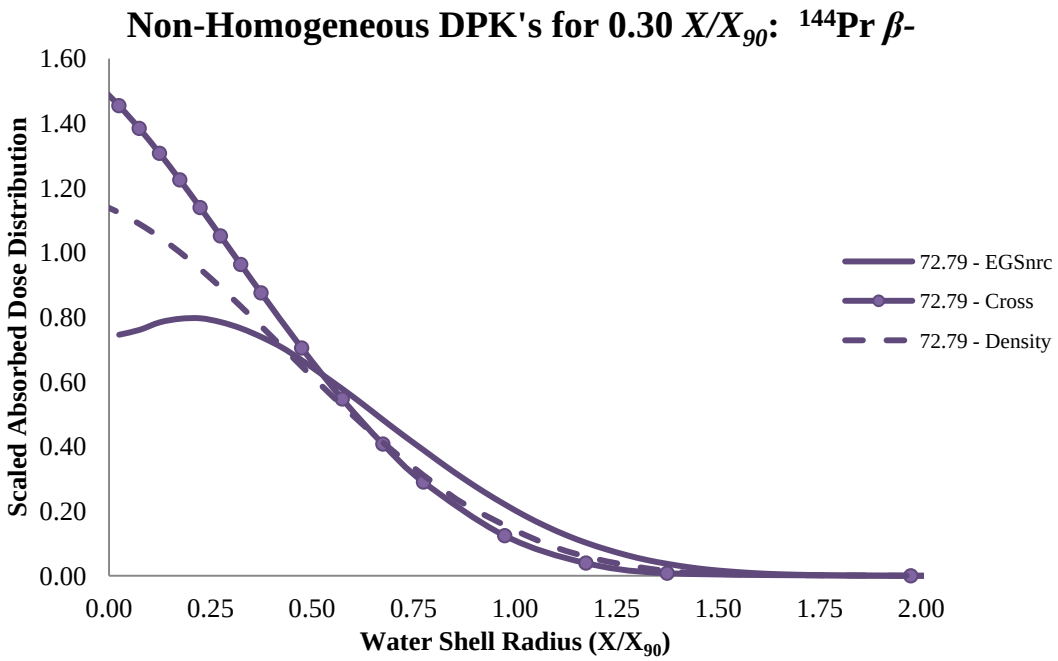

Fig. 5.35. Comparison of non-homogeneous DPK's for Z of 72.79 and absorption-sphere radius of 0.30 X/X_{90}.

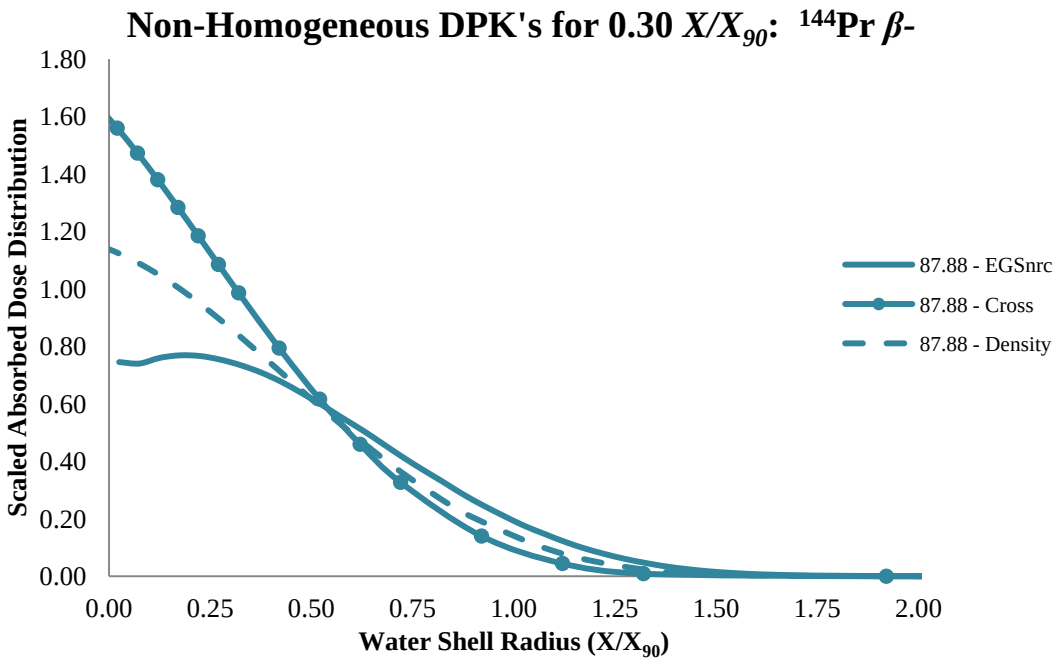

Fig. 5.36. Comparison of non-homogeneous DPK's for Z of 87.88 and absorption-sphere radius of 0.30 X/X_{90}.

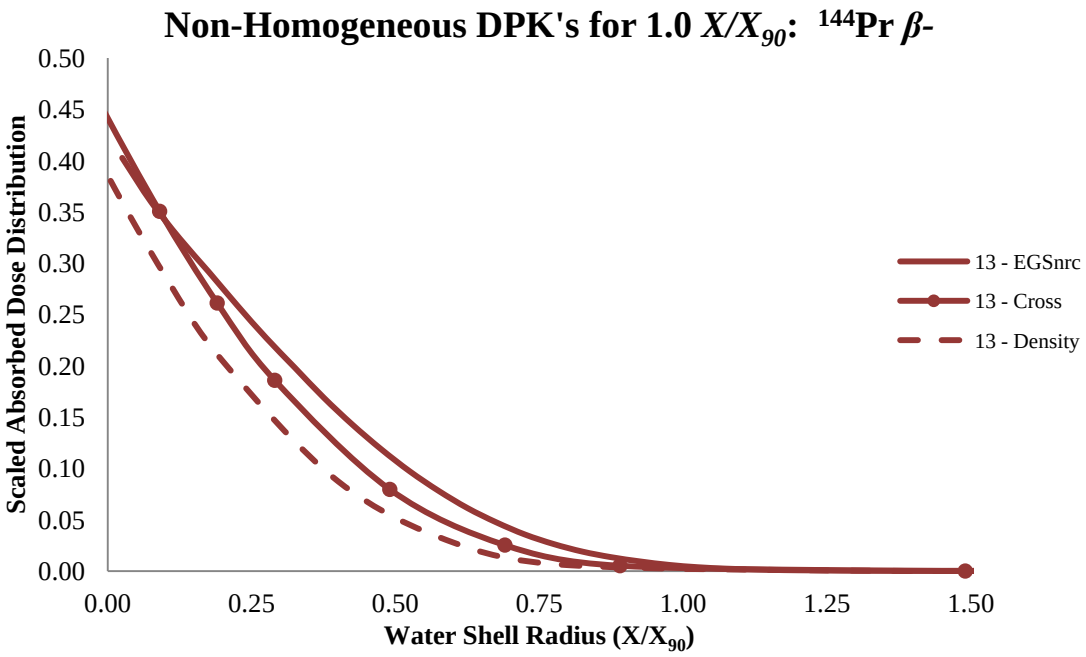

Fig. 5.37. Comparison of non-homogeneous DPK's for *Z* of 13 and absorption-sphere radius of 1.00 X/X_{90}.

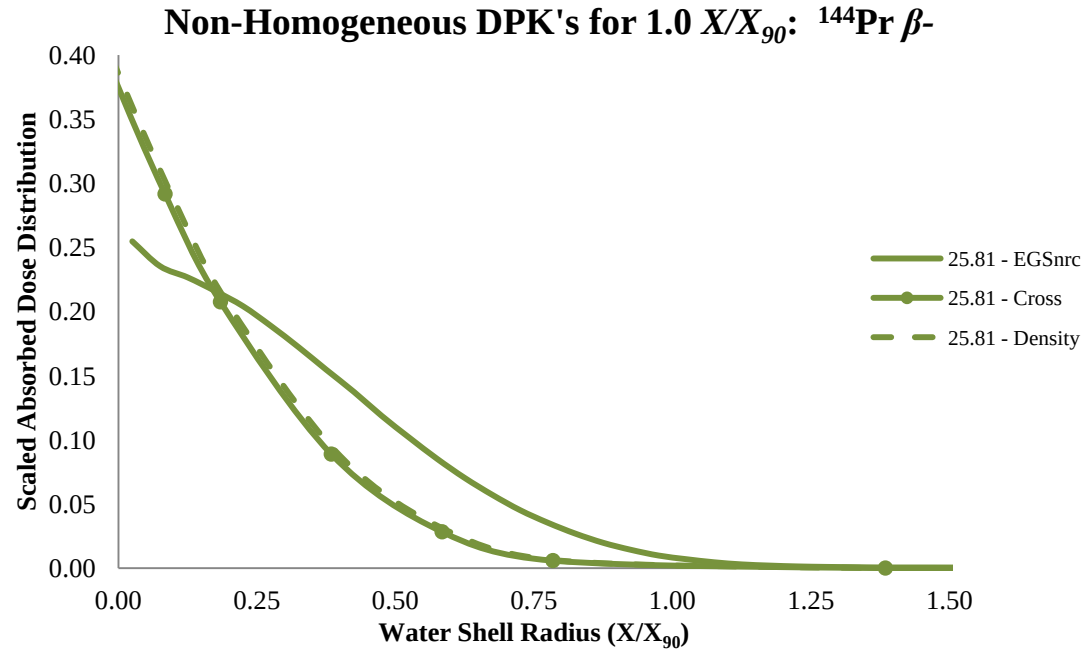

Fig. 5.38. Comparison of non-homogeneous DPK's for *Z* of 25.81 and absorption-sphere radius of 1.00 X/X_{90}.

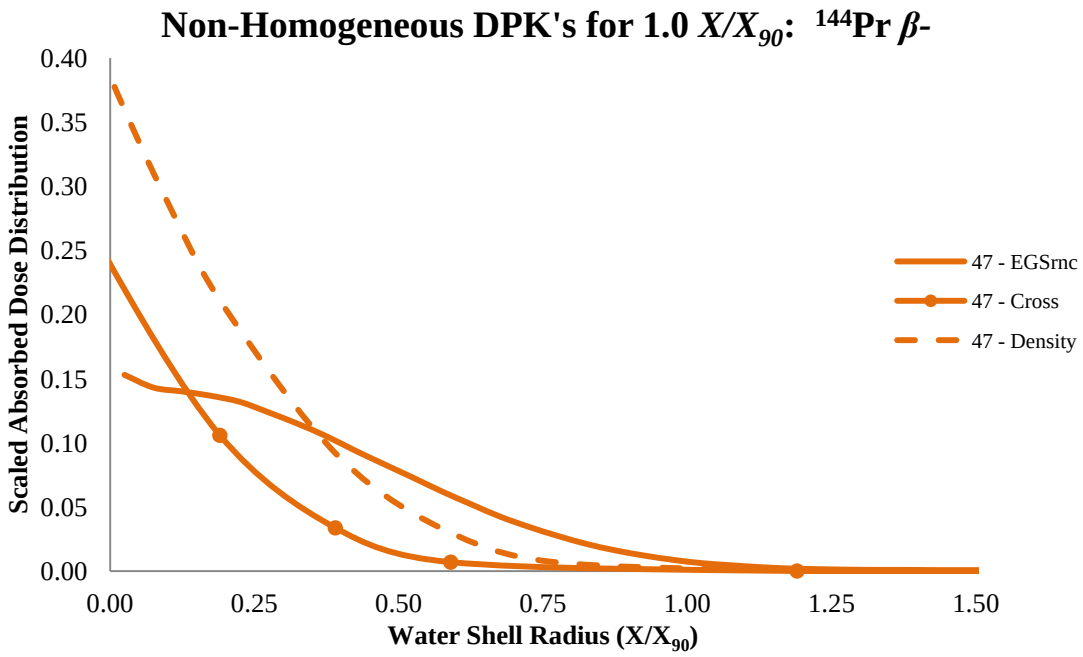

Fig. 5.39. Comparison of non-homogeneous DPK's for *Z* of 47 and absorption-sphere radius of 1.00 X/X_{90}.

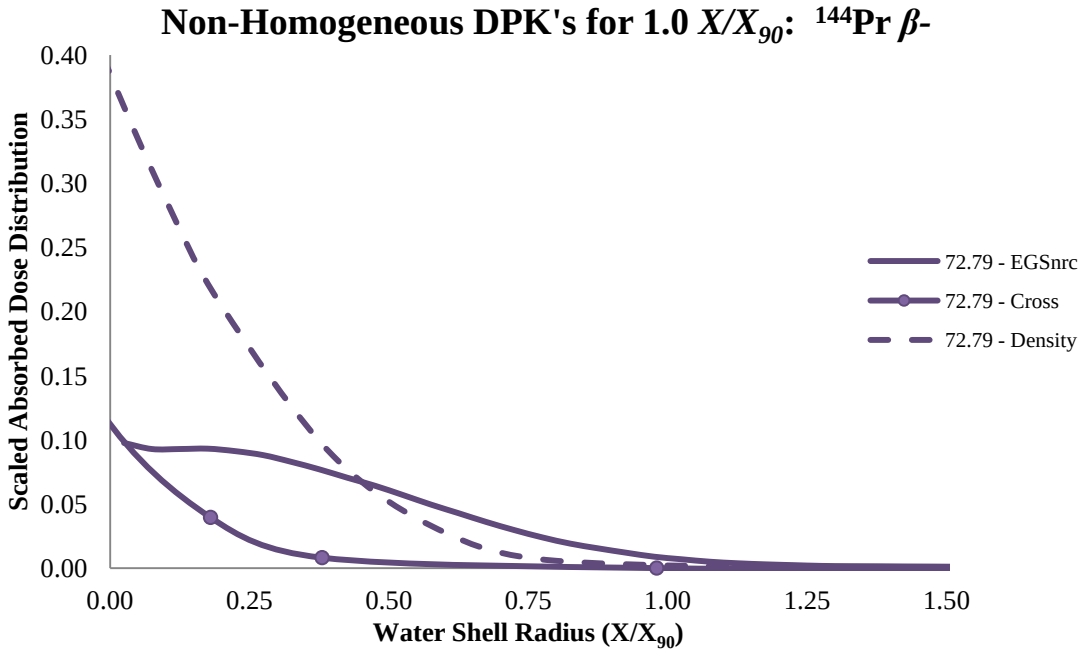

Fig. 5.40. Comparison of non-homogeneous DPK's for *Z* of 72.79 and absorption-sphere radius of 1.00 X/X_{90}.

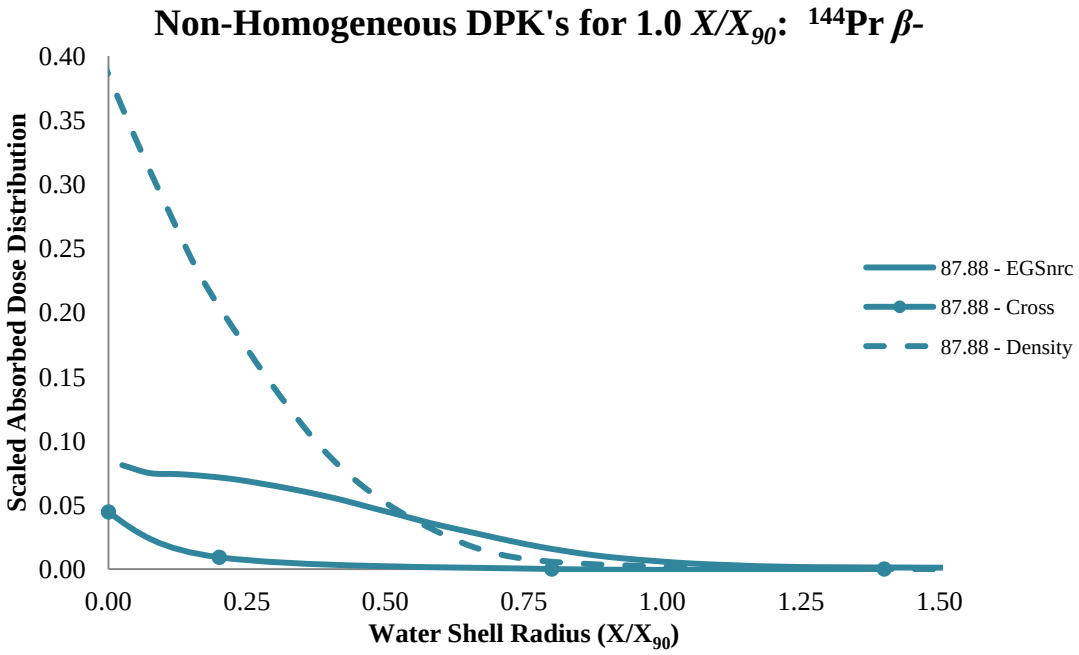

Fig. 5.41. Comparison of non-homogeneous DPK's for Z of 87.88 and absorption-sphere radius of 1.00 X/X_{90}.

5.5 Backscatter Model

5.5.1 Planar Dose Profiles

Planar dose profiles exhibited a near identical curvature for all scattering media (Fig. 5.46). With the exception of air, variation with respect to Z was very small, thereby improving the accuracy of linear interpolation within Z. The profiles were segmented at 1.0 MeV to better fit the significant drop in dose at low energies. TableCurve 3D surface fits were found to be the smoothest when the square root of dose rate was plotted verses normal depth and natural logarithm of energy. Sample profiles are provided for 1 cm^2 dose averaging areas with $E_0 \leq 1.0$ MeV (Fig. 5.42 - Fig. 5.44) and $E_0 \geq 1.0$ MeV (Fig. 5.45).

The influence of dose averaging area is only seen for electron energies greater than 1.0 MeV (Fig. 5.47 - Fig. 5.48). This is expected since the CSDA range of a 1.0 MeV electron is 0.437 cm and the radius of a 1.0 cm^2 dose area is 0.564 cm. While the TableCurve 3D plots

(Fig. 5.49) were unable to demonstrate this visibly, dose is expected to increase slightly at shallow depths for low-energy electrons in the air-water interface geometry when the dose area is increased to 10 cm^2. This is due to the increased probability of backscattering in the air volume and imparting energy in the larger dose area. However, a resulting increase (very slight) in the air backscatter factor for low-energy beta-particles is demonstrated in the next section (Fig. 5.57).

All profiles were fit with a Chebyshev Series (LnX-Y, Order 6). While this is a complex fit equation, it allowed for all curves to be fit with the same functional form and a high goodness of fit ($R^2 > 0.999$). As an example, a second-order Chebyshev is given by,

$$Z = a + bT_1(x') + cT_1(y') + dT_2(x') + eT_1(y') + fT_2(y'), \qquad (5.3)$$

where,

$$x' = \ln(x) = \ln(Normal\ Depth\ (cm)) \quad \text{scaled -1 to +1,}$$

$$y' = y = \ln(E\ (MeV)) \quad \text{scaled -1 to +1,}$$

$$T_n(x') = \cos(n * a * \cos(x')),$$

and Z is the square root of the dose rate per particle (Gy Bq^{-1} s^{-1}). An order 6 Chebyshev Series has 28 fit parameters (Table F 3 - Table F 6).

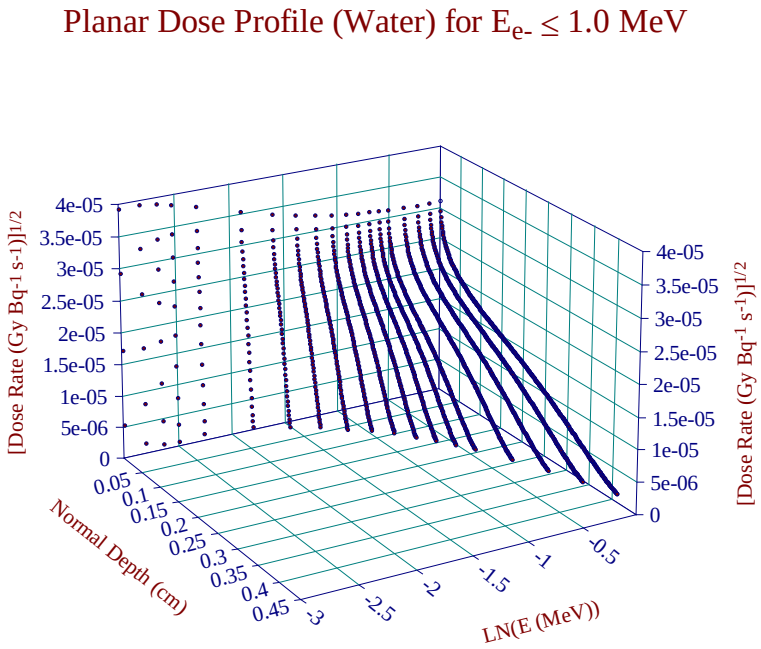

Fig. 5.42. TableCurve 3D planar dose profile for mono-energetic electrons ($E \leq 1.0$ MeV) positioned at the center of a water-water interface. Dose averaging area is 1 cm^2.

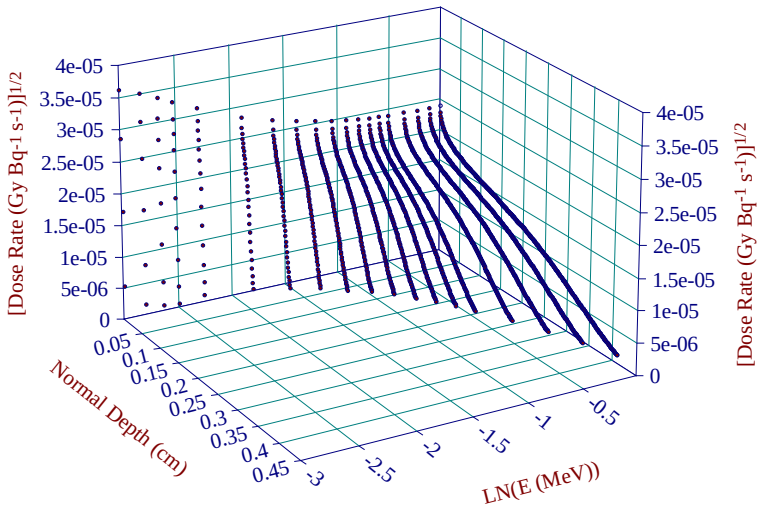

Fig. 5.43. TableCurve 3D planar dose profile for mono-energetic electrons ($E \leq 1.0$ MeV) positioned at the center of an air-water interface. Dose averaging area is 1 cm^2.

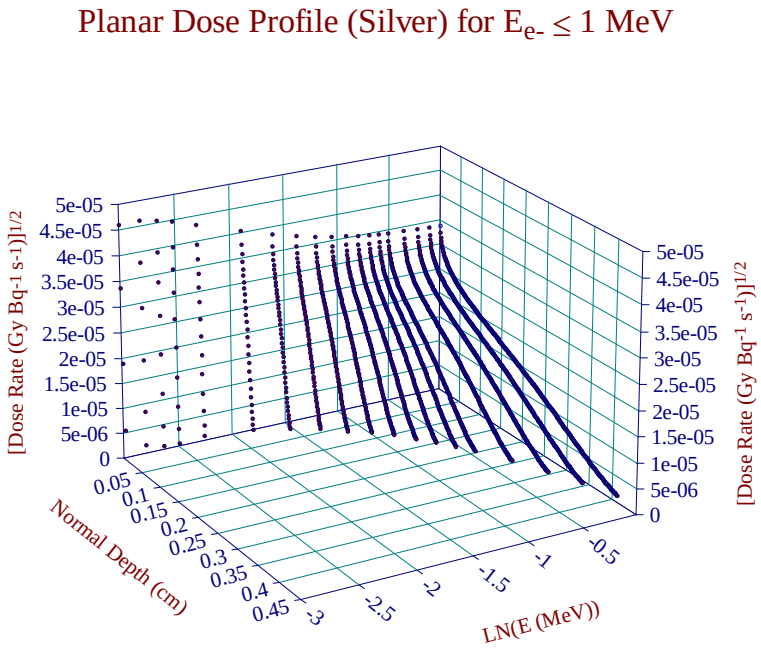

Fig. 5.44. TableCurve 3D planar dose profile for mono-energetic electrons ($E \leq 1.0$ MeV) positioned at the center of a silver-water interface. Dose averaging area is 1 cm^2.

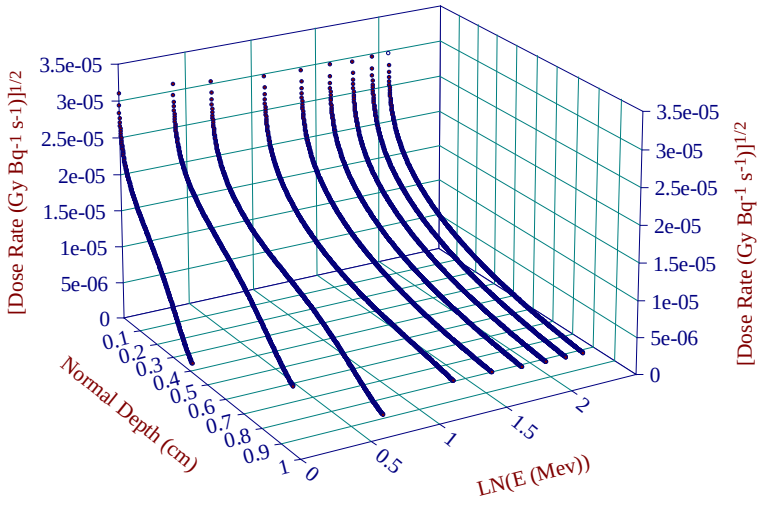

Fig. 5.45. TableCurve 3D planar dose profile for mono-energetic electrons ($E \geq 1.0$ MeV) positioned at the center of a water-water interface. Dose averaging area is 1 cm^2.

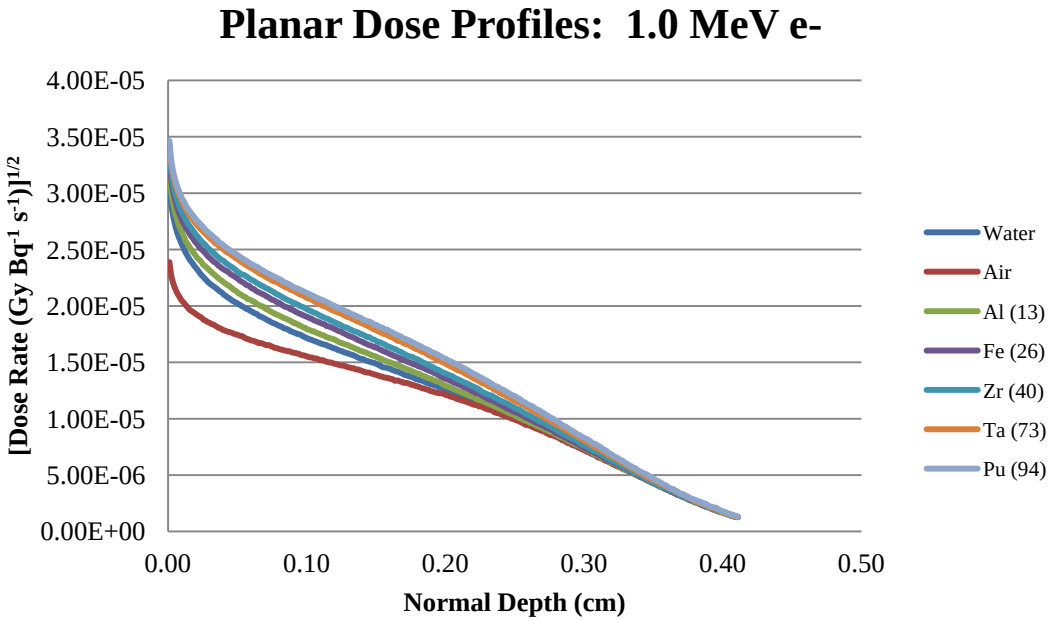

Fig. 5.46. Comparison of planar dose profile for 1.0 MeV electrons positioned at the center of the scattering medium-water interface. Dose averaging area is 1 cm^2.

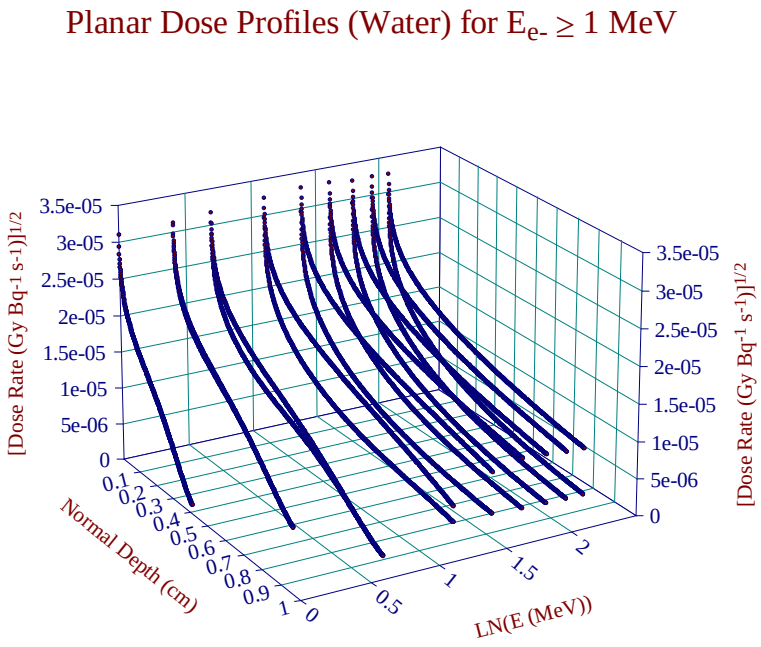

Fig. 5.47. Comparison of 1 and 10 cm^2 TableCurve 3D planar dose profile for mono-energetic electrons (E ≥ 1.0 MeV) positioned at the center of a water-water interface. The top layer is from the 10 cm^2 dose area.

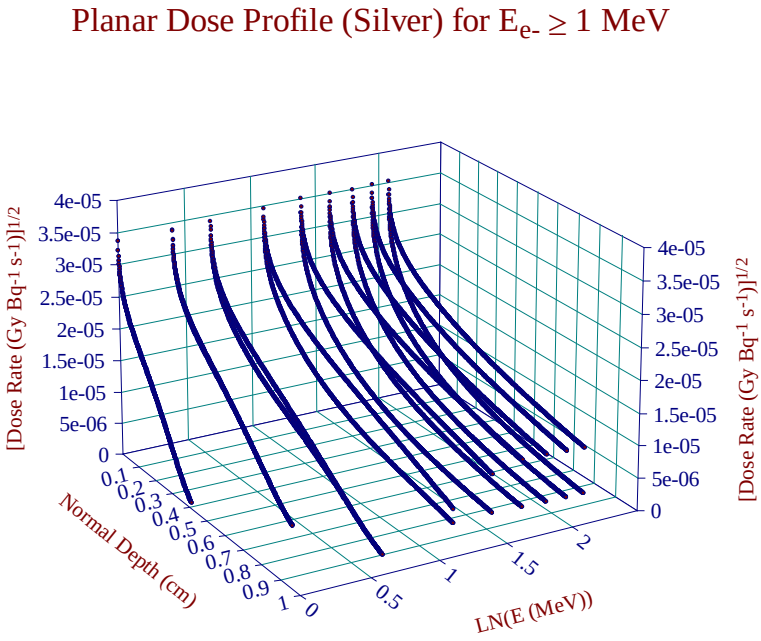

Fig. 5.48. Comparison of 1 and 10 cm^2 TableCurve 3D planar dose profile for mono-energetic electrons ($E \geq 1.0$ MeV) positioned at the center of a silver-water interface. The top layer is from the 10 cm^2 dose area.

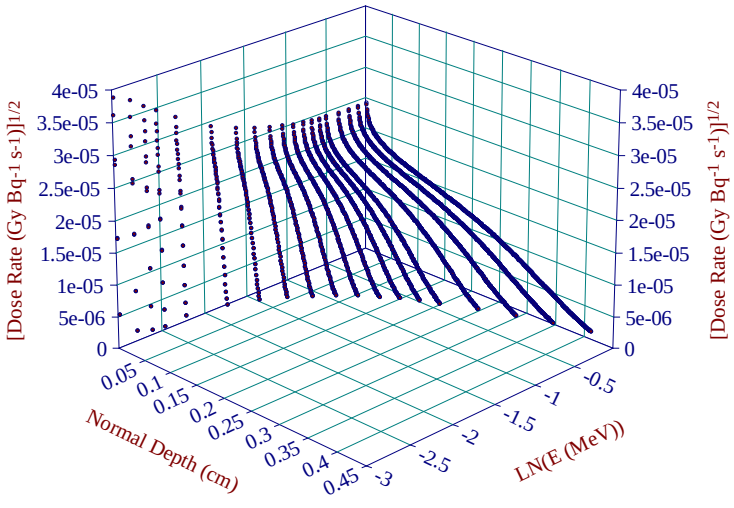

Fig. 5.49. Comparison of 1 and 10 cm^2 TableCurve 3D planar dose profile for mono-energetic electrons ($E \leq 1.0$ MeV) positioned at the center of an air-water interface. The top layer is from the 10 cm^2 dose area.

5.5.2 Point-Source Backscatter Correction Factors

To help demonstrate the validity and accuracy of the planar dose profiles used in calculating electron and beta-particle BSCF's, comparisons with the literature were made for dose averaging areas of 1 cm^2. As detailed in Section 2.5.2.1, the amount of air scatter correction data available is sparse (Cross 1991b, 1992c; Aydarous 2008). Cross' factors are very limited in their applicability. Firstly, he only defined them for a normal depth of 0.007 cm. When adopted by Durham (1992, 2006) for use in VARSKIN, modifications were made for other depths (as described in Section 2.5.2.1). Secondly, when Cross used the ACCEPT and CYLTRAN-P Monte Carlo transport codes (of the ITS family of codes) to develop his model, dose averaging areas were 100 cm^2. As explained previously, this results in an overestimation of backscattering in air, particularly at energies less than 2 MeV, and a subsequent underestimation in the correction needed when applied to smaller dose areas.

Comparisons can also be made to correction factors calculated by Aydarous (2008). Similar to Cross, Aydarous (using MCNP4) provided air scatter correction factors for normal depths of 0.007 cm only. However, data were provided for a 1 cm^2 dose area. The same modifications used by Durham in VARSKIN were applied here to Aydarous' data for comparisons with depth.

Beta-particle backscatter correction factors for an air-water interface geometry (1 cm^2 area) were calculated for a range of beta energies using the Chebyshev dose profile fits and Eq. (4.9). The results of the literature comparison are as expected (Fig. 5.50 - Fig. 5.53). At the normal depth of 0.007 cm, Aydarous' data shows close agreement with the model presented here, whereas Cross' data overestimates scattering effect of air. The close agreement at 0.007 cm, particularly with Aydarous' data, provides strong evidence of the model's ability to accurately calculate beta-particle point-source BSCF's for air scattering.

It should be noted that the depth adjustment used by Durham (1992, 2006) does provide a fairly accurate estimation of the BSCF at depths greater than 0.007 cm. For higher energy betas, such as ^{144}Pr (E_{av} = 1.217 MeV), the adjustment for depths less than 0.007 produced more inaccurate estimations as the BSCF was increased at shallower depths. The cause of this is not known and has not been discussed by Durham (2006). Also, Cross' data were only

adjusted for depths greater than 2.67 X/X_{99} and less than 224.29 X/X_{99}. Cross' BSCF is not defined for depths less than this value (Fig. 5.50). No such limitation was applied when adjusting Aydarous' data.

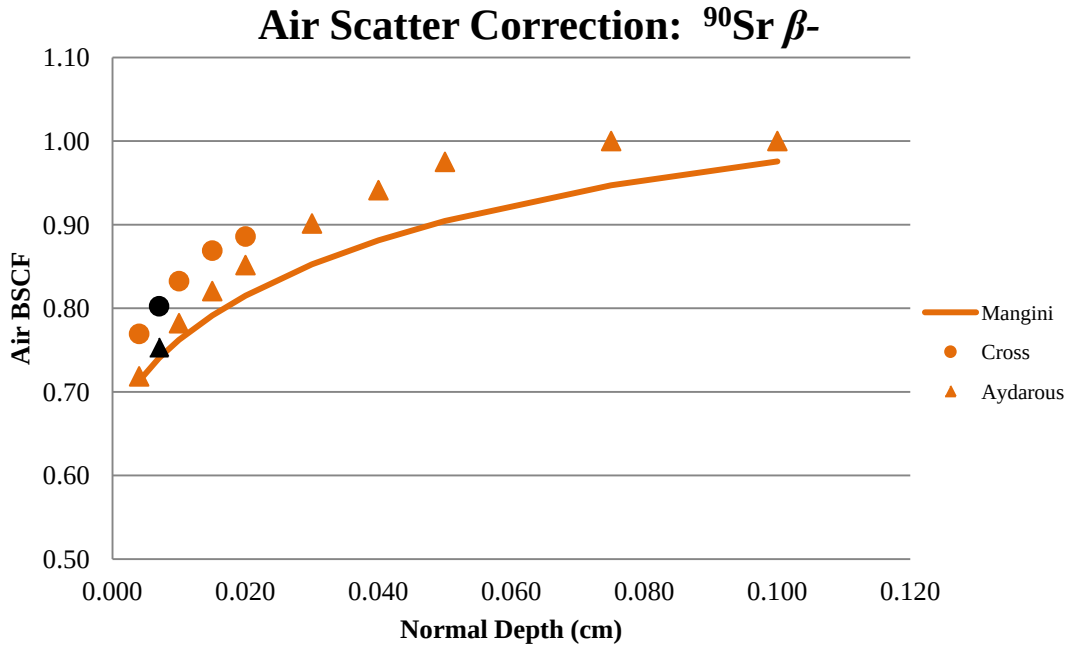

Fig. 5.50. Literature comparison of air BSCF for ^{90}Sr beta-particles. Black data points are at a normal depth of 0.007 cm. Average beta energy is 0.196 MeV.

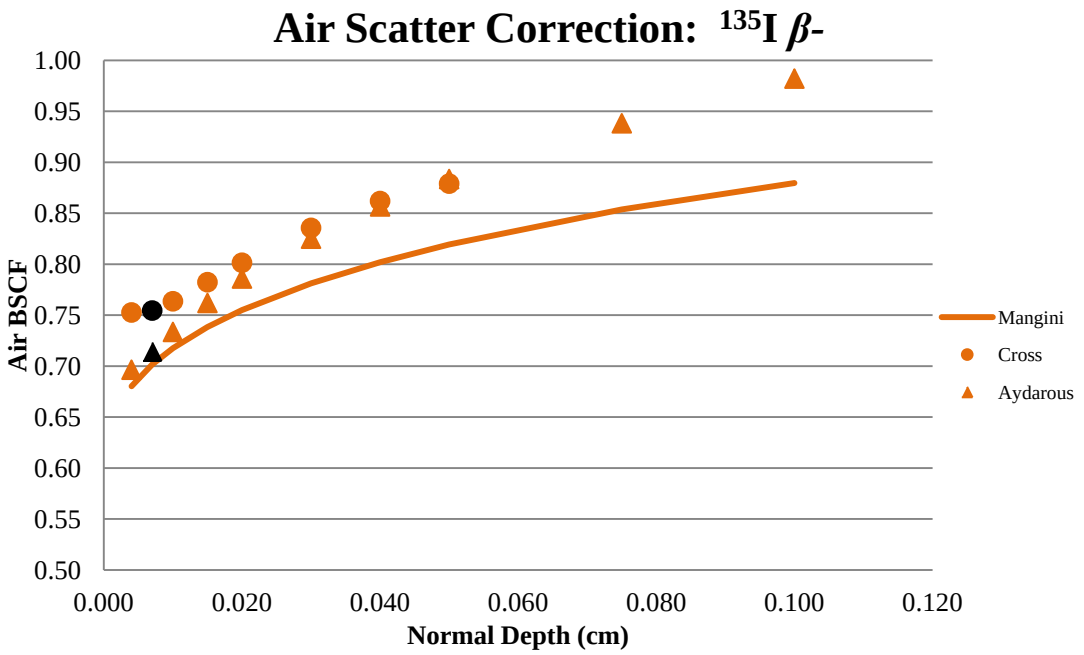

Fig. 5.51. Literature comparison of air BSCF for ^{135}I beta-particles. Black data points are at a normal depth of 0.007 cm. Average beta energy is 0.375 MeV.

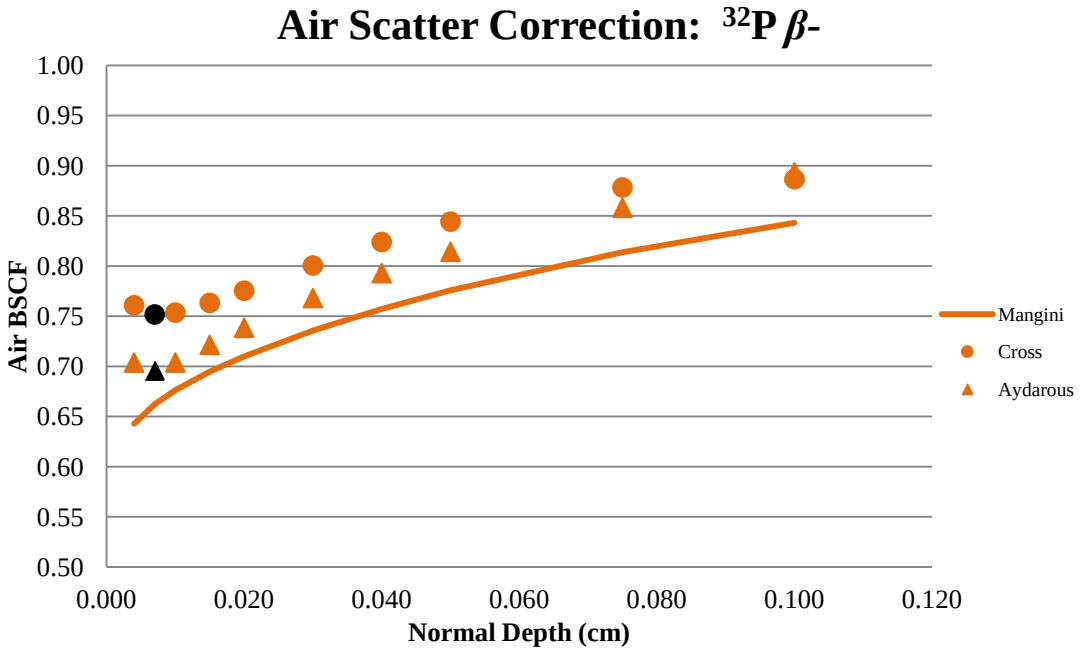

Fig. 5.52. Literature comparison of air BSCF for ^{32}P beta-particles. Black data points are at a normal depth of 0.007 cm. Average beta energy is 0.695 MeV.

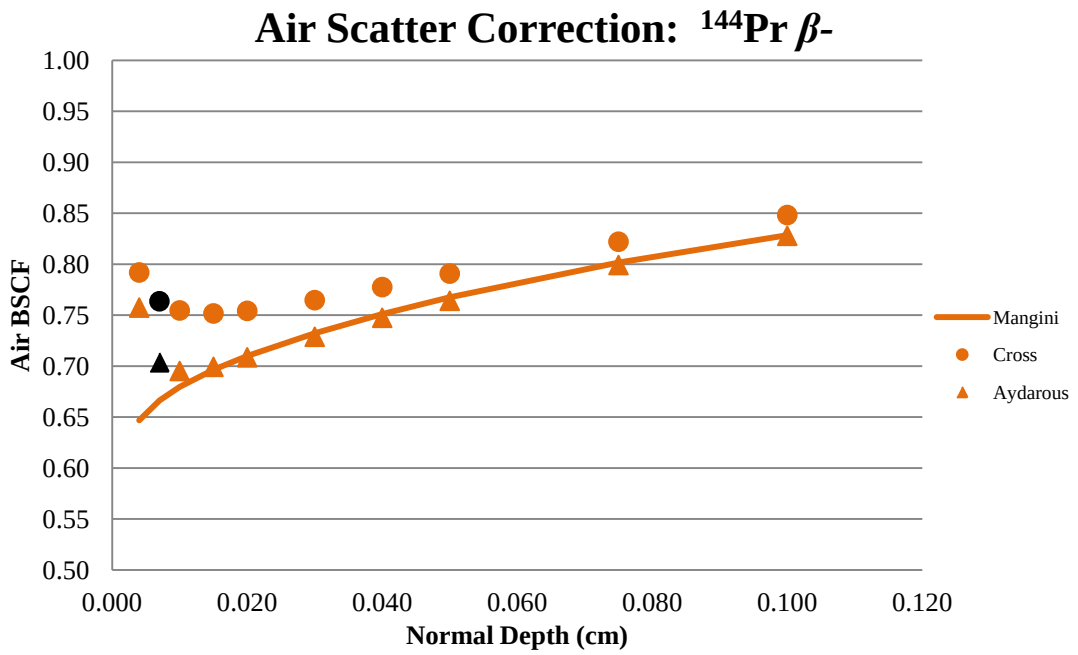

Fig. 5.53. Literature comparison of air BSCF for ^{144}Pr beta-particles. Black data points are at a normal depth of 0.007 cm. Average beta energy is 1.217 MeV.

Literature comparisons were also made for source scatter correction factors with both electron and beta-particle sources. As detailed in Section 2.5.2.2, Cho (1999) used EGS4 to examine the source BSCF for electron energies ranging from 0.1 to 3 MeV and scattering materials with Z of 13 to 78. The dose averaging area was 0.78 cm^2. Buffa (2004) preformed a similar study using EGSnrc in which he determined the backscatter factors over the same energy and Z. Unlike Cho however, Buffa chose his dose areas based on the CSDA range of the electron, where the radius of the dose averaging area was 10 times the CSDA electron range.

The 1 cm^2 model presented here agrees well with the literature for a range of scattering media at electron energies of 0.1 MeV (Fig. 5.54) and 0.5 MeV (Fig. 5.55). The largest discrepancies come from platinum (Z = 78), particularly at normal depths near the range of the electron. However, the maximum percent deviation with literature results was 6.15% (Cho, 0.5 MeV, Pt).

As Buffa (2004) demonstrated, if the range of the electrons is greater than the radius of the dose area, the backscatter factor will increase as the dose area is increased. This could explain the differences observed when comparing 1.0 MeV BSCF's for 1 cm^2 areas to Cho (1999) (Fig. 5.56). However, with a maximum percent deviation less than 5.0% and a difference in area of only 0.22 cm^2, the choice in Monte Carlo code or transport parameters are the more likely explanations (discussed in Section 2.5.2.2).

This is supported by a quick examination of predicted air and source (stainless steel) BSCF's for ^{60}Co and ^{144}Pr (Fig. 5.57, Fig. 5.58) with dose areas of 1 and 10 cm^2. Negligible differences are noted due to the relative difference between dose areas. Buffa's conclusion was based on dose-area radii of 0.00564cm and 0.0564 cm and an electron energy of 0.5 MeV (estimated range of 0.18 cm). A change in dose area radius of 0.564 cm to 1.784 cm for a ^{144}Pr beta-particle (estimated range of 1.25 cm) is not expected to make a noticeable difference in BSCF's.

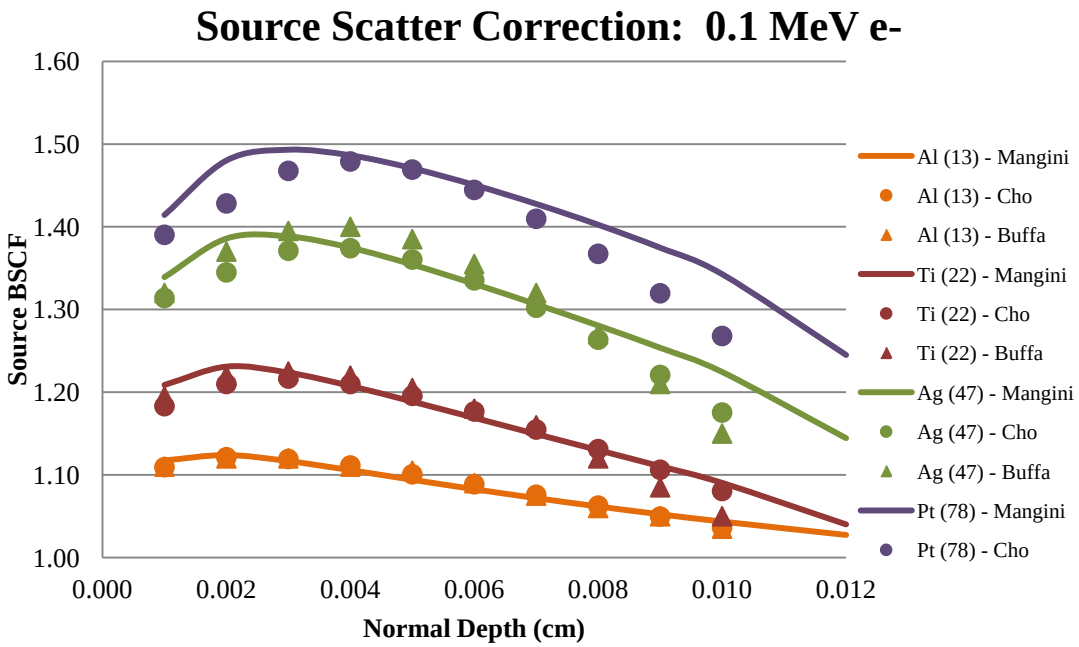

Fig. 5.54. Literature comparison of various source material BSCF's for 0.1 MeV electrons. Data for Cho and Buffa are plotted in their regions of validity.

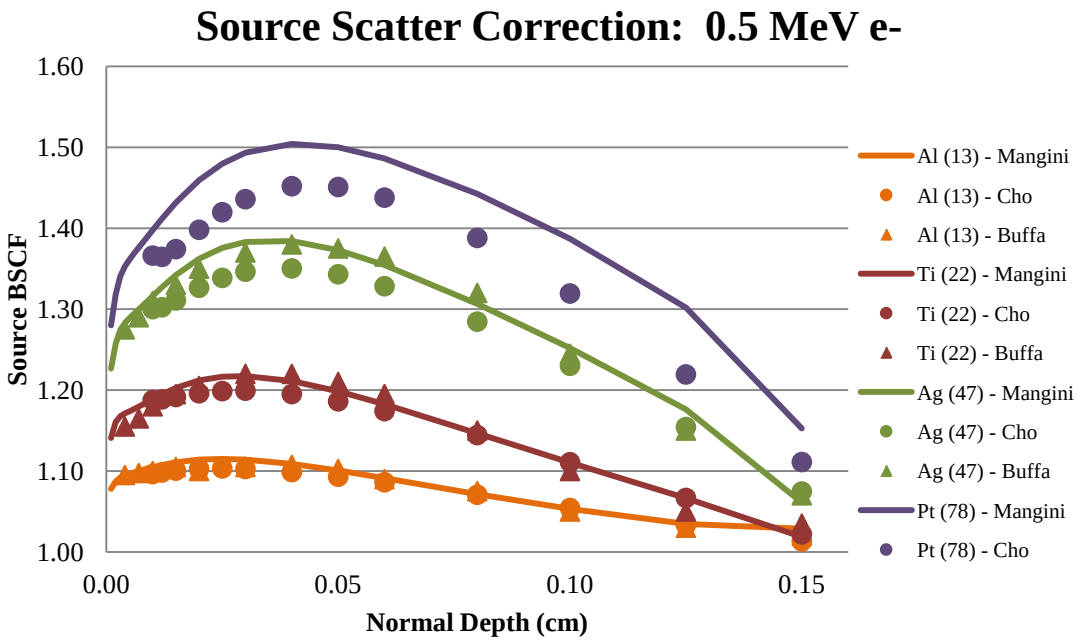

Fig. 5.55. Literature comparison of various source material BSCF's for 0.5 MeV electrons. Data for Cho and Buffa are plotted in their regions of validity.

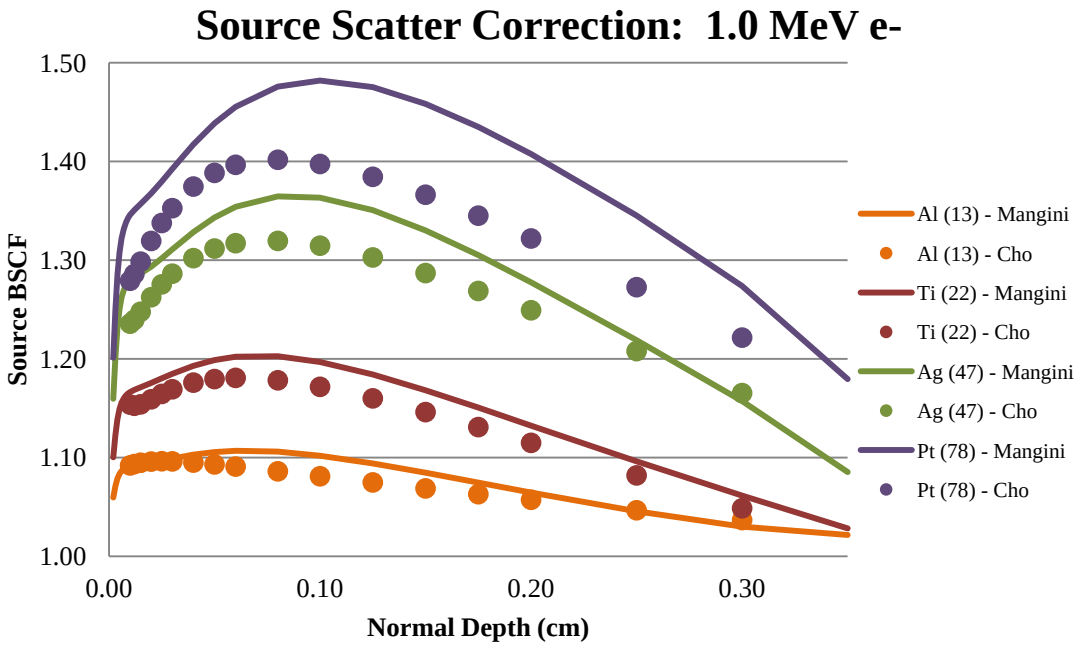

Fig. 5.56. Literature comparison of various source material BSCF's for 1.0 MeV electrons. Data for Cho is plotted in its region of validity.

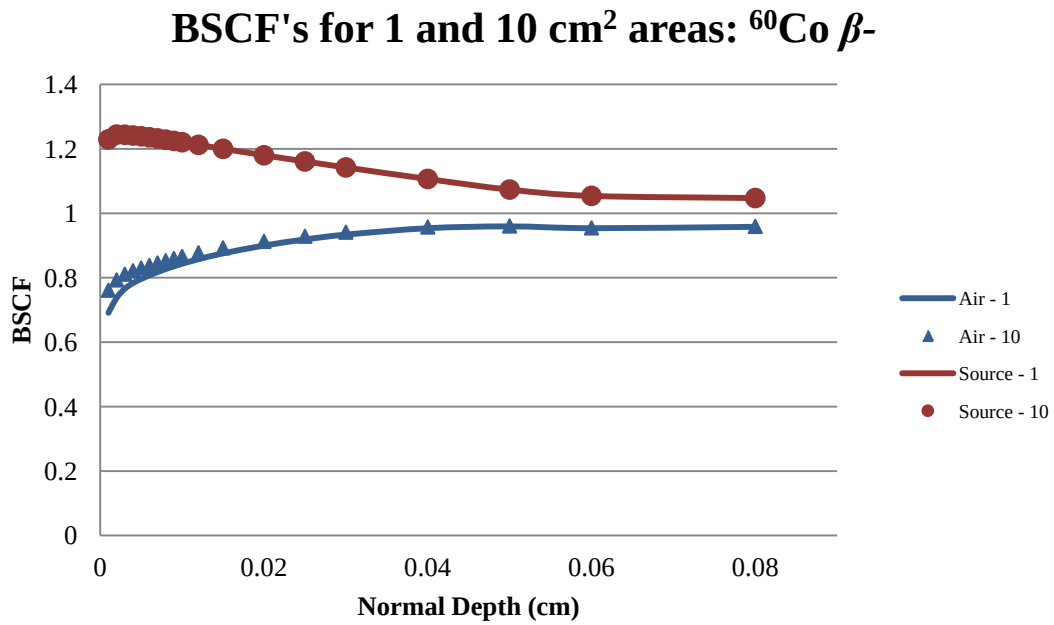

Fig. 5.57. Comparison of 1 and 10 cm^2 dose area BSCF's for ^{60}Co beta-particles. Source material is stainless steel.

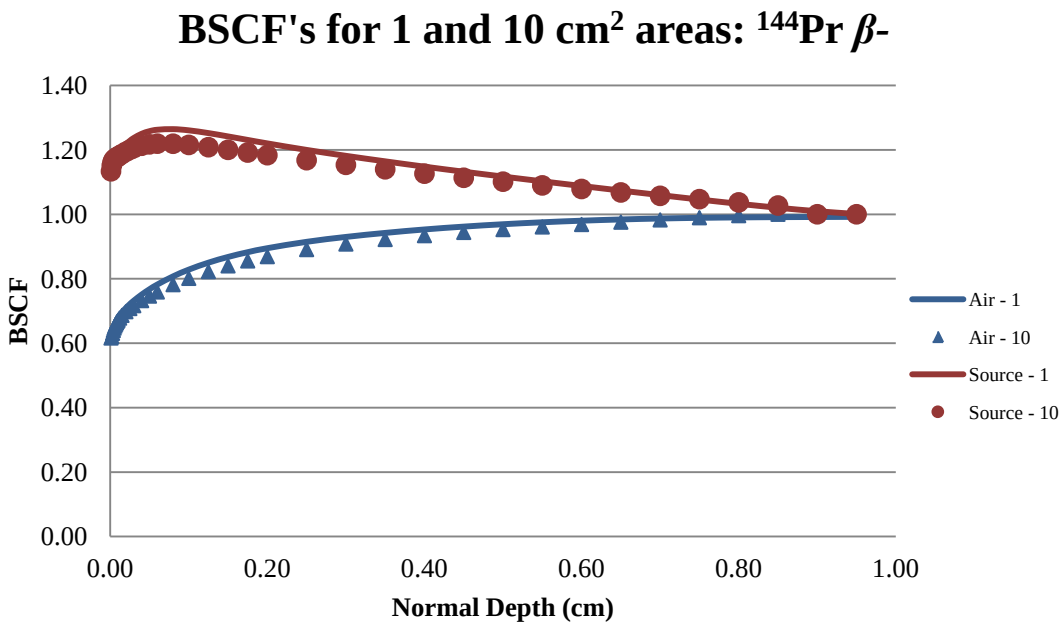

Fig. 5.58. Comparison of 1 and 10 cm^2 dose area BSCF's for ^{144}Pr beta-particles. Source material is stainless steel.

Lee (2004) used MCNP4 to determine beta backscatter factors directly (using defined beta-particle source) for ^{32}P, ^{90}Sr/^{90}Y, ^{45}Ca, ^{142}Pr, and ^{185}W for scattering materials with Z up to 78. Calculations were performed using the same geometrical setup as Cho (1999). Sample comparisons are made here using ^{45}Ca (E_{av} = 0.077 MeV), ^{142}Pr (E_{av} = 0.810 MeV), and ^{90}Sr/^{90}Y (E_{av} = 0.934 MeV). The scattering model results (Fig. 5.59 - Fig. 5.61) agree very well with the literature. The scattering media Z ranged from 8 (oxygen) to 78 (platinum). Once again, the largest discrepancy occurred at the end of the particle range for high-Z scattering media (9.5%, ^{45}Ca, W).

It is important to demonstrate successful interpolation in atomic number and the integration of mono-energetic electron planar dose profiles over a particular beta spectrum. As with the results with air scattering, the data presented here provide strong evidence of the model's ability to accurately calculate beta-particle point-source BSCF's for source scattering.

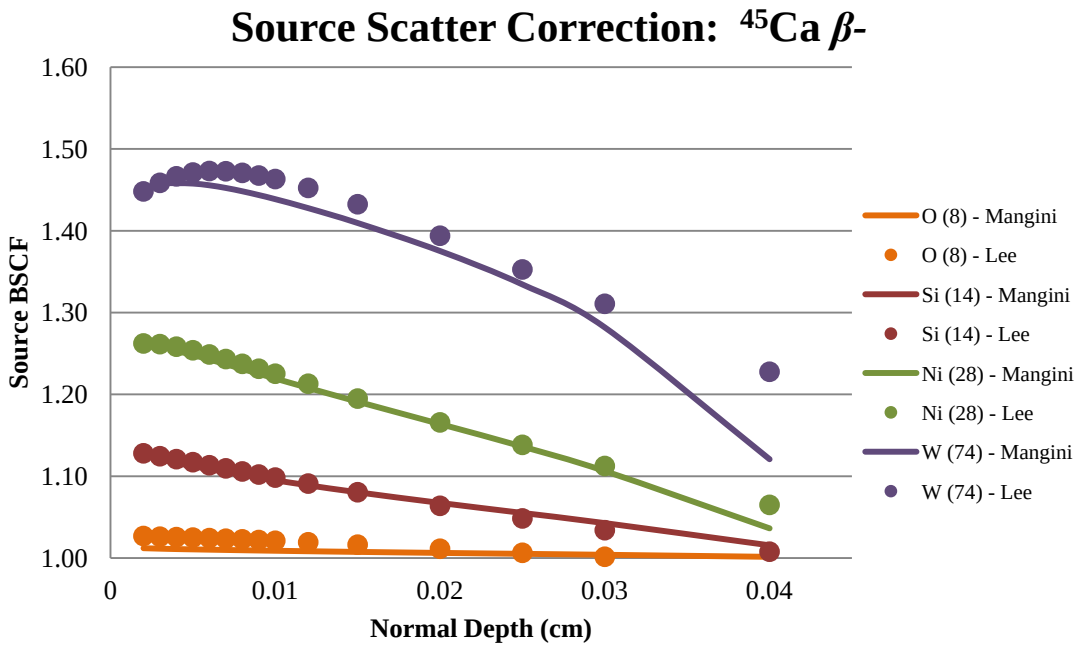

Fig. 5.59. Literature comparison of various source material BSCF's for ^{45}Ca beta-particles. Data for Lee is plotted in its region of validity.

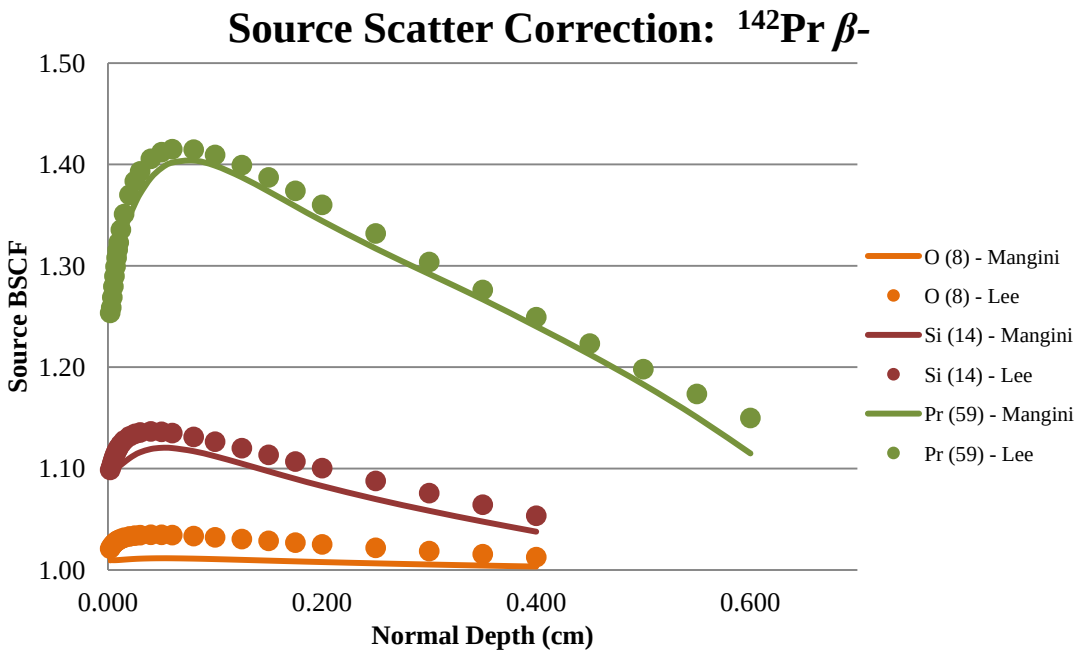

Fig. 5.60. Literature comparison of various source material BSCF's for ^{142}Pr beta-particles. Data for Lee is plotted in its region of validity.

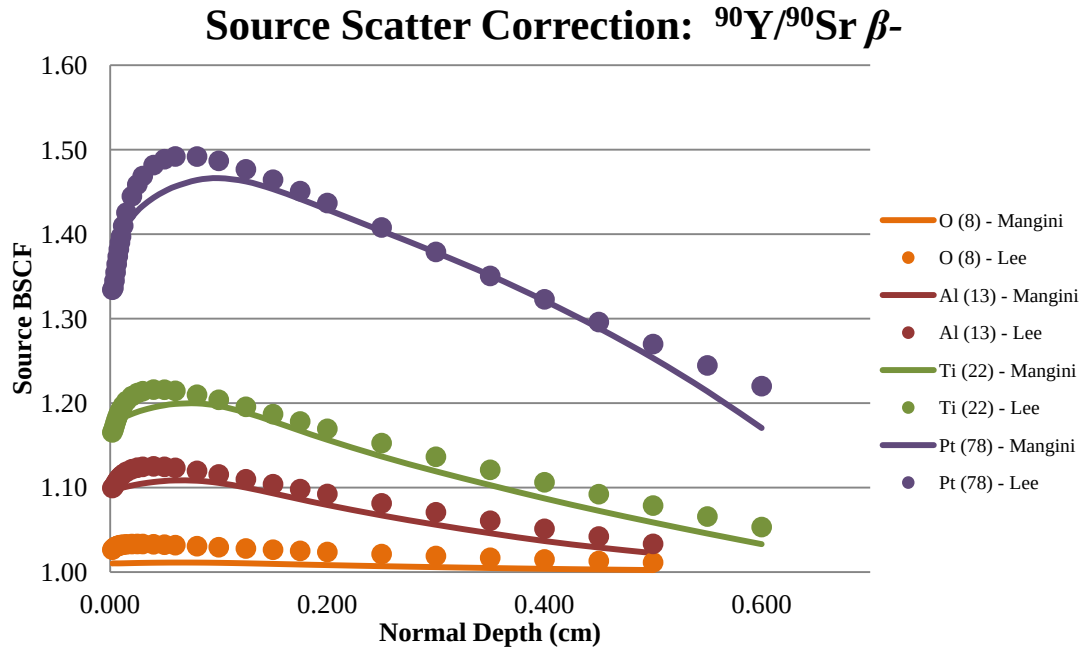

Fig. 5.61. Literature comparison of various source material BSCF's for ^{90}Y/^{90}Sr beta-particles. Data for Lee is plotted in its region of validity.

5.5.3 Scatter Medium Thickness

The intent of the scattering effectiveness study was to determine a simple equation that would estimate the fraction of complete backscatter contribution to dose when a finite amount of scattering material was present. In addition, the results can be used to analyze the effect of scattering contributions being cancelled out when scattering material is both directly above and directly below a given source-point (Fig. 4.8).

The depth-dependent scattering effectiveness for the selected beta-particle energy and scattering media combinations was determined at all scattering material thicknesses between 0.0001 and 1.5 X/X_{90}. Depth-dependence was eliminated by averaging over all depths for which the scattering effectiveness was defined (Fig. 5.62). Next, energy dependence was eliminated by taking the average over all beta-particle energies (Fig. 5.63). This allowed for a simple curve fit (R^2 = 0.9999), given by

$$SE(x) = \exp(2.766 + 1.082x - 3.861x^{1/2} + 0.843\ln(x)), \qquad (5.4)$$

where x is X/X_{90} for the scattering media.

The results from the scattering effectiveness study are in agreement with Buffa (2004). In order to have a complete backscatter contribution to dose, Buffa found the minimum thickness of the backscatter material to be about one third of the electron CSDA range. While the parameters of his study (electrons, CSDA range) vary from those used in the current study (beta-particles, X_{90}), comparisons can still be drawn. Given that the CSDA range of an electron in water is about 1.25 times larger than the X_{90} distance and that the X_{90} distance of a beta-particle is about 1.40 times larger than an electron of equal energy, the minimum thickness determined by Buffa can be approximated as 40 percent of the beta-particle X_{90} (as predicted in Fig. 5.63). This correlation will obviously vary with energy and scattering material. In fact, Buffa (2004) noted that the minimum thickness decreases slightly with increasing Z, and increases slightly with increasing electron energy. These dependencies were not examined in the study presented here.

The use of averages to eliminate both the slight depth and energy dependencies is deemed acceptable due to the amount of scattering cancellations that are expected to occur within a

given source. Other than points directly on the bottom or sides of the source, all source-points will experience a net source scattering contribution to dose. Integration over all source-points is likely to minimize errors introduced by the scattering effectiveness equation determined herein. The negligible differences observed in 1cm^2 and 10 cm^2 BSCF's (Fig. 5.57, Fig. 5.58) support the application of Eq. (5.4) to both dose averaging areas.

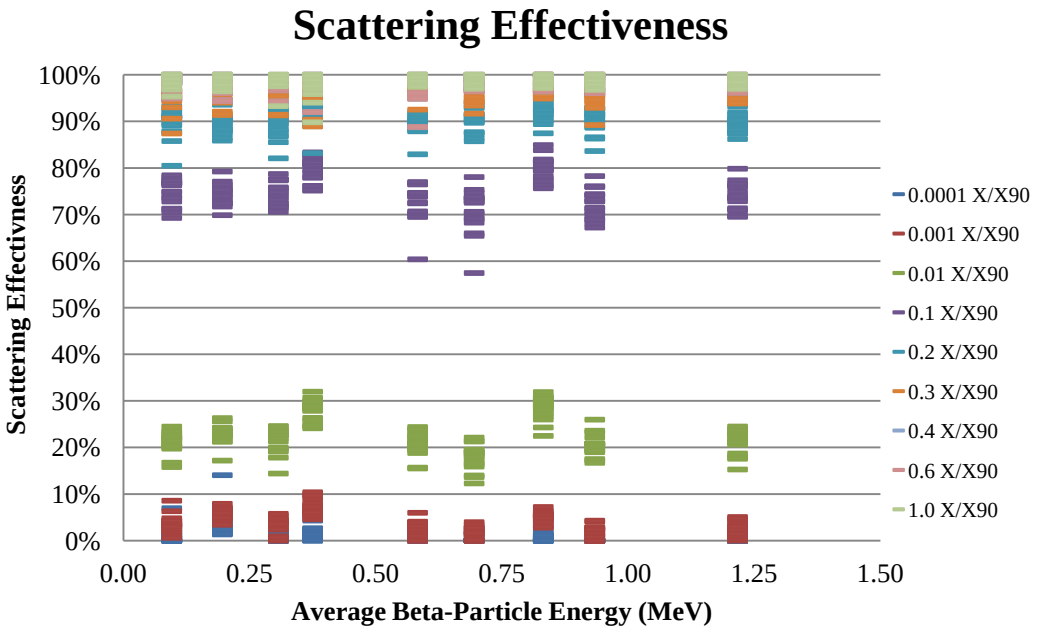

Fig. 5.62. Scattering effectiveness for all scattering materials as a function of average beta-particle energy. Data at each scattering medium thickness is averaged over all normal depths up to 1.0 cm. Dose averaging area is 1 cm^2.

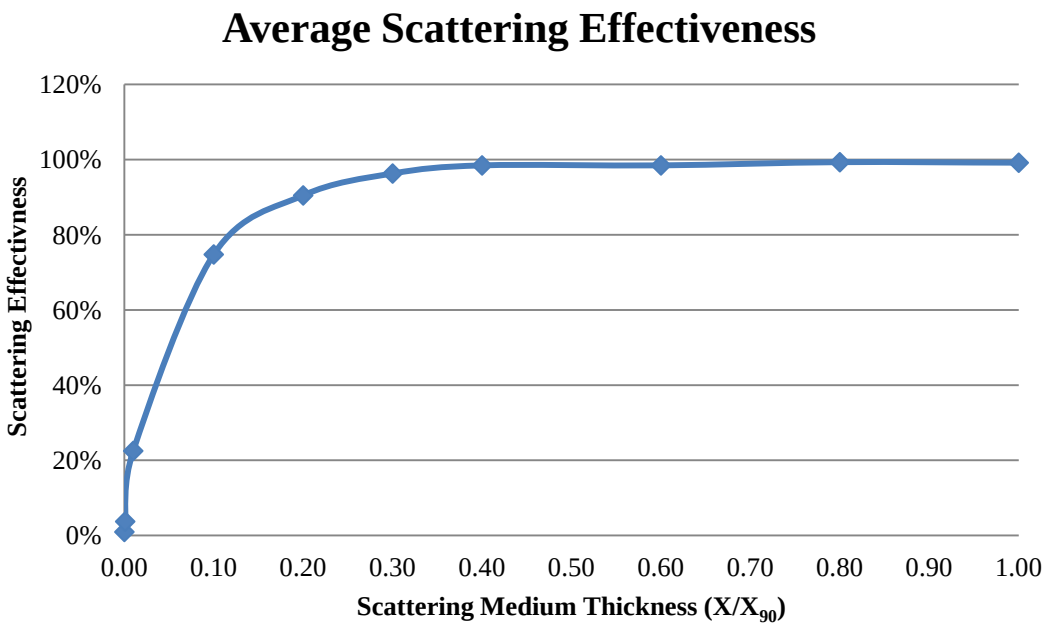

Fig. 5.63. Scattering effectiveness as a function of scattering medium thickness. Data is first averaged over all normal depths up to 1.0 cm, then over all beta-particle energies tested.

5.5.4 Volumetric Backscatter Correction

Given the number of variables, determining curve fits for volumetric BSCF's is extremely difficult, if at all possible. As a result, the volumetric backscatter model is intended for direct implementation into numerical integration process of deterministic computer codes such as VARSKIN 4 (Traub 1987; Durham 1992, 2006; Hamby 2011) and K-SKIN (Park 2009). To demonstrate the end result of model implementation, VARSKIN 4 was used to calculate volumetric BSCF's for the same nuclides and source materials as the non-homogeneous DPK's presented in Section 5.4. This was accomplished by taking the appropriate ratio of dose with and without the scattering model applied. Source geometries were cylinders (Fig. 5.64(a)), slabs (Fig. 5.65(a)), and spheres (Fig. 5.66(a)). There were 5 different source dimensions used with the smallest being 0.0005 cm and the largest being 0.05 cm (Table 4.5). Point-source BSCF's for both air and source scattering are also provided as reference points. The dose averaging area was 1 cm^2 in all cases.

In general, the smaller sources (sizes 1-3) tend to deviate little from the point-source BSCF for air. Source scattering only becomes a dominate factor for large sources (size 5) with high-energy beta-particles and high-Z source materials ((Fig. 5.66(a)). On the same hand, these observations are expected however as internal source-points for smaller sources will contribute significantly to the overall dose. These points are likely to experience a cancellation effect with regard to source scattering, while experiencing little decrease in the amount of applied air scattering corrections. On the other hand, source-points near the bottom or sides of larger sources will be the main contributors to the overall dose as beta-particles emitted near the center or top of the source are attenuated before they reach the tissue volume. Cancellation effects at these points are not expected to be as severe as the latter and will therefore provide a larger source scattering component to the volumetric BSCF.

Comparison with the literature is difficult as the only volumetric BSCF data available (Durham 2006) is very limited in applicability (as explained in Section 2.5.2.2). Durham's data is only defined for a normal depth of 0.007 cm, accounts only for air scattering from the top of the source (neglects sides), and ignores contributions to dose from source scattering. Despite these limitations, Durham's results (Fig. 5.64(b) - Fig. 5.66(b)) are plotted for applicable source sizes ($0.05X_{99} \leq \Delta t_{source} \leq X_{99}$).

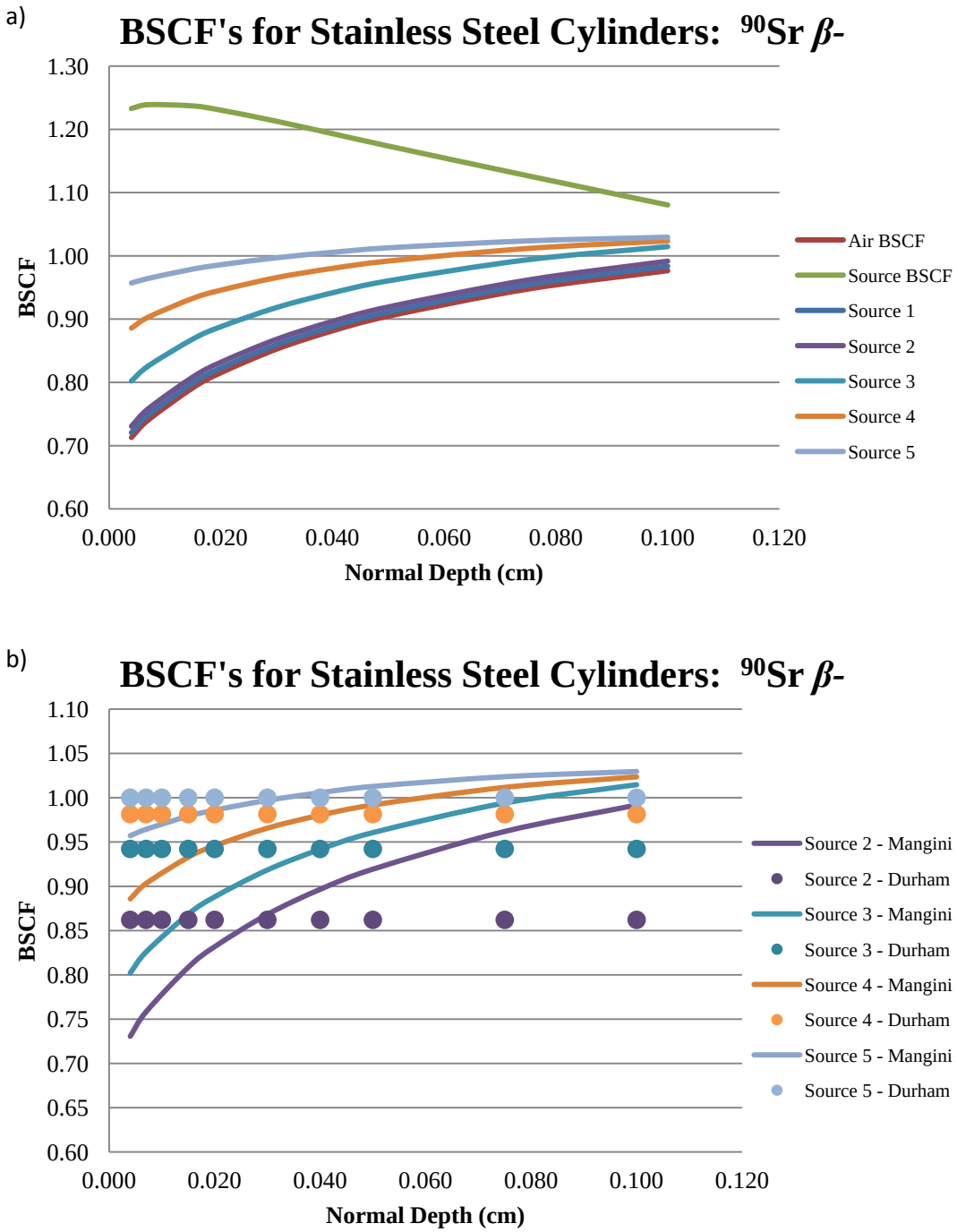

Fig. 5.64. (a) Volumetric ^{90}Sr BSCF's for a range of stainless steel cylindrical-source sizes. (b) Literature comparison of volumetric ^{90}Sr BSCF's for a range of stainless steel cylindrical-source sizes

a)

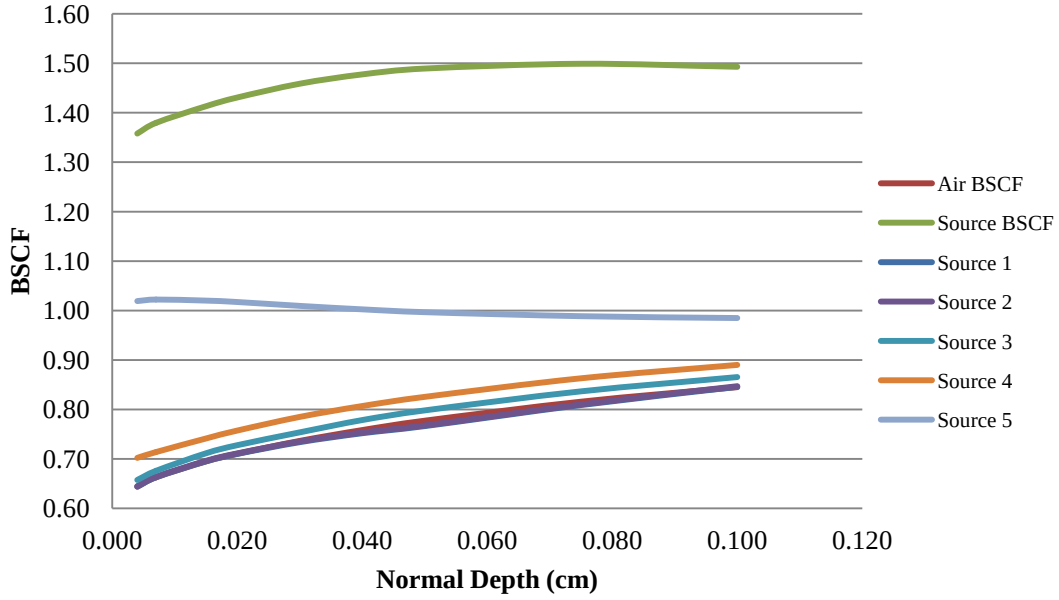

b)

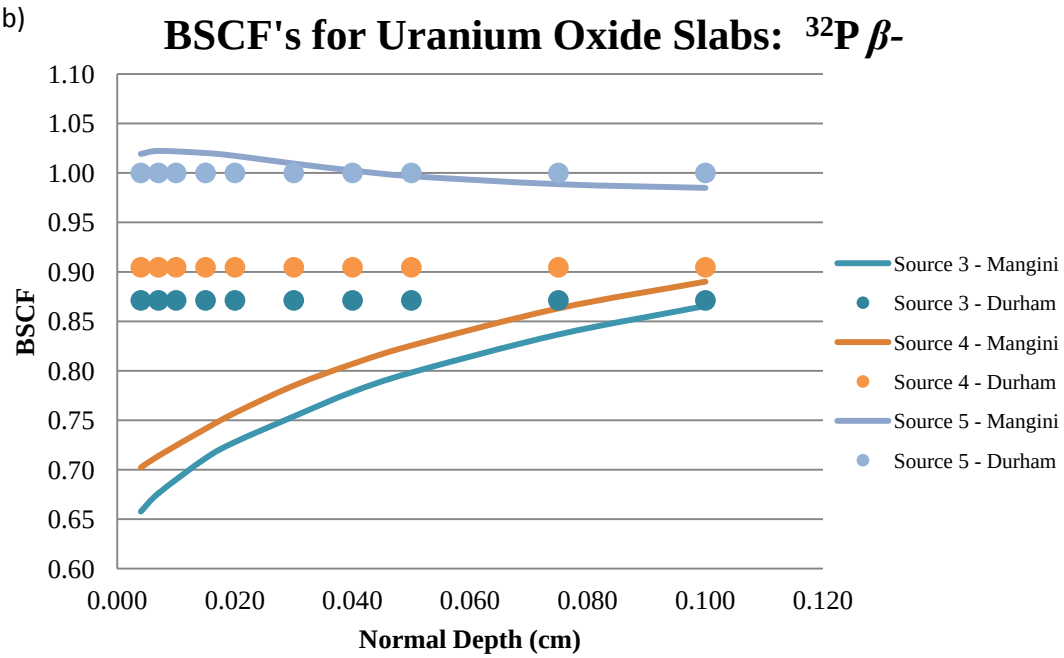

Fig. 5.65. (a) Volumetric ^{32}P BSCF's for a range of uranium oxide slab-source sizes. (b) Literature comparison of volumetric ^{32}P BSCF's for a range of uranium oxide slab-source sizes

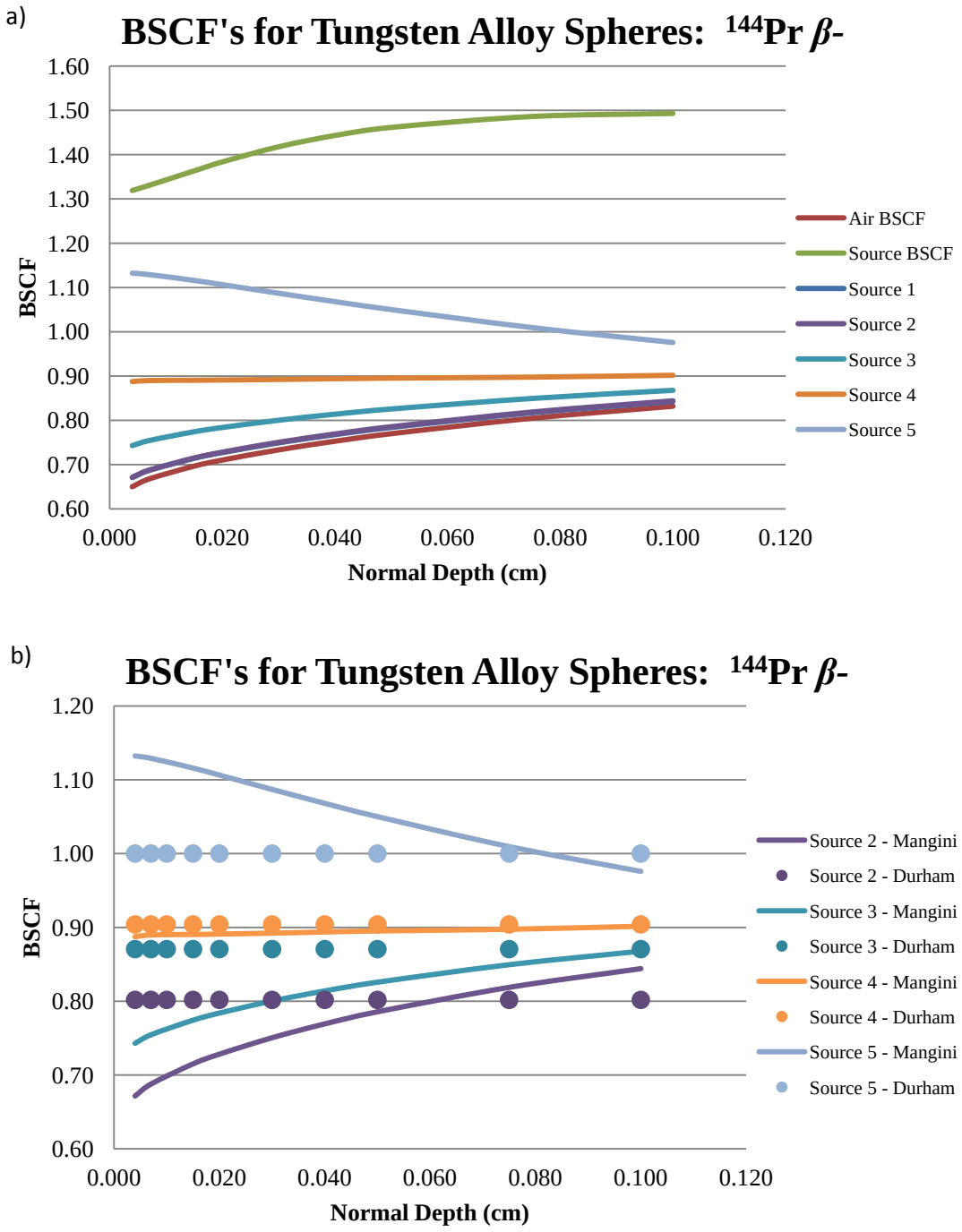

Fig. 5.66. (a) Volumetric ^{144}Pr BSCF's for a range of tungsten alloy spherical-source sizes. (b) Literature comparison of volumetric ^{144}Pr BSCF's for a range of tungsten alloy spherical - source sizes

5.6 Model Verification with Hot Particle Dosimetry

5.6.1 Overall Hot Particle Dosimetry Results

The verification study detailed in Section 4.7 produced outstanding results overall. This is easily observed by plotting the percent deviation with respect to EGSnrc simulations for all water depths, source sizes, source materials, and beta-particles tested for both 1 cm^2 (Fig. 5.67(a)) and 10 cm^2 (Fig. 5.67(b)) dose areas. The results demonstrate the overall model accuracy for both 1 and 10 cm^2 dose averaging areas with nearly all data points within a ±20% deviation with EGSnrc, and a majority within ±10%. The largest deviations were at depths near the end of low-energy beta-particle ranges. Error bars can be calculated using Eq. (5.5), however, given the number of data points in each plot (~10,000), they would be rendered useless. A more detailed analysis and literature comparison was performed by examining specific source material and beta-particle dose estimates.

Literature comparisons were made by running VARSKIN 4 with Cross' (1967, 1968, 1982, 1992a) scaling model, simple density scaling, Cross' (1991b, 1992c) point-source air scatter model, and Durham's (2006) volume-source air scatter model. As noted in Section 2.6, VARSKIN 4 uses simple density scaling by setting Cross' scaling factor (η_w) equal to unity for all materials. The scaling factors for the three test materials (provided in Section 5.4) were imported into VARSKIN 4 when making comparisons to Cross' scaling model.

Examining the percent deviations with respect to source material (Fig. 5.68 - Fig. 5.70) demonstrates a dramatic improvement as source Z is increased. The largest improvement over Cross' (scaling and scattering) and Durham's models occurs with uranium oxide (ρ=10.96 g cm^{-3}, Z_{eff} =87.88). This is not surprising given the limitations of Cross' scaling model and the non-homogeneous DPK results provided in Section 5.4. Deviations between Cross' model and EGSnrc non-homogeneous DPK's became greater as Z was increased. While the use of density scaling reduced these deviations, density-scaled DPK's still produce dose calculations that are significantly more off target than the new models (Fig. 5.69(a), Fig. 5.70(a)). Further examination of dose results is carried out in the next section using individual sources.

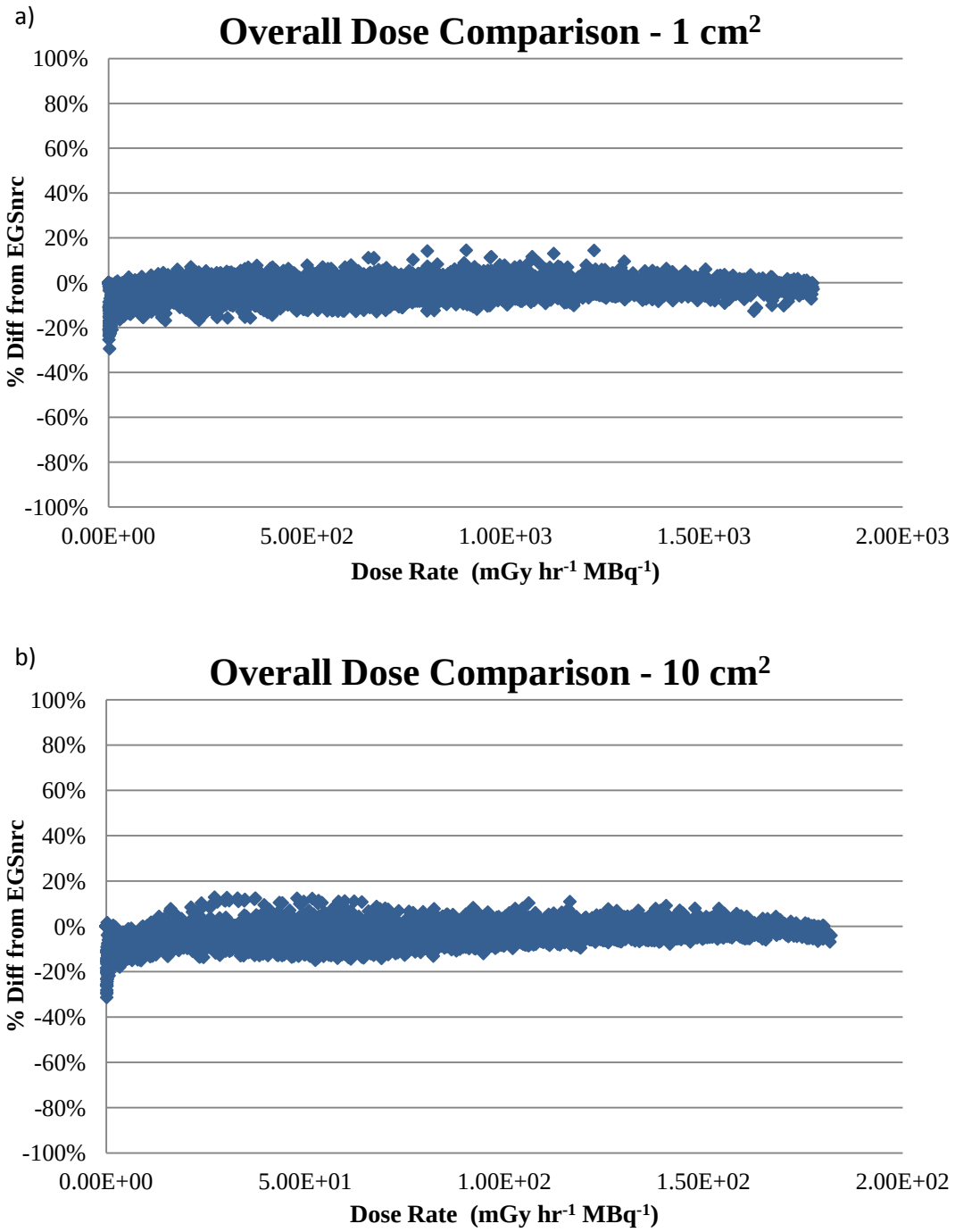

Fig. 5.67. (a) Percent deviation with respect to EGSnrc simulations for all 1 cm^2 (a) and 10 cm^2 (b) data points of model verification.

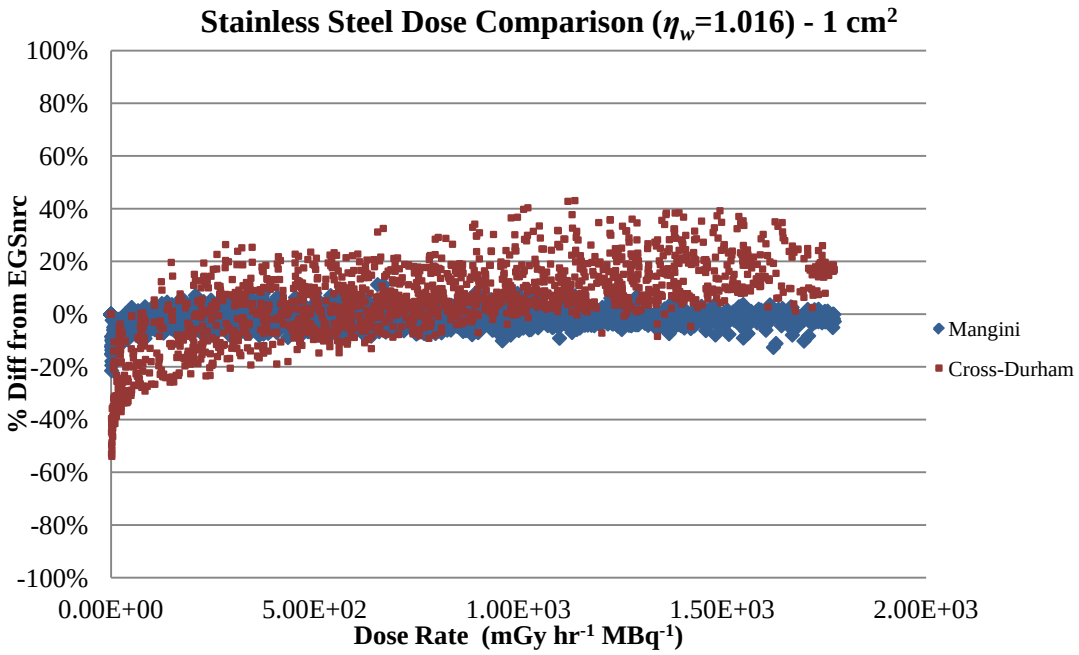

Fig. 5.68. Percent deviation with respect to EGSnrc simulations for all stainless steel (Z_{eff} of 25.81) dose points.

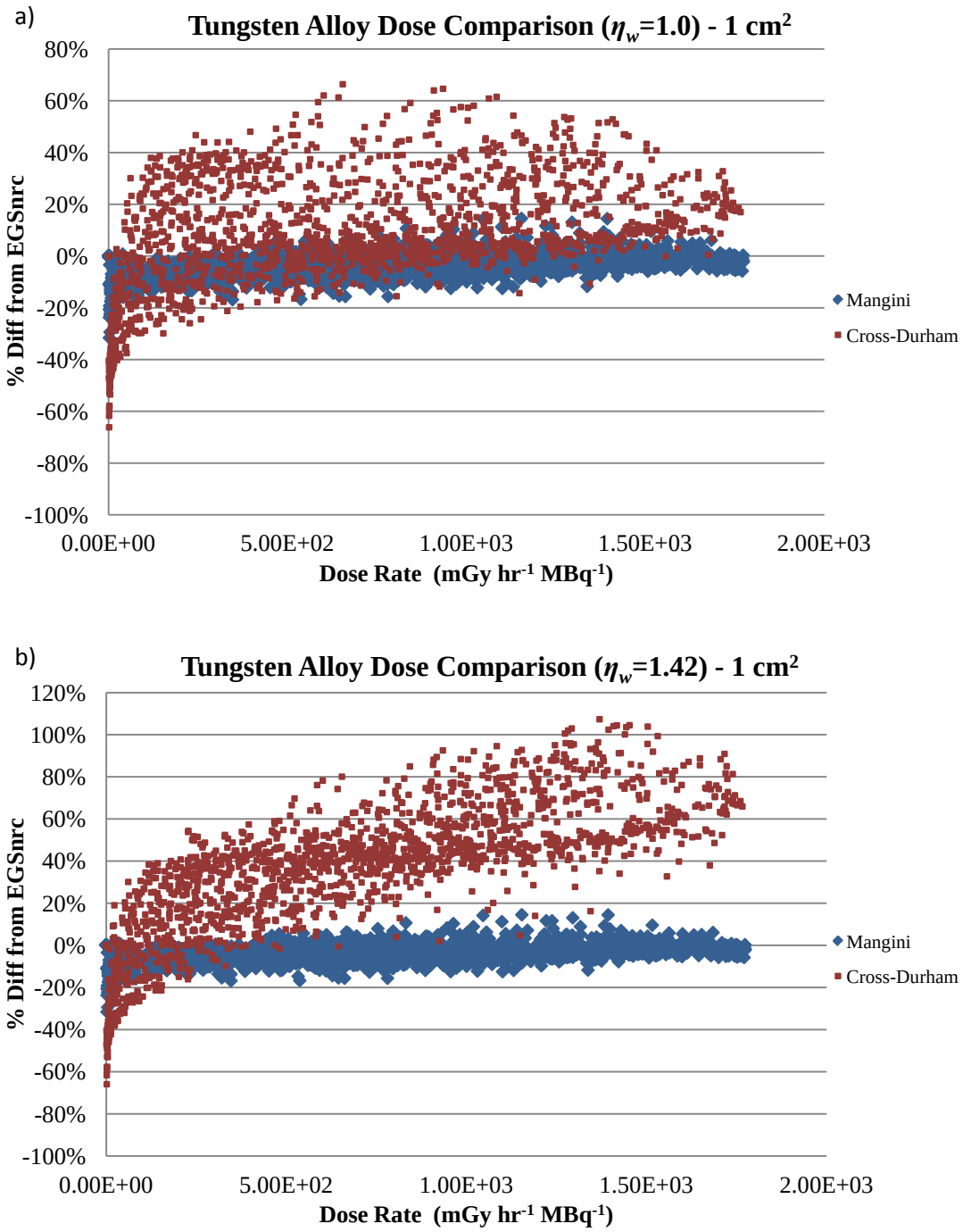

Fig. 5.69. Percent deviation with respect to EGSnrc simulations for all tungsten alloy (Z_{eff} of 72.79) dose points with (a) density scaling and (b) Cross scaling.

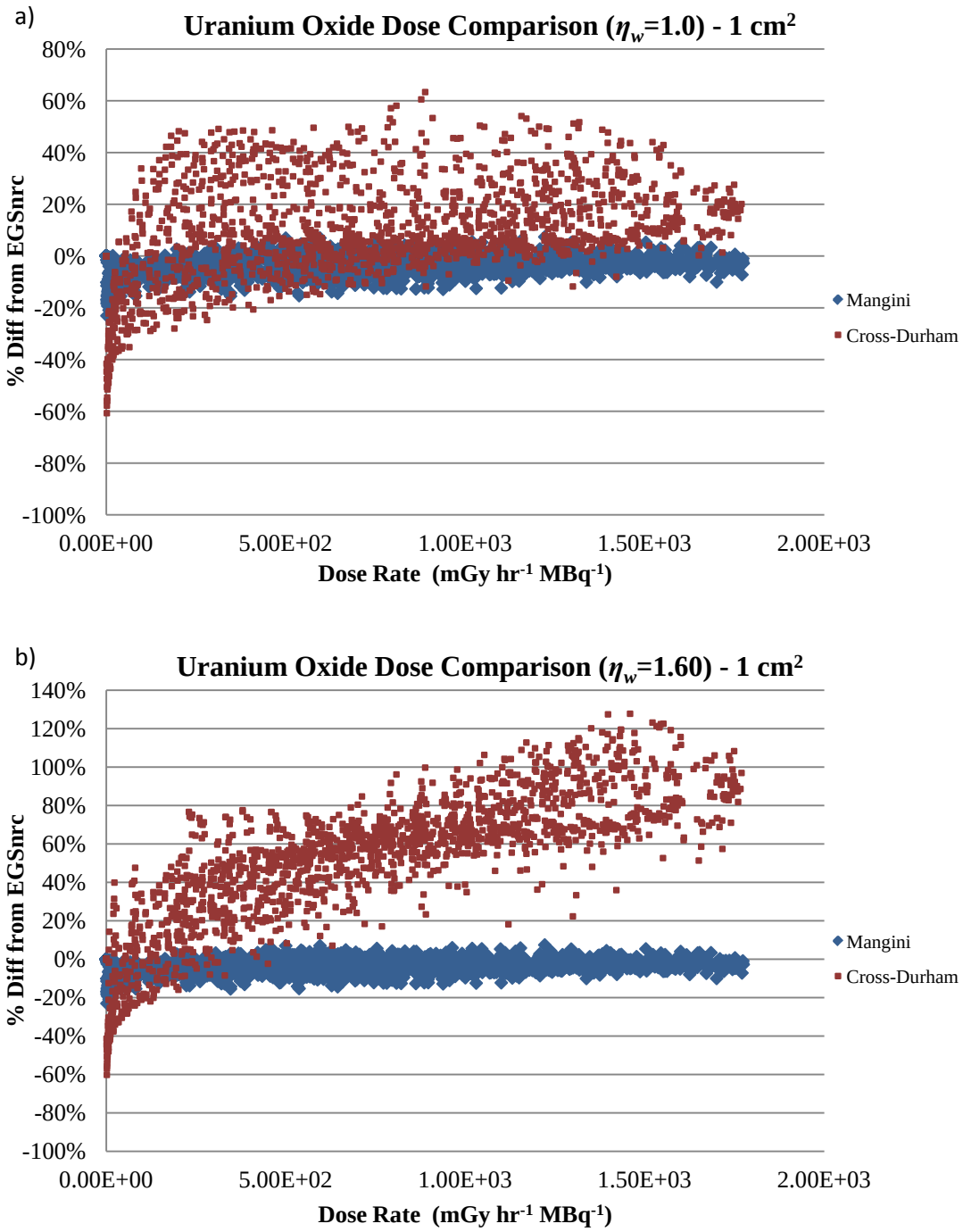

Fig. 5.70. Percent deviation with respect to EGSnrc simulations for all uranium oxide (Z_{eff} of 87.88) dose points with (a) density scaling and (b) Cross scaling.

5.6.2 Individual Hot Particle Dosimetry Results

Dose calculations for the beta-particles and source materials/geometries analyzed in Sections 5.4 and 5.5.4 are presented here (Fig. 5.71- Fig. 5.80). Source sizes 1, 3, and 5 were chosen to cover the range of tested source dimensions. Error bars for EGSnrc dose rates were found by multiplying relative errors by their corresponding dose rate. Error bars for percent deviations were found using error propagation of the percent deviation equation, given by

$$\sigma_u = \frac{x}{y^2}\sigma_y, \tag{5.5}$$

where u is percent deviation, x is the VARSKIN 4 dose rate, and y is the EGSnrc dose rate. The error associated with the deterministic calculation of VARSKIN 4 is unquantifiable and assumed to be zero. Non-visible error bars are smaller than their respective data-point markers.

When comparing dose calculations, it is difficult to attribute discrepancies with EGSnrc to the choice of scaling model or the choice of scattering model. Close comparison with the scaling model results presented in Section 5.4 and the scattering model results presented in Section 5.5.4 reveal that the pattern of improvements follows those of both models. Despite the overall close agreement between the Cross-Durham models and the models presented here for the relatively low-Z stainless steel source material, discrepancies can be traced back to the scaling and scattering models.

The Cross-Durham percent deviations for ^{90}Sr stainless steel cylinders of source sizes 3 and 5 (Fig. 5.72, Fig. 5.73) follow the same pattern demonstrated in comparable non-homogeneous DPK's (Fig. 5.20 - Fig. 5.23). The non-homogeneous DPK's presented an overestimation of energy deposition at shallow depths and an underestimation at deeper depths. While integration over a particular dose plan will incorporate contributions from both instances, dose at shallow depths will be dominated by small source-point to dose-point distances and will therefore demonstrate an overestimation of dose. Dose at deeper depths demonstrates an underestimation of dose, as these smaller source-point to dose-point distances are not present in the integration process.

Examination of the applicable BSCF's reveals a similar pattern (Fig. 5.64). Durham underestimates the BSCF at shallow depths and overestimates it at deeper depths for source sizes 3 and 5. This will result in an overestimation of dose at shallow depths and an underestimation at deeper depths. This analysis assumes that the scattering model presented here more accurately predicts the nature of volumetric BSCF's.

Despite the relatively low-*Z* of stainless steel, the new models are seen as an improvement over their respective counterparts in the literature and produce slightly better dose result, particularly for source sizes 1 and 3 where percent deviations are within ±10%. The maximum deviation of -15% (with an error of ±4.09%) is found at the deepest depth for size 5. Assigning this deviation to a particular model is difficult and is seen as unnecessary given the magnitude of the dose at this depth (2 orders of magnitude lower than the shallowest depth). Doses of this magnitude produce the largest underestimations for all cases tested here (Fig. 5.67) and are likely due to the nature of Monte Carlo transport codes versus deterministic codes.

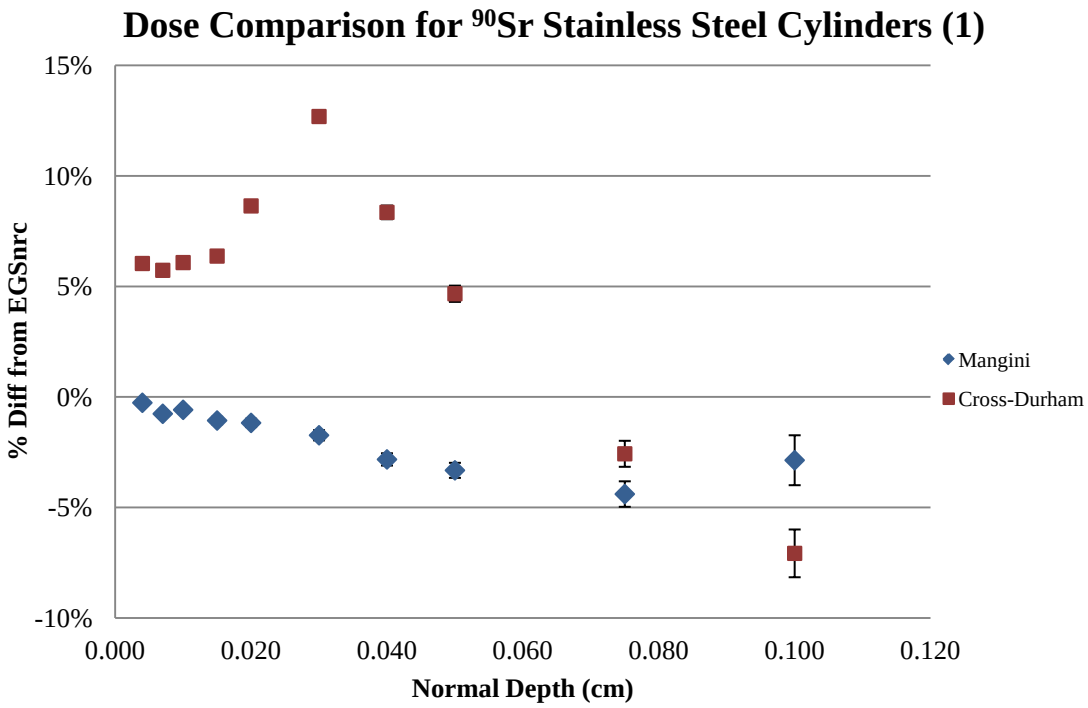

Fig. 5.71. Percent deviations with respect to EGSnrc for ^{90}Sr stainless steel cylinders of source size 1. Cross-Durham uses η_w = 1.016.

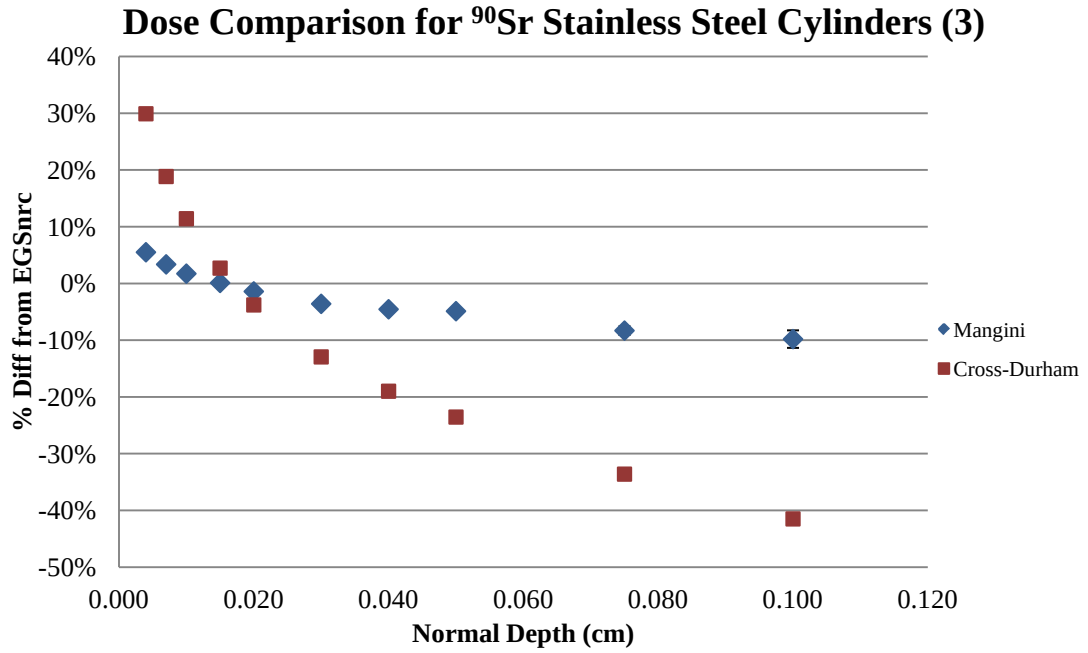

Fig. 5.72. Percent deviations with respect to EGSnrc for ^{90}Sr stainless steel cylinders of source size 3. Cross-Durham uses η_w = 1.016.

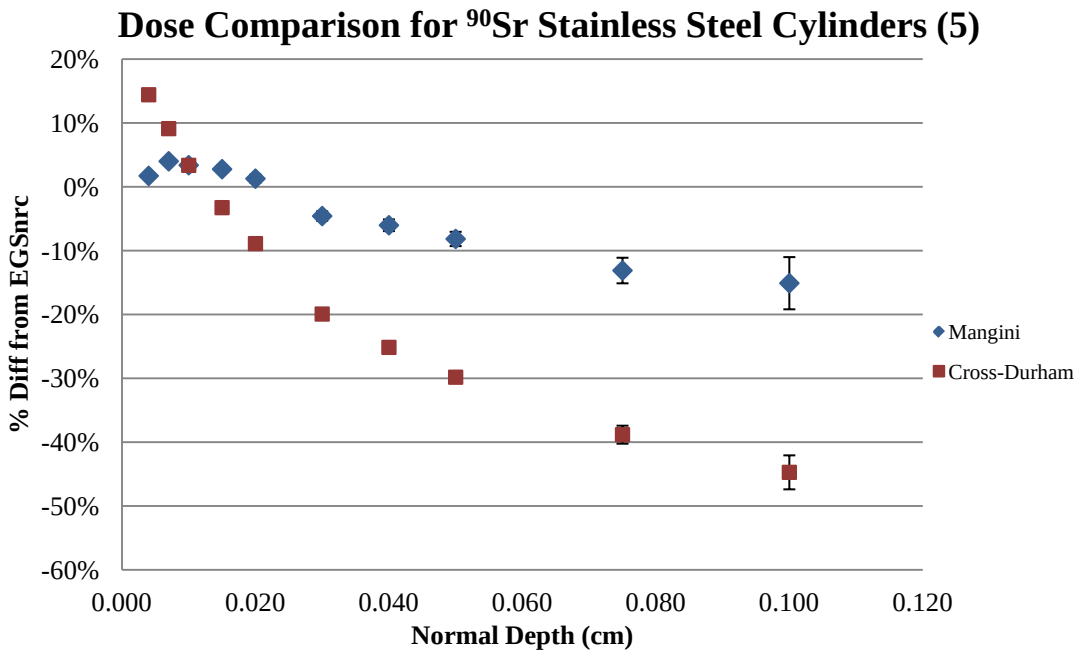

Fig. 5.73. Percent deviations with respect to EGSnrc for ^{90}Sr stainless steel cylinders of source size 5. Cross-Durham uses η_w = 1.016.

The percent deviations for ^{32}P uranium oxide slabs and ^{144}Pr tungsten alloy spheres are all within ±10% for the new scaling and scattering models. While this is similar to the results presented above for ^{90}Sr stainless steel cylinders, comparisons with the Cross-Durham models highlight the significantly improved accuracy of these new models. The use of density scaling is denoted by a η_w of 1.00 in the plot legend.

When the source material Z is increased from 25.81 (stainless steel) to 72.79 (tungsten alloy) and 87.88 (uranium oxide), the improvements in dose calculations become more evident at shallow depths (Fig. 5.74 - Fig. 5.80). The increase in average beta-particle energy (^{90}Sr = 0.196 MeV, ^{32}P = 0.695 MeV, and ^{144}Pr = 1.217 MeV), particularly for smaller sources, contributes to the overestimation of dose for the Cross-Durham models. These two aspects are discussed in more detail below using ^{32}P uranium oxide slabs. The change in source geometry from cylinders to slabs and spheres causes minor differences in dose calculations and will therefore not be addressed here. Such differences are discussed in the next section.

Dose calculations for source size 1 (Fig. 5.74) clearly demonstrates the results of the new scaling model's ability to properly account for spectral hardening and more accurately predicts non-homogeneous DPK's. Ultimately, Cross' scaling model greatly overestimates the DPK at shallow depths for small sources which directly correlates to a significant overestimation in dose. This effect is obviously less prominent for density scaling given the more accurate non-homogeneous DPK predicted by that model. The non-homogeneous DPK for a 0.10 X/X_{90} radius absorption sphere (Fig. 5.75) is provided to illustrate the effect of further decreasing the absorption-sphere radius (beyond the 0.30 value of Fig. 5.24). Density scaling produces a significantly more accurate DPK while Cross' scaling only slightly improves. Density-scaled non-homogeneous DPK results at smaller radii are expected to follow a similar pattern of improvement until a homogeneous geometry is finally reached. Cross-scaled DPK's will always show a significant overestimation when source material is present given its method of application. Since the X_{90} of a ^{32}P beta-particle is 0.363 cm, the overestimation is seen at all normal depths ($\leq$ 0.10 cm). The new model provides a nearly perfect fitting non-homogeneous DPK and a significantly more accurate dose estimation.

In terms of scatter corrections, source size 1 is approximated as a point-source by Durham and therefore does not apply a BSCF. However, as discussed in Section 4.6.2, Cross' point-source correction factors for air scattering slightly underestimates the needed correction at smaller dose areas as it is based on a 100 cm^2 dose area. Resulting deviations in dose estimates will be negligible when compared to scaling model deviations.

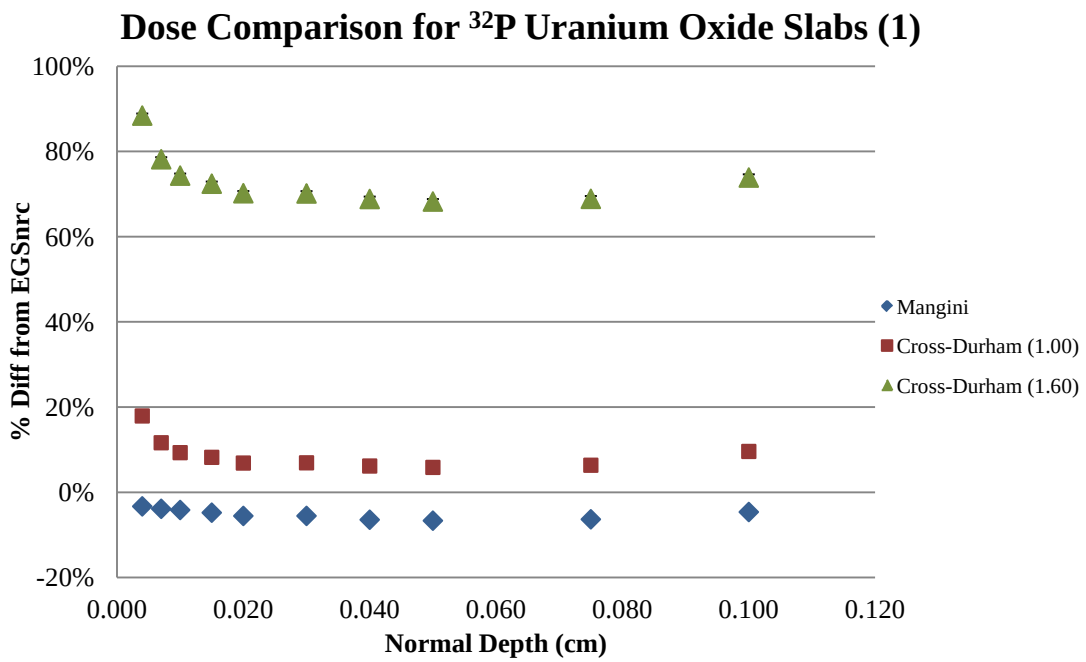

Fig. 5.74. Percent deviations with respect to EGSnrc for ^{32}P uranium oxide slabs of source size 1. η_w is provided in parenthesis in the legend.

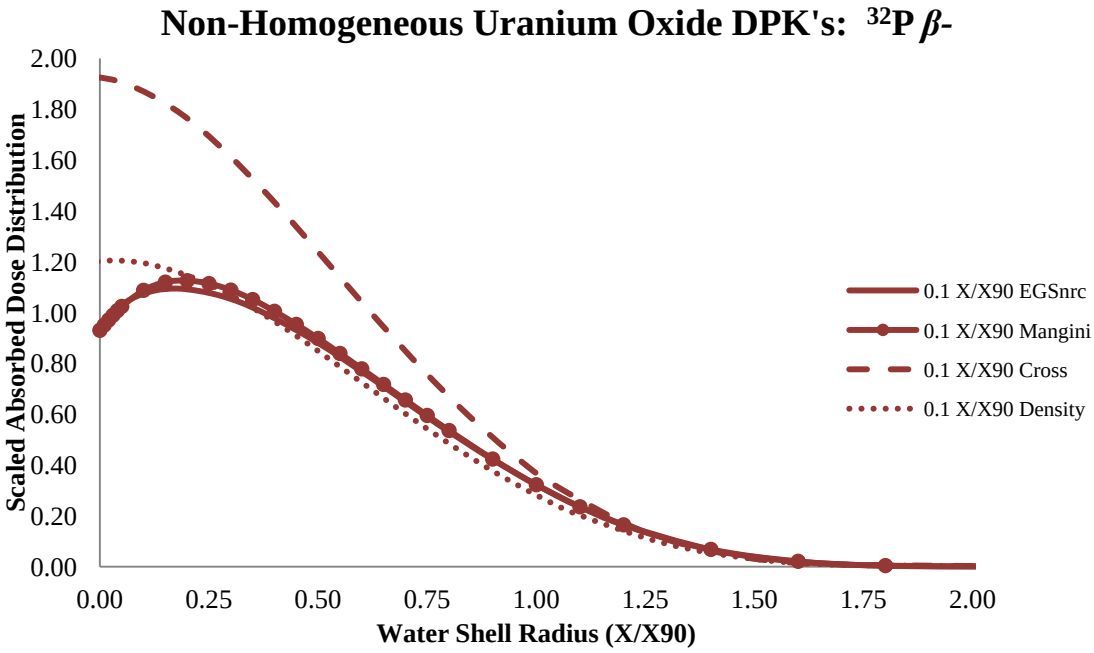

Fig. 5.75. Comparison of non-homogeneous DPK results for ^{32}P beta-particles positioned at the center of 0.1 X/X_{90} radius uranium oxide absorption spheres.

When source sizes 3 and 5 are examined, the impact of scattering models becomes more clear. As the source thickness increases, a decrease in the percent deviation at greater depths is expected for Cross-Durham (η_w = 1.60). This is due to Cross' underestimation in non-homogeneous DPK's for larger radii (Fig. 5.26, Fig. 5.27) and becomes increasingly evident for source size 5 when the percent deviation drops below 0% at greater depths. However, not only will dose be dominated at shallow depths by small radii non-homogeneous DPK's, but Durham's scattering model greatly overestimates the volumetric BSCF for source size 3 when compared to the model presented here (Fig. 5.65). The maximum overestimation occurs at normal depth of 0.004 cm and is found to be 32%. This, coupled with the overestimation in non-homogeneous DPK's, cause a 123% overestimation in dose by the Cross-Durham (η_w = 1.60) models at 0.004 cm (Fig. 5.76).

The results for the Cross-Durham (η_w = 1.00) case are supported by their representative DPK's and BSCF's as well. The 44% deviation at 0.004 cm for source size 3 is not nearly as large as the 123% deviation of Cross-Durham (η_w = 1.60). This is due to the more accurate DPK's predicted by density scaling for smaller absorption-sphere radii. However, the margin between the two models closes significantly when source size 5 is examined. This is due to the dramatic overestimation in DPK values at shallow depths for density scaling when Cross' scaling model produces an underestimation (Fig. 5.27).

Unlike Cross' scaling model and simple density scaling, the scaling model presented here is able to accurately predict the non-homogeneous DPK's for high-*Z* source materials. Additionally, the scattering model is able to better estimate volumetric BSCF's and minimize errors in dose calculations due to scattering contributions. When these two models are implemented into a DPK-based computer code for hot particle dose calculations, they produce extremely accurate results when compared to EGSnrc Monte Carlo simulations. The above discussion pertains to ^{144}Pr tungsten alloy spheres where similar results are observed (Fig. 5.78 - Fig. 5.80).

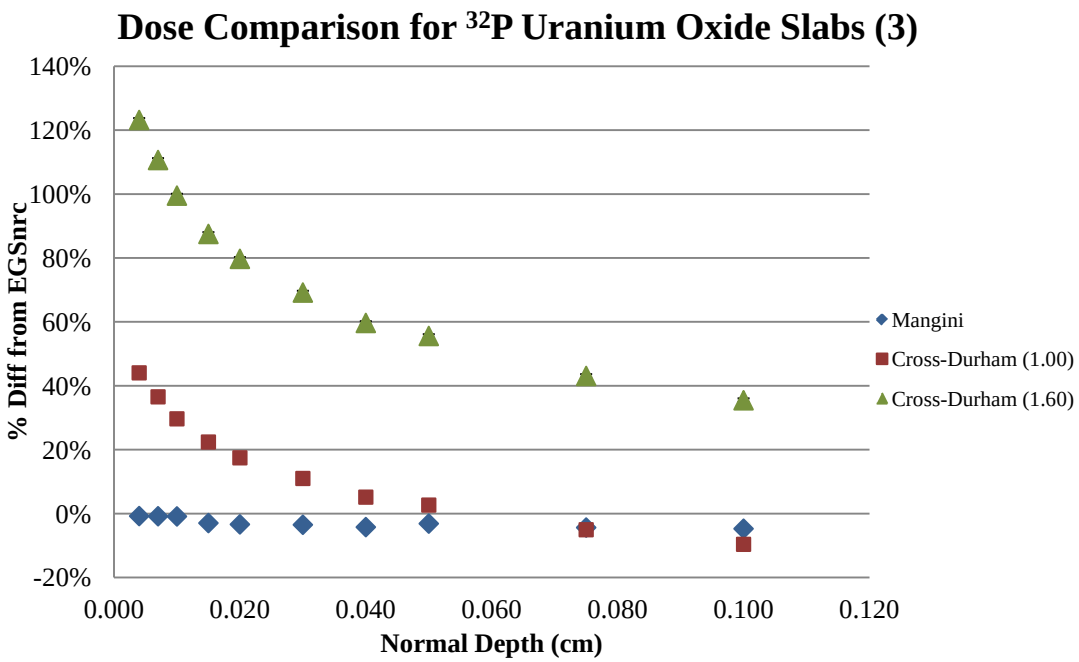

Fig. 5.76. Percent deviations with respect to EGSnrc for ^{32}P uranium oxide slabs of source size 3. η_w is provided in parenthesis in the legend.

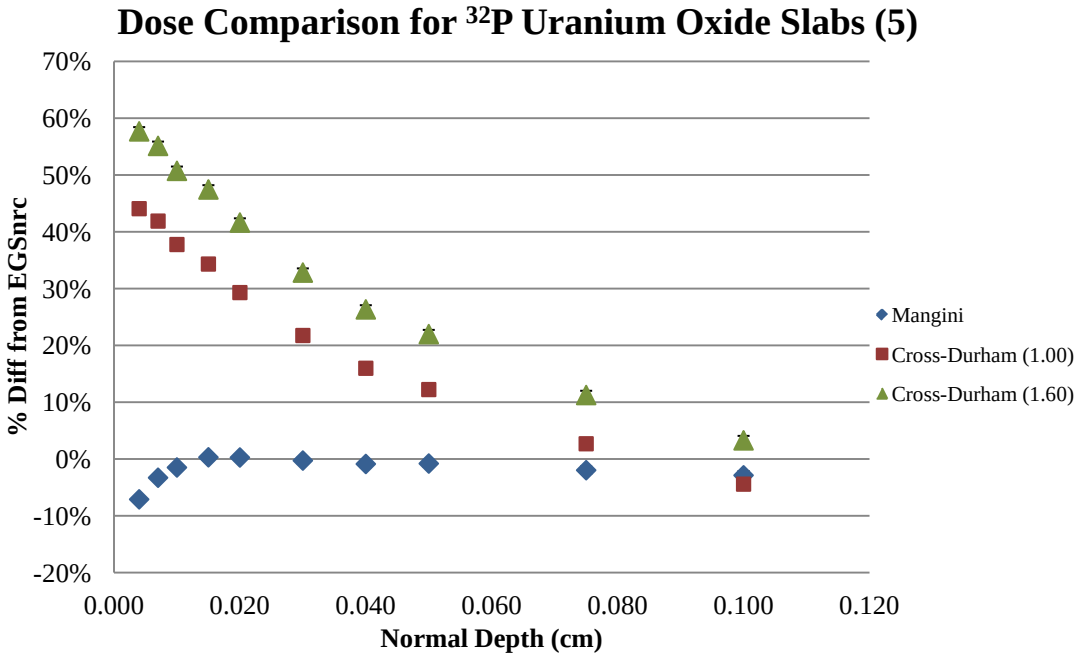

Fig. 5.77. Percent deviations with respect to EGSnrc for ^{32}P uranium oxide slabs of source size 5. η_w is provided in parenthesis in the legend.

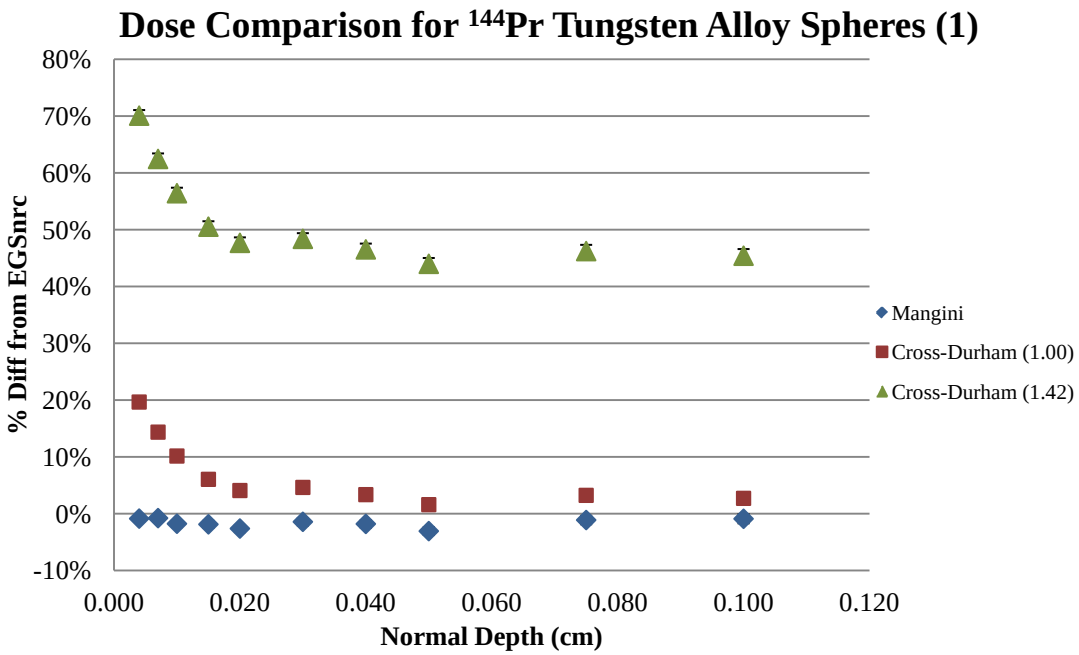

Fig. 5.78. Percent deviations with respect to EGSnrc for ^{144}Pr tungsten alloy spheres of source size 1. η_w is provided in parenthesis in the legend.

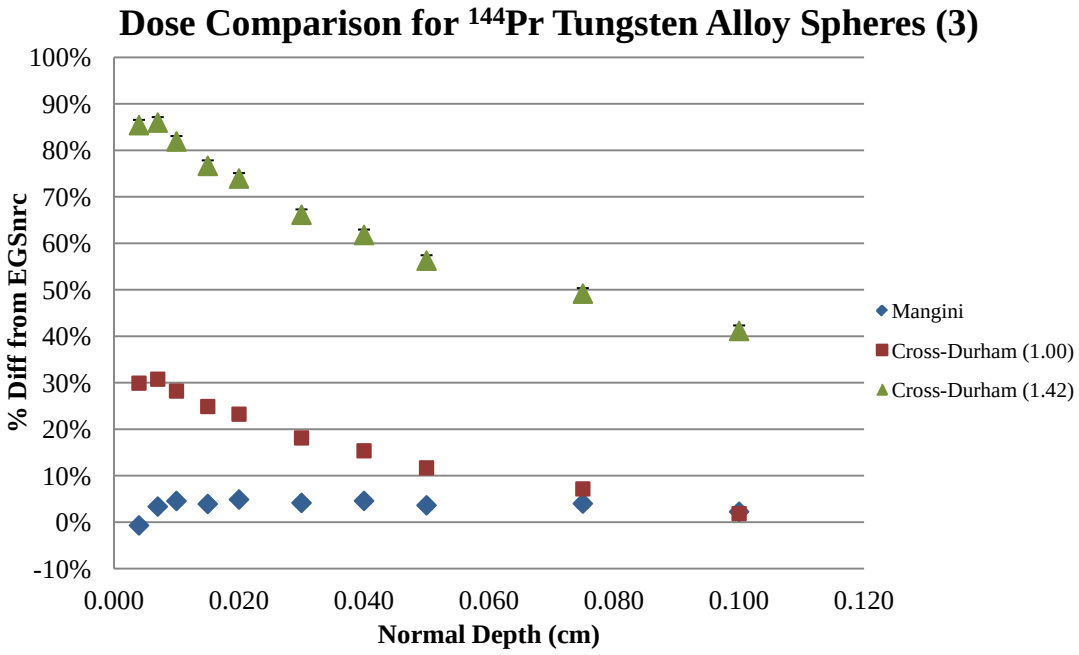

Fig. 5.79. Percent deviations with respect to EGSnrc for ^{144}Pr tungsten alloy spheres of source size 3. η_w is provided in parenthesis in the legend.

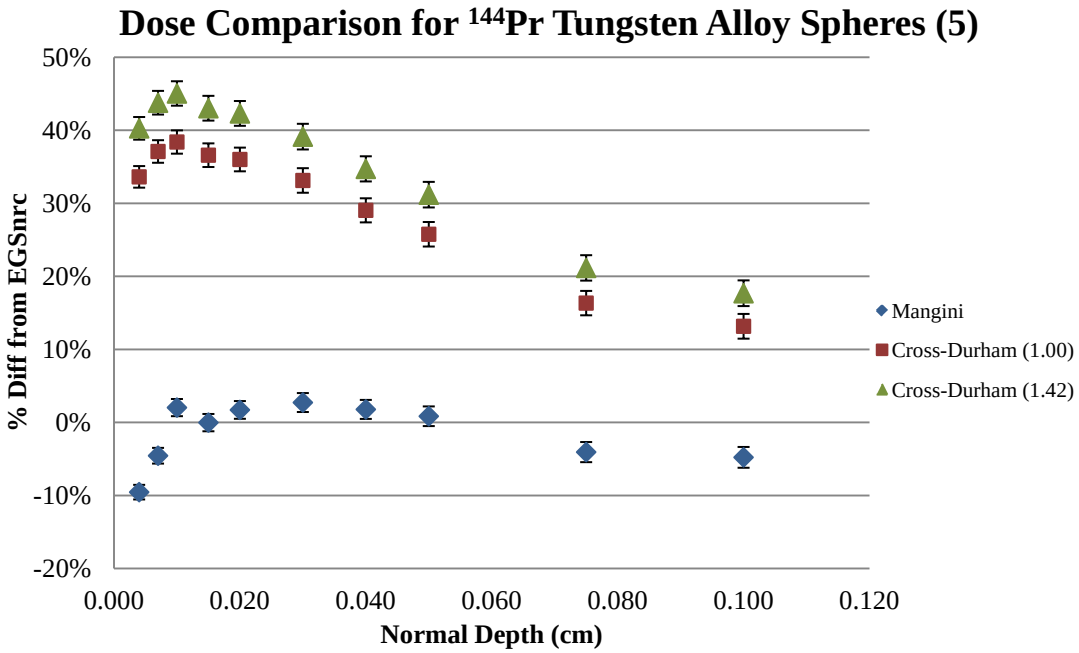

Fig. 5.80. Percent deviations with respect to EGSnrc for ^{144}Pr tungsten alloy spheres of source size 5. η_w is provided in parenthesis in the legend.

5.6.3 Source Geometry Effect on Dose

It is important that the scaling and scattering models be accurate for a variety of source geometries. This is especially true for the scattering model where the curvature of the source can create complex scattering environments. In order to demonstrate an independence of both models on source geometry, the overall results of Section 5.6.1 are presented for each geometry: cylinders (Fig. 5.81), spheres (Fig. 5.82), slabs (Fig. 5.83), and discs (Fig. 5.84).

The cylindrical and spherical sources produced nearly identical results. These geometries varied insignificantly since the radii were equal and the height of the cylinder was twice its radius. However, the curvature of the sphere, particularly at the bottom of the sphere, had little impact overall. Additionally, the box geometry of the slab and discs, coupled with the overall decreased thicknesses of the two, produced little variations.

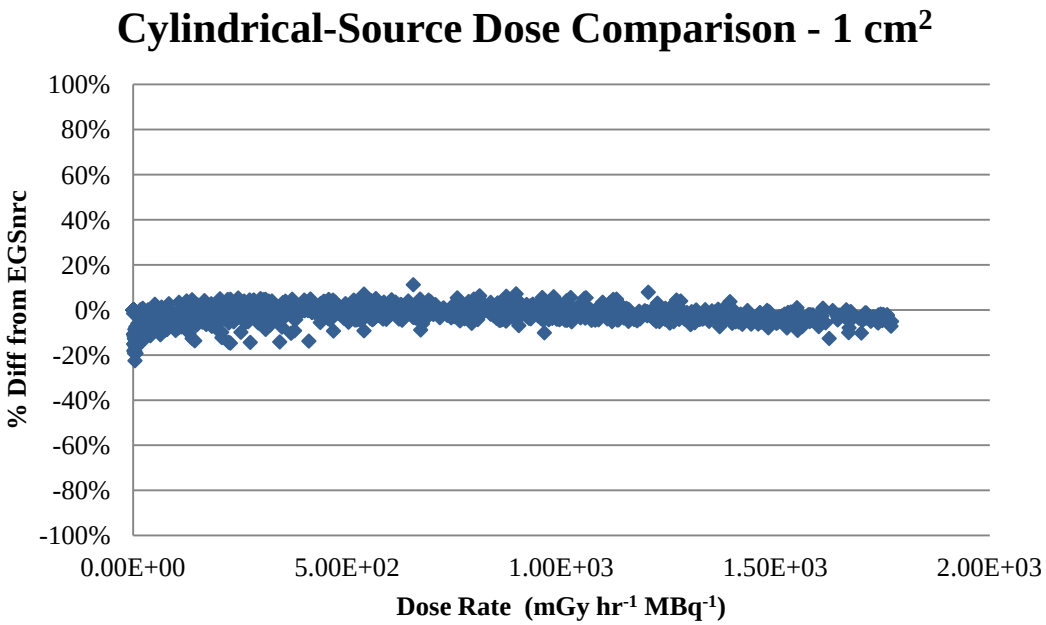

Fig. 5.81. Percent deviation with respect to EGSnrc simulations for all cylindrical sources.

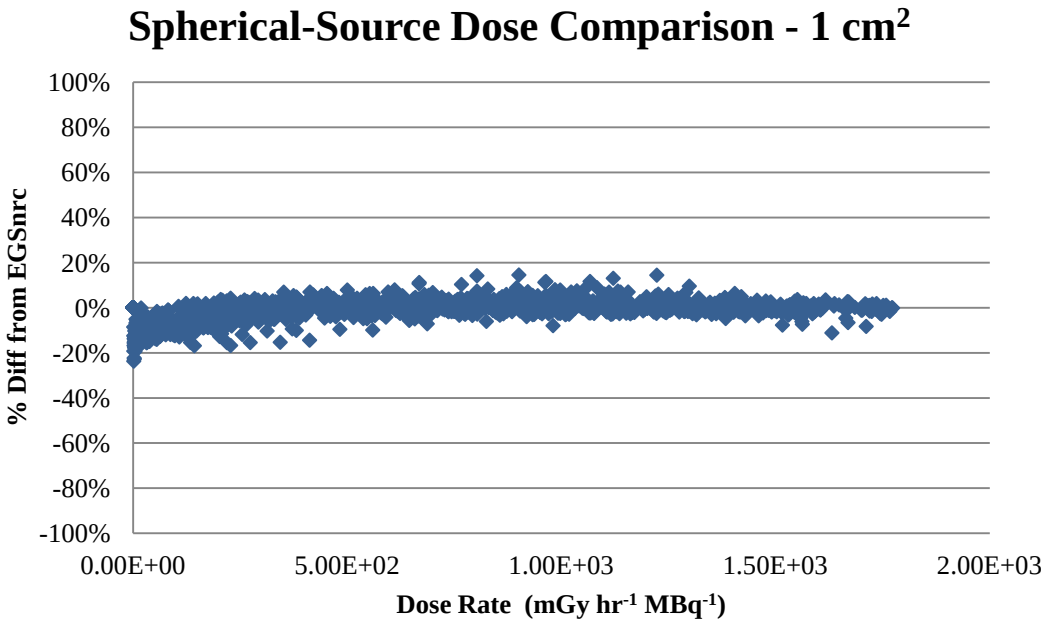

Fig. 5.82. Percent deviation with respect to EGSnrc simulations for all spherical sources.

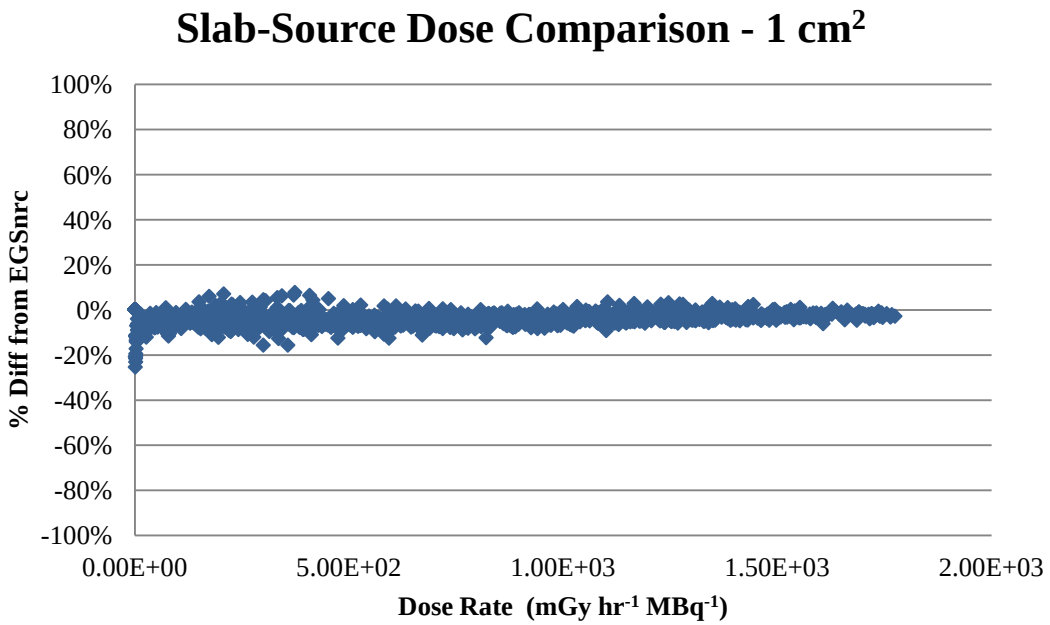

Fig. 5.83. Percent deviation with respect to EGSnrc simulations for all slab sources.

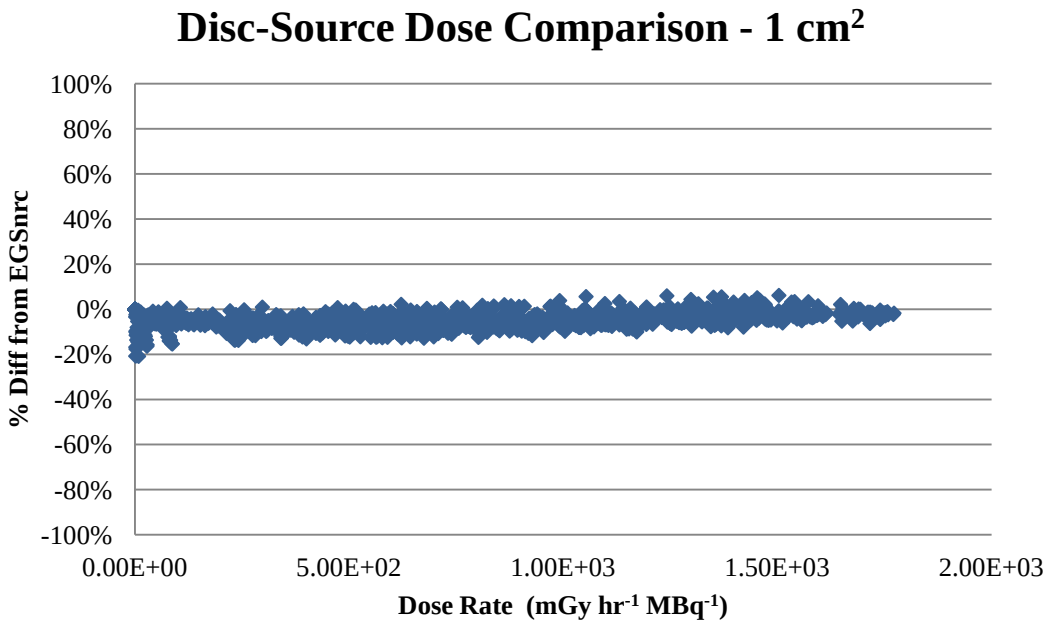

Fig. 5.84. Percent deviation with respect to EGSnrc simulations for all disc sources.

5.6.4 Source Scatter for Sides of Source

As discussed in Section 4.6.4.2, source-scatter corrections are required for large sources where source-points located on the side of the source are expected to contribute greatly to dose. Significant estimations had to be made regarding when to apply such a correction and how much of a correction to apply. However, it is easy to demonstrate that the criteria used provide sufficient scattering corrections when needed, while providing no correction when not. Based on the criteria described in Section 4.6.4.2, only source-points positioned a distance of 0.5 X/X_{90} below the top of the source will have a 100% scattering effectiveness applied. This prevents the side-scatter correction from being applied to small sources where side source-points have less of an impact on overall dose; this is demonstrated by comparing the percent deviations of source sizes 5 (Fig. 5.85) and 4 (Fig. 5.86), with and without the application of the additional correction. The additional correction factor is negligible for source size 4.

In addition, the side-scattering correction is only applied when the incident angle is greater than 70 degrees and when the density-corrected path length (includes source and air) to the edge of the dose region, or the maximum scattered beta path length, is less than the beta-particle's X_{90} distance. The latter limitation prevents the side-scatter correction from being applied to low-energy beta-particles for reasons discussed previously. This is demonstrated using the high-energy beta-particle of ^{144}Pr (E_{av} = 1.217 MeV) (Fig. 5.87) and the low-energy beta-particle of ^{90}Sr (E_{av} = 0.196 MeV) (Fig. 5.88) for 1 cm^2 dose averaging areas. While the additional correction is applied to large, high-energy beta-particle sources for the 1 cm^2 area, it is not expected to be applied when the area is increased to 10 cm^2 as the maximum scattered beta path length condition above is no longer upheld. This assumption is supported by the results presented here (Fig. 5.89).

The scattering angle of 70 degrees was chosen somewhat arbitrarily. On the other hand, if the scattering angle is too small, dose adjustments at greater depths are made resulting in a large overestimation of dose (top-bottom source scattering should adequately account for such scattering). On the other hand, if the angle is too large, minor adjustments are made at shallow depths resulting in large underestimations of dose. Determining this precise angle is a

great challenge and was deemed unnecessary due the number of assumptions already made in estimating the side-scatter contribution.

a)

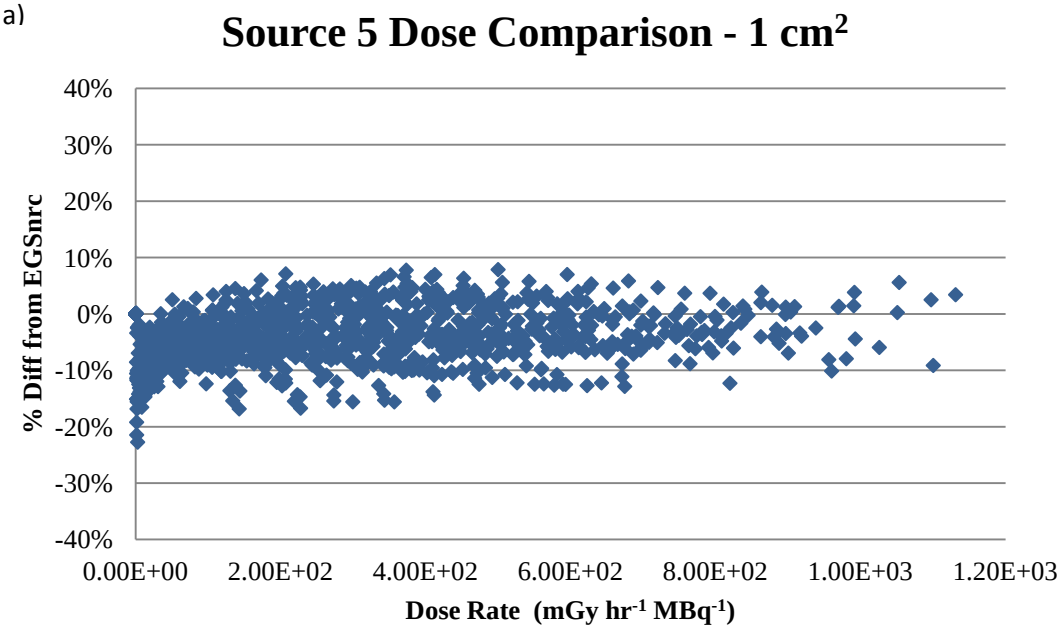

b)

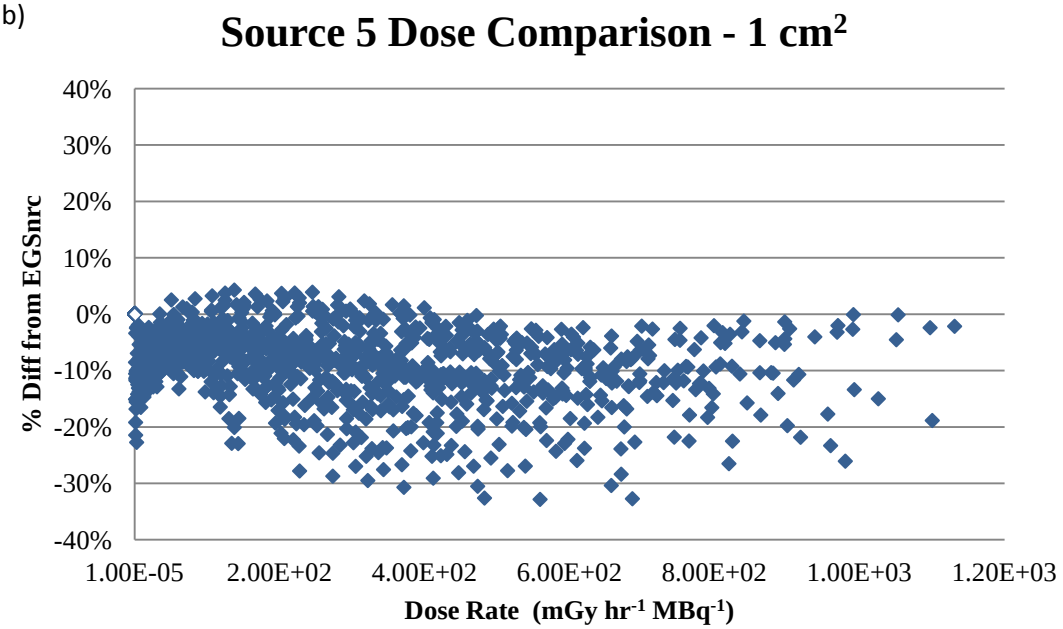

Fig. 5.85. Dose comparisons (1 cm^2 dose area) for source size 5 with (a) and without (b) the application of additional source-scatter correction to side source-points.

a)

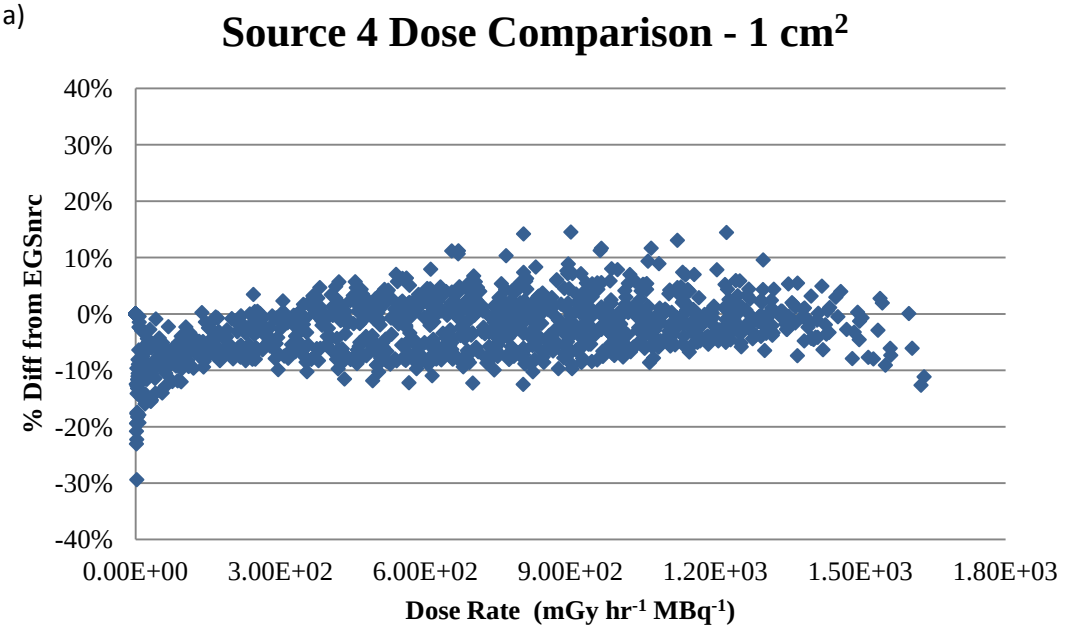

b)

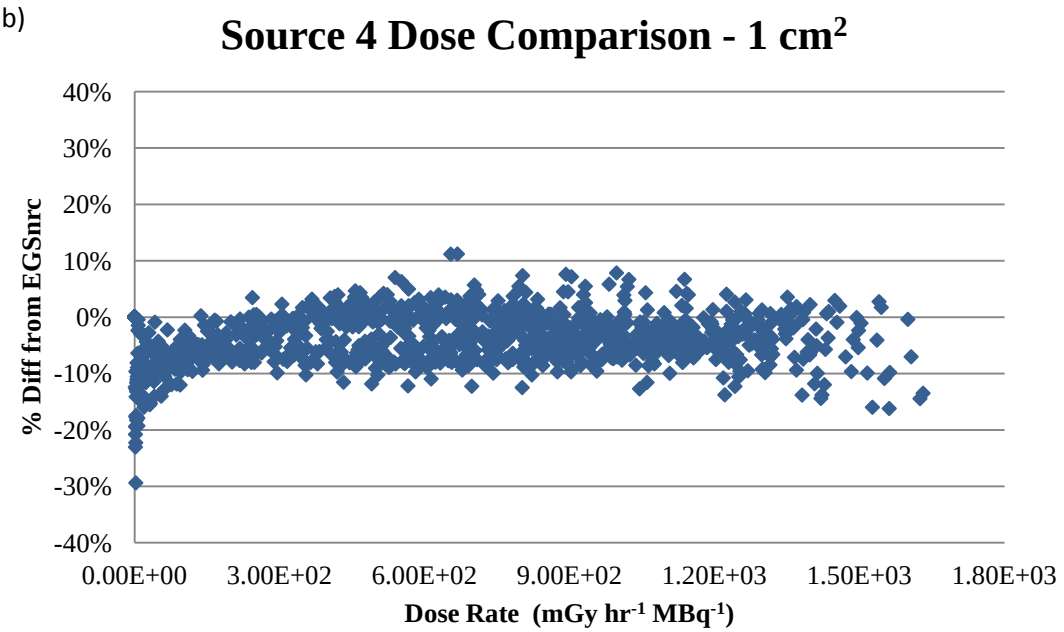

Fig. 5.86. Dose comparisons (1 cm^2 dose area) for source size 4 with (a) and without (b) the application of additional source-scatter correction to side source-points.

a)

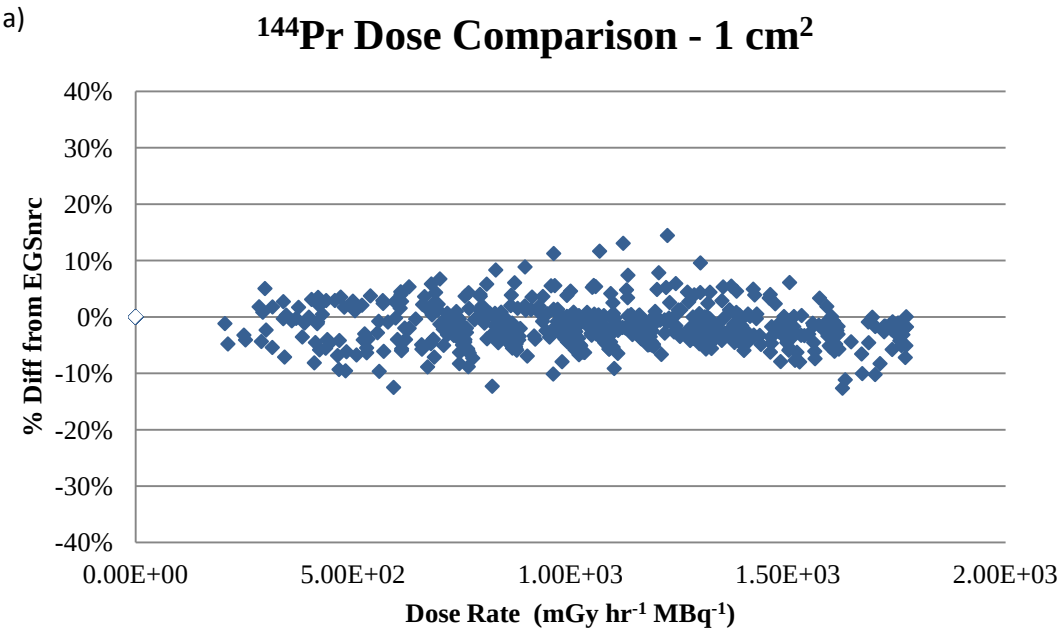

b)

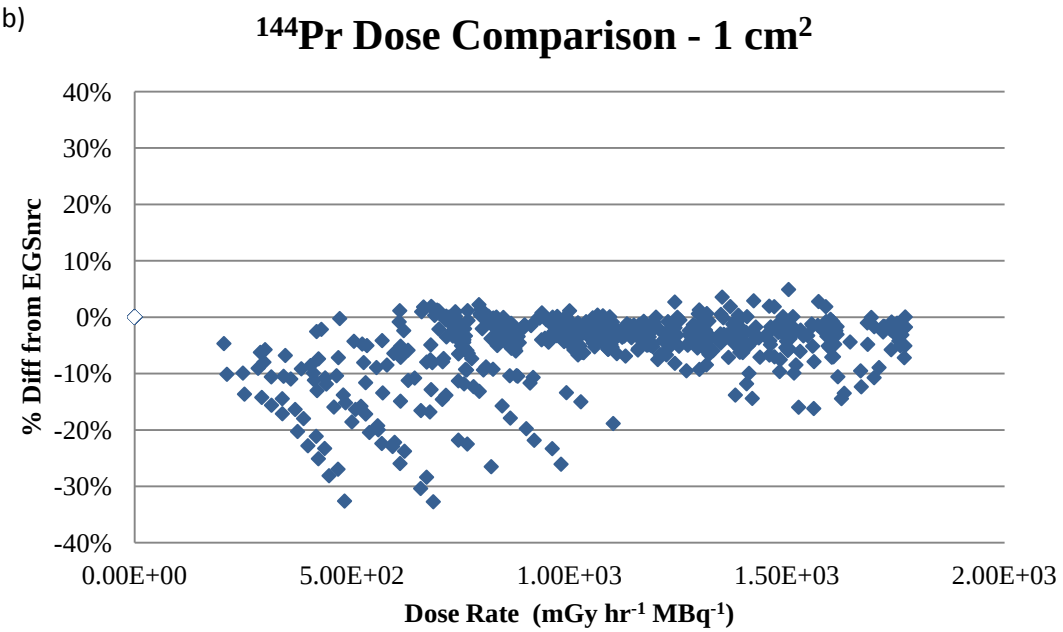

Fig. 5.87. Dose comparisons for ^{144}Pr sources (all sizes) with (a) and without (b) the application of additional source-scatter correction to side source-points.

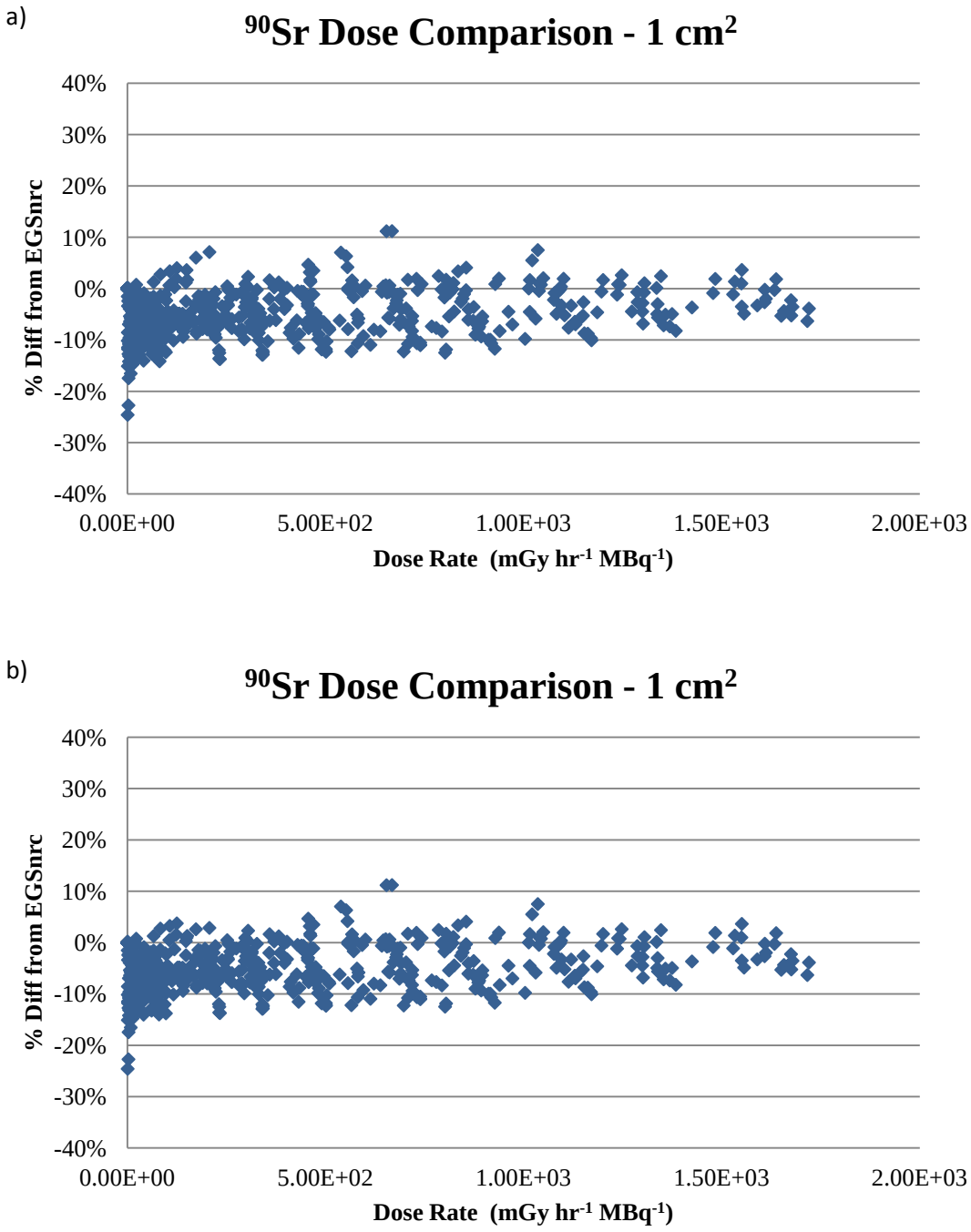

Fig. 5.88. Dose comparisons for ^{90}Sr sources (all sizes) with (a) and without (b) the application of additional source-scatter correction to side source-points.

a)

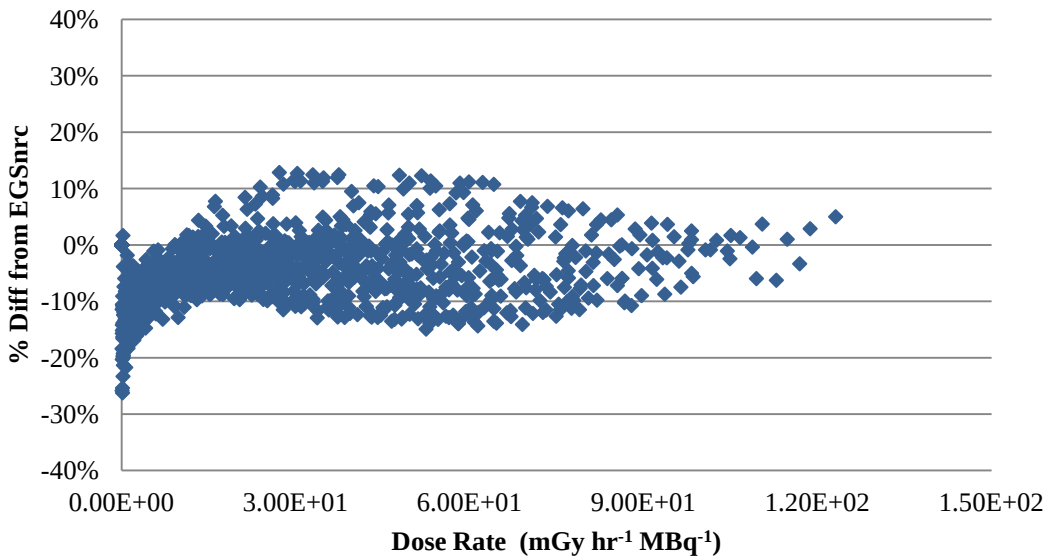

b)

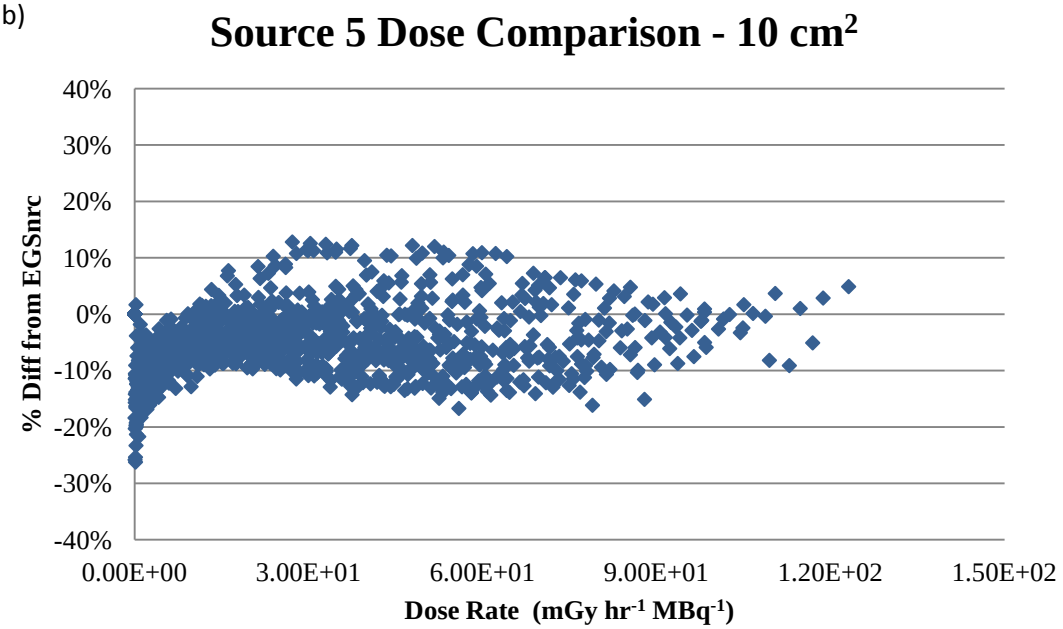

Fig. 5.89. Dose comparisons (10 cm^2 dose area) for source size 5 with (a) and without (b) the application of additional source-scatter correction to side source-points.

6 Conclusion

6.1 Scaling Model

A new energy-absorption scaling model has been developed to accurately calculate the amount of mono-energetic electron self-absorption that occurs in high-Z source materials. The model's intended purpose is to calculate non-homogeneous DPK's and consists of two scaling parameters: a depth scaling parameter that accounts for electron range and an energy scaling parameter that accounts for energy conservation. TableCurve 3D surface plotting (Fig. 5.14, Fig. 5.17) was used to determine well fitting surface plots ($R^2 \geq 0.999$ for all plots) for parameter determination for electron energies with $0.01 < E \leq 8.0$ MeV and source materials with $7.42 < Z \leq 94$.

Integration of scaling parameters over a particular beta spectrum provides the non-homogeneous DPK for a given source thickness. Comparisons with EGSnrc non-homogeneous DPKs (Fig. 5.20 - Fig. 5.30) demonstrated excellent agreement over a range of beta-particle energies and high-Z source materials by producing nearly identical DPK's for all absorption-sphere radii. In addition, when compared to Cross' (1967, 1968, 1982, 1992a) scaling model and density scaling, the ability to account for spectral hardening is clearly shown. This is in large part due to the scaling model's ability to accurately calculate non-homogeneous DPK's at each mono-energetic electron energy of a given beta-particle spectrum (Fig. 5.10 - Fig. 5.13).

6.2 Scattering Model

Unlike the scaling model, it is difficult to demonstrate the accuracy of the volumetric scattering model. Firstly, there is no comparable data in the literature with which to draw a comparison. The model developed by Durham (2006) fails to address internal source scattering and only accounts for air scattering for the top of the source. Secondly, it is not possible to use Monte Carlo transport codes to calculate the exact volumetric BSCF for model

comparison purposes (similar to non-homogeneous DPK's) due to the widely varying attenuation properties of the surrounding water compared to air.

Despite these obstacles, literature comparisons for point-source BSCF demonstrated the overall accuracy of the scattering model in calculating mono-energetic electron (Fig. 5.54- Fig. 5.56) and beta-particle (Fig. 5.50 - Fig. 5.53, Fig. 5.59 - Fig. 5.61) BSCF's for point-sources. The results of these comparisons are very important, particularly for beta-particles, since the BSCF's determined by our new scaling model are based on TableCurve 3D planar dose profiles (Fig. 5.42 - Fig. 5.45), and not direct Monte Carlo simulations (as in the literature).

The selective integration method, while based on a number of assumptions and estimations, produces volumetric BSCF's that behave as expected (Fig. 5.64 - Fig. 5.66). For relatively small sources, the BSCF is nearly equal to the air BSCF. Similarly, when the source is sufficiently large, the effects of air scattering are negligible as the air BSCF's shift toward the source BSCF. However, the volumetric BSCF was never equal to the source BSCF. This is due to source-scattering cancelations for a majority of source-points in the numerical integration process. Beyond these two observations, it is difficult to draw any defensible conclusions.

6.3 Hot Particle Skin Dosimetry

The overall goal of the research presented here is to improve the accuracy of deterministic computer codes in calculating hot particle skin doses at biologically significant skin depths and regulatory dose averaging areas. This goal has been accomplished with great success by implementation of both the scaling and the scattering models developed in this work.

While it was impractical to test all beta-emitters, source materials, source sizes, and source geometries, the parameters chosen cover a wide enough spectrum to conclude the overall success of both models. With the exception of the tail-end of low-energy beta-particle ranges, percent deviations with respect to EGSnrc simulations for all depths were ±20% (majority were ±10%) for 1 and 10 cm^2 dose areas (Fig. 5.67). These results are a dramatic

improvement when compared to similar deviations using Cross' point-source BSCF's, Durham's volumetric BSCF's, and Cross' scaling model (Fig. 5.68 - Fig. 5.80), particularly at the biologically significant depth of 0.007 cm (7.0 mg cm^{-2})

Definitively demonstrating the accuracy of the scaling model in calculating volumetric BSCF's was not possible. However, the dose verification results provide sufficient evidence to support its overall validity for both 1 and 10 cm^2 dose averaging areas. In fact, the results of the dose verification were used to demonstrate the geometry independence of the new scattering model (Fig. 5.81 - Fig. 5.84.) and the need for an additional side scattering contribution (Fig. 5.85 - Fig. 5.89).

The notion that a deterministic computer code can produce accurate results for all possible hot particle scenarios is absurd. Monte Carlo transport codes will always have the advantage of being able to account for nearly all geometrical and material configurations. However, the research presented here has allowed that gap to be closed by a rather large margin.

6.4 Future Work

Future work should be focused predominately on model verification and less on model improvement. The scaling and scattering models presented here were designed to be 'implementation ready' for deterministic dose-point kernel codes. The results of the hot particle skin dose verifications demonstrated this important aspect. While improvements to the models can certainly be made, especially for the scattering model, further improvements to hot particle skin dose estimations would likely be minor.

Skin dose verifications could be extended to include source covers, sources that are raised off the skin surface, and dose areas other than 1 and 10 cm^2. Source covers such as clothing, surgeon gloves, or cotton gloves would all have densities approximately equal to or less than that of water. Given the organic and hydrocarbon nature of such materials, their Z_{eff}, coupled with their low densities would provide similar scaling and scattering properties to that of water. Since both models assume water is the only material present outside of the source material, simple density scaling could be used and the source cover density thicknesses could

be added to the given water thicknesses. However, this assumption could be verified with further testing.

The use of an air gap would be similar to the source covers explained above. Density scaling could be used for all air distances. While verification of skin dose with volumetric sources already requires that the path length of the beta-particle in air be scaled with density, an air gap would accentuate this approximation and could potentially identify any issues. Additionally, source scattering from the bottom of the source assumes a source-water interface. It would be important to verify that the existence of a substantial air gap between the two has no impact on the scattering model.

Finally, dose testing for dose averaging areas between 1 and 10 cm^2 would provide evidence for successful interpolation between the respective BSCF's. However, given the slight variation demonstrated in Section 5.5.2, this exercise would likely be useless. The use of dose areas less than 1 cm^2 and greater than 10 cm^2 would be a more informative inquisition. Once again, these two areas were chosen based on ICRP and NCRP recommendations. It may be of some interest to a researcher to use a dose area outside the range of these two values. As discussed previously, source scattering corrections have a significant dose area dependency when the radius of the area is less than the range of the beta-particle (Bufa 2004). Additionally, air scattering corrections demonstrate a noticeable deviation when the dose area increases to values of 100 cm^2 (Cross 1991b, 1992c). By performing additional dose testing, an upper and lower dose area limitation of the current scattering model could be determined. A percent deviation with respect to EGSnrc could be set to some threshold value in order to recommend dose area limitations. Alternatively, the scattering model could be extended to include additional areas, such as 0.1 cm^2 and 100 cm^2. The assignment of an upper and lower limit would still be warranted however.

Bibliography

23391, 5. F. (1991). *10CFR20: Energy, Standards for Protection Against Radiation.* Nuclear Regulatory Commission . Office of the Federal Register.

Albert, E. A., Burns, F. J., & Heimbach, R. D. (1967). Skin Damage and Tumor formation from Grid and Sieve Patterns of Electron and Beta Radiation in the Rat. *Radiation Research, 30*, 525-540.

Aydarous, A. S. (2008). Calculating Effects of Backscattering on Skin Dosimetry for Nuclear Fuel Fragments. *Radiation Protection Dosimetry, 130*, 141-148.

Bakali, F. F., Bouassoule, T., Castelo, J., & Gonzalez, A. (2001). Hot particle dosimetry at nuclear power plants. *Radiation Measurements, 34*, 487-490.

Berger, M. J. (1971). Distribution of Absorbed Dose Around Point-sources of Electrons and Beta-particles in Water and Other Media. Medical Internal Radiation Dose Committee, Pamphlet No. 7, *Journal of Nuclear Medicine*, 12, 5–22.

Berger, M. J. (1963) Monte Carlo calculation of the penetration and diffusion of fast charged particles *Methods in Computational Physic*, 1, 135–215. ed Alder, B., Fernbach, S., & Rotenberg, M. New York: Academic.

Blunck, O. & Westphal, K. Zum. (1951). Energieverlust energiereicher Elektronen in d nnen Schichten, *Z. Physik, 130*, 641. (in German)

Bragg, W. H. & Kleeman, R. (1904) On the Ionization Curves of Radium. *Philosophical Magazine, 8*, 726-738.

Briessmeister, J. (1997) in *MCNP—A General Monte Carlo N-Particle Transport Code, Version 4B, LA-Report 12625-M*. Los Alamos, NM: Radiation Shielding Information Center

Brown, F. B. (ed) .(2003). *MCNP—A General Monte Carlo N-Particle Transport Code, Version 5 Report LA-UR-03-1987*. Los Alamos, NM: Los Alamos National Laboratory

Buffa, F. M. & Verhaegen, F. (2004). Backscatter and Dose Perturbations for Low-to Medium-energy electron Point-sources at the Interface between Materials with Different Atomic Numbers. *Radiation Research, 162*, 693-701.

Caffrey, J. (2012) Personal correspondence.

Cember, H. (1996). *Introduction to Health Physics*. (3rd ed.). New York: McGraw Hill.

Chabot, G.E., Skrable, K.W., & French, C.S. (1988). When hot particles are not on the skin; A beta dose distribution function for particles on and off the skin. *Radiation Protection Management, 5*, 31-42.

Charles, M. W., & Harrison, J. D. (2007). Hot Particle Dosimetry and Radiobiology - Past and Present. *Journal of Radiological Protection , 27,* A97-A109.

Charles, M. W. (1991). The Hot Particle Problem. *Radiation Protection Dosimetry, 39*, 39-47.

Charles, M. W. (1990). General considerations of the choice of dose limits, averaging areas and weighting factors for the skin in the light of revised skin cancer risk figures and experimental data on non-stochastic effects. *International Journal of Radiation Biology, 57*, 841-858.

Charles, M. W., Williams, J. P., & Coggle, J. E. (1988). Skin Carcinogenesis Following Uniform and Nonuniform β Irradiation. *Health Physics, 55,* 399-406.

Chibani, O., & Li, A. (2002). Monte Carlo dose calculations in homogeneous media at the interface: A comparison between GEPTS, EGSnrc, MCNP, and measurements. *Medical Physics*, *29*, 835-847.

Cho, S. H., Reece, W. D., & Kim, C. H. (2004). Validity of two simple rescaling methods for electron/beta dose-point kernels in heterogeneous source-target geometry. *Radiation Physics and Chemistry, 69*, 265-272.

Cho, S. H. & Reece, W. D. (1999). Monte Carlo calculations of the dose backscatter factor for mono-energetic electrons. *Physics in Medicine and Biology, 44*, 13-26.

Chung, M., Levine, S. H., & Jester, W. A. (1991). Monte Carlo Calculations and Silicon Detector Measurement of the Hot Particle Dose. *Health Physics*, *61*, 843-848.

Crawford, H. O., Turner, J. E., Hamm, R. N., Ashley, J. C. (1991). Effects of the Skin-Air Interface in Calculations of β-Particle Skin Dose at a Depth of 70μm. *Health Physics, 61*, 641-645.

Cross, W. G., Hokkanen, J., Mourtada, F., Sipila, P., Soares, C. G., & Vynckier, S. (2001). Calculation of beta-ray dose distributions from ophthalmic applicators and comparison with measurements in a model eye. *Medical Physics, 28*, 1385-1396.

Cross, W. G., Freedman, N. O, & Wong, P. Y. (1992a). Tables of beta-ray dose distributions in water. *Report No. AECL-10521*. Chalk River, Ontario: AECL Research.

Cross, W. G., Freedman, N. O, & Wong, P. Y. (1992b). Beta-Ray Dose Distributions from Point-sources in an Infinite Water Medium. *Health Physics, 63*, 160-171.

Cross, W. G., Freedman, N. O, & Wong, P. Y. (1992c). Beta Ray Dose Distributions from Skin Contamination. *Radiation Protection Dosimetry, 40*, 149-168.

Cross, W. G., Freedman, N. O, & Wong, P. Y. (1991a). Dose Distributions for Electrons and Beta Rays Incident Normally on Water. *Radiation Protection Dosimetry, 35*, 77-91.

Cross, W. G., Freedman, N. O, & Wong, P. Y. (1991b). Tables of Beta Ray Depth-Dose Distributions from Normally Incident Beams and Skin Contamination. *Radiation Protection Dosimetry, 39*, 101-104.

Cross, W. G., Ing, H., Freedman, N. O, & Mainville, J. (1982). Tables of beta-ray dose distributions in water, air, and other media. *Report No. AECL-7617*. Chalk River: Atomic Energy Canada Limited.

Cross, W. G. (1968). Variation of Beta Dose Attenuation in Different Media. *Physics in Medicine and Biology, 13*, 611-618.

Cross, W. G. (1967). The Distribution of Absorbed Energy from a Point Beta Source. *Canadian Journal of Physics, 45*, 2021-2040.

Durham, J. S. (2006). VARSKIN 3: A Computer Code for Assessing Skin Dose from Skin Contamination. *NUREG/CR-6918*. Washington, DC: U.S. Nuclear Regulatory Commission.

Durham, J. S. (1992). VARSKIN Mod 2 and SADDE Mod 2: Computer Codes for Assessing Skin Dose from Skin Contamination. *NUREG/CR-5873, PNL-7913*. Washington, DC: NRC.

Fox, R. A., Henson, P. W. (2000). The Dosimetry for a Coronary Artery Stent Coated with Radioactive Re-188 and P-32. *Physics in Medicine and Biology*, *45*, 3643-3655.

Goudsmit, S. & Saunderson, J. L. Multiple Scattering of Electrons, *Physical Review, 57*, 24-29.

Halbleib, J. A., Kensek, R. P., Mehlhorn, T. A., Valdez, G. D., Seltzer, S. M., & Berger, M. J. (1992) *ITS version 3.0: the integrated TIGER series of coupled electron/photon Monte Carlo transport codes Sandia Report SAND91-1634*. Albuquerque, New Mexico: Sandia National Laboratories.

Hamby, D. M., Lodwick, C. J., Palmer, T. S., Reese, S. R., & Higley, K. A. (2011). VARSKIN 4: A Computer Code for Skin Contamination Dosimetry. *NUREG/CR-6918*. Washington, DC: U.S. Nuclear Regulatory Commission.

Hopewell, J. W. (1991). Biological Effects of Irradiation on Skin and Recommended Dose Limits. *Radiation Protection Dosimetry*, *39*, 11-24.

Hopewell, J. W. (1990). The Skin: Its Structure and Response to Ionizing Radiation. *International Journal of Radiation Biology, 57*, 751-773.

International Commission on Radiation Protection. (2008). *Nuclear Decay Data for Dosimetric Calculations.* ICRP Publication 107. Ann. ICRP 38 (3).

International Commission on Radiation Protection. (2007). *The 2007 Recommendations of the International Commission on Radiological Protection*. ICRP Publication 103. Ann. ICRP 37 (2-4).

International Commission on Radiological Protection. (1992). *Annals of the ICRP: The Biological Basis for Dose Limitation in the Skin.* ICRP Publication 59 (22)

International Commission on Radiological Protection. (1991). *Annals of the ICRP: 1990 Recommendations of The International Commission on Radiological Protection.* ICRP Publication 60 (21).

Janicki, C., Duggan, D. M., Gonzalez, A., Coffey, C. W., & Rahdert, D. A. (1999). Dose model for a beta-emitting stent in a realistic artery consisting of soft tissue and plaque. *Medical Physics, 26*, 2451-2460.

Johns, H. E. & Cunningham, J. R. (1983). *The Physics of Radiology* (4th Ed). Springfield, IL: Charles C Thomas.

Kawrakow, I. (2000). Accurate condensed history Monte Carlo simulation of electron transport: I. EGSnrc, the new EGS4 version. *Medical Physics, 27,* 485–98

Kawrakow, I., & Bielajew, A. F. (1998). On the condensed history technique for electron transport. *Nuclear Instruments and Methods B, 142,* 253–80

Kawrakow, I., & Rogers, D. W. (2000). The EGSnrc code system: Monte Carlo simulation of electron and photon transport. *Technical Report* PIRS-701. Ottawa, Canada: National Research Council of Canada.

Knoll, G. F. (2000). *Radiation Detection and Measurement* (3rd ed.). Hoboken, NJ: John Wiley & Sons, Inc.

Kocher, D. C., & Eckerman, K. F. (1987). Electron Dose-Rate Conversion Factors for External Exposure of the Skin from Uniformly Deposited Activity on the Body Surface. *Health Physics, 53*, 135-141.

Landau, L. (1944). On the Energy Loss of Fast Particles by Ionization, *Journal of Physics-USSR, 8***,** 201.

Lee, S. W. & Reece, W. D. (2004). Dose backscatter factors for selected beta sources as a function of source, calcified plaque and contrast agent using Monte Carlo calculations. *Physics in Medicine and Biology, 49*, 583-599.

Loevinger, R. (1954). The Dosimetry of Beta Radiations. *Radiology, 62*, 74-82.

Loevinger, R. (1956). The Dosimetry of Beta Sources in Tissue. The Point-Source Function. *Radiology, 66*, 55-62.

Maigne, L., Perrot, Y., Schaart, D. R., Donnarieix, D., & Breton, V. (2011). Comparison of GATE/GEANT4 with EGSnrc and MCNP for electron dose calculations at energies between 15 keV and 20 MeV. *Physics in Medicine and Biology, 56*, 811-827.

Mainegra-Hing, E., Rogers, D. W. O., & Kawrakow, I. (2005). Calculation of energy deposition kernels for photons and dose-point kernels for electrons. *Medical Physics, 32*, 685–99

Marcu, S. M. & Prestwich, W. V. (1998). Application of the scaling factor method to estimation of beta dose distributions for dissimilar media separated by a planar interface. *Medical Physics, 25*, 1478-1486

Marcu, S. M. & Prestwich, W. V. (1998). A statistical investigation of the scaling factor method of beta-ray dose distribution derivation: The scaling factor for water to bone. *Medical Physics, 25*, 1473-1477

Martin, J. E. (2006). *Physics for Radiation Protection* (2nd Ed. ed.). Germany: Wiley-VCH.

Moliere, G. (1948) Theorie der Streuung schneller geladener Teilchen II: Mehrfach- und Vielfachstreuung, *Z. Naturforsch, 3,* 78. (in German)

National Council on Radiation Protection and Measurement. (2001, March 30). Extension of the Skin Dose Limit for Hot Particles to Other External Sources of Skin Irradiation. (9).

National Council on Radiation Protection and Measurements. (1999). *NCRP Report No. 130: Biological Effects and Exposure Limits for "Hot Particles"*. Bethesda, MD.

National Council on Radiation Protection and Measurements. (1989). *NCRP Report No. 106: Limit for Exposure to "Hot Particles" on the Skin.* Bethesda, MD.

Nelson,W. R., Hirayama, H. & Rogers, D. W. O. (1985). The EGS4 code system. *Report SLAC-265* Stanford, CA: Stanford Linear Accelerator Center.

Park, S., Choi, B., & Lee, J. (2009). Development of Point-Kernel Code for Skin Dose Calculation. *Nuclear Technology, 168*, 158-163.

Prestwich, W. V., Nunes, J., & Kwok, C. S. (1989). Beta Dose-point Kernels for Radionuclides of Potential Use in Radioimmunotherapy. *The Journal of Nuclear Medicine, 30*, 1036-1046.

Podgorsak, E. B. (2006). *Radiation Physics for Medical Physicists.* New York: Springer

Reece, W. D. (1991). Experiences and Problems of skin Irradiation Due to Hot Particles at Workplaces in the United States. *Radiation Protection Dosimetry, 28*, 1883-1897.

Reynaert, N., Jeraj, R. (2002). Parameter dependence of the MCNP electron transport in determining dose distributions. *Medical Physics*, *29*, 2446-2454.

Reynaert, N. & Hafeli, U. O. (2001). Self-absorption correction for ^{32}P, ^{198}Au and ^{188}Re stents: Dose-point kernel calculations versus Monte Carlo. *Medical Physics, 28*, 1883-1897.

Rogers, D. W. O. (2006). Fifty years of Monte Carlo simulations for medical physics. *Physics in Medicine and Biology, 51*, R287-R301.

Schaart, D.R. (2002). A comparison of MCNP4C electron transport with ITS 3.0 and experiment at incident energies between 100 keV and 20 MeV: influence of voxel size, substeps and energy indexing algorithm. *Physics in Medicine and Biology 47,* 1459-1484.

Seltzer, S. M. (1991). Electron-Photon Monte Carlo Calculations: The ETRAN Code. *Applied Radiation Isotopes, 42*, 917-941.

Seltzer, S. M. (1988). An overview of ETRAN Monte Carlo methods. *Monte Carlo Transport of Electrons and Photons.* 153–82. ed Jenkins, T. M., Nelson, W. R., Rindi, A ., Nahum, A. E., & Rogers, D. W. O. New York: Plenum.

Sherbini, S., DeCicco, J., Gray, A. T., & Struckmeyer, R. (2008). Verification of the VARSKIN Beta Skin Dose Calculation Computer Code. *Health Physics, 94*, 527-538.

Shultis, J. K. & Faw, R. E. (2008) *Fundamentals of Nuclear Science and Engineering*. Boca Raton, FL: CRC Press.

Shultis, J. K. & Faw, R. E. (1996). *Radiation Shielding*. Upper Saddle River, NJ: Prentice-Hall, Inc.

Sidlova, V. & Trojek, T. (2010). Testing Monte Carlo computer codes for simulations of electron transport in matter. *Applied Radiation and Isotopes, 68*, 961-964.

Simpkin, D. J. & Mackie, T. R. (1990). EGS4 Monte Carlo determination of beta dose kernels in water. *Medical Physics, 17*, 179-186.

Spencer, L. V. (1959). Energy Dissipation by Fast Electrons. *National Bureau of Standards Monograph 1*.

Spencer, L. V. (1955). Theory of electron Penetration. *Physical Review, 98*, 1597-1615.

Traub, R.J., W.D. Reece, R.I. Scherpelz, & L.A. Sigalla. (1987). Dose Calculation for Contamination of the Skin Using the Computer Code VARSKIN. *NUREG/CR-4418*. Washington, DC: NRC.

Turner, J. E. (2007). *Atoms, Radiation, and Radiation Protection* (3rd Ed). Germany: Wiley-VCH

United States Nuclear Regulatory Commission. (2002, July 9). *NRC Regulatory Issue Summary 2002-10 Revision of the Skin Dose Limit in 10 CFR Part 20.*

Uusijarvi, H., Chouin, N., Bernhardt, P., & Ferrer, L. (2009). Comparison of Electron Dose-Point Kernels in Water Generated by the Monte Carlo Codes, PENELOPE, GEANT4, MCNPX, and ETRAN. *Cancer Biotherapy and Radiopharmaceuticals, 24*, 461-467.

Wang, R. (2001). Monte Carlo dose calculations of beta-emitting sources for intravascular brachytherapy: A Comparison between EGS4, EGSnrc, and MCNP. *Medical Physics, 28*, 134-141.

Appendices

Appendix A – TCL Code Example: EGSnrc DPK's

```
#TCL Script for creating multiple EGSnrc input files.  Input files
#are for the EDKnrc user code.  Using this user code, energy
#deposition kernels can be determined.
file mkdir PHIsmall_H2O
set tcl_precision 10

#define the 30 energies and their CSDA ranges
set energy [list  1.00E-02 2.00E-02 3.00E-02 4.00E-02 5.00E-02\
 6.00E-02 7.00E-02 8.00E-02 1.00E-01 1.50E-01 2.00E-01 2.50E-01\
 3.00E-01 3.50E-01 4.00E-01 4.50E-01 5.00E-01 5.50E-01 6.00E-01\
 7.00E-01 8.00E-01 9.00E-01 1.00E+00 2.00E+00 3.00E+00 4.00E+00\
 5.00E+00 6.00E+00 7.00E+00 8.00E+00 ]
set energyn [list  1 2 3 4 5 6 7 8 9 10 11 12 13 14 15 16 17 18 19
20\
 21 22 23 24 25 26 27 28 29 30 ]
set Rcsda [list 2.52E-04 8.57E-04 1.76E-03 2.92E-03 4.32E-03 5.94E-
03\
 7.76E-03 9.77E-03 1.43E-02 2.82E-02 4.49E-02 6.37E-02 8.42E-02\
 1.06E-01 1.29E-01 1.52E-01 1.77E-01 2.01E-01 2.27E-01 2.78E-01\
 3.30E-01 3.83E-01 4.37E-01 9.79E-01 1.51E+00 2.04E+00 2.55E+00\
 3.05E+00 3.55E+00 4.03E+00 5.15E-04 1.27E-03 7.08E-01 ]

#define transport variables and shell radii
#"sdvac" variable allows for easy transition to non-homogeneous DPK's
    foreach  E $energy EN $energyn X $Rcsda {
        file delete PHIsmall_H2O/phiH2O${EN}.egsinp
        set ECUT 0.512
        set smax 0.0
        set media water
        set ncase 1000000
        set X [expr { $X/1}]
        set sdmax [expr { $X*10 }]
        set sdvac 0.000000
        set step [expr { 0.0025*$X }]
        set sd0h  [expr { 0.05*$X+$sdvac }]
        set sd1  [expr { 0.1*$X+$sdvac }]
        set sd1h  [expr { 0.15*$X+$sdvac }]
        set sd2  [expr { 0.2*$X+$sdvac }]
        set sd2h  [expr { 0.25*$X+$sdvac }]
        set sd3  [expr { 0.3*$X+$sdvac }]
        set sd3h  [expr { 0.35*$X+$sdvac }]
        set sd4  [expr { 0.4*$X+$sdvac }]
        set sd4h  [expr { 0.45*$X+$sdvac }]
        set sd5  [expr { 0.5*$X+$sdvac }]
        set sd5h  [expr { 0.55*$X+$sdvac }]
        set sd6  [expr { 0.6*$X+$sdvac }]
        set sd6h  [expr { 0.65*$X+$sdvac }]
        set sd7  [expr { 0.7*$X+$sdvac }]
        set sd7h  [expr { 0.75*$X+$sdvac }]
        set sd8  [expr { 0.8*$X+$sdvac }]
        set sd8h  [expr { 0.85*$X+$sdvac }]
        set sd9  [expr { 0.9*$X+$sdvac }]
        set sd9h  [expr { 0.95*$X+$sdvac }]
        set sd10  [expr { 1.0*$X+$sdvac }]
```

```
        set sd10h  [expr { 1.05*$X+$sdvac }]
        set sd11  [expr { 1.1*$X+$sdvac }]
        set sd11h  [expr { 1.15*$X+$sdvac }]
        set sd12  [expr { 1.2*$X+$sdvac }]
        set sd12h  [expr { 1.25*$X+$sdvac }]
        set sd13  [expr { 1.3*$X+$sdvac }]
        set sd13h  [expr { 1.35*$X+$sdvac }]
        set sd14  [expr { 1.4*$X+$sdvac }]
        set sd14h  [expr { 1.45*$X+$sdvac }]
        set sd15  [expr { 1.5*$X+$sdvac }]
        set sd15h  [expr { 1.55*$X+$sdvac }]
        set sd16  [expr { 1.6*$X+$sdvac }]

#write and name the EGSnrc input files

        set f [open phiH2O${EN}.egsinp w]

        puts $f "TITLE= Energy deposition kernel for $E MeV
electrons"
        puts $f ""
        puts $f ""
        puts $f "############################"
        puts $f ":start I/O control:"
        puts $f ""
        puts $f "IRESTART= first"
        puts $f ""
        puts $f "STORE DATA ARRAYS= yes"
        puts $f ""
        puts $f "PRINT OUT EDK FILE= yes"
        puts $f ":stop I/O control:"
        puts $f "############################"
        puts $f ""
        puts $f "############################"
        puts $f ":start Monte Carlo inputs:"
        puts $f ""
        puts $f "NUMBER OF HISTORIES= $ncase "
        puts $f ""
        puts $f "INITIAL RANDOM NO. SEEDS= 1, 66"
        puts $f ""
        puts $f "IFULL= ENERGY DEPOSITION KERNEL"
        puts $f ""
        puts $f "DOPPLER BROADENING= On"
        puts $f ""
        puts $f ":stop Monte Carlo inputs:"
        puts $f "############################"
        puts $f ""
        puts $f "############################"
        puts $f ":start geometrical inputs:"
        puts $f ""
        puts $f "NUMBER OF CONES= 0"
        puts $f ""
        puts $f " NUMBER OF SPHERES = 33"
        puts $f ""
        puts $f " RADII= $sd0h, "
```

```
puts $f "        $sd1,$sd1h, "
puts $f "        $sd2,$sd2h, "
puts $f "        $sd3,$sd3h, "
puts $f "        $sd4,$sd4h, "
puts $f "        $sd5,$sd5h, "
puts $f "        $sd6,$sd6h, "
puts $f "        $sd7,$sd7h, "
puts $f "        $sd8,$sd8h, "
puts $f "        $sd9,$sd9h, "
puts $f "        $sd10,$sd10h, "
puts $f "        $sd11,$sd11h, "
puts $f "        $sd12,$sd12h, "
puts $f "        $sd13,$sd13h, "
puts $f "        $sd14,$sd14h,$sd15, "
puts $f "        $sd15h,$sd16,$sdmax "
puts $f " "
puts $f "MEDIA= $media; "
puts $f ""
puts $f "MEDNUM= 1    # define what medium goes where"
puts $f "             # use region numbers to define this"
puts $f ""
puts $f "START REGION= 2   #This puts water everywhere"
puts $f "STOP REGION= 1153"
puts $f ""
puts $f ":stop geometrical inputs:"
puts $f "#########################"
puts $f ""
puts $f "#########################"
puts $f ":start source inputs:"
puts $f ""
puts $f "INCIDENT PARTICLE= electron  "
puts $f ""
puts $f ""
puts $f "INCIDENT ENERGY= mono-energetic "
puts $f "INCIDENT KINETIC ENERGY(MEV)= $E "
puts $f ""
puts $f ""
puts $f "SOURCE NUMBER= 1 # isotropic point source AT origin"
puts $f ""
puts $f ":stop source inputs:"
puts $f "#########################"
puts $f ""
puts $f "#########################"
puts $f ":start MC transport parameter:"
puts $f ""
puts $f "Global ECUT= $ECUT "
puts $f "Global PCUT= 0.001 "
puts $f "Global SMAX= $smax "
puts $f ""
puts $f "ESTEPE= .25 "
puts $f "XImax= 0.0 "
puts $f ""
puts $f "Skin depth for BCA= 3 "
puts $f ""
```

```
        puts $f "Boundary crossing algorithm= EXACT "
        puts $f ""
        puts $f "Electron-step algorithm= PRESTA-II "
        puts $f ""
        puts $f "Spin effects= on "
        puts $f ""
        puts $f "Brems angular sampling= KM "
        puts $f ""
        puts $f "Brems cross sections= BH "
        puts $f ""
        puts $f "Bound Compton scattering= On "
        puts $f ""
        puts $f "Pair angular sampling= Simple "
        puts $f ""
        puts $f "Photoelectron angular sampling= On "
        puts $f ""
        puts $f "Rayleigh scattering= On "
        puts $f ""
        puts $f "Atomic relaxations= On "
        puts $f ""
        puts $f ":stop MC transport parameter:"
        puts $f "##########################"
        puts $f ""
        puts $f "##########################"
        puts $f ":start variance reduction:"
        puts $f ""
        puts $f " ELECTRON RANGE REJECTION= on "
        puts $f " ESAVEIN= 1.0 "
        puts $f ""
        puts $f " EXPONENTIAL TRANSFORM C= 0.0000 "
        puts $f ""
        puts $f " PHOTON FORCING= Off "
        puts $f " START FORCING= 1 "
        puts $f " STOP FORCING AFTER= 2 "
        puts $f ""
        puts $f ":stop variance reduction:"
        puts $f "##########################"

        close $f

        file rename phiH2O${EN}.egsinp
PHIsmall_H2O/phiH2O${EN}.egsinp
    }
```

Appendix B – FORTRAN Code Example: Energy and Depth Scaling

```
C---FORTRAN code used to calculate depth and
C---energy scaling parameters
      program nonhomoDPK

      dimension xw(32),enw(32),errw(32),xw99(3),xww(32),Sxs(22)
      dimension xx(32),enx(32),errx(32),xxs(32),xx99(3),xwi(1500)
      dimension fracxn(32),fracwn(32),fracwni(1500),fracxni(1500)
      dimension enwi(1500),enxi(1500),errwP(32),errxP(32),xxi(1500)
      dimension fracx(32),fracw(32),fracwi(1500),fracxi(1500)
      dimension enxBi(1500),enxB(32),enwBi(1500),enwB(32)
      real b(300),c(300),d(300)

      data Sxs/.05,.1,.15,.2,.25,.3,.35,.4,.45,.5,.55,.6,.65,.7,
     1         .75,.8,.85,.9,.95,1.0,1.05,1.1/

      n = 300
      m = 300
      irecord = 32
      irecordi = 1500

C-------------------------------------------------------------------
--------------------------
      open(unit=3, file = 'RR/Data/energyW.out', status='old')
      do 11 i=1,irecord
            Read(3,*) enw(i)
   11 continue
      Close(3)

      open(unit=5, file = 'RR/Data/errorW.out', status='old')
      do 13 i=1,irecord
            Read(5,*) errw(i)
   13 continue
      Close(5)

      open(unit=7, file = 'RR/Data/radiusW.out', status='old')
      do 15 i=1,irecord
            Read(7,*) xw(i)
   15 continue
      Close(7)

      open(unit=14, file = 'RR/Data/errorWP.out', status='old')
      do 20 i=1,irecord
            Read(14,*) errwP(i)
   20 continue
      Close(14)

      open(unit=9, file = 'RR/Data/extraW.out', status='old')
      Read(9,*) x90W
      Close(9)

      Do i = 1,irecord  !zero out anything with error GE 5.0
```

```
            if(errw(i).ge.5.0) enw(i) = 0.0
            if(errw(i).le.0.0) enw(i) = 0.0
      End Do

      Do i = 1,irecord
            enwB(i) = enw(i)
      End Do

      Do i = 1,irecord  !cut off the radiative tail after primary DPK
ends
            if(errwP(i).le.0.0) enw(i) = 0.0
      End Do

      open(unit=4, file = 'RR/Data/energyX.out', status='old')
      Read(4,*) enxx
      do 12 i=1,irecord
            Read(4,*) enx(i)
   12 continue
      Read(4,*) enbrem
      Close(4)

      open(unit=6, file = 'RR/Data/errorX.out', status='old')
      Read(6,*) err_enxx
      do 14 i=1,irecord
            Read(6,*) errx(i)
   14 continue
      Close(6)

      open(unit=8, file = 'RR/Data/radiusX.out', status='old')
      Read(8,*) xx_enxx
      do 16 i=1,irecord
            Read(8,*) xx(i)
   16 continue
      Close(8)

      open(unit=10, file = 'RR/Data/extraX.out', status='old')
      Read(10,*) x90X
      Read(10,*) Sx
      Read(10,*) Ex
      Close(10)

      open(unit=12, file = 'RR/Data/errorXP.out', status='old')
      Read(12,*) err_enxxP
      do 18 i=1,irecord
            Read(12,*) errxP(i)
   18 continue
      Close(12)


      Do i = 1,irecord  !zero out anything with error GE 5.0
            if(errx(i).ge.5.0) enx(i) = 0.0
            if(errx(i).le.0.0) enx(i) = 0.0
      End Do
```

```
      Do i = 1,irecord
            enxB(i) = enx(i)
      End Do

      Do i = 1,irecord  !cut off the brems tail after primary ends

            if(errxP(i).le.0.0) enx(i) = 0.0
      End Do

c---find absorption sphere radius and adjust non-homo DPK's
accordingly
      xplus=x90X*Sxs(Sx)

      do 410 i=1,irecord
      xx(i)= xx(i) - xplus
  410 continue

c------------ Generate DPK's -------------------------

c---normalize DPK's to account for radiative loss past electron range
      totnw=0.0
      totnx=enxx

      do 501 i=1,irecord
      totnw=totnw+enw(i)
      totnx=totnx+enx(i)
  501 continue

      fracn=enxx/totnx
      fracwn(1)= enw(1)/totnw
      fracxn(1)= fracn + enx(1)/totnx

c---find % deposition at each x
      do 600 i=2,irecord
      fracwn(i)=fracwn(i-1) + enw(i)/totnw
      fracxn(i)=fracxn(i-1) + enx(i)/totnx
  600 continue

c---non-normalized fractions
      frac=enxx
      fracw(1)= enwB(1)
      fracx(1)= frac + enxB(1)
c---find % deposition at each x
      do 601 i=2,irecord
      fracw(i)=fracw(i-1) + enwB(i)
      fracx(i)=fracx(i-1) + enxB(i)
  601 continue

C---cubic spline fits and expansion of DPK's to 1500 data points
      Call spline(irecord,xw,fracwn,b,c,d)
      Do i = 1,1500
            xwi(i) = Float(i)*xw(32)/1500
            fracwni(i) = slvsp(irecord,xwi(i),xw,fracwn,b,c,d)
      End Do
```

```
      Call spline(irecord,xx,fracxn,b,c,d)
      Do i = 1,1500
            xxi(i) = Float(i)*xx(32)/1500
            fracxni(i) = slvsp(irecord,xxi(i),xx,fracxn,b,c,d)
      End Do

      Call spline(irecord,xw,fracw,b,c,d)
      Do i = 1,1500
            xwi(i) = Float(i)*xw(32)/1500
            fracwi(i) = slvsp(irecord,xwi(i),xw,fracw,b,c,d)
      End Do

      Call spline(irecord,xx,fracx,b,c,d)
      Do i = 1,1500
            xxi(i) = Float(i)*xx(32)/1500
            fracxi(i) = slvsp(irecord,xxi(i),xx,fracx,b,c,d)
      End Do

      Call spline(irecord,xw,enw,b,c,d)
      Do i = 1,1500
            enwi(i) = slvsp(irecord,xwi(i),xw,enw,b,c,d)
      End Do

      Call spline(irecord,xx,enxB,b,c,d)
      Do i = 1,1500
            enxBi(i) = slvsp(irecord,xxi(i),xx,enxB,b,c,d)
      End Do

      Call spline(irecord,xw,enwB,b,c,d)
      Do i = 1,1500
            enwBi(i) = slvsp(irecord,xwi(i),xw,enwB,b,c,d)
      End Do

      Call spline(irecord,xx,enx,b,c,d)
      Do i = 1,1500
            enxi(i) = slvsp(irecord,xxi(i),xx,enx,b,c,d)
      End Do

      do j=1, irecordi
        if (enxi(j).lt.0.0) enxi(j)=0.0
      end do

      i=1
      f99 = 0.99

c---find depth scaling using 99% energy deposition point in
normalized DPK's

      do j=1, irecordi
        if (fracwni(j).ge.f99) goto 700
      end do
  700 xw99(1) = xwi(j)
```

```
      do i=1, irecordi
        if (fracxni(i).ge.f99) goto 703
      end do
  703 xx99(1) = xxi(i)

      xshift=xw99(1)-xx99(1)

      do 713 i=1,irecordi
      xwi(i)= (xwi(i) - xshift)
  713 continue

      do 714 i=1,irecord
      xw(i)= (xw(i) - xshift)
  714 continue

c---find energy scaling using normalized DPK's

      do j=1, irecordi
        if (xwi(j).ge.xxi(1)) goto 606
      end do
  606 fracww = fracwi(j)
      xx90x = xplus/x90X
      xx90w = xshift/x90W
      Rfracx = (1-fracxi(1)-(1-totnx))
      Rfracw = (1-fracww-(1-totnw))
      xx90wp = xplusw
      reducer = Rfracx/Rfracw

c---for plotting

      do 716 i=1,irecord
      enx(i)=enx(i)
      enwB(i)=enwB(i)*reducer
  716 continue

c---Write the output files

      OPEN(16, FILE='RR/Data/xplus.out',STATUS='Unknown')
      write(16,*) xplus
      close(16)

      OPEN(17, FILE='RR/Data/xshift.out',STATUS='Unknown')
      write(17,*) xshift
      close(17)

      OPEN(18, FILE='RR/Data/xx90x.out',STATUS='Unknown')
      write(18,*) xx90x
      close(18)

      OPEN(19, FILE='RR/Data/xx90w.out',STATUS='Unknown')
      write(19,*) xx90w
      close(19)

      OPEN(20, FILE='RR/Data/RfracX.out',STATUS='Unknown')
```

```
      write(20,*) Rfracx
      close(20)

      OPEN(21, FILE='RR/Data/RfracW.out',STATUS='Unknown')
      write(21,*) Rfracw
      close(21)

      OPEN(22, FILE='RR/Data/RfracWp.out',STATUS='Unknown')
      write(22,*) Rfracwp
      close(22)

      OPEN(23, FILE='RR/Data/xx90wp.out',STATUS='Unknown')
      write(23,*) xx90wp
      close(23)

      close(25)
      OPEN(26, FILE='RR/Data/xx.out',STATUS='Unknown')
      do j = 1, irecord
         write(26,*)xx(j)
      end do
      close(26)

      OPEN(27, FILE='RR/Data/xw.out',STATUS='Unknown')
      do j = 1, irecord
         write(27,*) xw(j)
      end do
      close(27)

      OPEN(28, FILE='RR/Data/enx.out',STATUS='Unknown')
      do j = 1, irecord
         write(28,*) enxB(j)
      end do
      close(28)

      OPEN(29, FILE='RR/Data/enw.out',STATUS='Unknown')
      do j = 1, irecord
         write(29,*) enwB(j)
      end do
      close(29)

      stop
      end

C
**********************************************************************
***
      SUBROUTINE SPLINE(M,X,Y,B,C,D)
**********************************************************************
***
C  THIS SUBROUTINE GENERATES A SPLINE FIT TO A 1 DIMENSIONAL ARRAY,
C  FORCING THE SPLINE TO PASS THROUGH THE DATA
      INTEGER N,M
      REAL X(M),Y(M),B(M),C(M),D(M)
C
```

```
      N=M
      NM1=N-1
      IF(N.LT.2) RETURN
      IF(N.LT.3) GO TO 50
C
      D(1)=X(2)-X(1)
      C(2)=(Y(2)-Y(1))/D(1)
      DO 10 I=2,NM1
         D(I)=X(I+1)-X(I)
         B(I)=2.*(D(I-1)+D(I))
         C(I+1)=(Y(I+1)-Y(I))/D(I)
         C(I)=C(I+1)-C(I)
10    CONTINUE
C
      B(1)=-1.*D(1)
      B(N)=-1.*D(N-1)
      C(1)= 0.
      C(N)= 0.
      IF (N.EQ.3) GO TO 15
      C(1)=C(3)/(X(4)-X(2)) - C(2)/(X(3)-X(1))
      C(N)=C(N-1)/(X(N)-X(N-2)) - C(N-2)/(X(N-1)-X(N-3))
      C(1)=C(1)*D(1)**2/(X(4)-X(1))
      C(N)=-C(N)*D(N-1)**2/(X(N)-X(N-3))
C
15    DO 20 I=2,N
         T=D(I-1)/B(I-1)
         B(I)=B(I)-T*D(I-1)
         C(I)=C(I)-T*C(I-1)
20    CONTINUE
C
      C(N)=C(N)/B(N)
      DO 30 IB=1,NM1
         I=N-IB
         C(I)=(C(I)-D(I)*C(I+1))/B(I)
30    CONTINUE
C
      B(N)=(Y(N)-Y(NM1))/D(NM1)+D(NM1)*(C(NM1)+2.*C(N))
      DO 40 I=1,NM1
         B(I)=(Y(I+1)-Y(I))/D(I)-D(I)*(C(I+1)+2.*C(I))
         D(I)=(C(I+1)-C(I))/D(I)
         C(I)=3.*C(I)
40    CONTINUE
         C(N)=3.*C(N)
         D(N)=D(N-1)
      RETURN
C
50    B(I)=(Y(2)-Y(1))/(X(2)-X(1))
      C(1)=0.
      D(1)=0.
      B(2)=B(1)
      C(2)=0.
      D(2)=0.
      RETURN
      END
```

```
C
C ***********************************************************
        REAL FUNCTION SLVSP(M,A,X,Y,B,C,D)
        INTEGER N,M
        REAL A,X(M),Y(M),B(M),C(M),D(M)
C
C  THIS SUBROUTINE EVALUATES THE CUBIC SPLINE FUNCTION FOR A 1-D
ARRAY
C
        INTEGER I,J,K
        REAL DX
        DATA I/1/
         N=M
        IF(I.GE.N)I=1
        IF(A.LT.X(I)) GO TO 10
        IF(A.LE.X(I+1)) GO TO 30
C
10      I=1
        J=N+1
20      K=(I+J)/2
        IF(A.LT.X(K))J=K
        IF(A.GE.X(K))I=K
        IF(J.GT.I+1) GO TO 20
C
30      DX=A-X(I)
        SLVSP=Y(I)+DX*(B(I)+DX*(C(I)+DX*D(I)))
        RETURN
        END
c
```

Appendix C – Bash Shell Script Example: Planar Dose Profiles

```
#!/bin/bash
#This is a bash shell scripts used to parse EGSnrc output data
#for planar dose profiles and creates usable data files for
#plotting and curve fit analysis

rm -f parse.out
g77 -o parse.out parse.f

mkdir Data

#create water energy and error files by parsing EGSnrc outputs
for G in  {1..31} ; do

    rm -f Data/extraw.out
    rm -f Data/energy1w.out
    rm -f Data/energy10w.out
    rm -f Data/error1w.out
    rm -f Data/error10w.out

    grep -A 0 "INCIDENT KINETIC ENERGY" H2O/LST/H2O${G}.egslst >
output1
    cut -c 60-66 output1 >> Data/extraw.out

    for j in {148..1147}
        do
             sed -n "${j}p" H2O/LST/H2O${G}.egslst >> output2
        done
    cut -c 13-23 output2 >> Data/energy1w.out
    cut -c 27-32 output2 >> Data/error1w.out

    for j in {1151..2150}
        do
             sed -n "${j}p" H2O/LST/H2O${G}.egslst >> output3
        done
    cut -c 13-23 output3 >> Data/energy10w.out
    cut -c 27-32 output3 >> Data/error10w.out

    rm -f output1
    rm -f output2
    rm -f output3

#cycle through all materials and continue parsing
    for H in  Al Ti Fe Ga Rb Zr Ru Ag Sn Ba Nd Gd Yb Ta Pt Pb Ac Pu ;
do

        rm -f Data/extrax.out
        rm -f Data/energy1x.out
        rm -f Data/energy10x.out
        rm -f Data/error1x.out
        rm -f Data/error10x.out

        mkdir Data/${H}
        echo $H >> Data/extrax.out
```

```
        for j in {149..1148}
        do
             sed -n "${j}p" Source/${H}/LST/${H}${G}.egslst >>
output1
        done
        cut -c 13-23 output1 >> Data/energy1x.out
        cut -c 27-32 output1 >> Data/error1x.out

        for j in {1152..2151}
        do
             sed -n "${j}p" Source/${H}/LST/${H}${G}.egslst >>
output2
        done
        cut -c 13-23 output2 >> Data/energy10x.out
        cut -c 27-32 output2 >> Data/error10x.out

        rm -f output1
        rm -f output2

        #run FORTRAN code to determine 10 cm2 data and zero out data
w/ large error
        ./parse.out

        #create output files for TableCurve 3D plotting
        cat Data/ENW1.out >> Data/${G}/ENW1${G}.out
        cat Data/ENW10.out >> Data/${G}/ENW10${G}.out
        cat Data/ENX1.out >> Data/${H}/ENX1${H}.out
        cat Data/ENX10.out >> Data/${H}/ENX10${H}.out
        cat Data/Depth.out >> Data/${H}/Depth.out
        cat Data/ANUM.out >> Data/${H}/ANUM.out
        cat Data/Energy.out >> Data/${H}/Energy.out

    done

done
```

Appendix D – BATCH Script Example: EGSnrc Volume Sources

```
::This is a BATCH script used to execute EGSnrc "cavity"
::input files for volumetric sources

::Cylce through all source sizes
SET startS=1
SET stopS=5

::Cylce through all nuclides and source materials
FOR %%N IN ( Pr Mn P Se Sn Y Bi I Co ) DO (
    FOR %%F IN (SS TA UO) DO (

        MD Cy\%%F\LOG
        FOR /L %%H IN (%startS%,1,%stopS%) DO (
            ::move imput files do execution folder, execute, and
catalogue desired outputs
            MOVE C:\egsnrc_mp\cavity\Cy\%%F\Cy%%N%%F%%H.egsinp
C:\egsnrc_mp\cavity\Cy%%N%%F%%H.egsinp
            cavity -i Cy%%N%%F%%H -p water_1KeV -b
            MOVE C:\egsnrc_mp\cavity\Cy%%N%%F%%H.egsinp
C:\egsnrc_mp\cavity\Cy\%%F\Cy%%N%%F%%H.egsinp
            MOVE C:\egsnrc_mp\cavity\Cy%%N%%F%%H.egslog
C:\egsnrc_mp\cavity\Cy\%%F\LOG\Cy%%N%%F%%H.egslog
            DEL C:\egsnrc_mp\cavity\Cy%%N%%F%%H.egsdat
        )
    )
)
```

Appendix E – Additional EGSnrc Input Files

Planar Dose Profiles: "doserznrc" user code input file example

```
###########################################################################
#
TITLE= Planar Dose data for 8.0 Mev electrons with lead scattering
material

############################
:start I/O control:

IWATCH= off
STORE INITIAL RANDOM NUMBERS= no
IRESTART= first
STORE DATA ARRAYS= yes
OUTPUT OPTIONS= dose summary
ELECTRON TRANSPORT= normal
DOSE ZBOUND MIN= 1
DOSE ZBOUND MAX= 1010
DOSE RBOUND MIN= 0
DOSE RBOUND MAX= 60

:stop I/O control:
############################

############################
:start Monte Carlo inputs:

NUMBER OF HISTORIES= 1000000
INITIAL RANDOM NO. SEEDS= 1, 3
MAX CPU HOURS ALLOWED= 90.000
IFULL= dose and stoppers
STATISTICAL ACCURACY SOUGHT= 0.0000
SCORE KERMA= no

:stop Monte Carlo inputs:
############################

############################
:start geometrical inputs:

#Define geometry using groups of planes.  The 1000 planes
#carve out the dose volumes of different radii

METHOD OF INPUT= groups
Z OF FRONT FACE= 0
NSLAB= 1, 1, 1000, 1
SLAB THICKNESS= 5, 5e-004, 1e-003, 5
RADII= 0.56419, 1.7841, 5.641896
MEDIA= lead, water

DESCRIPTION BY= planes
```

```
MEDNUM= 1, 2, 2, 2, 2, 2
START ZSLAB= 1, 2, 3, 3, 3, 1003
STOP ZSLAB= 1, 2, 1002, 1002, 1002, 1003
START RING= 3, 1, 1, 2, 3, 1
STOP RING= 3, 3, 1, 2, 3, 3

:stop geometrical inputs:

#########################

#########################
:start source inputs:

#position electron source at interface

INCIDENT PARTICLE= electron
SOURCE NUMBER= 3
SOURCE OPTIONS= 0, 0, 5, 5
INCIDENT ENERGY= mono-energetic
INCIDENT KINETIC ENERGY(MEV)= 8.00E+00

:stop source inputs:
#########################

#########################
:start MC transport parameter:

Global ECUT= 0.512
Global PCUT= 0.001
Global SMAX= 0.0
ESTEPE= 0.25
XImax= 0.0
Skin depth for BCA= 3
Boundary crossing algorithm= EXACT
Electron-step algorithm= PRESTA-II
Spin effects= on
Brems angular sampling= KM
Brems cross sections= BH
Photon cross sections= si
Electron Impact Ionization= Off
Bound Compton scattering= Off
Pair angular sampling= Simple
Photoelectron angular sampling= Off
Rayleigh scattering= Off
Atomic relaxations= On
Set PCUT= 0
Set PCUT start region= 1
Set PCUT stop region= 1
Set ECUT= 0
Set ECUT start region= 1
Set ECUT stop region= 1
Set SMAX= 0
Set SMAX start region= 1
Set SMAX stop region= 1
```

```
:stop MC transport parameter:
#########################

#########################
:start variance reduction:

BREM SPLITTING= off
NUMBER OF BREMS PER EVENT= 1
CHARGED PARTICLE RUSSIAN ROULETTE= off
ELECTRON RANGE REJECTION= off
ESAVEIN= 0.0
RUSSIAN ROULETTE DEPTH= 0.0000
RUSSIAN ROULETTE FRACTION= 0.0000
EXPONENTIAL TRANSFORM C= 0.0000
PHOTON FORCING= on
START FORCING= 1
STOP FORCING AFTER= 1
CS ENHANCEMENT FACTOR= 1
CS ENHANCEMENT START REGION= 1, 1
CS ENHANCEMENT STOP REGION= 1, 1

:stop variance reduction:
#########################

#########################
:start plot control:

PLOTTING= off
LINE PRINTER OUTPUT= off
EXTERNAL PLOTTER OUTPUT= off
EXTERNAL PLOT TYPE= Histogram
PLOT RADIAL REGION IX= 1, 2
PLOT PLANAR REGION IZ= 10

:stop plot control:
 ########################
```

Volume Source Skin Dose Calculations: "cavity" user code input file example

```
##################################################################
# 'cavity' input file for skin dose from Bi210 Stainless Steel
# spherical source, size 5.  Dose area is 1 cm^2
##################################################################################
#######
:start geometry definition:
    ################################### The planes
    :start geometry:
        library   = egs_planes
        type      = EGS_Zplanes
        name      = outer_planes
        positions = -10 0 4
        :stop geometry:
    ################################### The cylinders
    :start geometry:
        library   = egs_cylinders
        type      = EGS_ZCylinders
        name      = outer_cylinders
        radii     = 4
    :stop geometry:
    ################################### The simulation container
geometry
    :start geometry:
        library   = egs_ndgeometry
        name      = air_tis_container
        dimensions= outer_planes outer_cylinders
        :start media input:
            media = water air
            set medium = 0 1
            set medium = 1 0
        :stop media input:
    :stop geometry:
    #Define dose depths
    :start geometry:
        library   = egs_cones
        type      = EGS_ConeStack
        name      = dose_depths
        axis      = 0 0 0.0035  0 0 1
        #35-45 um
        :start layer:
            thickness    = 0.001
            top radii    = 0.56418
            bottom radii = 0.56418
            media        = water
        :stop layer:
        #45-65 um
        :start layer:
            thickness    = 0.002
            top radii    = 0.56418
            bottom radii = 0.56418
```

```
    media        = water
:stop layer:
#65-75 um
:start layer:
    thickness    = 0.001
    top radii    = 0.56418
    bottom radii = 0.56418
    media        = water
:stop layer:
#75-95 um
:start layer:
    thickness    = 0.002
    top radii    = 0.56418
    bottom radii = 0.56418
    media        = water
:stop layer:
#95-105 um
:start layer:
    thickness    = 0.001
    top radii    = 0.56418
    bottom radii = 0.56418
    media        = water
:stop layer:
#105-145 um
:start layer:
    thickness    = 0.004
    top radii    = 0.56418
    bottom radii = 0.56418
    media        = water
:stop layer:
#145-155 um
:start layer:
    thickness    = 0.001
    top radii    = 0.56418
    bottom radii = 0.56418
    media        = water
:stop layer:
#155-195 um
:start layer:
    thickness    = 0.004
    top radii    = 0.56418
    bottom radii = 0.56418
    media        = water
:stop layer:
#195-205 um
:start layer:
    thickness    = 0.001
    top radii    = 0.56418
    bottom radii = 0.56418
    media        = water
:stop layer:
#205-295 um
:start layer:
    thickness    = 0.009
```

```
    top radii    = 0.56418
    bottom radii = 0.56418
    media        = water
:stop layer:
#295-305 um
:start layer:
    thickness    = 0.001
    top radii    = 0.56418
    bottom radii = 0.56418
    media        = water
:stop layer:
#305-395 um
:start layer:
    thickness    = 0.009
    top radii    = 0.56418
    bottom radii = 0.56418
    media        = water
:stop layer:
#395-405 um
:start layer:
    thickness    = 0.001
    top radii    = 0.56418
    bottom radii = 0.56418
    media        = water
:stop layer:
#405-495 um
:start layer:
    thickness    = 0.009
    top radii    = 0.56418
    bottom radii = 0.56418
    media        = water
:stop layer:
#495-505 um
:start layer:
    thickness    = 0.001
    top radii    = 0.56418
    bottom radii = 0.56418
    media        = water
:stop layer:
#505-745 um
:start layer:
    thickness    = 0.024
    top radii    = 0.56418
    bottom radii = 0.56418
    media        = water
:stop layer:
#745-755 um
:start layer:
    thickness    = 0.001
    top radii    = 0.56418
    bottom radii = 0.56418
    media        = water
:stop layer:
#755-995 um
```

```
        :start layer:
            thickness    = 0.024
            top radii    = 0.56418
            bottom radii = 0.56418
            media        = water
        :stop layer:
        #995-1005 um
        :start layer:
            thickness    = 0.001
            top radii    = 0.56418
            bottom radii = 0.56418
            media        = water
        :stop layer:
    :stop geometry:

##########################################################################
####
    # Add source MATERIAL if needed...
    :start geometry:
        library = egs_spheres
        name = source_sphere
        radii = 0.01
        :start media input:
            media = stainless
            set medium = 0 0
        :stop media input:
    :stop geometry:
    :start geometry:
        library  = egs_gtransformed
        my geometry = source_sphere
        name     = source_volume
        :start transformation:
            translation = 0 0 -0.010001
        :stop transformation:
    :stop geometry:

##########################################################################
####
    # Put them together...
    :start geometry:
        library  = egs_genvelope
        name = geometry_with_source
        base geometry = air_tis_container
        inscribed geometries = dose_depths source_volume

    :stop geometry:
    simulation geometry = geometry_with_source
:stop geometry definition:
##########################################################################
##########
:start source definition:
########################################### define the source:
    :start source:
        library = egs_isotropic_source
```

```
         name = the_source
         :start shape:
                 type = sphere
                 radius = 0.01
                 midpoint = 0, 0, -0.010001
                 axis = 0, 0, 1
         :stop shape:
         :start spectrum:
              type = tabulated spectrum
              energies = 1.05E-03 1.15E-03 1.25E-03 1.35E-03 1.45E-03,
      1.55E-03 1.70E-03 1.90E-03 2.10E-03 2.30E-03,
      2.50E-03 2.70E-03 2.90E-03 3.10E-03 3.40E-03,
      3.80E-03 4.25E-03 4.75E-03 5.25E-03 5.75E-03,
      6.25E-03 6.75E-03 7.25E-03 7.75E-03 8.25E-03,
      8.75E-03 9.50E-03 1.05E-02 1.15E-02 1.25E-02,
      1.35E-02 1.45E-02 1.55E-02 1.70E-02 1.90E-02,
      2.10E-02 2.30E-02 2.50E-02 2.70E-02 2.90E-02,
      3.10E-02 3.40E-02 3.80E-02 4.25E-02 4.75E-02,
      5.25E-02 5.75E-02 6.25E-02 6.75E-02 7.25E-02,
      7.75E-02 8.25E-02 8.75E-02 9.50E-02 1.05E-01,
      1.15E-01 1.25E-01 1.35E-01 1.45E-01 1.55E-01,
      1.70E-01 1.90E-01 2.10E-01 2.30E-01 2.50E-01,
      2.70E-01 2.90E-01 3.10E-01 3.40E-01 3.80E-01,
      4.25E-01 4.75E-01 5.25E-01 5.75E-01 6.25E-01,
      6.75E-01 7.25E-01 7.75E-01 8.25E-01 8.75E-01,
      9.50E-01 1.05E+00 1.13E+00 1.1615
               probabilities =1.28E+00 1.28E+00 1.28E+00 1.28E+00
1.28E+00,
      1.28E+00 1.28E+00 1.28E+00 1.28E+00 1.28E+00,
      1.28E+00 1.28E+00 1.28E+00 1.28E+00 1.28E+00,
      1.28E+00 1.28E+00 1.28E+00 1.28E+00 1.28E+00,
      1.28E+00 1.28E+00 1.28E+00 1.28E+00 1.28E+00,
      1.28E+00 1.29E+00 1.29E+00 1.29E+00 1.29E+00,
      1.29E+00 1.29E+00 1.29E+00 1.29E+00 1.29E+00,
      1.30E+00 1.30E+00 1.30E+00 1.30E+00 1.31E+00,
      1.31E+00 1.32E+00 1.32E+00 1.33E+00 1.33E+00,
      1.34E+00 1.34E+00 1.35E+00 1.36E+00 1.36E+00,
      1.37E+00 1.37E+00 1.37E+00 1.38E+00 1.39E+00,
      1.40E+00 1.40E+00 1.41E+00 1.41E+00 1.42E+00,
      1.43E+00 1.43E+00 1.43E+00 1.43E+00 1.42E+00,
      1.41E+00 1.40E+00 1.39E+00 1.35E+00 1.31E+00,
      1.24E+00 1.16E+00 1.07E+00 9.65E-01 8.56E-01,
      7.43E-01 6.29E-01 5.15E-01 4.05E-01 3.01E-01,
      1.27E-01 2.04E-02 0.00E+00

              spectrum type = 1
         :stop spectrum:
         geometry = geometry_with_source
         charge = -1
     :stop source:
     simulation source = the_source
:stop source definition:
##################################### Run control
:start run control:
```

```
    ncase = 1000000
:stop run control:
##################################### Scoring options
:start scoring options:
    calculation type = dose
    :start calculation geometry:
        geometry name = geometry_with_source
        cavity regions = 2
        cavity mass = 0.001000
    :stop calculation geometry:
    :start calculation geometry:
        geometry name = geometry_with_source
        cavity regions = 4
        cavity mass = 0.001000
    :stop calculation geometry:
    :start calculation geometry:
        geometry name = geometry_with_source
        cavity regions = 6
        cavity mass = 0.001000
    :stop calculation geometry:
        :start calculation geometry:
        geometry name = geometry_with_source
        cavity regions = 8
        cavity mass = 0.00100
    :stop calculation geometry:
    :start calculation geometry:
        geometry name = geometry_with_source
        cavity regions = 10
        cavity mass = 0.001000
    :stop calculation geometry:
        :start calculation geometry:
        geometry name = geometry_with_source
        cavity regions = 12
        cavity mass = 0.001000
    :stop calculation geometry:
    :start calculation geometry:
        geometry name = geometry_with_source
        cavity regions = 14
        cavity mass = 0.001000
    :stop calculation geometry:
        :start calculation geometry:
        geometry name = geometry_with_source
        cavity regions =16
        cavity mass = 0.001000
    :stop calculation geometry:
    :start calculation geometry:
        geometry name = geometry_with_source
        cavity regions = 18
        cavity mass = 0.001000
    :stop calculation geometry:
        :start calculation geometry:
        geometry name = geometry_with_source
        cavity regions = 20
        cavity mass = 0.001000
```

```
    :stop calculation geometry:
:stop scoring options:
######################################## variance reduction
:start variance reduction:
:stop variance reduction:
######################################## Transport parameters
:start MC transport parameter:
:stop MC transport parameter:
```

Appendix F – Scaling and Scattering Model Curve Fit Parameters

Table F 1. *DSP* curve fit parameters for Eq. (5.1)

	Fit Parameter								
Z	**a**	**b**	**c**	**d**	**e**	**f**	**g**	**h**	**i**
13	-1.43E-01	-7.91E-02	2.21E-02	9.25E-04	1.07E+00	2.18E-02	6.27E-06	1.35E-05	-7.71E-03
22	-1.31E-02	-2.75E-01	6.04E-02	4.95E-05	1.21E+00	7.05E-02	1.09E-03	2.96E-04	-2.39E-02
26	3.48E-02	-3.47E-01	7.36E-02	7.61E-04	1.26E+00	8.89E-02	1.77E-03	3.53E-04	-3.05E-02
31	2.59E-02	-3.45E-01	6.81E-02	5.03E-04	1.26E+00	8.50E-02	2.36E-03	4.58E-04	-2.89E-02
37	-8.27E-03	-1.92E-01	3.14E-02	1.31E-03	1.15E+00	4.09E-02	2.72E-03	4.23E-04	-1.27E-02
40	9.78E-02	-3.90E-01	7.25E-02	1.21E-03	1.30E+00	9.30E-02	3.41E-03	5.58E-04	-3.14E-02
44	1.16E-01	-4.57E-01	8.26E-02	2.48E-03	1.34E+00	1.10E-01	4.56E-03	6.32E-04	-3.76E-02
47	1.35E-01	-4.59E-01	8.09E-02	2.57E-03	1.35E+00	1.07E-01	4.56E-03	6.45E-04	-3.67E-02
50	1.26E-01	-4.44E-01	7.55E-02	1.70E-03	1.34E+00	1.02E-01	4.19E-03	6.34E-04	-3.48E-02
56	1.19E-01	-3.79E-01	5.67E-02	2.17E-03	1.29E+00	8.06E-02	4.76E-03	6.43E-04	-2.61E-02
60	1.90E-01	-4.74E-01	7.23E-02	3.04E-03	1.36E+00	1.05E-01	6.12E-03	7.78E-04	-3.49E-02
64	1.82E-01	-4.94E-01	7.11E-02	3.58E-03	1.37E+00	1.07E-01	7.15E-03	8.74E-04	-3.54E-02
70	2.07E-01	-5.10E-01	7.11E-02	3.64E-03	1.38E+00	1.10E-01	6.87E-03	8.16E-04	-3.63E-02
73	2.50E-01	-5.79E-01	7.54E-02	5.15E-03	1.44E+00	1.26E-01	9.05E-03	9.79E-04	-4.31E-02
78	2.78E-01	-6.11E-01	7.73E-02	5.77E-03	1.46E+00	1.35E-01	1.01E-02	1.05E-03	-4.61E-02
82	2.77E-01	-5.58E-01	6.63E-02	4.23E-03	1.43E+00	1.19E-01	9.54E-03	1.09E-03	-3.95E-02
89	2.40E-01	-5.72E-01	6.42E-02	4.18E-03	1.44E+00	1.22E-01	1.04E-02	1.17E-03	-4.04E-02
94	3.55E-01	-6.35E-01	6.59E-02	5.33E-03	1.49E+00	1.35E-01	1.21E-02	1.32E-03	-4.62E-02

Table F 2. *ESP* curve fit parameters for Eq. (5.2)

	Fit Parameters									
Z	**a**	**b**	**c**	**d**	**e**	**f**	**g**	**h**	**i**	**j**
13	-2.26E-02	1.01E+00	-2.33E-01	6.89E-03	2.61E-01	-6.04E-01	-2.30E-01	7.77E-03	1.15E-01	-2.35E-01
22	-3.36E-02	9.89E-01	2.59E-01	1.77E-02	3.17E-01	-9.08E-01	2.57E-01	1.73E-02	-6.79E-02	1.63E-01
26	-4.75E-02	9.87E-01	2.20E-01	2.03E-02	4.60E-01	-1.26E+00	2.19E-01	2.00E-02	-7.91E-02	1.85E-01
31	-4.82E-02	9.88E-01	1.95E-01	1.78E-02	4.96E-01	-1.36E+00	1.95E-01	1.80E-02	-8.57E-02	1.95E-01
37	-3.88E-02	9.89E-01	1.96E-01	9.63E-03	4.69E-01	-1.39E+00	1.96E-01	9.68E-03	-9.23E-02	2.34E-01
40	-5.58E-02	9.88E-01	1.68E-01	2.14E-02	6.35E-01	-1.81E+00	1.69E-01	2.20E-02	-9.37E-02	2.35E-01
44	-6.34E-02	9.89E-01	1.60E-01	2.68E-02	7.52E-01	-2.09E+00	1.64E-01	2.80E-02	-9.19E-02	2.46E-01
47	-6.35E-02	9.89E-01	1.46E-01	2.60E-02	7.77E-01	-2.22E+00	1.50E-01	2.75E-02	-9.86E-02	2.61E-01
50	-6.16E-02	9.90E-01	1.53E-01	2.60E-02	7.52E-01	-2.19E+00	1.57E-01	2.71E-02	-9.05E-02	2.67E-01
56	-5.65E-02	9.90E-01	1.41E-01	2.05E-02	7.20E-01	-2.21E+00	1.44E-01	2.15E-02	-9.43E-02	2.92E-01
60	-6.85E-02	9.90E-01	1.30E-01	2.68E-02	8.80E-01	-2.67E+00	1.35E-01	2.84E-02	-1.03E-01	3.27E-01
64	-7.14E-02	9.92E-01	1.26E-01	2.95E-02	9.20E-01	-2.77E+00	1.32E-01	3.14E-02	-9.79E-02	3.33E-01
70	-7.15E-02	9.93E-01	1.21E-01	3.09E-02	9.67E-01	-3.00E+00	1.28E-01	3.30E-02	-9.18E-02	3.67E-01
73	-8.22E-02	9.96E-01	1.23E-01	3.81E-02	1.11E+00	-3.34E+00	1.31E-01	4.07E-02	-8.90E-02	3.89E-01
78	-8.58E-02	9.97E-01	1.20E-01	3.98E-02	1.19E+00	-3.61E+00	1.30E-01	4.26E-02	-7.86E-02	4.22E-01
82	-8.56E-02	9.98E-01	1.12E-01	3.95E-02	1.18E+00	-3.71E+00	1.21E-01	4.19E-02	-7.50E-02	4.44E-01
89	-8.67E-02	9.99E-01	1.01E-01	4.23E-02	1.16E+00	-3.59E+00	1.09E-01	4.46E-02	-6.20E-02	4.27E-01
94	-9.25E-02	1.00E+00	1.09E-01	4.65E-02	1.35E+00	-4.38E+00	1.20E-01	4.94E-02	-4.72E-02	5.17E-01

Table F 3. Planar dose profile fit parameters for 1 cm^2 dose averaging areas and electron energies ≤ 1.0 MeV.

	Fit Parameter										
Z	**a**	**b**	**c**	**d**	**e**	**f**	**g**	**h**	**i**	**j**	**k**
Air	-2.36E-04	-4.25E-04	3.98E-04	-2.23E-04	6.48E-04	-1.98E-04	-7.84E-05	3.33E-04	-3.11E-04	6.43E-05	-1.79E-05
Water	-1.89E-04	-3.53E-04	3.27E-04	-1.78E-04	5.26E-04	-1.60E-04	-6.10E-05	2.63E-04	-2.47E-04	5.07E-05	-1.37E-05
13	-1.62E-04	-3.09E-04	2.85E-04	-1.50E-04	4.53E-04	-1.36E-04	-4.90E-05	2.18E-04	-2.08E-04	4.24E-05	-1.03E-05
22	-1.43E-04	-2.77E-04	2.54E-04	-1.30E-04	4.01E-04	-1.20E-04	-3.95E-05	1.84E-04	-1.79E-04	3.64E-05	-7.47E-06
26	-1.39E-04	-2.71E-04	2.49E-04	-1.25E-04	3.91E-04	-1.17E-04	-3.74E-05	1.77E-04	-1.74E-04	3.53E-05	-6.75E-06
31	-1.36E-04	-2.67E-04	2.44E-04	-1.22E-04	3.83E-04	-1.14E-04	-3.52E-05	1.71E-04	-1.69E-04	3.45E-05	-6.03E-06
37	-1.36E-04	-2.66E-04	2.44E-04	-1.21E-04	3.82E-04	-1.14E-04	-3.44E-05	1.69E-04	-1.69E-04	3.44E-05	-5.63E-06
40	-1.34E-04	-2.63E-04	2.41E-04	-1.18E-04	3.76E-04	-1.12E-04	-3.31E-05	1.65E-04	-1.65E-04	3.37E-05	-5.17E-06
44	-1.37E-04	-2.68E-04	2.45E-04	-1.21E-04	3.84E-04	-1.14E-04	-3.40E-05	1.69E-04	-1.69E-04	3.44E-05	-5.39E-06
47	-1.37E-04	-2.68E-04	2.46E-04	-1.21E-04	3.84E-04	-1.14E-04	-3.39E-05	1.68E-04	-1.68E-04	3.43E-05	-5.33E-06
50	-1.40E-04	-2.73E-04	2.50E-04	-1.23E-04	3.92E-04	-1.17E-04	-3.46E-05	1.72E-04	-1.72E-04	3.51E-05	-5.39E-06
56	-1.40E-04	-2.73E-04	2.50E-04	-1.23E-04	3.91E-04	-1.16E-04	-3.44E-05	1.71E-04	-1.71E-04	3.46E-05	-5.31E-06
60	-1.45E-04	-2.82E-04	2.59E-04	-1.28E-04	4.06E-04	-1.21E-04	-3.64E-05	1.80E-04	-1.79E-04	3.64E-05	-5.80E-06
64	-1.45E-04	-2.82E-04	2.59E-04	-1.28E-04	4.06E-04	-1.21E-04	-3.59E-05	1.79E-04	-1.79E-04	3.64E-05	-5.54E-06
70	-1.48E-04	-2.87E-04	2.63E-04	-1.31E-04	4.13E-04	-1.23E-04	-3.71E-05	1.83E-04	-1.82E-04	3.68E-05	-5.90E-06
73	-1.47E-04	-2.85E-04	2.62E-04	-1.29E-04	4.10E-04	-1.22E-04	-3.64E-05	1.81E-04	-1.80E-04	3.65E-05	-5.68E-06
78	-1.52E-04	-2.94E-04	2.70E-04	-1.34E-04	4.23E-04	-1.26E-04	-3.84E-05	1.88E-04	-1.86E-04	3.76E-05	-6.19E-06
82	-1.55E-04	-2.99E-04	2.75E-04	-1.37E-04	4.31E-04	-1.29E-04	-3.91E-05	1.92E-04	-1.91E-04	3.88E-05	-6.23E-06
89	-1.58E-04	-3.04E-04	2.80E-04	-1.40E-04	4.39E-04	-1.31E-04	-4.06E-05	1.97E-04	-1.94E-04	3.93E-05	-6.71E-06
94	-1.62E-04	-3.11E-04	2.87E-04	-1.44E-04	4.51E-04	-1.35E-04	-4.19E-05	2.03E-04	-2.01E-04	4.08E-05	-6.97E-06

Table F 3 (Continued)

	Fit Parameter										
Z	**l**	**m**	**n**	**o**	**p**	**q**	**r**	**s**	**t**	**u**	**v**
Air	1.09E-04	-1.45E-04	9.45E-05	-1.35E-05	-2.61E-06	2.15E-05	-3.82E-05	3.58E-05	-1.75E-05	1.80E-06	-2.17E-07
Water	8.36E-05	-1.12E-04	7.31E-05	-1.04E-05	-1.98E-06	1.61E-05	-2.85E-05	2.69E-05	-1.32E-05	1.34E-06	-1.61E-07
13	6.56E-05	-8.96E-05	5.96E-05	-8.45E-06	-1.36E-06	1.16E-05	-2.12E-05	2.05E-05	-1.03E-05	1.08E-06	-7.64E-08
22	5.10E-05	-7.28E-05	4.98E-05	-7.09E-06	-8.24E-07	7.68E-06	-1.51E-05	1.55E-05	-8.19E-06	8.99E-07	-1.12E-08
26	4.77E-05	-6.92E-05	4.78E-05	-6.82E-06	-6.58E-07	6.71E-06	-1.38E-05	1.44E-05	-7.74E-06	8.68E-07	3.18E-08
31	4.44E-05	-6.60E-05	4.64E-05	-6.71E-06	-5.12E-07	5.68E-06	-1.23E-05	1.35E-05	-7.51E-06	8.58E-07	4.68E-08
37	4.30E-05	-6.50E-05	4.60E-05	-6.63E-06	-4.07E-07	5.12E-06	-1.17E-05	1.32E-05	-7.37E-06	8.48E-07	6.90E-08
40	4.10E-05	-6.29E-05	4.49E-05	-6.52E-06	-2.98E-07	4.48E-06	-1.09E-05	1.26E-05	-7.18E-06	8.42E-07	9.13E-08
44	4.22E-05	-6.45E-05	4.59E-05	-6.66E-06	-3.44E-07	4.73E-06	-1.12E-05	1.30E-05	-7.38E-06	8.54E-07	8.21E-08
47	4.18E-05	-6.39E-05	4.56E-05	-6.64E-06	-3.25E-07	4.61E-06	-1.10E-05	1.27E-05	-7.30E-06	8.61E-07	9.39E-08
50	4.30E-05	-6.60E-05	4.69E-05	-6.75E-06	-2.86E-07	4.71E-06	-1.16E-05	1.32E-05	-7.47E-06	8.64E-07	1.01E-07
56	4.25E-05	-6.51E-05	4.61E-05	-6.60E-06	-2.62E-07	4.55E-06	-1.12E-05	1.28E-05	-7.21E-06	8.42E-07	1.17E-07
60	4.54E-05	-6.91E-05	4.88E-05	-7.00E-06	-3.46E-07	5.19E-06	-1.23E-05	1.39E-05	-7.77E-06	8.93E-07	1.12E-07
64	4.46E-05	-6.86E-05	4.88E-05	-7.00E-06	-2.84E-07	4.80E-06	-1.20E-05	1.38E-05	-7.77E-06	8.82E-07	1.12E-07
70	4.61E-05	-6.99E-05	4.93E-05	-7.07E-06	-3.49E-07	5.21E-06	-1.24E-05	1.40E-05	-7.83E-06	9.08E-07	1.09E-07
73	4.51E-05	-6.88E-05	4.88E-05	-7.01E-06	-3.11E-07	4.91E-06	-1.19E-05	1.37E-05	-7.74E-06	9.01E-07	1.11E-07
78	4.79E-05	-7.21E-05	5.05E-05	-7.19E-06	-3.91E-07	5.56E-06	-1.29E-05	1.44E-05	-7.97E-06	9.09E-07	1.03E-07
82	4.90E-05	-7.44E-05	5.23E-05	-7.47E-06	-3.61E-07	5.61E-06	-1.35E-05	1.52E-05	-8.38E-06	9.38E-07	1.14E-07
89	5.11E-05	-7.62E-05	5.30E-05	-7.56E-06	-4.58E-07	6.22E-06	-1.41E-05	1.55E-05	-8.50E-06	9.73E-07	1.06E-07
94	5.30E-05	-7.92E-05	5.53E-05	-7.89E-06	-4.89E-07	6.54E-06	-1.50E-05	1.65E-05	-8.97E-06	1.01E-06	9.54E-08

Table F 3 (Continued)

	Fit Parameter					
Z	**w**	**x**	**y**	**z**	**aa**	**ab**
Air	2.07E-06	-4.62E-06	5.74E-06	-4.14E-06	1.70E-06	-1.64E-07
Water	1.47E-06	-3.25E-06	4.08E-06	-2.99E-06	1.20E-06	-1.12E-07
13	8.37E-07	-2.10E-06	2.73E-06	-2.04E-06	8.87E-07	-1.03E-07
22	2.51E-07	-1.00E-06	1.57E-06	-1.30E-06	6.38E-07	-8.39E-08
26	6.92E-08	-7.60E-07	1.32E-06	-1.13E-06	5.79E-07	-8.90E-08
31	-1.13E-07	-4.52E-07	1.04E-06	-1.03E-06	5.59E-07	-7.43E-08
37	-2.33E-07	-2.83E-07	9.26E-07	-9.29E-07	5.32E-07	-8.31E-08
40	-3.66E-07	-1.04E-07	7.57E-07	-8.59E-07	5.15E-07	-8.12E-08
44	-3.27E-07	-1.34E-07	8.23E-07	-9.11E-07	5.31E-07	-8.08E-08
47	-3.64E-07	-8.95E-08	7.18E-07	-8.65E-07	5.27E-07	-8.23E-08
50	-4.09E-07	-1.48E-07	8.48E-07	-8.94E-07	5.30E-07	-8.34E-08
56	-4.50E-07	-7.91E-08	7.30E-07	-8.15E-07	4.85E-07	-7.96E-08
60	-3.62E-07	-2.30E-07	9.44E-07	-9.73E-07	5.33E-07	-8.38E-08
64	-4.45E-07	-1.03E-07	8.89E-07	-9.58E-07	5.28E-07	-7.64E-08
70	-3.93E-07	-1.85E-07	8.93E-07	-9.57E-07	5.60E-07	-8.89E-08
73	-4.34E-07	-8.74E-08	8.00E-07	-9.08E-07	5.57E-07	-9.19E-08
78	-3.62E-07	-2.46E-07	9.57E-07	-9.77E-07	5.58E-07	-9.18E-08
82	-4.08E-07	-2.71E-07	1.10E-06	-1.11E-06	5.76E-07	-8.01E-08
89	-3.05E-07	-4.18E-07	1.16E-06	-1.12E-06	6.27E-07	-9.46E-08
94	-2.91E-07	-4.95E-07	1.35E-06	-1.26E-06	6.69E-07	-9.63E-08

Table F 4. Planar dose profile fit parameters for 1 cm^2 dose averaging areas and electron energies ≥ 1.0 MeV.

	Fit Parameter										
Z	**a**	**b**	**c**	**d**	**e**	**f**	**g**	**h**	**i**	**j**	**k**
Air	1.51E-05	-1.25E-05	3.12E-06	-4.74E-06	4.62E-06	-1.75E-06	-2.14E-06	4.25E-06	-3.55E-06	8.22E-07	-9.48E-07
Water	1.76E-05	-1.56E-05	2.06E-06	-4.39E-06	5.56E-06	-1.69E-06	-1.91E-06	4.60E-06	-3.63E-06	9.39E-07	-8.84E-07
13	1.86E-05	-1.64E-05	2.21E-06	-4.73E-06	5.32E-06	-2.00E-06	-1.82E-06	4.62E-06	-3.52E-06	9.31E-07	-7.69E-07
22	1.93E-05	-1.67E-05	2.37E-06	-5.05E-06	5.35E-06	-1.99E-06	-1.90E-06	4.59E-06	-3.64E-06	8.76E-07	-7.38E-07
26	1.96E-05	-1.69E-05	2.54E-06	-5.19E-06	5.42E-06	-1.93E-06	-1.98E-06	4.58E-06	-3.73E-06	9.10E-07	-7.54E-07
31	1.96E-05	-1.70E-05	2.48E-06	-5.26E-06	5.54E-06	-1.99E-06	-2.02E-06	4.70E-06	-3.80E-06	9.15E-07	-7.64E-07
37	1.91E-05	-1.69E-05	1.77E-06	-5.13E-06	5.96E-06	-2.04E-06	-1.98E-06	5.14E-06	-3.84E-06	1.07E-06	-7.91E-07
40	1.98E-05	-1.71E-05	2.48E-06	-5.40E-06	5.73E-06	-2.00E-06	-2.09E-06	4.80E-06	-3.88E-06	9.32E-07	-7.82E-07
44	2.00E-05	-1.71E-05	2.55E-06	-5.48E-06	5.82E-06	-1.97E-06	-2.14E-06	4.85E-06	-3.93E-06	9.39E-07	-8.00E-07
47	2.00E-05	-1.71E-05	2.58E-06	-5.54E-06	5.87E-06	-2.00E-06	-2.18E-06	4.92E-06	-3.97E-06	9.63E-07	-8.12E-07
50	2.00E-05	-1.72E-05	2.53E-06	-5.55E-06	5.91E-06	-2.02E-06	-2.18E-06	4.96E-06	-4.02E-06	9.68E-07	-8.17E-07
56	1.99E-05	-1.72E-05	2.29E-06	-5.56E-06	6.05E-06	-2.13E-06	-2.18E-06	5.14E-06	-4.06E-06	9.72E-07	-8.29E-07
60	2.02E-05	-1.72E-05	2.50E-06	-5.64E-06	6.07E-06	-2.06E-06	-2.24E-06	5.08E-06	-4.08E-06	9.88E-07	-8.42E-07
64	2.02E-05	-1.73E-05	2.54E-06	-5.70E-06	6.13E-06	-2.06E-06	-2.28E-06	5.14E-06	-4.13E-06	9.92E-07	-8.60E-07
70	2.03E-05	-1.73E-05	2.51E-06	-5.75E-06	6.24E-06	-2.08E-06	-2.32E-06	5.20E-06	-4.19E-06	9.96E-07	-8.75E-07
73	2.03E-05	-1.73E-05	2.60E-06	-5.79E-06	6.30E-06	-2.08E-06	-2.35E-06	5.23E-06	-4.19E-06	1.00E-06	-8.93E-07
78	2.04E-05	-1.73E-05	2.64E-06	-5.84E-06	6.35E-06	-2.10E-06	-2.39E-06	5.29E-06	-4.23E-06	1.02E-06	-9.11E-07
82	2.04E-05	-1.73E-05	2.59E-06	-5.86E-06	6.39E-06	-2.10E-06	-2.39E-06	5.33E-06	-4.27E-06	1.02E-06	-9.13E-07
89	2.04E-05	-1.74E-05	2.59E-06	-5.89E-06	6.44E-06	-2.11E-06	-2.42E-06	5.38E-06	-4.31E-06	1.04E-06	-9.29E-07
94	2.05E-05	-1.74E-05	2.67E-06	-5.95E-06	6.52E-06	-2.15E-06	-2.47E-06	5.46E-06	-4.33E-06	1.04E-06	-9.57E-07

Table F 4 (Continued)

	Fit Parameter										
Z	**l**	**m**	**n**	**o**	**p**	**q**	**r**	**s**	**t**	**u**	**v**
Air	3.18E-06	-2.87E-06	1.63E-06	-2.04E-07	-3.70E-07	1.76E-06	-1.36E-06	8.23E-07	-3.28E-07	1.09E-07	-4.11E-08
Water	3.05E-06	-2.84E-06	1.56E-06	-2.67E-07	-3.91E-07	1.55E-06	-1.35E-06	7.37E-07	-3.00E-07	1.69E-07	-3.76E-08
13	3.14E-06	-2.65E-06	1.55E-06	-1.49E-07	-3.27E-07	1.58E-06	-1.22E-06	7.71E-07	-3.22E-07	9.78E-08	-6.29E-08
22	3.12E-06	-2.70E-06	1.52E-06	-2.08E-07	-2.44E-07	1.67E-06	-1.13E-06	8.23E-07	-2.54E-07	1.08E-07	-6.73E-08
26	3.09E-06	-2.74E-06	1.50E-06	-1.99E-07	-2.23E-07	1.66E-06	-1.18E-06	7.93E-07	-2.85E-07	9.69E-08	-5.02E-08
31	3.17E-06	-2.78E-06	1.53E-06	-2.11E-07	-2.25E-07	1.70E-06	-1.19E-06	8.17E-07	-2.72E-07	9.22E-08	-6.07E-08
37	3.36E-06	-2.83E-06	1.58E-06	-1.89E-07	-3.04E-07	1.67E-06	-1.31E-06	8.02E-07	-3.15E-07	9.20E-08	-6.28E-08
40	3.21E-06	-2.83E-06	1.56E-06	-2.13E-07	-2.28E-07	1.71E-06	-1.23E-06	8.12E-07	-2.68E-07	9.10E-08	-4.13E-08
44	3.19E-06	-2.85E-06	1.56E-06	-2.07E-07	-2.45E-07	1.69E-06	-1.26E-06	7.92E-07	-2.81E-07	9.47E-08	-2.48E-08
47	3.26E-06	-2.90E-06	1.57E-06	-1.96E-07	-2.50E-07	1.71E-06	-1.28E-06	8.18E-07	-3.05E-07	9.46E-08	-2.62E-08
50	3.29E-06	-2.89E-06	1.57E-06	-2.11E-07	-2.38E-07	1.74E-06	-1.28E-06	8.27E-07	-2.87E-07	9.09E-08	-3.57E-08
56	3.41E-06	-2.94E-06	1.60E-06	-2.45E-07	-2.42E-07	1.82E-06	-1.25E-06	8.86E-07	-2.36E-07	1.07E-07	-6.32E-08
60	3.35E-06	-2.96E-06	1.59E-06	-2.10E-07	-2.45E-07	1.76E-06	-1.31E-06	8.42E-07	-2.90E-07	9.47E-08	-3.47E-08
64	3.38E-06	-2.99E-06	1.61E-06	-2.12E-07	-2.65E-07	1.78E-06	-1.33E-06	8.43E-07	-2.91E-07	1.02E-07	-2.34E-08
70	3.43E-06	-3.03E-06	1.63E-06	-2.38E-07	-2.61E-07	1.82E-06	-1.35E-06	8.46E-07	-2.61E-07	1.01E-07	-2.51E-08
73	3.43E-06	-3.05E-06	1.64E-06	-2.31E-07	-2.82E-07	1.78E-06	-1.37E-06	8.48E-07	-2.64E-07	1.02E-07	-1.33E-08
78	3.47E-06	-3.08E-06	1.64E-06	-2.23E-07	-2.94E-07	1.79E-06	-1.40E-06	8.57E-07	-2.82E-07	9.88E-08	-1.03E-08
82	3.49E-06	-3.09E-06	1.65E-06	-2.22E-07	-2.96E-07	1.83E-06	-1.40E-06	8.59E-07	-2.98E-07	1.04E-07	-1.37E-08
89	3.53E-06	-3.12E-06	1.66E-06	-2.45E-07	-2.92E-07	1.83E-06	-1.41E-06	8.74E-07	-2.69E-07	9.86E-08	-1.64E-08
94	3.58E-06	-3.17E-06	1.70E-06	-2.25E-07	-3.12E-07	1.85E-06	-1.44E-06	8.81E-07	-2.95E-07	9.43E-08	-1.50E-08

Table F 4 (Continued)

	Fit Parameter					
Z	**w**	**x**	**y**	**z**	**aa**	**ab**
Air	9.62E-07	-1.32E-06	7.65E-07	-6.68E-08	-2.30E-07	4.87E-08
Water	9.37E-07	-1.22E-06	6.77E-07	6.40E-08	-3.49E-07	6.73E-08
13	7.62E-07	-1.26E-06	5.88E-07	-2.14E-08	-2.68E-07	5.54E-08
22	6.98E-07	-1.19E-06	5.73E-07	-3.75E-09	-2.84E-07	6.12E-08
26	7.30E-07	-1.13E-06	5.96E-07	9.57E-09	-2.63E-07	5.31E-08
31	7.24E-07	-1.15E-06	5.98E-07	5.18E-09	-2.64E-07	6.44E-08
37	7.06E-07	-1.24E-06	5.54E-07	1.50E-08	-2.88E-07	5.58E-08
40	7.35E-07	-1.13E-06	6.05E-07	9.33E-09	-2.65E-07	5.92E-08
44	7.56E-07	-1.13E-06	6.03E-07	1.07E-08	-2.65E-07	5.81E-08
47	7.66E-07	-1.14E-06	6.18E-07	1.36E-08	-2.69E-07	5.85E-08
50	7.53E-07	-1.15E-06	6.19E-07	6.16E-09	-2.63E-07	5.83E-08
56	7.26E-07	-1.20E-06	6.14E-07	-8.28E-09	-2.89E-07	6.00E-08
60	7.77E-07	-1.15E-06	6.21E-07	1.79E-08	-2.71E-07	6.43E-08
64	7.84E-07	-1.17E-06	6.29E-07	1.36E-08	-2.86E-07	6.33E-08
70	7.81E-07	-1.17E-06	6.40E-07	2.98E-09	-2.78E-07	5.65E-08
73	8.02E-07	-1.18E-06	6.39E-07	4.51E-09	-2.80E-07	6.29E-08
78	8.19E-07	-1.19E-06	6.43E-07	9.00E-09	-2.84E-07	6.46E-08
82	8.16E-07	-1.20E-06	6.62E-07	1.14E-08	-2.83E-07	5.64E-08
89	8.25E-07	-1.21E-06	6.58E-07	-4.53E-09	-2.76E-07	6.00E-08
94	8.49E-07	-1.24E-06	6.65E-07	5.27E-09	-2.74E-07	6.30E-08

Table F 5. Planar dose profile fit parameters for 10 cm^2 dose averaging areas and electron energies ≤ 1.0 MeV.

	Fit Parameter										
Z	**a**	**b**	**c**	**d**	**e**	**f**	**g**	**h**	**i**	**j**	**k**
Air	-2.29E-04	-4.14E-04	3.87E-04	-2.16E-04	6.30E-04	-1.91E-04	-7.59E-05	3.21E-04	-3.00E-04	6.16E-05	-1.74E-05
Water	-1.89E-04	-3.53E-04	3.27E-04	-1.78E-04	5.26E-04	-1.60E-04	-6.10E-05	2.63E-04	-2.47E-04	5.07E-05	-1.37E-05
13	-1.62E-04	-3.09E-04	2.85E-04	-1.51E-04	4.54E-04	-1.36E-04	-4.92E-05	2.18E-04	-2.08E-04	4.24E-05	-1.04E-05
22	5.12E-06	-1.17E-05	1.32E-05	-7.37E-06	8.48E-07	6.90E-08	-2.33E-07	-2.83E-07	9.26E-07	-9.29E-07	5.32E-07
26	-1.39E-04	-2.71E-04	2.49E-04	-1.25E-04	3.91E-04	-1.17E-04	-3.74E-05	1.77E-04	-1.74E-04	3.53E-05	-6.75E-06
31	-1.37E-04	-2.67E-04	2.45E-04	-1.22E-04	3.84E-04	-1.14E-04	-3.54E-05	1.71E-04	-1.70E-04	3.46E-05	-6.10E-06
37	-1.36E-04	-2.66E-04	2.44E-04	-1.21E-04	3.82E-04	-1.14E-04	-3.44E-05	1.69E-04	-1.69E-04	3.44E-05	-5.63E-06
40	-1.34E-04	-2.63E-04	2.41E-04	-1.18E-04	3.76E-04	-1.12E-04	-3.31E-05	1.65E-04	-1.65E-04	3.37E-05	-5.17E-06
44	-1.37E-04	-2.68E-04	2.45E-04	-1.21E-04	3.84E-04	-1.14E-04	-3.40E-05	1.69E-04	-1.69E-04	3.44E-05	-5.39E-06
47	-1.37E-04	-2.68E-04	2.46E-04	-1.21E-04	3.84E-04	-1.14E-04	-3.39E-05	1.68E-04	-1.68E-04	3.43E-05	-5.33E-06
50	-1.40E-04	-2.73E-04	2.50E-04	-1.23E-04	3.92E-04	-1.17E-04	-3.46E-05	1.72E-04	-1.72E-04	3.51E-05	-5.39E-06
56	-1.40E-04	-2.73E-04	2.50E-04	-1.23E-04	3.91E-04	-1.16E-04	-3.44E-05	1.71E-04	-1.71E-04	3.46E-05	-5.31E-06
60	-1.45E-04	-2.82E-04	2.59E-04	-1.28E-04	4.06E-04	-1.21E-04	-3.64E-05	1.80E-04	-1.79E-04	3.64E-05	-5.80E-06
64	-1.45E-04	-2.82E-04	2.59E-04	-1.28E-04	4.06E-04	-1.21E-04	-3.59E-05	1.79E-04	-1.79E-04	3.64E-05	-5.54E-06
70	-1.48E-04	-2.87E-04	2.63E-04	-1.31E-04	4.13E-04	-1.23E-04	-3.71E-05	1.83E-04	-1.82E-04	3.68E-05	-5.90E-06
73	-1.47E-04	-2.85E-04	2.62E-04	-1.29E-04	4.10E-04	-1.22E-04	-3.64E-05	1.81E-04	-1.80E-04	3.65E-05	-5.68E-06
78	-1.52E-04	-2.94E-04	2.70E-04	-1.34E-04	4.23E-04	-1.26E-04	-3.84E-05	1.88E-04	-1.86E-04	3.76E-05	-6.19E-06
82	-1.55E-04	-2.99E-04	2.75E-04	-1.37E-04	4.31E-04	-1.29E-04	-3.91E-05	1.92E-04	-1.91E-04	3.88E-05	-6.23E-06
89	-1.58E-04	-3.04E-04	2.80E-04	-1.40E-04	4.39E-04	-1.31E-04	-4.06E-05	1.97E-04	-1.94E-04	3.93E-05	-6.71E-06
94	-1.62E-04	-3.11E-04	2.87E-04	-1.44E-04	4.51E-04	-1.35E-04	-4.19E-05	2.03E-04	-2.01E-04	4.08E-05	-6.97E-06

Table F 5 (Continued)

	Fit Parameter										
Z	**l**	**m**	**n**	**o**	**p**	**q**	**r**	**s**	**t**	**u**	**v**
Air	1.05E-04	-1.38E-04	9.00E-05	-1.27E-05	-2.55E-06	2.08E-05	-3.64E-05	3.36E-05	-1.63E-05	1.69E-06	-2.22E-07
Water	8.36E-05	-1.12E-04	7.31E-05	-1.04E-05	-1.98E-06	1.61E-05	-2.85E-05	2.69E-05	-1.32E-05	1.34E-06	-1.61E-07
13	6.58E-05	-8.98E-05	5.96E-05	-8.45E-06	-1.37E-06	1.16E-05	-2.13E-05	2.05E-05	-1.03E-05	1.08E-06	-7.94E-08
22	-8.31E-08	-1.34E-04	-2.63E-04	2.41E-04	-1.18E-04	3.76E-04	-1.12E-04	-3.31E-05	1.65E-04	-1.65E-04	3.37E-05
26	4.77E-05	-6.92E-05	4.78E-05	-6.82E-06	-6.58E-07	6.71E-06	-1.38E-05	1.44E-05	-7.74E-06	8.68E-07	3.18E-08
31	4.46E-05	-6.62E-05	4.65E-05	-6.71E-06	-5.24E-07	5.77E-06	-1.24E-05	1.36E-05	-7.51E-06	8.58E-07	4.61E-08
37	4.30E-05	-6.50E-05	4.60E-05	-6.63E-06	-4.07E-07	5.12E-06	-1.17E-05	1.32E-05	-7.37E-06	8.48E-07	6.90E-08
40	4.10E-05	-6.29E-05	4.49E-05	-6.52E-06	-2.98E-07	4.48E-06	-1.09E-05	1.26E-05	-7.18E-06	8.42E-07	9.13E-08
44	4.22E-05	-6.45E-05	4.59E-05	-6.66E-06	-3.44E-07	4.73E-06	-1.12E-05	1.30E-05	-7.38E-06	8.54E-07	8.21E-08
47	4.18E-05	-6.39E-05	4.56E-05	-6.64E-06	-3.25E-07	4.61E-06	-1.10E-05	1.27E-05	-7.30E-06	8.61E-07	9.39E-08
50	4.30E-05	-6.60E-05	4.69E-05	-6.75E-06	-2.86E-07	4.71E-06	-1.16E-05	1.32E-05	-7.47E-06	8.64E-07	1.01E-07
56	4.25E-05	-6.51E-05	4.61E-05	-6.60E-06	-2.62E-07	4.55E-06	-1.12E-05	1.28E-05	-7.21E-06	8.42E-07	1.17E-07
60	4.54E-05	-6.91E-05	4.88E-05	-7.00E-06	-3.46E-07	5.19E-06	-1.23E-05	1.39E-05	-7.77E-06	8.93E-07	1.12E-07
64	4.46E-05	-6.86E-05	4.88E-05	-7.00E-06	-2.84E-07	4.80E-06	-1.20E-05	1.38E-05	-7.77E-06	8.82E-07	1.12E-07
70	4.61E-05	-6.99E-05	4.93E-05	-7.07E-06	-3.49E-07	5.21E-06	-1.24E-05	1.40E-05	-7.83E-06	9.08E-07	1.09E-07
73	4.51E-05	-6.88E-05	4.88E-05	-7.01E-06	-3.11E-07	4.91E-06	-1.19E-05	1.37E-05	-7.74E-06	9.01E-07	1.11E-07
78	4.79E-05	-7.21E-05	5.05E-05	-7.19E-06	-3.91E-07	5.56E-06	-1.29E-05	1.44E-05	-7.97E-06	9.09E-07	1.03E-07
82	4.90E-05	-7.44E-05	5.23E-05	-7.47E-06	-3.61E-07	5.61E-06	-1.35E-05	1.52E-05	-8.38E-06	9.38E-07	1.14E-07
89	5.11E-05	-7.62E-05	5.30E-05	-7.56E-06	-4.58E-07	6.22E-06	-1.41E-05	1.55E-05	-8.50E-06	9.73E-07	1.06E-07
94	5.30E-05	-7.92E-05	5.53E-05	-7.89E-06	-4.89E-07	6.54E-06	-1.50E-05	1.65E-05	-8.97E-06	1.01E-06	9.54E-08

Table F 5 (Continued)

	Fit Parameter					
Z	**w**	**x**	**y**	**z**	**aa**	**ab**
Air	2.00E-06	-4.39E-06	5.35E-06	-3.71E-06	1.48E-06	-1.51E-07
Water	1.47E-06	-3.25E-06	4.08E-06	-2.99E-06	1.20E-06	-1.12E-07
13	8.40E-07	-2.11E-06	2.73E-06	-2.04E-06	8.87E-07	-1.03E-07
22	-5.17E-06	4.10E-05	-6.29E-05	4.49E-05	-6.52E-06	-2.98E-07
26	6.92E-08	-7.60E-07	1.32E-06	-1.13E-06	5.79E-07	-8.90E-08
31	-9.96E-08	-4.76E-07	1.06E-06	-1.03E-06	5.59E-07	-7.42E-08
37	-2.33E-07	-2.83E-07	9.26E-07	-9.29E-07	5.32E-07	-8.31E-08
40	-3.66E-07	-1.04E-07	7.57E-07	-8.59E-07	5.15E-07	-8.12E-08
44	-3.27E-07	-1.34E-07	8.23E-07	-9.11E-07	5.31E-07	-8.08E-08
47	-3.64E-07	-8.95E-08	7.18E-07	-8.65E-07	5.27E-07	-8.23E-08
50	-4.09E-07	-1.48E-07	8.48E-07	-8.94E-07	5.30E-07	-8.34E-08
56	-4.50E-07	-7.91E-08	7.30E-07	-8.15E-07	4.85E-07	-7.96E-08
60	-3.62E-07	-2.30E-07	9.44E-07	-9.73E-07	5.33E-07	-8.38E-08
64	-4.45E-07	-1.03E-07	8.89E-07	-9.58E-07	5.28E-07	-7.64E-08
70	-3.93E-07	-1.85E-07	8.93E-07	-9.57E-07	5.60E-07	-8.89E-08
73	-4.34E-07	-8.74E-08	8.00E-07	-9.08E-07	5.57E-07	-9.19E-08
78	-3.62E-07	-2.46E-07	9.57E-07	-9.77E-07	5.58E-07	-9.18E-08
82	-4.08E-07	-2.71E-07	1.10E-06	-1.11E-06	5.76E-07	-8.01E-08
89	-3.05E-07	-4.18E-07	1.16E-06	-1.12E-06	6.27E-07	-9.46E-08
94	-2.91E-07	-4.95E-07	1.35E-06	-1.26E-06	6.69E-07	-9.63E-08

Table F 6. Planar dose profile fit parameters for 10 cm^2 dose averaging areas and electron energies ≥ 1.0 MeV.

	Fit Parameter										
Z	**a**	**b**	**c**	**d**	**e**	**f**	**g**	**h**	**i**	**j**	**k**
Air	1.68E-05	-1.11E-05	5.03E-06	-4.36E-06	6.29E-06	-1.85E-06	-2.39E-06	4.69E-06	-3.33E-06	3.40E-07	-1.17E-06
Water	2.03E-05	-1.46E-05	4.80E-06	-4.32E-06	6.48E-06	-2.14E-06	-2.11E-06	4.59E-06	-3.17E-06	2.10E-07	-1.01E-06
13	2.11E-05	-1.50E-05	5.19E-06	-4.68E-06	6.56E-06	-1.97E-06	-2.19E-06	4.55E-06	-3.27E-06	2.45E-07	-9.76E-07
22	2.17E-05	-1.52E-05	5.20E-06	-4.89E-06	6.82E-06	-1.99E-06	-2.27E-06	4.66E-06	-3.27E-06	2.30E-07	-9.70E-07
26	2.19E-05	-1.53E-05	5.22E-06	-4.96E-06	6.97E-06	-2.00E-06	-2.32E-06	4.75E-06	-3.33E-06	2.52E-07	-9.90E-07
31	2.20E-05	-1.54E-05	5.22E-06	-5.05E-06	7.11E-06	-2.04E-06	-2.37E-06	4.85E-06	-3.38E-06	2.49E-07	-1.00E-06
37	2.20E-05	-1.55E-05	5.00E-06	-5.12E-06	7.13E-06	-2.20E-06	-2.38E-06	4.93E-06	-3.46E-06	2.03E-07	-9.94E-07
40	2.22E-05	-1.55E-05	5.21E-06	-5.16E-06	7.31E-06	-2.09E-06	-2.43E-06	4.97E-06	-3.43E-06	2.51E-07	-1.02E-06
44	2.23E-05	-1.55E-05	5.24E-06	-5.22E-06	7.39E-06	-2.08E-06	-2.46E-06	5.06E-06	-3.49E-06	2.61E-07	-1.04E-06
47	2.24E-05	-1.56E-05	5.28E-06	-5.28E-06	7.45E-06	-2.11E-06	-2.49E-06	5.13E-06	-3.53E-06	2.81E-07	-1.05E-06
50	2.24E-05	-1.56E-05	5.26E-06	-5.29E-06	7.49E-06	-2.13E-06	-2.51E-06	5.15E-06	-3.55E-06	2.77E-07	-1.06E-06
56	2.25E-05	-1.56E-05	5.23E-06	-5.36E-06	7.59E-06	-2.20E-06	-2.55E-06	5.23E-06	-3.59E-06	2.76E-07	-1.07E-06
60	2.26E-05	-1.57E-05	5.26E-06	-5.38E-06	7.66E-06	-2.18E-06	-2.56E-06	5.27E-06	-3.60E-06	2.85E-07	-1.08E-06
64	2.26E-05	-1.57E-05	5.30E-06	-5.43E-06	7.71E-06	-2.20E-06	-2.59E-06	5.34E-06	-3.65E-06	2.85E-07	-1.10E-06
70	2.27E-05	-1.57E-05	5.29E-06	-5.48E-06	7.83E-06	-2.22E-06	-2.63E-06	5.41E-06	-3.70E-06	2.88E-07	-1.11E-06
73	2.28E-05	-1.58E-05	5.33E-06	-5.51E-06	7.88E-06	-2.24E-06	-2.65E-06	5.46E-06	-3.71E-06	2.92E-07	-1.13E-06
78	2.28E-05	-1.58E-05	5.36E-06	-5.55E-06	7.94E-06	-2.25E-06	-2.68E-06	5.52E-06	-3.75E-06	3.15E-07	-1.15E-06
82	2.28E-05	-1.58E-05	5.34E-06	-5.57E-06	7.99E-06	-2.26E-06	-2.69E-06	5.56E-06	-3.78E-06	3.14E-07	-1.15E-06
89	2.29E-05	-1.58E-05	5.35E-06	-5.61E-06	8.05E-06	-2.28E-06	-2.72E-06	5.62E-06	-3.82E-06	3.23E-07	-1.17E-06
94	2.29E-05	-1.58E-05	5.40E-06	-5.65E-06	8.11E-06	-2.32E-06	-2.75E-06	5.70E-06	-3.83E-06	3.16E-07	-1.19E-06

Table F 6 (Continued)

	Fit Parameter										
Z	**l**	**m**	**n**	**o**	**p**	**q**	**r**	**s**	**t**	**u**	**v**
Air	3.09E-06	-2.48E-06	8.43E-07	-7.49E-08	-5.09E-07	1.50E-06	-1.29E-06	5.18E-07	-1.65E-07	8.13E-09	-9.23E-08
Water	2.86E-06	-2.19E-06	7.68E-07	-4.67E-08	-4.43E-07	1.35E-06	-1.12E-06	4.95E-07	-1.38E-07	9.42E-08	-8.82E-08
13	2.77E-06	-2.25E-06	7.27E-07	-6.48E-08	-4.08E-07	1.27E-06	-1.13E-06	4.62E-07	-1.88E-07	2.01E-08	-6.16E-08
22	2.76E-06	-2.24E-06	7.30E-07	-6.39E-08	-3.89E-07	1.23E-06	-1.13E-06	4.42E-07	-1.70E-07	2.04E-08	-4.38E-08
26	2.79E-06	-2.25E-06	7.18E-07	-7.49E-08	-3.82E-07	1.24E-06	-1.14E-06	4.61E-07	-1.64E-07	2.58E-08	-4.30E-08
31	2.84E-06	-2.28E-06	7.38E-07	-8.04E-08	-3.88E-07	1.27E-06	-1.16E-06	4.78E-07	-1.57E-07	3.17E-08	-4.40E-08
37	2.89E-06	-2.27E-06	7.11E-07	-7.32E-08	-3.83E-07	1.29E-06	-1.17E-06	4.75E-07	-1.77E-07	3.18E-08	-3.27E-08
40	2.89E-06	-2.32E-06	7.57E-07	-8.51E-08	-3.92E-07	1.29E-06	-1.18E-06	4.84E-07	-1.55E-07	1.74E-08	-3.55E-08
44	2.91E-06	-2.34E-06	7.62E-07	-8.33E-08	-3.98E-07	1.31E-06	-1.18E-06	4.78E-07	-1.57E-07	2.13E-08	-4.06E-08
47	2.97E-06	-2.37E-06	7.65E-07	-6.10E-08	-4.04E-07	1.32E-06	-1.21E-06	4.95E-07	-1.91E-07	3.09E-08	-3.92E-08
50	2.98E-06	-2.35E-06	7.63E-07	-7.69E-08	-4.04E-07	1.33E-06	-1.22E-06	4.97E-07	-1.66E-07	2.17E-08	-3.62E-08
56	3.03E-06	-2.41E-06	7.74E-07	-7.94E-08	-4.08E-07	1.35E-06	-1.24E-06	4.98E-07	-1.64E-07	2.03E-08	-3.93E-08
60	3.04E-06	-2.40E-06	7.72E-07	-7.72E-08	-4.02E-07	1.35E-06	-1.24E-06	5.13E-07	-1.68E-07	2.01E-08	-4.53E-08
64	3.08E-06	-2.44E-06	7.97E-07	-6.82E-08	-4.25E-07	1.38E-06	-1.25E-06	5.08E-07	-1.81E-07	3.23E-08	-3.07E-08
70	3.13E-06	-2.47E-06	8.11E-07	-1.00E-07	-4.20E-07	1.41E-06	-1.28E-06	5.18E-07	-1.43E-07	2.26E-08	-3.56E-08
73	3.16E-06	-2.49E-06	8.27E-07	-9.75E-08	-4.28E-07	1.42E-06	-1.29E-06	5.27E-07	-1.46E-07	2.54E-08	-4.36E-08
78	3.21E-06	-2.53E-06	8.16E-07	-8.20E-08	-4.38E-07	1.44E-06	-1.30E-06	5.37E-07	-1.73E-07	3.33E-08	-4.24E-08
82	3.22E-06	-2.53E-06	8.25E-07	-8.33E-08	-4.43E-07	1.46E-06	-1.31E-06	5.41E-07	-1.77E-07	2.97E-08	-4.13E-08
89	3.26E-06	-2.56E-06	8.37E-07	-9.89E-08	-4.41E-07	1.46E-06	-1.33E-06	5.49E-07	-1.65E-07	2.74E-08	-4.66E-08
94	3.32E-06	-2.60E-06	8.77E-07	-8.19E-08	-4.57E-07	1.50E-06	-1.34E-06	5.51E-07	-1.87E-07	2.10E-08	-4.34E-08

Table F 6 (Continued)

	Fit Parameter					
Z	**w**	**x**	**y**	**z**	**aa**	**ab**
Air	8.68E-07	-9.10E-07	4.44E-07	-1.44E-07	2.00E-07	1.73E-08
Water	7.67E-07	-7.82E-07	3.67E-07	-1.75E-07	1.36E-07	3.41E-08
13	7.27E-07	-7.21E-07	3.69E-07	-1.11E-07	1.80E-07	3.90E-08
22	6.51E-07	-6.46E-07	3.25E-07	-1.21E-07	1.80E-07	3.96E-08
26	6.33E-07	-6.40E-07	3.14E-07	-1.20E-07	1.78E-07	2.44E-08
31	6.36E-07	-6.50E-07	3.19E-07	-1.36E-07	1.72E-07	4.15E-08
37	6.43E-07	-6.04E-07	3.32E-07	-1.30E-07	2.04E-07	3.95E-08
40	6.13E-07	-6.41E-07	3.19E-07	-1.30E-07	1.90E-07	3.37E-08
44	6.20E-07	-6.48E-07	3.14E-07	-1.38E-07	1.87E-07	3.69E-08
47	6.29E-07	-6.54E-07	3.32E-07	-1.35E-07	1.74E-07	3.35E-08
50	6.18E-07	-6.50E-07	3.31E-07	-1.48E-07	1.90E-07	3.65E-08
56	6.35E-07	-6.54E-07	3.42E-07	-1.55E-07	1.95E-07	3.93E-08
60	6.32E-07	-6.47E-07	3.22E-07	-1.38E-07	1.93E-07	4.05E-08
64	6.37E-07	-6.64E-07	3.37E-07	-1.40E-07	1.76E-07	4.55E-08
70	6.41E-07	-6.66E-07	3.41E-07	-1.59E-07	2.02E-07	3.48E-08
73	6.57E-07	-6.79E-07	3.49E-07	-1.55E-07	1.91E-07	4.40E-08
78	6.62E-07	-6.98E-07	3.51E-07	-1.44E-07	1.73E-07	4.00E-08
82	6.61E-07	-7.08E-07	3.59E-07	-1.54E-07	1.85E-07	3.68E-08
89	6.75E-07	-7.13E-07	3.64E-07	-1.61E-07	1.93E-07	3.38E-08
94	6.94E-07	-7.35E-07	3.75E-07	-1.60E-07	1.97E-07	3.74E-08

Appendix G – Beta-Particle Spectra

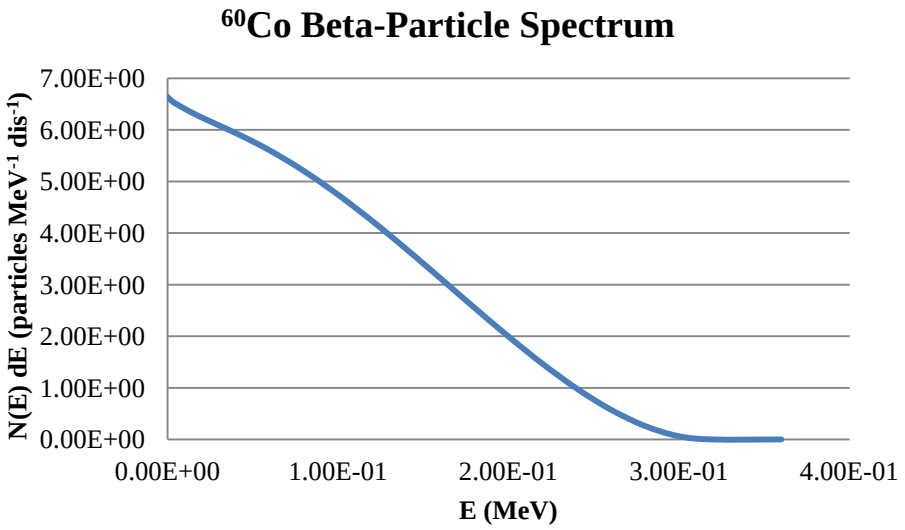

Fig. G 1. ICRP 107 beta-particle spectrum for ^{60}Co.

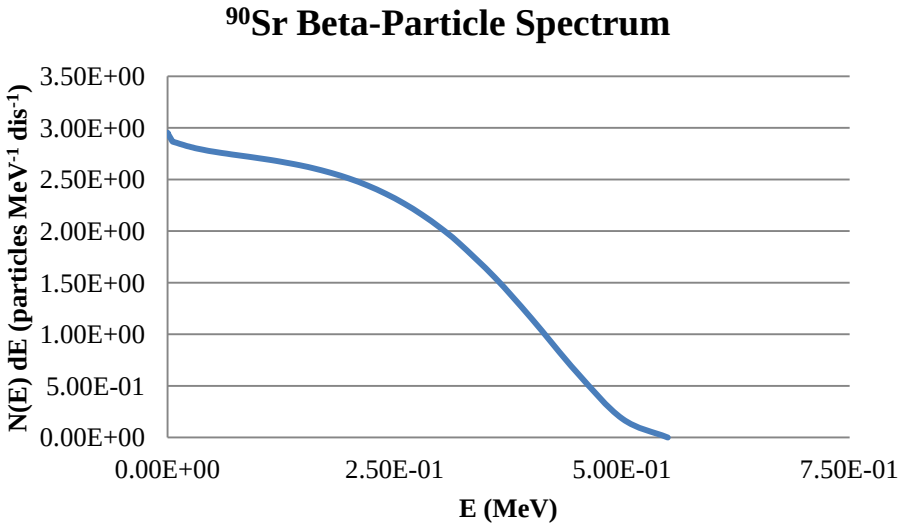

Fig. G 2. ICRP 107 beta-particle spectrum for ^{90}Sr.

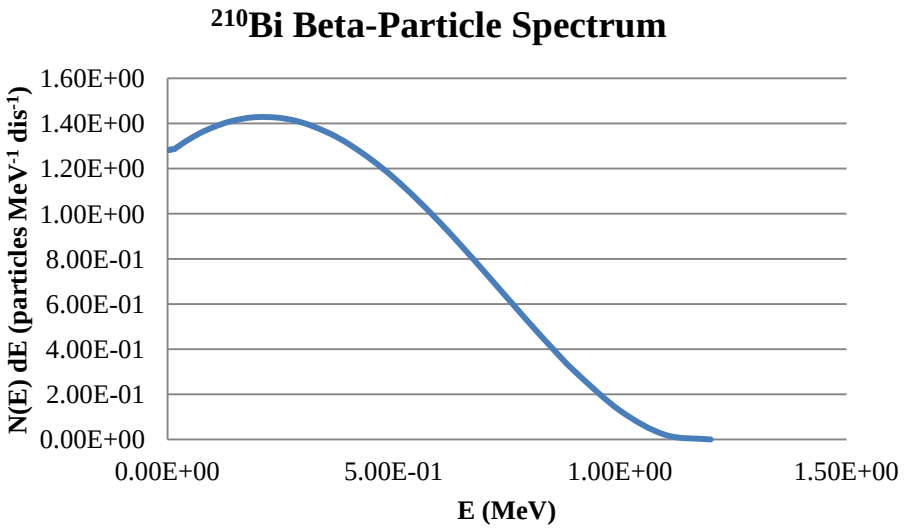

Fig. G 3. ICRP 107 beta-particle spectrum for ^{210}Bi.

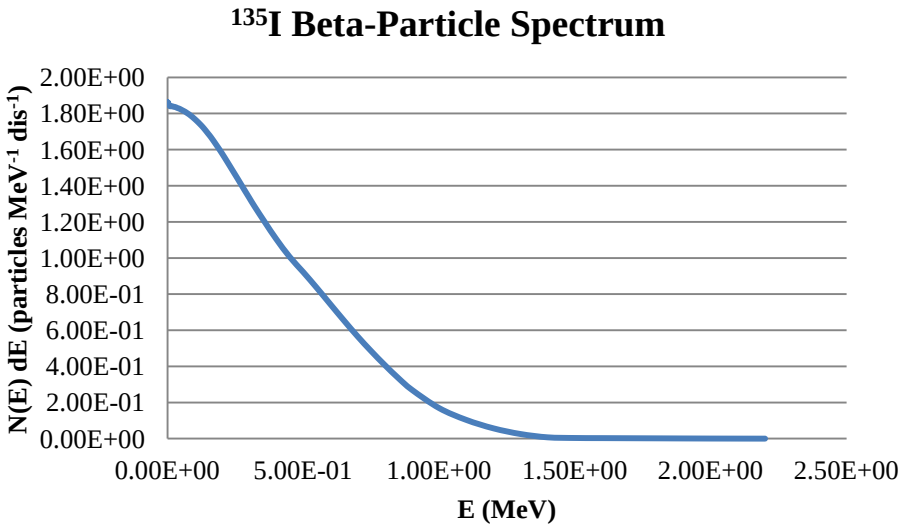

Fig. G 4. ICRP 107 beta-particle spectrum for ^{135}I.

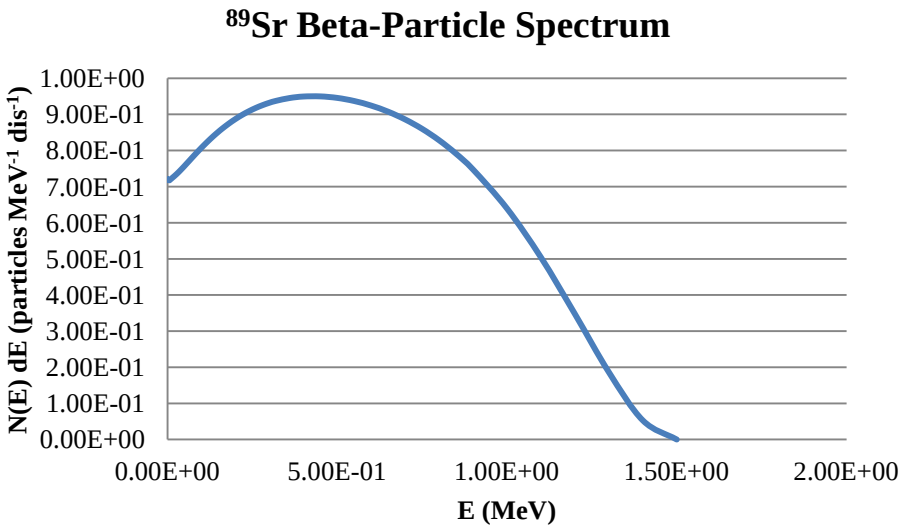

Fig. G 5. ICRP 107 beta-particle spectrum for ^{89}89.

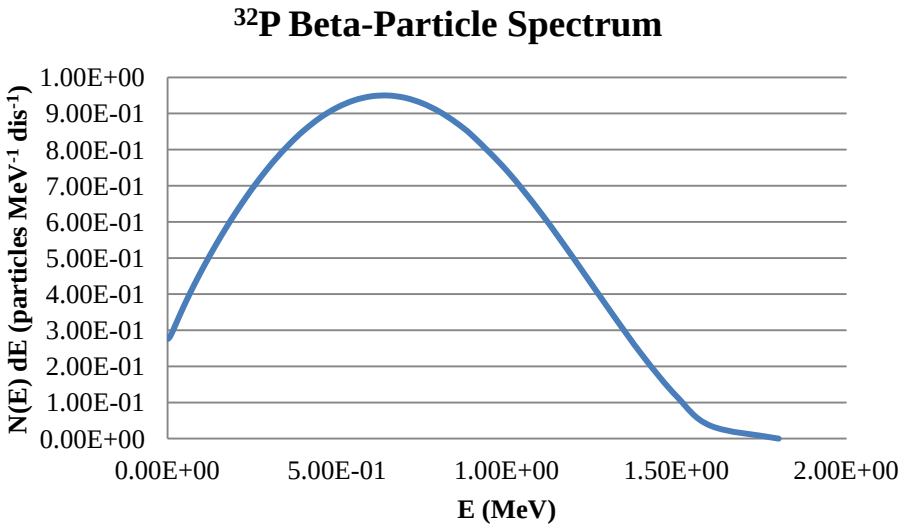

Fig. G 6. ICRP 107 beta-particle spectrum for ^{32}P.

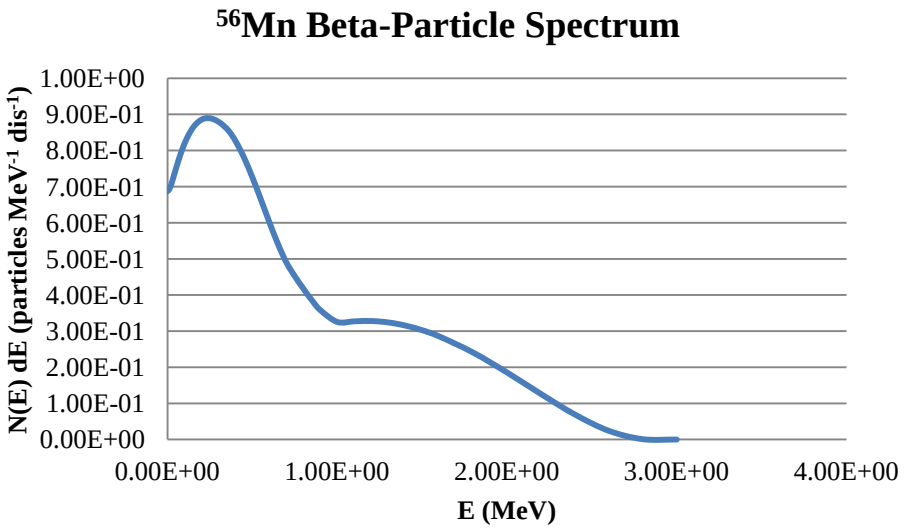

Fig. G 7. ICRP 107 beta-particle spectrum for ^{56}Mn.

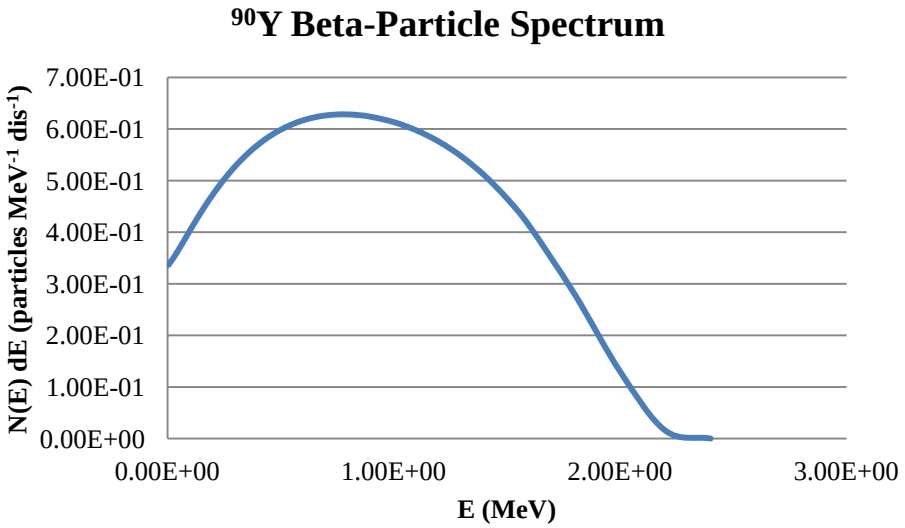

Fig. G 8. ICRP 107 beta-particle spectrum for ^{90}Y.

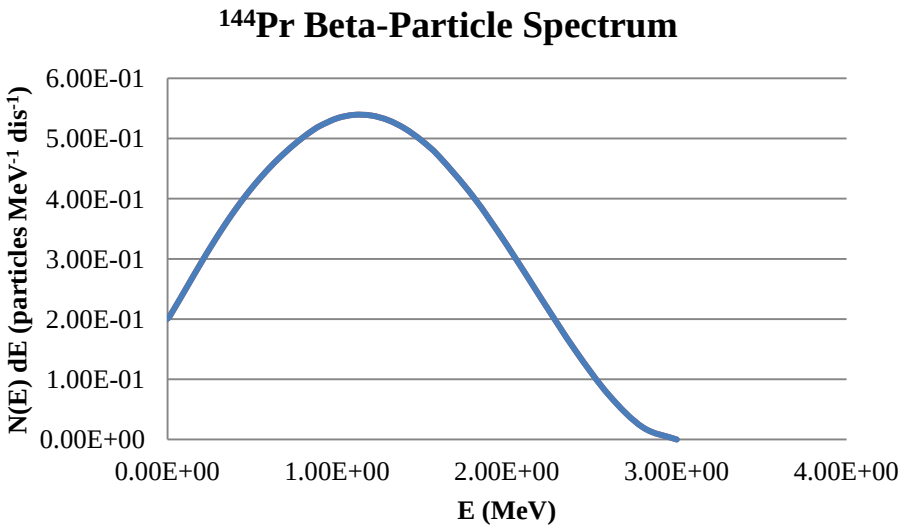

Fig. G 9. ICRP 107 beta-particle spectrum for ^{144}Pr.